Dissertation zur Erlangung des Doktorgrades
der Fakultät für Chemie und Pharmazie
der Ludwig-Maximilians-Universität München

---

# Single-Molecule Fluorescence Spectroscopy

## From Two to Three Colors and Beyond

---

Anders Barth

aus

Bad Oldesloe, Deutschland

2018

## Erklärung

Diese Dissertation wurde im Sinne von § 7 der Promotionsordnung vom 28. November 2011 von Herrn Prof. Don C. Lamb, Ph.D., betreut.

## Eidesstattliche Versicherung

Diese Dissertation wurde eigenständig und ohne unerlaubte Hilfe erarbeitet.

München, 20.12.2018

Anders Barth

| | |
|---|---|
| Dissertation eingereicht am: | 05.11.2018 |
| 1. Gutachter | Prof. Don C. Lamb, Ph.D. |
| 2. Gutachter | Prof. Dr. Christoph Bräuchle |
| Mündliche Prüfung am: | 04.12.2018 |

# Abstract

## Single-Molecule Fluorescence Spectroscopy: From Two to Three Colors and Beyond

by Anders BARTH

Single-molecule fluorescence spectroscopy is a powerful tool for the study of physical and biological processes through the use of fluorescent probes. By combining the femtoliter-sized observation volume of a confocal microscope with low concentrations of analytes, single fluorescent molecules can be observed as they freely diffuse in solution. From the many parameters of the fluorescence signal, a wealth of information is obtained about the structure, dynamics and interactions of the studied system. The objective of this thesis was the development, implementation and application of quantitative single-molecule fluorescence methods. To this end, a software framework for the analysis of solution-based single-molecule measurements of Förster resonance energy transfer (FRET) has been developed as part of the *PAM* software package. In addition, the new method of three-color photon distribution analysis (3C-PDA) is introduced in this thesis, enabling a quantitative analysis of single-molecule three-color FRET experiments. The developed analysis framework has been applied to elucidate coordinated conformational changes in the Hsp70 chaperone protein BiP, to study the conformational dynamics of a small fragment of the cellulosome, to investigate energy transfer pathways in complex artificial dye arrangements and to quantify the nanosecond dynamics of an intrinsically disordered peptide. For several studies, molecular dynamics (MD) simulations have also been used to support and cross-validate the experimental results. Here, the focus is to provide a comprehensive overview of the used methodologies, their theoretical background and their application to the various experimental systems.

# Contents

# Chapter 1

# Introduction

## Fluorescence microscopy and spectroscopy

Nowadays, fluorescence is one the most commonly used tools in the life sciences, facilitated by many developments over the past three decades. The discovery and optimization of fluorescent proteins (awarded the Nobel prize in chemistry in 2008) turned fluorescence live-cell imaging into the standard tool that it is today, providing the means to observe specific components of the cellular machinery in real time. On the microscopy side, the circumvention of the diffraction limit by super-resolved imaging methods such as stochastic optical reconstruction microscopy (STORM), photo-activated localization microscopy (PALM) and stimulated emission depletion microscopy (STED) has transformed our understanding of cellular processes on the nanometer scale, and was awarded the Nobel prize in chemistry in 2014. Owing to the high achievable signal-to-noise ratio in fluorescence microscopy, it becomes possible to image and study single-molecules. As originally documented by Stokes (Stokes, 1852), the fluorescence emission is red-shifted with respect to the wavelength of the excitation source, allowing scattered excitation light to be efficiently filtered. The informational content of the fluorescence signal is not limited to its intensity, however. A number of parameters of the fluorescence signal, such as the wavelength, lifetime and polarization, are highly sensitive to the environment of the fluorophore. Combined with the possibility to specifically label the molecule of interest, this renders fluorescent probes excellent reporters for *in vitro* or *in vivo* studies, where they are nowadays routinely used to monitor the conformation and interactions of biomolecules through the spectroscopic readout. Still, the fluorescence intensity also encodes a wealth of information about dynamic parameters in its fluctuations, as used in fluorescence fluctuation spectroscopy.

## Studying biomolecules on the single-molecule level

The observation of single molecules sets high experimental demands. To be able to detect the weak signal of a single molecule, it is important to reduce the background signal to a minimum. The main background contributions originate from Rayleigh and Raman scattering of the solvent. While the use of emission filters with high extinction ratios removes most of the scattered excitation light, the Raman signal often overlaps with the fluorescence emission. To increase the signal-to-noise ratio, the observation volume has to be reduced to the size of about 1 femtoliter ($10^{-15}$ l), e.g. through the use of confocal optics or total internal reflection microscopy. The detection of the weak signal also requires detectors with single photon sensitivity and high detection efficiency such as avalanche photodiodes (APD) or charge-coupled devices (CCD). With these tools, the first observations of single fluorescent molecules have been reported for molecules embedded in solids through their absorption (Moerner and Kador, 1989; Orrit and Bernard, 1990) and in solution by means of their fluorescent signal (Brooks Shera et al., 1990). Since then, applications of fluorescence have been used to study many important biological processes on the single-molecule level.

A key method hereby is Förster resonance energy transfer (FRET, Förster, 1948). By placing two spectrally different fluorophores on the molecule or complex of interest, it is possible to measure their distance from the efficiency of energy transfer between them (causing FRET to be commonly referred to as a "molecular ruler", Stryer and Haugland, 1967). The applications of FRET are plenty. Following its first realization on the single-molecule level (Ha et al., 1996), single-pair FRET is now routinely used to study the conformations and dynamics of proteins and nucleic acids from nanoseconds to seconds and minutes. The ability to reveal the heterogeneity of the studied system molecule by molecule makes it possible to detect conformational states that would otherwise be lost in the ensemble, and to watch molecules switch between them in real time.

The measurement of single-molecule FRET in this work is performed on freely diffusing molecules using the small observation volume of a confocal microscope. At picomolar concentrations, single-molecules are seen as spikes or bursts of fluorescence, giving rise to the name "burst analysis" (Zander et al., 1996). From the photons of individual single-molecule events, different quantities such as the FRET efficiency, anisotropy or lifetime can be calculated, revealing the molecule-wise distributions and allowing the identification of the different species present in the sample. The single-molecule FRET efficiency distribution then directly reflects the conformational heterogeneity of the studied system. However, why stop at two colors? By introducing a third fluorophore, all three interdye distances can be determined from the experiment, opening up a new dimension in the analysis. By measuring the co-occurrence of distances, correlated distance changes during conformational transitions can be detected. A large part of this work has focused on developing a quantitative framework for single-molecule three-color FRET using burst analysis. A related method to burst analysis is fluorescence correlation spectroscopy (FCS). By analyzing the fluctuations of the fluorescence signal of molecules diffusing into and out of the confocal volume, information may be obtained about their number and diffusion time. However, FCS is not limited to the study of diffusion. Since the method is sensitive to any process that affects the fluorescence signal, it may likewise be applied to study the conformational dynamics of biomolecules when combined with fluorescence quenching or FRET, as demonstrated in this work.

While instrumentation has not seen significant changes over the last decade, many new analysis methods are continuously being developed. The stochastic nature of photon emission and the low signal obtained from single molecules have led to the application of advanced statistical methods to obtain quantitative information from noisy data. Necessitated by the low number of photons detected from freely diffusing molecules, the question of how to extract the maximum amount of information from the data is a recurring theme in this work. In recent years, considerable efforts have also been undertaken to take advantage of the structural information provided by single-molecule FRET. By combining the distance information from multiple FRET sensors with structural modeling, it becomes possible to refine the structure even of dynamic complexes (Kalinin et al., 2012; Muschielok et al., 2008). With advancements in computing power, it has also become feasible (and affordable) to perform detailed atomistic simulations of large biomolecular systems. For several projects in this thesis, molecular dynamics (MD) simulations provided additional insights into the studied systems and were used for cross-validation of the experimental and theoretical results.

## Outline

Following a short introduction on fluorescence and its fundamental properties, the different concepts and methods related to this thesis are described in chapter 2. After introducing the theoretical basis of Förster resonance energy transfer (FRET) and photoinduced electron transfer (PET), which are used as reporters on intramolecular distances, the sections on confocal microscopy, time-correlated single-photon counting and pulsed interleaved excitation describe the principles of the applied instrumentation. In the following sections, the methods of fluorescence correlation spectroscopy and single-molecule FRET by burst analysis are described in detail and examples from work published along this thesis are used to highlight key aspects. The last sections introduce the basics of molecular dynamics simulation, applied in several projects of this thesis, and present an overview of different aspects of model-based data analysis. Chapter 3 provides a short overview of the work published during this thesis, given by the development of a quantitative framework for the analysis of single-molecule three-color FRET experiments by burst analysis, called three-color photon distribution analysis (3C-PDA), the analysis of energy transfer pathways in artificial dye assemblies, the quantification of the conformational dynamics of a two-domain protein, the study of the quenching dynamics of a small peptide and the introduction of the *PAM* software package for the analysis of fluorescence data.

# Chapter 2

# Concepts and Methods

## 2.1 Fluorescence

### 2.1.1 The basics of fluorescence

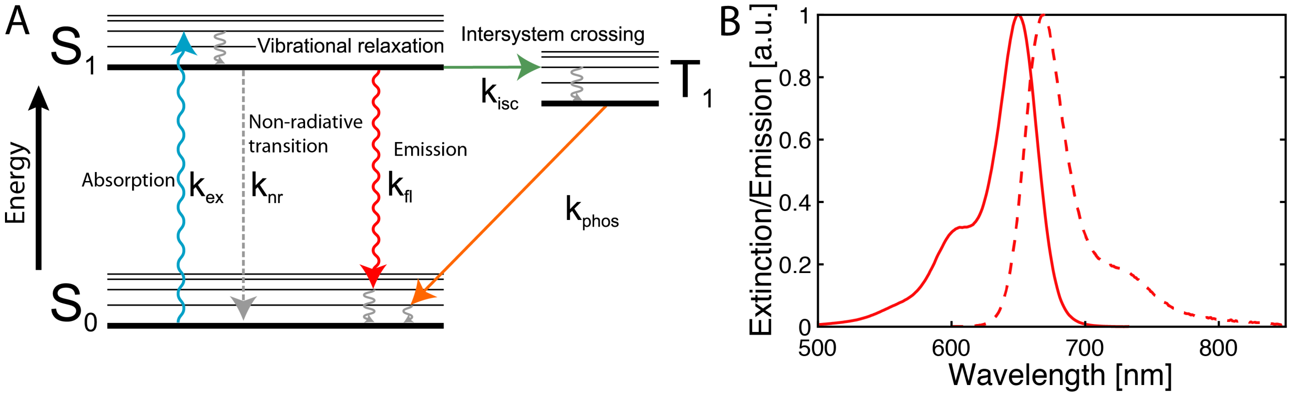

FIGURE 2.1: The basics of fluorescence. (**A**) A Jablonski diagram depicting the processes occurring during fluorescence. $S_0$, $S_1$: singlet ground and first excited state, $T_1$: triplet state, $k_{\text{ex}}$: excitation rate, $k_{\text{nr}}$: non-radiative relaxation rate, $k_{\text{fl}}$: fluorescence emission rate, $k_{\text{isc}}$: intersystem crossing rate, $k_{\text{phos}}$: phosphorescence emission rate. (**B**) Extinction (solid line) and emission spectrum (dashed line) of the fluorophore Alexa647 in water.

Fluorescence is the relaxation from an electronic excited state $S_n$ to the ground state $S_0$ by emission of a photon, after being excited by absorption of a photon. The processes occurring after excitation of the fluorescent molecule are illustrated using a Jablonski diagram (Figure 2.1 A, Jabłoński, 1935). Excitation generally occurs from the vibronic ground state of $S_0$ to a higher vibronic state of $S_1$. The nuclear coordinates remain unchanged during the quasi-instantaneous electronic transition, occurring on the femtosecond timescale. Consequently, the transition probabilities from the vibronic ground state of $S_0$ to the different vibronic states of $S_1$ are determined by the overlap of the vibronic wave functions (Franck-Condon principle, Condon, 1926, 1928; Franck and Dymond, 1926). Because significant overlap exists for different vibrational states of $S_1$, broad absorption spectra are usually observed for fluorescent molecules (Figure 2.1 B). After excitation, the molecule relaxes to the vibronic ground state of $S_1$ on the picosecond timescale. The transition back to $S_0$ thus occurs from the vibronic ground state of $S_1$, rendering the emission spectrum independent of the excitation wavelength (Kasha's rule, Kasha, 1950). Since the vibronic wave functions of $S_1$ and $S_0$ are similar, relaxation occurs to higher vibronic states of $S_0$ with similar transition probabilities as for absorption. Thus, the energy of the emitted photons is reduced (Stokes shift, Stokes, 1852) and the emission spectrum shows a similar shape as the absorption spectrum, but with inverse energy dependence (mirror image rule, see Figure 2.1 B). The dwell time in the $S_1$ state is on the order of nanoseconds.

There exist several competing pathways for the relaxation from the $S_1$ state. Non-radiative pathways are for example given by internal conversion or electron transfer to or from potential redox partners. A transition that is theoretically forbidden is intersystem crossing from the singlet excited state to a triplet state $T_1$ through spin inversion of the excited state electron. The transition becomes weakly allowed through spin-orbit coupling, and consequently is a slow process occurring on the micro- to millisecond timescale. Since relaxation to the $S_0$ state again requires a spin inversion, it is also slow, leading to minute to hour long relaxation times in phosphorescent solids. In aqueous solutions, however, triplet oxygen ($^3O_2$) is an efficient triplet quencher, resulting in faster relaxation rates and thus a reduction of the population of dark states.

### 2.1.2 Fluorescence lifetime

The time the molecule spends in the excited state encodes valuable information about the properties and the local environment of the fluorophore. The fluorescence lifetime is defined as the average time the molecule spends in the excited $S_1$ state. Relaxation from the first excited electronic state $S_1$ may occur through emission of a photon with radiative rate $k_\mathrm{r}$, or through non-radiative pathways with rate $k_\mathrm{nr}$. The average time spent in the excited state is then given by:

$$\tau = (k_\mathrm{r} + k_\mathrm{nr})^{-1} \tag{2.1}$$

The quantum yield of the fluorophore $Q$ describes the fraction of excitation events that result in the emission of a photon. It is related to the intrinsic (or natural) lifetime $\tau_\mathrm{n} = k_\mathrm{r}^{-1}$ of the fluorophore:

$$Q = \frac{k_\mathrm{r}}{k_\mathrm{r} + k_\mathrm{nr}} = \frac{\tau}{\tau_\mathrm{n}} \tag{2.2}$$

The quantum yield and lifetime are thus affected by all processes that affect $k_\mathrm{r}$ or $k_\mathrm{nr}$. Most commonly, $k_\mathrm{nr}$ is increased through collisional (dynamic) quenching, reducing the quantum yield and lifetime, or by long range energy transfer processes such as FRET. If the quenched state persists on timescales much longer than the fluorescence lifetime (static quenching), no reduction of the lifetime is observed although the average quantum yield is still reduced.

The time evolution of the population of the first excited state $S_1(t)$ (which is proportional to the the fluorescence intensity $I$) is given by an exponential decay:

$$S_1(t) \propto I(t) = I_0 \exp\left(-t/\tau\right) \tag{2.3}$$

where $I_0$ is the initial intensity. The fluorescence decay can be measured using the method of time-correlated single photon counting (TCSPC, see 2.5).

For mixtures of fluorophores with different lifetimes, or if the fluorophore experiences different environments, the fluorescence decay is multi-exponential with the number of components $N$:

$$I(t) = \sum_{i=1}^{N} I_{0,i} \exp(-t/\tau_i) \tag{2.4}$$

In the case of a multi-exponential decay, it is important to consider how the average fluorescence lifetime $\langle\tau\rangle$ is defined (Sillen and Engelborghs, 1998). Generally, the lifetime is defined as the average time spent in the excited state, which is equivalent to the intensity-averaged fluorescence lifetime given by:

$$\langle\tau\rangle_\mathrm{intensity} = \frac{\sum_{i=1}^{N} I_{0,i}\tau_i^2}{\sum_{i=1}^{N} I_{0,i}\tau_i} \tag{2.5}$$

According to the definition of the average, the intensity-weighted lifetime is thus the correct parameter. However, it is also useful to consider the amplitude-averaged or species-averaged lifetime, which weights the lifetime components by their number fractions, defined by:

$$\langle\tau\rangle_\mathrm{species} = \frac{\sum_{i=1}^{N} I_{0,i}\tau_i}{\sum_{i=1}^{N} I_{0,i}} \tag{2.6}$$

The amplitude-averaged lifetime is the corresponding mono-exponential lifetime that results in the same steady-state intensity as the multi-exponential decay. This can be seen from the fact that $\langle\tau\rangle_\mathrm{species}$ is given by the area under the curve and is thus proportional to the time-averaged intensity. It follows that $\langle\tau\rangle_\mathrm{species}$ is related to the average radiative rate and is thus the average lifetime that should be used if FRET efficiencies are calculated based on the donor lifetime using fluorophores with multi-exponential decay behavior (see section 2.2.2). An example for a multi-exponential fluorescence decay is given in Figure 2.2 A.

### 2.1.3 Fluorescence anisotropy

When polarized excitation is employed, the polarization of the fluorescence signal contains valuable information about the rotational properties of the fluorophore, reporting on the shape and size of biomolecules or the local environment of the fluorescent probe. Experimentally, the polarization of the fluorescence signal is measured by the anisotropy $r$ which is defined by:

$$r = \frac{I_{\|} - I_{\perp}}{I_{\|} + 2I_{\perp}} \tag{2.7}$$

where $I_{\|}$ and $I_{\perp}$ are the parallel and perpendicular polarization contributions of the fluorescence signal with respect to the polarization of the incident light.

Fluorophores preferentially absorb photons whose polarization is aligned with their absorption dipole moment. Polarized excitation thus results in selective excitation of molecules of a given orientation. This photoselection is not strict but shows an angular dependence proportional to $\cos^2\theta$, where $\theta$ is the angle between the absorption dipole moment and the polarization of the incident light. The anisotropy of the emitted signal depends on the angular distribution of $\theta$:

$$r = \frac{3\langle\cos^2\theta\rangle - 1}{2} \tag{2.8}$$

where $\langle ... \rangle$ denotes averaging. Due to the excitation of molecules in different orientations, one thus obtains $\langle\cos^2\theta\rangle = 3/5$ and $r_{\text{max}} = 0.4$. This is the maximum anisotropy for fluorophores in solution. For most fluorophores, the absorption and emission dipole moments are not perfectly collinear, resulting in lower fundamental anisotropies $r_0$ in the range of $0.3 - 0.4$. Free fluorophores in solution rotate on the timescale of $\sim$100 ps, faster than the fluorescence lifetime of most fluorophores. Hence, their emission is depolarized and anisotropy values close to zero are observed. On the other hand, if the fluorescent probes are attached to larger biomolecules, their rotation is restricted and higher anisotropy values are measured. The anisotropy is often used to study biomolecular interactions, whereby the binding of an interaction partner is observed as an increase of the anisotropy.

**Rotation of fluorescent probes**

The anisotropy of the fluorescence signal can be used to study the rotation of the fluorescent probe by measuring the time-resolved anisotropy decay:

$$r(t) = \frac{I_{\|}(t) - I_{\perp}(t)}{I_{\|}(t) + 2I_{\perp}(t)} \tag{2.9}$$

For a freely rotating spherical molecule, the anisotropy decay is then given by:

$$r(t) = r_0 \exp(-t/\rho) \tag{2.10}$$

where $\rho$ is the rotational correlation time. For a spherical molecule, it is given by $\rho = \frac{\eta V}{RT}$ where $\eta$ is the viscosity of the medium, $V$ is the volume of the sphere, $R$ is the gas constant and $T$ is the temperature.

In the case of a single exponential decay of the intensity (i.e. $I(t) = I_{\|}(t) + 2I_{\perp}(t) \propto \exp\left[-t/\tau\right]$), the steady-state anisotropy $\langle r \rangle$ can be related to the lifetime $\tau$ and rotational correlation time $\rho$ by the Perrin equation (Perrin, 1926):

$$\langle r \rangle = \frac{\int_0^\infty r(t) I(t) dt}{\int_0^\infty I(t) dt} = \frac{r_0}{1 + \tau/\rho} \tag{2.11}$$

Often, the rotation of the fluorophore is restricted by the environment, a situation that is commonly observed if fluorescent probes are covalently attached to larger biomolecules. In this case, the anisotropy does not decay to zero, but plateaus at a residual value $r_\infty$:

$$r(t) = (r_0 - r_\infty) \exp\left(-t/\rho\right) + r_\infty \tag{2.12}$$

When the rotational correlation time of the macromolecule $\rho_p$ is on the order of the fluorescence lifetime, it can also be resolved from the anisotropy decay provided the rotational motions are independent and well separated in time (i.e. $\rho_f \ll \rho_p$):

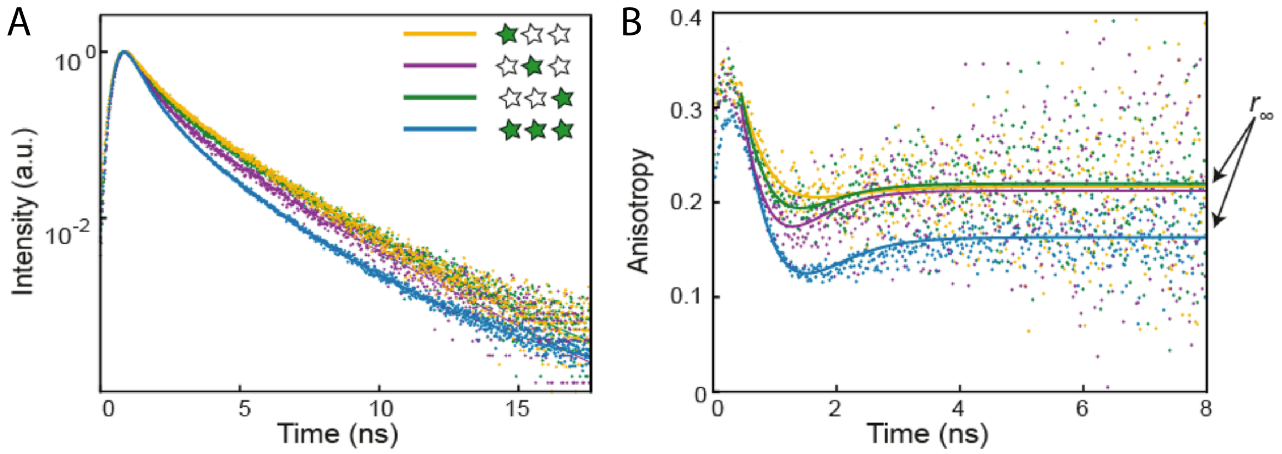

FIGURE 2.2: Complex anisotropy decays: Intensity (**A**) and anisotropy (**B**) decays of Cy3 dyes attached to DNA origami nanostructures. Adapted from Nicoli et al., 2017.

$$r(t) = \left[(r_0 - r_\infty)\exp\left(-t/\rho_f\right) + r_\infty\right]\exp(-t/\rho_p) \tag{2.13}$$

### Complex anisotropy decays

While the depolarization of the fluorescence signal usually shows exponential behavior even in the case of multi-exponential fluorescence decays, more complex anisotropy decays can arise if the different lifetime components show different decays of the anisotropy. Due to the different fluorescence lifetimes, the contributions of the individual species are time dependent. Considering two species with different lifetimes, the contribution of species 1 at time $t$ is given by:

$$F_1(t) = \frac{I_{0,1}e^{-t/\tau_1}}{I_{0,1}e^{-t/\tau_1} + I_{0,2}e^{-t/\tau_2}} = \left[1 + \frac{I_{0,2}}{I_{0,1}}e^{t\left(\frac{1}{\tau_1}-\frac{1}{\tau_2}\right)}\right]^{-1} \tag{2.14}$$

The resulting anisotropy decay is then given by:

$$r(t) = F_1(t)r_1(t) + (1 - F_1(t))r_2(t) \tag{2.15}$$

where each individual anisotropy decay is given by:

$$r_i(t) = (r_0 - r_{\infty,i})\exp(-t/\rho_i) + r_{\infty,i} \tag{2.16}$$

An example for a complex anisotropy decay is given in Figure 2.2 B for the fluorophore Cy3 attached to DNA origami nanostructures. The corresponding fluorescence decays show multi-exponential behavior (Figure 2.2 A). The characteristic "dip-and-rise" behavior of the anisotropy is often observed for cyanine dyes, for which the fluorescence lifetime and anisotropy are coupled (Stennett et al., 2015). Cyanine dyes undergo isomerization between the fluorescent *trans*-state and the non-fluorescent *cis*-state (Levitus and Ranjit, 2011). The transition between the two isomeric forms occurs upon relaxation from the excited state. Since it involves rotation of the molecule around the central stretch of $\pi$-bonds, steric hindrance has a pronounced effect on the isomerization rate, which in turn affects the quantum yield and thus lifetime of the fluorophores. Thus, a higher anisotropy signal is directly coupled with a longer fluorescence lifetime. In the given example in Figure 2.2, two lifetime components are observed at ~300 ps and ~2.6 ns. The short-lifetime component shows a rapid decay of the anisotropy to a residual value close to 0, while the long-lifetime component shows a larger residual anisotropy of ~ 0.2. The time-dependent contribution of the two species then results in the observed complex decay which can be analytically described by equation 2.15 (solid lines in Figure 2.2 B).

## 2.2 Förster resonance energy transfer

### 2.2.1 Theory

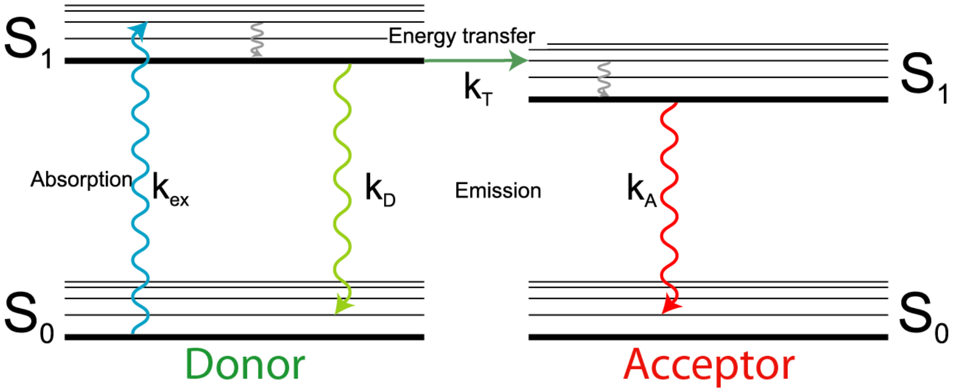

FIGURE 2.3: A Jablonski diagram depicting FRET between a donor and acceptor fluorophore. $S_0$, $S_1$: singlet ground and first excited state, $k_{\mathrm{ex}}$: excitation rate, $k_{\mathrm{D}}$, $k_{\mathrm{A}}$: fluorescence emission rates of the donor and acceptor fluorophores, $k_{\mathrm{T}}$: rate of energy transfer.

Förster resonance energy transfer (FRET) is the radiationless transfer of energy from an excited donor fluorophore (D) to an acceptor fluorophore (A) (Förster, 1948). The rate of the transfer process $k_{\mathrm{T}}$ is highly dependent on the separation distance $R$ between the two fluorophores:

$$k_{\mathrm{T}} = \frac{1}{\tau_D}\left(\frac{R_0}{R}\right)^6 \tag{2.17}$$

where $\tau_D$ is the fluorescence lifetime of the donor and the parameter $R_0$ is the Förster radius. The efficiency of the energy transfer is then given by:

$$E = \frac{k_{\mathrm{T}}}{k_{\mathrm{r}} + k_{\mathrm{nr}} + k_{\mathrm{T}}} = \frac{1}{1 + \left(\frac{R}{R_0}\right)^6} \tag{2.18}$$

where $k_{\mathrm{r}}$ and $k_{\mathrm{nr}}$ are the rates of radiative and non-radiative decay of the donor fluorophore. The Förster radius, at which the FRET efficiency is 50%, depends on a number of properties of the fluorophores and the surrounding environment:

$$R_0^6 = \frac{9000\,(\ln 10)\,Q_D J(\lambda)\kappa^2}{128\pi^5 N_{\mathrm{A}} n^4} \tag{2.19}$$

where $Q_D$ is the quantum yield of the donor, $J(\lambda)$ is the overlap integral, $\kappa^2$ is a factor accounting for the relative orientation of the emission dipole moment of the donor and the absorption dipole moment of the acceptor, $N_{\mathrm{A}}$ is Avogadro's number and $n$ is the refractive index of the medium. The orientation factor $\kappa^2$ depends on the angle between the emission dipole moment of the donor and the absorption dipole moment of the acceptor, $\theta_T$, and the angles between the respective dipole moments and the inter-dye distance vector, $\theta_D$ and $\theta_A$:

$$\kappa^2 = \left(\cos\theta_T - 3\cos\theta_D\cos\theta_A\right)^2 \tag{2.20}$$

$\kappa^2$ can assume values in the interval $[0, 4]$, however its value converges to $\kappa^2_{\mathrm{iso}} = 2/3$ for isotropic averaging over all possible angles, an assumption that is often made in FRET experiments. More accurate estimates of the distribution of possible values of $\kappa^2$ may be obtained from the residual anisotropies of the donor and acceptor fluorophores (Ivanov et al., 2009; Sindbert et al., 2011).

The dependency of the FRET efficiency on the inter-dye distance is shown in Figure 2.4 A for the dye pairs Atto488-Atto647N, Atto488-Atto565 and Atto565-Atto647N with Förster radii of 56 Å, 63 Å and 68 Å, respectively. To visualize the sensitivity of the FRET efficiency with respect to the separation distance, the derivative $\partial E\,(R)\,/\partial R$ is shown in panel B. In general, the sensitive range for FRET is in the interval from 0.5 $R_0$ to 2 $R_0$. It is most sensitive at distances close to $R_0$, where a small change in distance results in a large change of the FRET

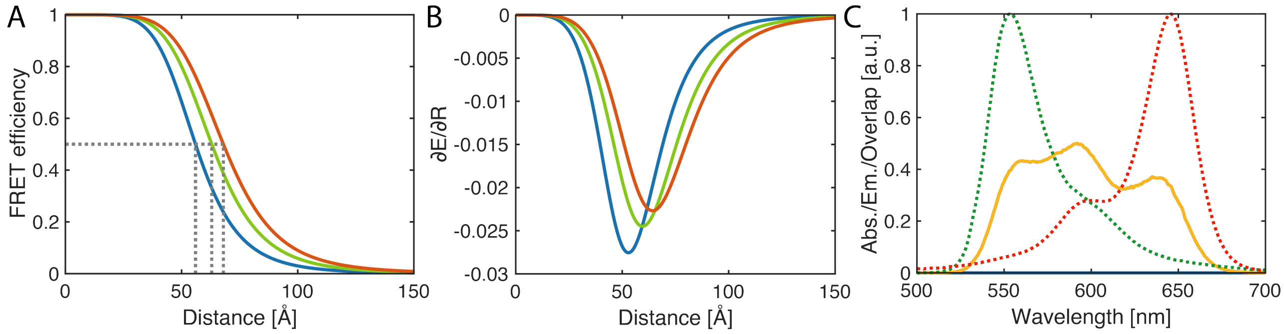

FIGURE 2.4: The theory of FRET. (**A**) The distance dependence of the FRET efficiency for three different Förster distances of 56 Å, 63 Å and 68 Å, corresponding to the dye pairs Atto488-Atto647N, Atto488-Atto565 and Atto565-Atto647N. The Förster radii are indicated by the dashed lines. (**B**) Distance-derivatives of the FRET efficiency for the Förster distances shown in A. (**C**) The overlap integral (solid line) for the dye pair Atto532-Atto647N is plotted together with the emission spectrum of the donor (dotted green line) and the extinction spectrum of the acceptor (dotted red line). All spectra are given in arbitrary units.

efficiency. Consequently, this also means that an error in the measured FRET efficiency only has a small effect on the resulting distance, making FRET also most robust and least error prone in the distance region around $R_0$.

The overlap integral $J(\lambda)$ in equation 2.19 depends on the normalized emission spectrum of the donor $F_D(\lambda)$ and the extinction spectrum of the acceptor $\epsilon_A(\lambda)$:

$$J(\lambda) = \int_0^\infty F_D(\lambda)\epsilon_A(\lambda)\lambda^4 d\lambda \tag{2.21}$$

Commonly, the overlap integral is schematically shown simply (and wrongly) as the overlapping region between the spectra, disregarding the fact that the spectra are multiplied and scaled with the fourth power of the wavelength. The correct spectral overlap according to equation 2.21 is shown in Figure 2.4 C for the dye pair Atto532-Atto647N.

### 2.2.2 Measuring FRET

There are a number of approaches to measure the FRET efficiency. Looking from the perspective of the donor, FRET shows as a quenching effect which can be assessed from the loss of the donor intensity in the presence of the acceptor:

$$E = 1 - \frac{F_{DA}}{F_D} \tag{2.22}$$

This approach, however, requires precise measurements of the donor intensity and complete labeling of the acceptor. A simple way to obtain the two intensities is through acceptor photobleaching. Analogously, the FRET efficiency can also be determined from the donor lifetime in the absence ($\tau_{D(0)}$) and in the presence of the acceptor ($\tau_{D(A)}$):

$$E = \frac{k_T}{k_r + k_{nr} + k_T} = 1 - \frac{k_r + k_{nr}}{k_r + k_{nr} + k_T} = 1 - \frac{\tau_{D(A)}}{\tau_{D(0)}} \tag{2.23}$$

In contrast to intensity-based measurements, no correction factors need to be considered to obtain a quantitative FRET efficiency. The lifetime approach also works if the acceptor labeling is incomplete, in which case the lifetimes of unquenched and quenched donor fluorophores can be extracted using a bi-exponential model function.

Single-molecule measurements of the FRET efficiency are most commonly performed by splitting the fluorescence emission after excitation of the donor into donor and acceptor spectral channels ($F_{DD}$, $F_{DA}$), from which the FRET efficiency is calculated by:

$$E = \frac{F_{DA}}{F_{DD} + F_{DA}} \tag{2.24}$$

Experimentally, a number of correction factors have to be considered. Due to the broad fluorescence emission spectra, a part of the donor fluorescence is usually detected in the acceptor channel (spectral crosstalk). Likewise, the broad fluorescence excitation spectra result in non-negligible excitation of the acceptor fluorophore by the donor excitation laser (direct excitation). Lastly, donor and acceptor fluorophores have different quantum yields and the photon detection efficiency of the detectors shows a spectral dependence. These effects have to be accounted for in the calculation of accurate FRET efficiencies as described in section 2.10.2.

### 2.2.3 Three-color FRET

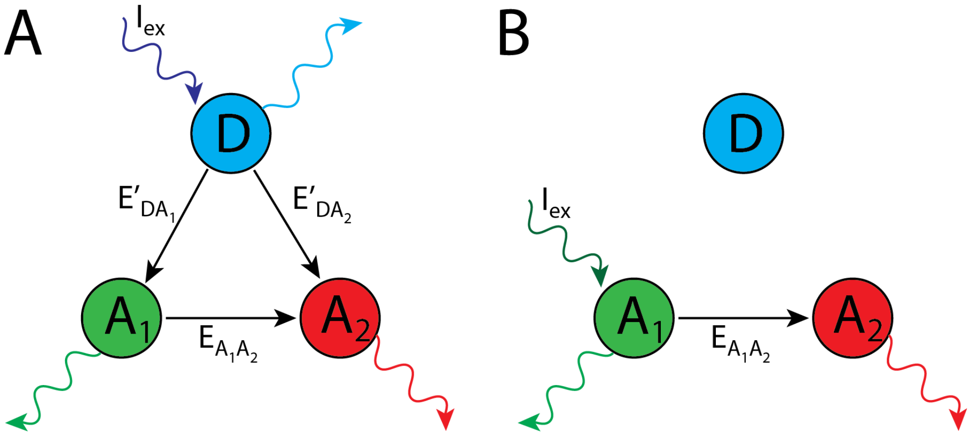

FIGURE 2.5: Transition pathways in a three-color FRET system after excitation of the blue dye (**A**) and after excitation of the green dye (**B**).

In three-color FRET, a donor fluorophore $D$ may transfer its energy to two acceptors $A_1/A_2$. The first acceptor $A_1$ can further transfer its energy to the second acceptor $A_2$. The distance-related FRET efficiencies between the donor and acceptor $i \in \{1,2\}$, as defined from the rates in analogy to equation 2.18, are given by:

$$E_{DA_i} = \frac{k_{T,i}}{k_r + k_{T,i}} \tag{2.25}$$

On the other hand, the transition probabilities as given in Figure 2.5 A are given by:

$$E'_{DA_i} = \frac{k_{T,i}}{k_r + k_{T,1} + k_{T,2}} \tag{2.26}$$

However, these quantities are not directly related to distances. The quenching of the donor fluorophore by the second acceptor (which in itself depends on the distance) changes the donor quantum yield and thus the Förster radius for the FRET process to the other acceptor. Instead, distance-related FRET efficiencies are calculated from the detected signal by:

$$E_{A_1A_2} = \frac{I_{A_2}^{A_{1,ex}}}{I_{A_1}^{A_{1,ex}} + I_{A_2}^{A_{1,ex}}} \tag{2.27}$$

$$E_{DA_1} = \frac{I_{A_1}^{D_{ex}}}{I_D^{D_{ex}}\left(1 - E_{A_1A_2}\right) + I_{A_1}^{D_{ex}}} \tag{2.28}$$

$$E_{DA_2} = \frac{I_{A_2}^{D_{ex}} - E_{A_1A_2}\left(I_{A_1}^{D_{ex}} + I_{A_2}^{D_{ex}}\right)}{I_D^{D_{ex}} + I_{A_2}^{D_{ex}} - E_{A_1A_2}\left(I_D^{D_{ex}} + I_{A_1}^{D_{ex}} + I_{A_2}^{D_{ex}}\right)} \tag{2.29}$$

A detailed derivation of these equations is given in the supporting information of Paper 1 (Barth et al., 2018b). A consequence of these equations is that an independent measurement of the FRET efficiency between the two acceptors $E_{A_1A_2}$ is required to calculate the three-color FRET efficiencies. This might seem surprising since, after all, three signals are obtained after excitation of the blue fluorophore. The FRET efficiency, however, is a ratiometric quantity. The three signals only define two independent ratios, necessitating the additional measurement of $E_{A_1A_2}$. In other words, without the knowledge of the transfer probability from $A_1$ to $A_2$, it is not possible to determine whether a photon emitted by $A_2$ originated from direct energy from $D$, or from two-step energy transfer over $A_1$. The interdependence of the FRET efficiencies also poses additional challenges for data analysis, since any error or uncertainty in $E_{A_1A_2}$ propagates to the calculation of the three-color FRET efficiencies (see section 3.1). Experimentally, the FRET efficiency $E_{A_1A_2}$ is intermittently probed by alternating excitation of $D$ and $A_1$ through pulsed interleaved excitation (PIE, see section 2.6).

### 2.2.4 Homo-FRET

While most FRET studies are performed using spectrally different fluorophores, FRET can likewise occur between identical molecules. The efficiency of homo-FRET is limited by the overlap between the absorption and emission spectrum and consequently highest for fluorophores with a small Stokes shift. Homo-FRET may thus seem an unlikely phenomenon. The Förster radius for the widely used fluorophore Cy3, however, is 46 Å (Nicoli et al., 2017), not much smaller than the Förster radius of many commonly used blue-red dye pairs in hetero-FRET (Vandenberk et al., 2018). Energy transfer between identical fluorophores (homo-FRET) cannot be measured spectrally or by the fluorescence lifetime (see appendix A.1). However, in the presence of homo-FRET, the measured fluorescence anisotropy is decreased. In fact, FRET was first observed in dye solutions as a concentration-dependent decrease of the anisotropy of the fluorescence signal through energy transfer between freely diffusing molecules (Förster, 1948). Since resonance energy transfer can occur over a wide range of angles between the donor and acceptor dipole moments, it results in a significant amount of depolarization. As a consequence, the transfer anisotropy, i.e. the anisotropy of FRET-sensitized acceptor emission, is usually close to zero and the fluorescence signal is thus almost entirely depolarized (see appendix A.2 for more details). An example for the measurement of homo-FRET by the fluorescence anisotropy is given in Figure 3.3 A for an assembly of three Cy3 fluorophores arranged in close proximity on a DNA origami nanostructure (for details, see section 3.2 and Nicoli et al., 2017).

## 2.3 Photoinduced electron transfer

Fluorescence can be quenched if molecular contacts are formed due to collision (dynamic quenching) or formation of stable complexes (static quenching). Quenching generally requires overlap of the molecular orbitals and is thus only effective at short distances below ∼10 Å. There are three main mechanisms of quenching: intersystem crossing, Dexter energy transfer and photoinduced electron transfer (PET). In the first case, the molecule transitions from the excited singlet state to the triplet state upon collision with oxygen or heavy atom halogens such as iodine (Evans, 1957). The same interaction also rescues the molecule from the triplet state and returns it to the singlet ground state. Dexter energy transfer is similar to FRET, but involves the transfer of electrons between the donor and acceptor fluorophore either in two steps or concertedly (Dexter, 1953). The excited electron of the donor is hereby transferred to to the acceptor, which in turn transfers a ground state electron to the donor. At close donor-acceptor distances, there is thus always competition between Dexter energy transfer and FRET, resulting in a complete quenching of the donor. Photoinduced electron transfer is described in more detail below as it was used in this work.

In PET, a single electron is transferred from the lowest unoccupied molecular orbital (LUMO) of the donor to the LUMO of the acceptor, leading to the formation of a charge transfer complex of oppositely charged electron donor and acceptor, $[D^+A^-]^*$. The charge transfer complex relaxes to the ground state non-radiatively and dissociates after the electron is transferred back to the donor.

$$D + A \xrightarrow{h\nu} D^* + A \rightarrow \left[D^+A^-\right]^* \rightarrow D^+ + A^- \rightarrow D + A \tag{2.30}$$

The fluorophore may hereby act as either electron donor or acceptor. The direction of energy transfer is determined by the redox properties of the fluorophore and the quencher. The change in free enthalpy $\Delta G$ during PET are described by the Rehm-Weller equation (Rehm and Weller, 1970):

$$\Delta G = E(D^+|D) - E(A|A^-) - \Delta G_{0,0} - \frac{e^2}{\epsilon d} \tag{2.31}$$

where $E(D^+|D)$ and $E(A|A^-)$ describe the reduction potentials of the ionized electron donor and the neutral electron acceptor, $\Delta G_{0,0}$ is the energy of the zero-zero transition to the lowest excited singlet state of the fluorophore, $S_0 \rightarrow S_1$, and the last term describes the coulombic attraction energy which can be neglected in polar solvents ($e$ is the elementary charge, $\epsilon$ the dielectric constant of the medium and $d$ the separation distance).

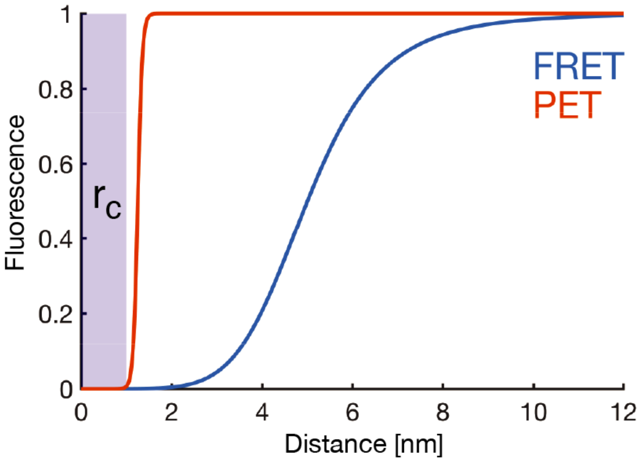

FIGURE 2.6: Comparison of the quenching of fluorescence for FRET (blue) and PET (red).

During PET, the electron donor is oxidized and the acceptor is reduced, resulting in the energy difference $E(D^+|D) - E(A|A^-)$ that is unfavorable in the absence of excitation of the fluorophore. Only through the energy gained by relaxation from the excited state does the process become exergonic. In other words, if the fluorophore acts as the electron donor, its ionization potential from the $S_1$ state is reduced in the excited state, increasing its ability to donate an electron. Correspondingly, if the fluorophore is the electron acceptor, it can accommodate the electron in the ground state orbital, thus increasing its electron affinity in the excited-state complex.

Due to the requirement of orbital overlap, PET shows a drastically different distance dependence described by (Lakowicz et al., 1993):

$$k_{\mathrm{PET}}(r) = k_Q \exp\left(-\frac{r - r_c}{a}\right) \tag{2.32}$$

where $k_Q$ is the rate of quenching below the contact distance $r_c$ and $a$ is a scaling constant describing the decrease of the electron density. A comparison of the distance dependence of PET compared to FRET is given in Figure 2.6. While FRET is sensitive over a large range of distances, PET essentially shows an "all-or-nothing" quenching behavior and is useful for investigating dynamics at short distances, where FRET is insensitive.

The fluorophore is statically quenched in the charge-transfer complex. The collision leading to the quenched complex, on the other hand, effectively represents a non-radiative relaxation pathway for the fluorophore which is described by the rate of contact formation $k_c$. Thus, the fluorescence lifetime is also affected by the quenching if $k_c$ is on the order of the inverse fluorescence lifetime of the unquenched state $1/\tau_u$. Then, the fluorescence lifetime in the presence of the quencher $\tau_q$ is given by the Stern-Volmer equation (Stern and Volmer, 1919):

$$\tau_q = (k_c + 1/\tau_u)^{-1} \tag{2.33}$$

The most commonly used fluorophore for PET studies nowadays is the oxazine fluorophore Atto655 (or the related MR121) (Doose et al., 2009). A convenient quencher for Atto655 in proteins is the natural amino acid tryptophan, which may either be natively present or can be introduced via mutagenesis to probe a specific intra- or intermolecular interaction. In nucleic acids, guanine bases are a potential quencher for PET, to which Atto655 is also sensitive (Vandenberk et al., 2018). In both cases, Atto655 acts as an electron acceptor. Another family of fluorescent dyes that are susceptible to PET-based quenching are rhodamine fluorophores, such as Rhodamine 6G or Atto565.

## 2.4 Confocal microscopy

The confocal microscope, invented by Marvin Minsky (Minsky, 1961), has found widespread application in fluorescence microscopy due to its small observation volume and high achievable excitation densities, resulting in an excellent signal-to-noise ratio. The key idea in confocal microscopy is the use of a pinhole that is placed in the detection pathway in a conjugate plane to the excitation source, resulting in the rejection of out-of-focus light (Figure 2.7 A). The image of a point source through a lens is described by the Airy disk (Airy, 1835) and the achievable lateral resolution, limited by the diffraction of light, is given by the Rayleigh criterion (F.R.S, 1879):

$$\Delta x = \frac{0.61\lambda}{NA} \tag{2.34}$$

where $NA$ is the numerical aperture of the objective lens, given by $NA = n \sin \alpha$ with the refractive index of the transmitting medium $n$ and the half-opening angle of the objective $\alpha$. The resolution as given in equation 2.34 describes the minimal distance between two point emitters at which they can still be distinguished by the microscope, defined by the distance where the maximum of the Airy disk of the first emitter coincides with the first minimum of the second emitter. In practical applications, the resolution additionally depends on the achievable signal-to-noise ratio, especially in single-molecule microscopy. The effective numerical aperture of the objective lens depends on the diameter of the collimated laser beam at the back aperture ($\varnothing$) through $NA \approx \varnothing/2f$ where $f$ is the focal length. As a consequence, the size of the laser spot is inversely proportional to the beam diameter, $\omega_r \propto 1/\varnothing$, which can be used to tune the size of the confocal volume (Banks et al., 2016; Hess and Webb, 2002).

The confocal observation volume is often called the point spread function (PSF) since it describes how a point source is seen through the microscope. While technically one observes the product of the excitation and detection profiles, each given by an Airy disk, the PSF is often simply approximated by a 3D Gaussian function:

$$\mathrm{PSF}(x,y,z) \propto \exp\left[-2\left(\frac{x^2+y^2}{\omega_r^2}+\frac{z^2}{\omega_z^2}\right)\right] \tag{2.35}$$

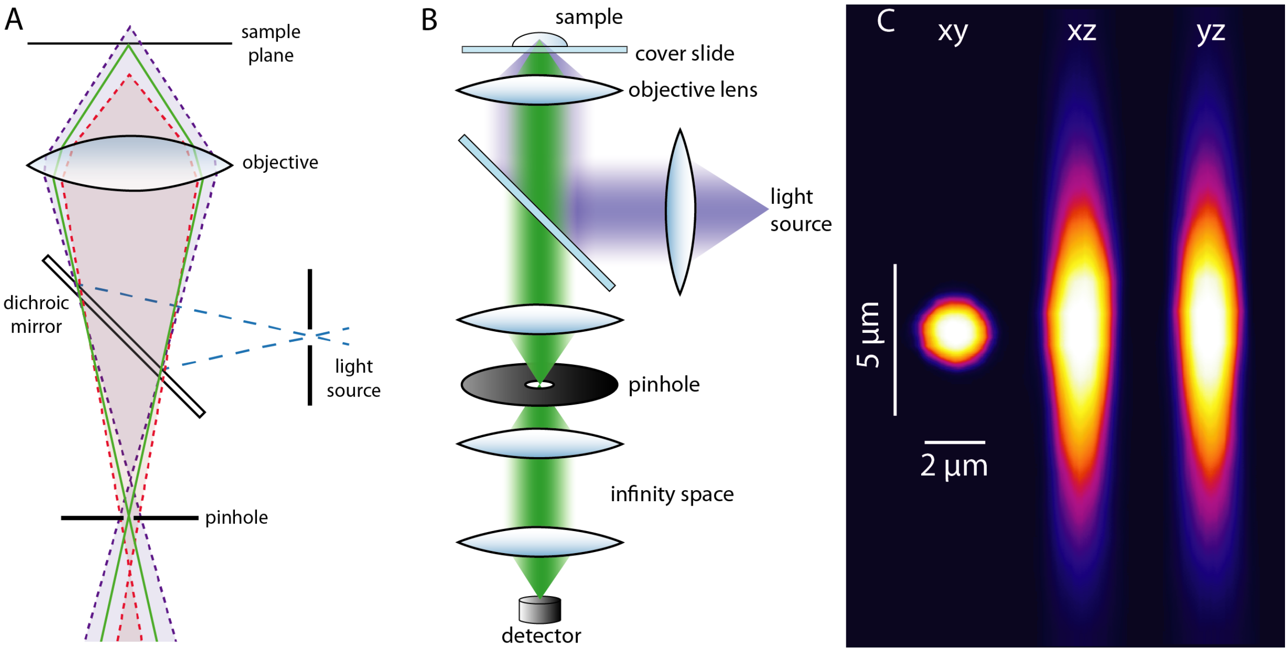

FIGURE 2.7: Confocal microscopy. **(A)** Scheme of a confocal microscope based on the original patent (Minsky, 1961). The confocal arrangement of the light source and detection pinhole rejects out-of-focus light (blue and red dashed lines), while light from the sample plane passes through (green line). **(B)** Modern confocal microscope with infinity-corrected objective and tube lens. The resulting infinity space can be used to install optics without introducing distortions. **(C)** Confocal volume of the three-color PIE-MFD setup described in section 2.7, measured by a bead scan using 480 nm excitation (bead size ~60 nm). The collimated laser beam diameter before the objective was ~3 mm, resulting in a reduced effective numerical aperture of the objective lens and thus increased focus size.

where $\omega_r$ and $\omega_z$ are the lateral and axial dimensions of the PSF. Note that $\omega_r$ and $\omega_z$ are defined as the distances from the center of the PSF to the point where the intensity has decayed to $1/e^2$ of the maximum value in accordance with the definition of the effective volume in fluorescence correlation spectroscopy (see section 2.9).

Naturally, both the lateral and the axial size of the confocal volume depend on the size of the pinhole (Naredi-Rainer et al., 2013), however the axial size is usually a factor of 5-10 larger than the lateral size. The optimal size of the pinhole $d_{\mathrm{PH}}$ should correspond to the size of the Airy disc at the given magnification $M$ of the objective lens:

$$d_{\mathrm{PH}} = M\frac{1.22\lambda}{NA} \tag{2.36}$$

If a larger pinhole is chosen, an increasing amount of out-of-focus light reaches the detector. Smaller pinhole diameters, on the other hand, reduce the collected signal and thus the signal-to-noise ratio at the gain of a slightly higher resolution. Considering an excitation wavelength of 480 nm, a high numerical aperture objective ($NA = 1.2$-$1.4$) yields typical dimensions of the confocal volume of $\omega_r \approx 200\,\mathrm{nm}$ and $\omega_z \approx 1$-$2\,\mu\mathrm{m}$. For the example given in Figure 2.7 B, the diameter of the excitation beam was chosen to significantly underfill the back aperture of the objective lens ($\varnothing \approx 3\,\mathrm{mm}$). This results in an increased size of the PSF ($\omega_r \approx 600\,\mathrm{nm}$ and $\omega_z \approx 2$-$3\,\mu\mathrm{m}$) due to the reduced effective numerical aperture, despite the use of a 1.27 $NA$ objective lens.

In modern implementations of the confocal principle (see Figure 2.7 B), the use of infinity-corrected objectives simplifies the experimental setup. Since all light originating from the sample is collimated throughout the infinity path of the microscope, additional optical elements such as polarizing beam splitters or emission filters can be inserted without introducing distortions.

## 2.5 Time-correlated single photon counting

Time-correlated single photon counting (TCSPC) detection enables the measurement of the arrival time of single photons with picosecond accuracy by measuring the time delay between a photon detection event and a synchronization signal that is used to drive the lasers. The timing information in TCSPC is hence split into the macro-time $t$, measured by the number of synchronization periods that passed from the start of the measurement, and the micro-time $\Delta t$, given by the delay between the last synchronization signal and the photon detection time (see Figure 2.8 A). The measurement of the micro-time is performed by a time-to-amplitude converter (TAC). The TAC is a linear voltage ramp generator that is triggered by one signal and stopped by another (start-stop mode). In practice, there are much less photon detection events compared to synchronization signals, which is why the photon detection event is used as the start signal and the subsequent synchronization signal as the stop signal. The arrival time of the signals is hereby measured using a constant-fraction discriminator (CFD) that provides an intensity-independent timing of the detected pulse. The voltage from the TAC is digitized by an analog-to-digital converter (ADC) that determines the maximum obtainable timing resolution. The precise arrival time $T_{\mathrm{arrival}}$ is then given by:

$$T_{\mathrm{arrival}} = t + \Delta t = n_{\mathrm{sync}}\frac{1}{f} + n_{\mathrm{ADC}}\frac{T_{\mathrm{TAC}}}{N_{\mathrm{ADC}}} \tag{2.37}$$

where $n_{\mathrm{sync}}$ is the number of synchronization signals detected since the start of the measurement, $f$ is the synchronization signal frequency, $n_{\mathrm{ADC}}$ and $N_{\mathrm{ADC}}$ are the measured and maximum number of ADC bins and $T_{\mathrm{TAC}}$ is the maximum time range covered by the TAC. Values for $f$ are usually in the range of 10 MHz to 80 MHz, resulting in a resolution of the macrotime of 12.5 ns to 100 ns. The value for $T_{\mathrm{TAC}}$ is typically chosen to be equal to $1/f$. The resolution of the ADC is then determined by its maximum binning $N_{\mathrm{ADC}}$, which most commonly is $2^{12} = 4096$ yielding a typical timing resolution of 1 ps to 25 ps, depending on $T_{\mathrm{TAC}}$.

## 2.6 Pulsed interleaved excitation

Pulsed-interleaved excitation is the method of alternating laser excitation on the nanosecond timescale (Müller et al., 2005). Experimentally, two pulsed lasers are operated at an identical frequency with a delay corresponding to half the repetition period given by $\Delta T \approx \frac{1}{2f}$ (Figure 2.8 A). Using TCSPC, one can then use the micro-time information to distinguish photons not only based on the detection channel, but also with respect to the excitation source, to sort them into PIE channels (Figure 2.8 B). This way, three PIE channels are defined in a two-color experiment, containing green photons after green excitation ($GG$), red photons after red excitation

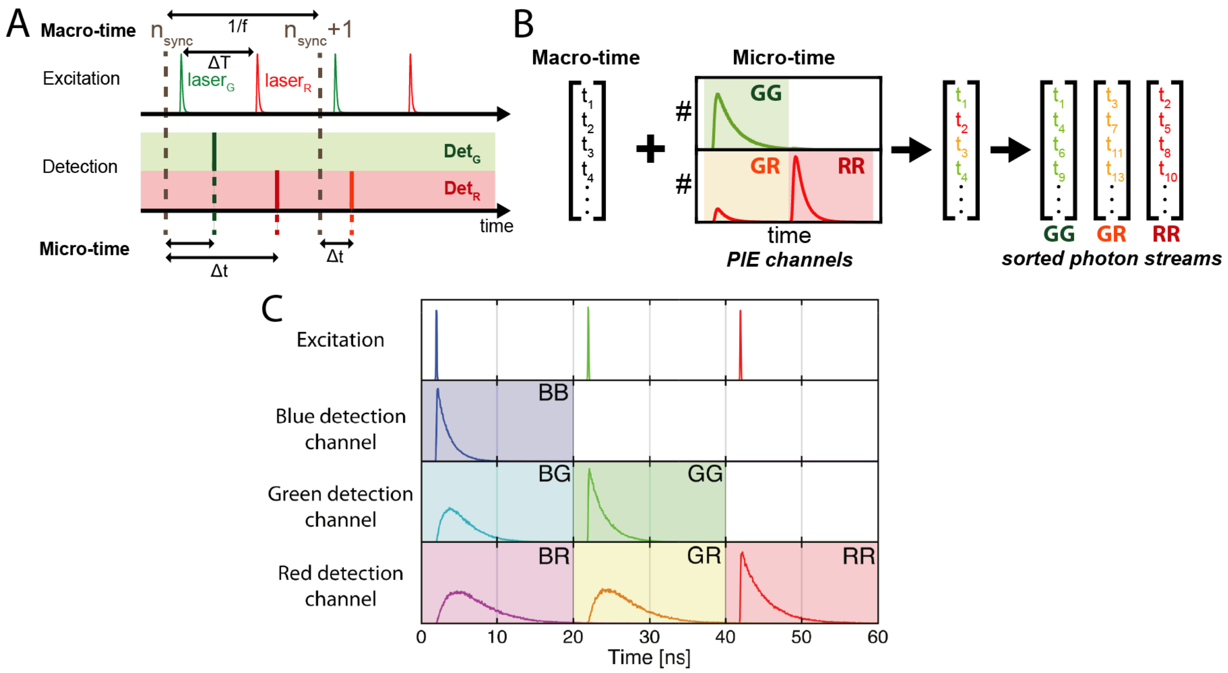

FIGURE 2.8: The principle of photon sorting in pulsed-interleaved excitation. **(A)** A green and a red laser, operated at the frequency $f$, are alternated on the nanosecond timescale by introducing a delay $\Delta T$ to the red laser pulse. The arrival times of single photons are measured by the macro-time, which counts the number of repetition periods $n_{\text{sync}}$ since the start of the measurement, and the micro-time that measures the delay o the previous synchronization signal $\Delta t$. Three detection events are illustrated: green detection after green excitation, red detection after red excitation (dark red) and red detection after green excitation (light red). **(B)** Photon macro-times can be sorted into PIE channels using the micro-time information to obtain sorted photon streams. **(C)** Three-color PIE introduces a third laser, here blue, to the excitation sequence, adding three additional PIE channels after blue excitation. Adapted from Schrimpf et al., 2018a (A-B) and Barth et al., 2018b (C).

($RR$) and red photons after green excitation ($GR$). Usually, no significant signal is detected in the green channel after red excitation since the emission filter for the green channel has negligible overlap with the emission spectrum of the red fluorophore. The PIE channel $RG$ can thus be omitted.

The PIE channels $GG$ and $RR$ only contain the pure fluorescence signal of the green and red fluorophores. The PIE channel $GR$, on the other hand, contains signal originating from spectral crosstalk of the green dye, direct excitation of the red dye by the green laser, and FRET-sensitized acceptor emission. While, in this work, PIE is mostly used for application in single-molecule FRET by burst analysis (see section 2.10), it was originally developed to improve fluorescence cross-correlation spectroscopy (see section 2.9.4). By removing the contribution of crosstalk and direct excitation to the cross-correlation signal through the use of the PIE channel $RR$ instead of the total signal detected in the acceptor channel, even weak biological interactions can be studied quantitatively. In single-molecule FRET, the intermittent excitation of the acceptor fluorophore provides vital information about the photophysical state of the acceptor and the labeling stoichiometry, and allows the determination of all needed correction factors from the data set directly (Kudryavtsev et al., 2012).

A possible artifact in PIE is temporal crosstalk for long fluorescence lifetimes, e.g. between the PIE channels $RR$ and $GR$, which cannot be entirely avoided due to the exponential decay of the fluorescence intensity. However, considering typical fluorescence lifetimes for organic fluorophores in the range of ~4 ns, a time range of ~18 ns covers 99% of the decay, reducing the temporal crosstalk to below 1%. In this work, PIE has also been extended to three colors by the use of three excitation lasers which are alternated at 16.7 MHz with a delay of 20 ns (Figure 2.8 C), defining a total number of 6 PIE channels.

The related method of alternating laser excitation (ALEX, Kapanidis et al., 2005) achieves alternating excitation on the timescale of 10-100 $\mu$s using continuous wave (cw) lasers and fast shutters. Using PIE, it is possible to calculate fluorescence correlation functions down to the sub-microsecond regime, whereas ALEX is limited to the timescale of the alternation period. However, the photostress exerted on the fluorophores is reduced in ALEX compared to PIE due to the higher peak power densities of the excitation lasers in pulsed excitation, resulting in higher photobleaching rates. On the other hand, the valuable fluorescence lifetime information is not available in ALEX experiments.

## 2.7 Experimental setups

### 2.7.1 Three-color PIE-MFD setup

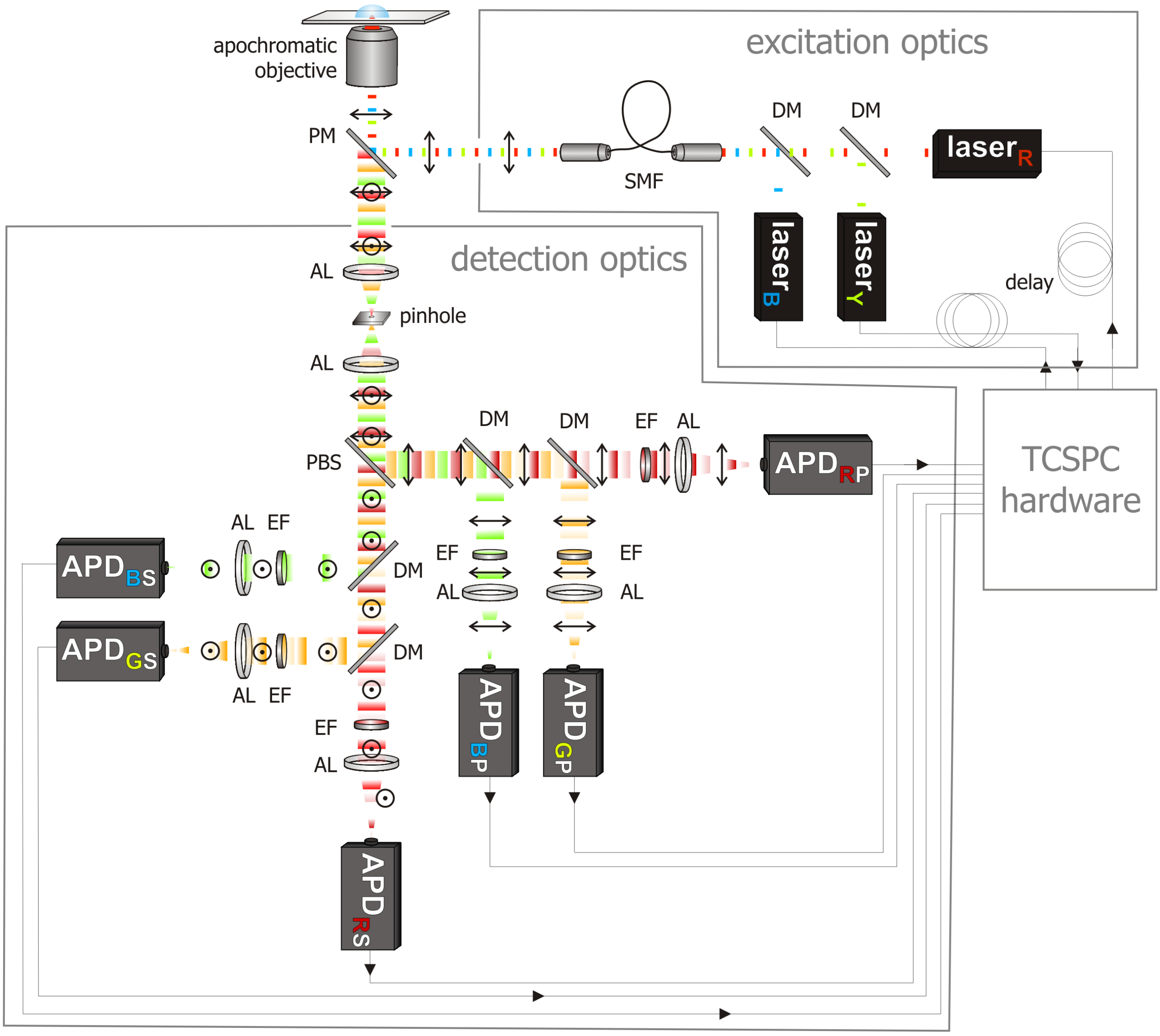

FIGURE 2.9: Scheme of the single-molecule three-color PIE-MFD confocal setup used in this work. DM: dichroic mirror, SMF: single-mode fiber, PM: polychroic mirror, AL: achromatic lens, PBS: polarizing beam splitter, EF: emission filter, APD: avalanche photodiode, P/S: parallel/perpendicular polarization, TCSPC: time-correlated single photon counting.

Three-color FRET experiments with pulsed interleaved excitation (PIE) (Kudryavtsev et al., 2012; Müller et al., 2005) and multiparameter fluorescence detection (MFD) (Widengren et al., 2006) were performed on a home built confocal three-color dual-polarization detection setup based on a Nikon Eclipse Ti-DH inverted microscope (Figure 2.9). For pulsed interleaved excitation, the three lasers (LDH-D-C-485, LDH-D-TA-560, LDH-D-C-640, PicoQuant, Berlin, Germany) are synchronized by a laser driver (Sepia II, PicoQuant) at a frequency of 16.67 MHz with a 20 ns delay between consecutive pulses to minimize temporal crosstalk between PIE channels. The lasers are combined into a polarization maintaining single-mode fiber (QPMJ-A3A 405/640, OZ Optics, Ottawa, Canada), collimated to a beam diameter of ∼3 mm (60SMS-1-4-RGBV11-47, Schäfter+Kirchhoff, Hamburg, Germany) and focused into the sample by a 60x 1.27 NA water immersion objective (Plan Apo IR 60x 1.27 WI, Nikon, Düsseldorf, Germany). Fluorescence is separated from the excitation light by a polychroic mirror (zt405/488/561/633, AHF Analysentechnik, Tübingen, Germany) and focused through a 50 µm pinhole. The signal is then split into parallel and perpendicular polarization with respect to the excitation by a polarizing beam splitter (Thorlabs, Dachau, Germany) and spectrally separated into the three spectral channels by two dichroic mirrors (BS560 imaging, 640DCXR, AHF Analysentechnik) and three emission filters per polarization (ET525/50, ET607/36, ET670/30, AHF Analysentechnik, see Figure 2.10). Photons are detected using six single-photon-counting avalanche photodiodes (2x COUNT-100B, LaserComponents, Olching, Germany, and 4x SPCM-AQR14, Perkin Elmer, Waltham, Massachusetts) and registered by TCSPC electronics (HydraHarp400, PicoQuant), which was synchronized with the laser driver. The confocal volume of the setup, as measured by a bead scan, is shown in Figure 2.7 C.

**Filter choices** At a first glance, the choice of emission filters for the green and red detection channels in Figure 2.10 may not seem ideal. After all, the green emission filter cuts away the lower-wavelength part of the spectrum, while the red emission filter only covers the peak region, ignoring the long-wavelength tail of the spectrum. The reason for this specific choice of filters is the Raman scattering of water, which shows a main band at 3200-3600 $\text{cm}^{-1}$ (Cross et al., 1937). The excitation with light of 480 nm and 561 nm wavelengths then results in Raman signals in the spectral regions of 570-580 nm and 690-710 nm, necessitating the choice of narrower emission filters that do not overlap with the Raman regions. For details, see Barth, 2013.

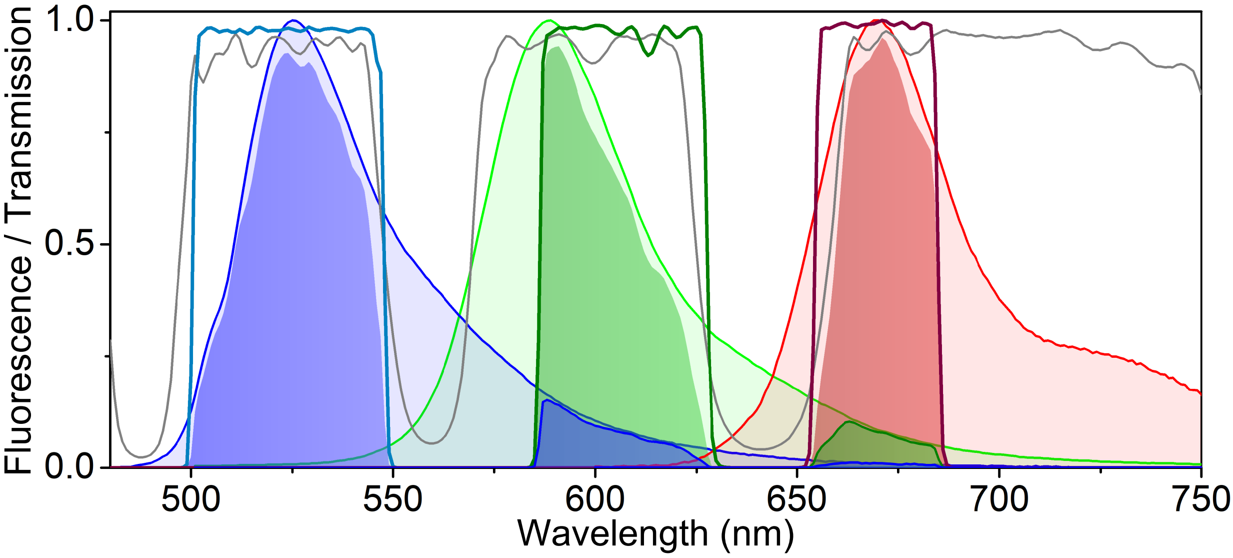

FIGURE 2.10: Transmission spectra of the polychroic mirror (gray line) and the emission filters for the blue, green and red detectors (colored accordingly) used in the three-color PIE confocal microscope. Emission spectra of the dyes Atto488 (blue), Atto565 (green) and Atto647N (red) are given as light shaded areas. The part of the emission that is detected in the different channels is given as dark shaded areas.

### 2.7.2 Two-color PIE-MFD setup

The single-molecule FRET measurement on the cohesin dyad (see section 3.3 and Barth et al., 2018a) were performed on a similar setup equipped with two pulsed lasers for excitation at 532 nm and 640 nm (PicoTA 530 and LDH-D-C640, PicoQuant) operated at a repetition rate of 26.66 MHz with a delay of 18 ns. Fluorescence is collected by a 60x water immersion objective (Plan Apo IR 60x/1.27 WI, Nikon) and focused through a 75 µm pinhole. After separating the signal into parallel and perpendicular polarization, it is split spectrally by a dichroic mirror (640DCXR, AHF Analysentechnik) and passed through emission filters (donor: Brightline HQ582/75, acceptor: Brightline HQ700/75, AHF Analysentechnik) before being detected on single-photon-counting avalanche photodiodes (SPCM-AQR, Perkin-Elmer). Single-photon detection events are recorded on four TCSPC cards (SPC-154, Becker&Hickl).

## 2.8 Quantitative analysis of fluorescence decays

The quantitative analysis of fluorescence decays is complicated by the non-ideal characteristics of the excitation pulse and detection electronics. The laser pulses have a finite width and the detector and electronics are subject to timing inaccuracies. In this work, diode lasers with pulse widths in the range of ≈ 100 ps were used. Femtosecond laser pulses are, for example, achieved by Ti:sapphire lasers, while flashlamps result in excitation pulses on the nanosecond timescale. The detectors with the narrowest timing response are photomultiplier tubes (PMT), which typically show a transit time spread of less than 100 ps. Avalanche photodiodes (APD) have about a factor 3-4 higher sensitivity (PMT: ∼20% detection efficiency, APD: ∼60-70%), but show a timing uncertainty on the order of 0.5-1 ns, depending on the specific model. These effects are summarized in the instrument response function (IRF) that characterizes the timing response of the system to a zero lifetime sample. It can be measured either from a scattering solution (e.g. Rayleigh/Raman scattering of water or a colloidal silica solution), or from a highly quenched fluorescence sample (e.g. of a fluorophore in a saturated solution of potassium iodide, Szabelski et al., 2009).

To circumvent these problems, an approximate analysis can be performed by fitting the model functions only to the tail of the fluorescence decay ("tail fitting"), starting from time scales longer than the instrument response function. Using this approach, however, it is impossible to resolve short fluorescence lifetimes on the order of the width of the IRF.

Instead, the discussed effects can be accounted for directly in the analysis of the fluorescence decay by convolution of the model function $M(t)$ with the instrument response function $IRF(t)$:

$$I(t) = IRF(t) * M(t) = \int_0^t IRF(t-t')M(t')dt' \tag{2.38}$$

where $I(t)$ is the measured intensity decay and $*$ denotes the mathematical operation of convolution. The model function may hereby be given by a simple single or multi-exponential decay or describe more complex situations such as a distribution of rates, a situation that is common in FRET experiments where a distribution of donor-acceptor distances is usually observed. If polarized detection is employed, the anisotropy information can also be included into the fit function by performing a global analysis of parallel and perpendicular decays.

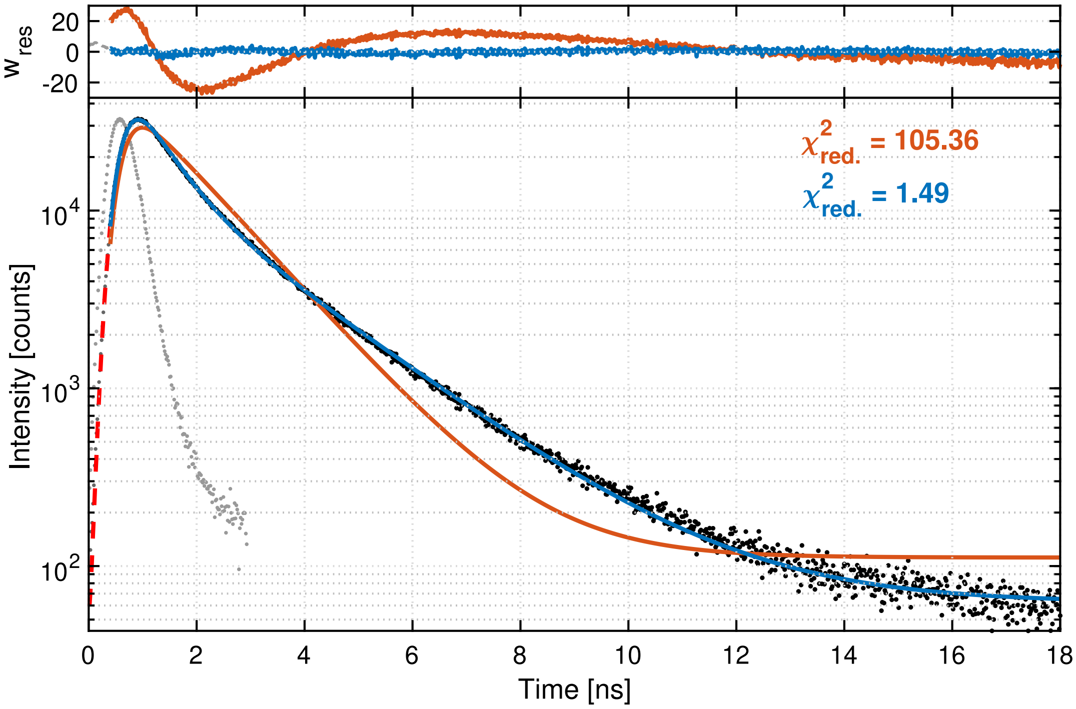

FIGURE 2.11: An example analysis of a fluorescence decay by reconvolution fitting, measured on an APD and excited by a diode laser. The full width at half maximum (FWHM) of the instrument response function, shown in gray, is ∼600 ps. A single exponential function is not sufficient to describe the data (red line). Inclusion of a second component results in an improved fit.

## 2.9 Fluorescence correlation spectroscopy

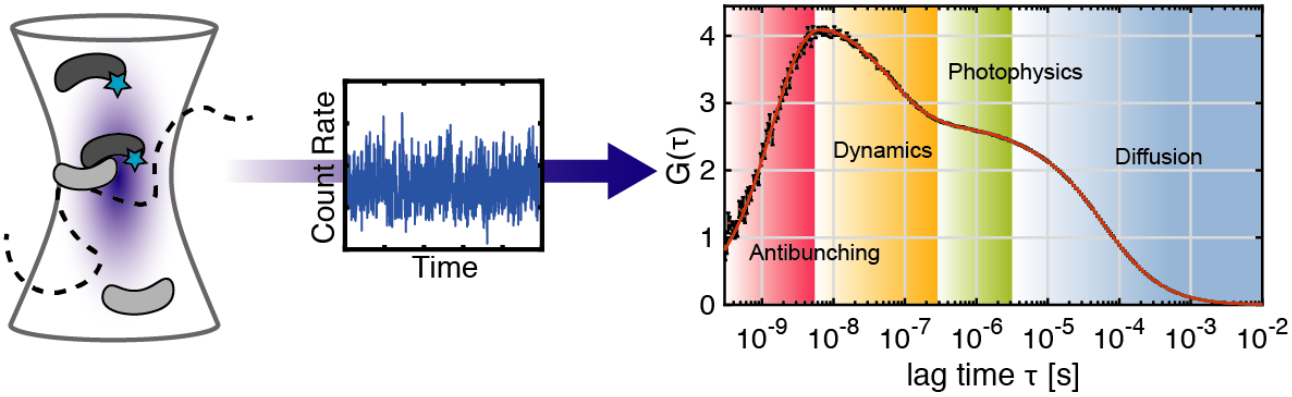

FIGURE 2.12: An overview of fluorescence correlation spectroscopy. Freely diffusing molecules are measured in solution as they diffuse through the confocal volume (left), resulting in fluctuations of the measured intensity (middle), which are analyzed through the correlation function (right). The accessible timescale of FCS measurements ranges from picoseconds to seconds, allowing a variety of processes to be studied.

Fluorescence correlation spectroscopy analyzes the time-dependence of fluctuations of the fluorescence intensity to obtain information about dynamic processes. The second-order autocorrelation function is defined by:

$$G(\tau) = \frac{\langle \delta I(t) \delta I(t+\tau) \rangle}{\langle I(t) \rangle^2} \tag{2.39}$$

where $\tau$ is the lag time, $\langle ... \rangle$ denotes the time average, $I(t)$ is the fluorescence intensity and $\delta I(t) = I(t) - \langle I(t) \rangle$ is the time-dependent fluctuation of the fluorescence intensity. The amplitude of the autocorrelation function is inversely proportional to the average particle number $\langle N \rangle$ and thus concentration. This is easily shown by considering the intensity is given by the particle number $N(t)$ multiplied by the molecular brightness $\epsilon$, $I(t) = \epsilon N(t)$. The occupancy of the confocal volume $N(t)$ follows a Poisson distribution with a mean value $\langle N \rangle$. For a Poisson distribution the variance is equal to the mean, i.e. $\sigma^2 = \mu$. The correlation function at $\tau = 0$ is then given by:

$$G(0) = \frac{\langle \delta I(t)^2 \rangle}{\langle I(t) \rangle^2} = \frac{\epsilon^2 \langle N^2 \rangle}{\epsilon^2 \langle N \rangle^2} = \frac{\langle N \rangle}{\langle N \rangle^2} = \frac{1}{\langle N \rangle} \tag{2.40}$$

Here, the illumination of the confocal volume was assumed to be uniform. The approximate Gaussian illumination profile of the confocal volume effectively reduces the amplitude of the fluctuations. This is accounted for by the $\gamma_{\text{FCS}}$-factor that is given by $2^{3/2}$ in one-photon excitation.

$$G(0) = \frac{\gamma_{\text{FCS}}}{\langle N \rangle} = \frac{2^{-\frac{3}{2}}}{\langle N \rangle} \tag{2.41}$$

The $\gamma_{\text{FCS}}$-factor is sometimes neglected for the determination of the average particle number in the confocal volume, in which case $\langle N \rangle$ will be overestimated. To relate the average particle number to a concentration, it is necessary to know the effective volume of the observation spot. If the $\gamma_{\text{FCS}}$-factor is considered, the effective probe volume is given by:

$$V_{\text{eff},\gamma} = \pi^{3/2} \omega_r^2 \omega_z \tag{2.42}$$

Otherwise, if the $\gamma_{\text{FCS}}$-factor is not considered, the missing correction has to be included in the definition of the effective volume, i.e. $V_{\text{eff, no}\,\gamma} = \left(\frac{\pi}{2}\right)^{3/2} \omega_r^2 \omega_z$. When the correct formula is used for the the effective volume, the determined concentration is thus identical. A conceptual difference, however, arises with respect to the reported molecular brightness value $\varepsilon$ of the fluorophore, given by:

$$\varepsilon = \frac{\langle I \rangle}{\langle N \rangle} \tag{2.43}$$

When using $\gamma_{\text{FCS}}$ to determine the average particle number, $\varepsilon$ reports the peak brightness of the fluorophore at the center of the point-spread function. Otherwise, $\varepsilon$ is equivalent to the average brightness in the observation volume.

The autocorrelation functions measures the self-similarity of the signal as a function of the lag time, revealing the timescale of dynamic processes that affect the fluorescence intensity. The total correlation function is then given by the product over the individual contributions of diffusion, photophysics, dynamic quenching and photon antibunching, which will be described in detail below:

$$G(\tau) = G_{\text{diffusion}}(\tau) G_{\text{photophysics}}(\tau) G_{\text{dynamic}}(\tau) G_{\text{antibunching}}(\tau) \tag{2.44}$$

### 2.9.1 Diffusion

The diffusion of molecules through the small confocal volume of approximately 1 fL results in intensity fluctuations whose time evolution is determined by the diffusion properties of the molecules of interest. In the case of Brownian motion, an analytical form for the autocorrelation function is obtained through approximation of the confocal volume by a 3D Gaussian function (see section 2.4, Magde et al., 1972):

$$G(\tau) = \frac{\gamma}{\langle N \rangle} \left(1 + \frac{\tau}{\tau_D}\right)^{-1} \left(1 + \frac{\tau}{p^2 \tau_D}\right)^{-1/2} \tag{2.45}$$

Here, $\tau_D$ is the diffusion time which is related to the diffusion coefficient $D$ and the lateral size of the confocal volume $\omega_r$ by:

$$\tau_D = \frac{\omega_r^2}{4D} \tag{2.46}$$

The factor $p$ accounts for the different size of the confocal volume in the axial dimension and is given by $p = \omega_z / \omega_r \approx$ 5-10. The measurement of absolute diffusion coefficients requires a precise knowledge about the size of the confocal volume. Rather than imaging the point spread function directly, one can also measure a sample with known diffusion coefficient (e.g. a solution of fluorescent dyes) and deduce the parameters of the confocal volume from the FCS curve. Precise measurements of absolute diffusion coefficients independent of external references can be performed by correlating signal obtained from spatially separated regions of known distances, as performed in two-focus FCS (Dertinger et al., 2008), pair-correlation spectroscopy (Digman and Gratton, 2009) or raster image correlation spectroscopy (Digman et al., 2005).

### 2.9.2 Photophysics

FCS is sensitive to all factors that affect the fluorescence intensity. Among them are the photophysics of the fluorophore itself, such as transitions to triplet or radical ion states, which result in switching between bright and dark states (photoblinking). Triplet state transitions usually occur on the microsecond timescale, thus faster than the diffusion, making them measurable by FCS. Their contribution to the correlation function is given by (Widengren et al., 1994):

$$G_{\text{triplet}}(\tau) = 1 + \frac{T}{1 - T} e^{-t/\tau_T} \tag{2.47}$$

where $T$ is the fraction of molecules in the dark (triplet) state and $\tau_T$ depends on the transition rates. It is given by:

$$\tau_T = \left(k_{T_1 \to S_0} + \frac{k_{S_0 \to S_1} k_{S_1 \to T_1}}{k_{S_0 \to S_1} + k_{S_1 \to S_0}}\right)^{-1} \tag{2.48}$$

where $k_{i \to j}$ describes the rate constant from state $i$ to $j$. Generally, the rate of fluorescence $k_{S_1 \to S_0}$ is much larger than the transition rate to the triplet state $k_{S_1 \to T_0}$ and the excitation rate $k_{S_0 \to S_1}$. In this case, the second term in the equation can be neglected and $\tau_T \approx k^{-1}_{T_1 \to S_0}$, meaning that the measured timescale is equivalent to the average time the fluorophore spends in the dark state. However, it is important to consider that $\tau_T$ is also a function of the excitation rate. A higher excitation rate increases the $S_1$ population and thus the likelihood to transition to the triplet state, reducing the measured timescale $\tau_T$ by increasing the rate of dark state formation.

In addition to the simple situation described here, it is also possible to study much more complicated photophysical transition in fluorophores by FCS. An example are the kinetics of the *cis-trans* transitions in cyanine fluorophores (Widengren and Petra Schwille, 2000).
Another process that can be monitored by FCS is photobleaching. If the molecule photobleaches during the transit through the confocal volume, the apparent diffusion time will be reduced. The rate of bleaching is hereby dependent on the position of the fluorophore in the probe volume and it is generally modeled using an additional exponential term (Widengren and Rigler, 1996). Optical saturation at high laser powers has an adverse effect (Gregor et al., 2005), resulting in an increase of the apparent diffusion time. This effect can be understood by considering that saturation alters the shape of the PSF. Maximum excitation is achieved over the central region of the PSF, leading to a box-like profile with harder edges and an overall enlargement of the effective detection volume.

### 2.9.3 Photon antibunching

At lag times comparable to the fluorescence lifetime (< 10 ns), an anti-correlation is observed in the FCS curve (Figure 2.12). The reason stems from the fact that a single fluorophore can only emit one photon at a time, after which it has to be re-excited before emitting the next photon. This effect is generally referred to as photon antibunching. The measurement of antibunching requires that the fluorescence emission is separated onto two detectors on independent detection channels to circumvent the dead time. The antibunching contribution to the correlation function is given by:

$$G_{\mathrm{ab}} = 1 - \frac{1}{n} e^{-t/\tau_{\mathrm{ab}}} \tag{2.49}$$

where $n$ is the number of fluorescent emitters per diffusing molecule. The timescale of the antibunching depends on the fluorescence lifetime $\tau_{\mathrm{F}}$ and the excitation rate $k_{\mathrm{ex}}$:

$$\tau_{\mathrm{ab}} = \frac{1}{1/\tau_{\mathrm{F}} + k_{\mathrm{ex}}} \tag{2.50}$$

Generally, the rate of fluorescence is orders of magnitude larger compared to the excitation rate, in which case $\tau_{\mathrm{ab}} \approx \tau_{\mathrm{F}}$. The amplitude of the antibunching term depends on the number of independent emitters per diffusing molecule, $G(0) = 1 - 1/n$. If multiple fluorophore labels are present on one molecule, there is a probability that the other fluorophores emit a photon during the dark period, reducing the antibunching contrast. This effect can be used to count the number of emitters, allowing one e.g. to address the stoichiometry of molecular complexes.
A distinction has to be made between measurements of photon antibunching on isolated molecules (e.g. immobilized on a surface) and molecules freely diffusion in solution. For isolated molecules, antibunching results in complete anitcorrelation (i.e. $G(0) = -1$, see for example Steiner et al., 2017). This is not observed for freely diffusing molecules in solution due to the finite probability to find another molecule in the focal volume. This probability is independent of the lag time $\tau$, i.e. $G(0) = G(\infty) = 0$.
Instead of computing the full correlation function according to equation 2.39, the correlation function on the nanosecond range can also be approximated by the histogram of arrival time differences (see Figure 2.13). The difference between the interphoton time histogram and the full correlation function is that the correlation function accounts for the time delays between all photons, while, in the interphoton time histogram, only the next photon is considered. This effect is commonly referred to as pile-up and can be compensated by considering that photon detection events are Poisson distributed. The interphoton time $\tau$ thus follows an exponential distribution $\tau \sim k \exp(-k\tau)$ where $k$ is the count rate of the detected signal. Then, the probability to detect a photon after an interphoton time $t > \tau$ is given by:

$$P(t > \tau) = 1 - \int_0^{\tau} k \exp(-kt) dt = \exp(-k\tau) \tag{2.51}$$

The true correlation function is then calculated from the interphoton time histogram $h(\tau)$ by (Nettels et al., 2007):

$$G(\tau) = h(\tau) \exp(k\tau) \tag{2.52}$$

### 2.9.4 Fluorescence cross-correlation spectroscopy

Instead of correlating a single channel with itself, it is also possible to investigate the correlation between different channels. The cross-correlation function (CCF) is then defined by:

$$G_{\text{CCF}}(\tau) = \frac{\langle \delta I_1(t)\delta I_2(t+\tau)\rangle}{\langle I_1(t)\rangle\langle I_2(t)\rangle} \tag{2.53}$$

Fluorescence cross-correlation spectroscopy is most often used to correlate the two signals of two different dye labels, enabling the sensitive detection and absolute quantification of biomolecular interactions. In this case, the amplitude of the cross-correlation function is proportional to the number of particles that carry both fluorophores $N_{12}$ and inversely proportional to the total number of particles of carrying label 1 or 2, $N_{1,t}$ and $N_{2,t}$:

$$G_{\text{CCF}}(0) = \gamma\frac{N_{12}}{N_{1,t}N_{2,t}} \tag{2.54}$$

The cross-correlation functions is highly sensitive to trace amount of interacting molecules. Experimentally, however, the cross-correlation signal is often affected by spectral crosstalk of the lower-wavelength fluorophore into the higher-wavelength detection channel, causing a non-zero signal even in the absence of interactions. While these effects can be accounted for in the analysis of the data (P. Schwille et al., 1997), the method of pulsed interleaved excitation (PIE) provides an elegant way to remove residual cross-correlation entirely (see section 2.6 and Müller et al., 2005). Other applications of cross-correlation spectroscopy are the removal of detector afterpulsing by cross-correlation of the split signal from two independent detectors (Zhao et al., 2003), the study of the rotation of biomolecules by cross-correlation of parallel and perpendicular emission (Pieper and Enderlein, 2011), and the quantification of dynamic processes by cross-correlation of donor and FRET-sensitized acceptor fluorescence in FRET experiments (described in the next section).

### 2.9.5 Conformational dynamics

Besides the measurement of diffusion constants or cross-correlation signal to probe molecular interactions, FCS is also a powerful tool to study conformational dynamics. In the simplest case, the system is assumed to be described by two states, $s_1$ and $s_2$, that interconvert with rates $k_{12}$ and $k_{21}$:

$$s_1 \underset{k_{21}}{\overset{k_{12}}{\rightleftharpoons}} s_2 \tag{2.55}$$

The equilibrium constant is then given by $K = k_{12}/k_{21}$ and the fraction of molecules found in state 1 or 2 by:

$$f_1 = \frac{k_{21}}{k_{12}+k_{21}} \qquad f_2 = 1 - f_1 \tag{2.56}$$

To enable the detection of dynamics by FCS, it is required to couple the conformational transitions to a modulation of the fluorescence intensity. This is most commonly achieved by introducing quenchers, e.g. in PET or FRET, but fluorescence enhancement (for example protein induced fluorescence enhancement, Hwang et al., 2011) may likewise be used.

#### PET

In the case of fluorescence quenching by PET, it is usually assumed that the quenched state is completely dark. In this case, the dynamic contribution to the correlation function is simply given by a single exponential term (Markus Sauer and Hannes Neuweiler, 2014).

$$G_{\text{dyn}}^{\text{PET}}(t) = 1 + A\exp\left(-t/\tau_R\right) \tag{2.57}$$

The relaxation time $\tau_R$ and amplitude $A$ are given by:

$$\tau_R = \frac{1}{k_o + k_c} \qquad A = \frac{k_c}{k_o} \tag{2.58}$$

To understand why the amplitude of the kinetic term is given by equation 2.58, consider that the molecule is found in the unquenched state with brightness $\varepsilon$ with probability $p_{on} = k_o/(k_o + k_c)$. The average intensity is then simply $\langle I \rangle = p_{on}\varepsilon$. The mean square of the signal $\langle I^2 \rangle$ can be computed as well:

$$\langle I^2 \rangle = p_{\text{on}}\varepsilon^2 + p_{\text{off}}0^2 = p_{\text{on}}\varepsilon^2 \tag{2.59}$$

The correlation function is then given by:

$$\begin{aligned} G_{\text{dyn}}^{\text{PET}}(0) &= \frac{\langle (\delta I)^2 \rangle}{\langle I \rangle^2} = \frac{\langle I^2 \rangle}{\langle I \rangle^2} - 1 \\ &= \frac{p_{\text{on}}\varepsilon^2}{p_{\text{on}}^2\varepsilon^2} - 1 = \frac{1}{p_{\text{on}}} - 1 = \frac{k_o + k_c}{k_o} - 1 = \frac{k_c}{k_o} \end{aligned}$$

Naturally, the ratio of the variance to the mean is largest when the mean is small, i.e. when the system is mostly in the quenched state as is the case for a large quenching rate $k_c$ compared to the unquenching rate $k_o$. Using equation 2.56, one finds $A = f_1/(1 - f_1)$, which makes $G_{\text{dyn}}^{\text{PET}}$ identical to the expression for $G_{\text{triplet}}$ obtained before.

### FRET

Conformational dynamics can also be studied by FRET, however the analysis of the correlation functions is more complicated. Different to the situation in PET-FCS, where the fluorophore is either fluorescent or dark, the modulation of the fluorescence intensity in FRET results in two different brightnesses for donor and acceptor fluorophore in the different conformational states. In FRET-FCS, however, information from both the donor and acceptor channels is available, which can be taken advantage of by a global analysis of the two autocorrelation functions ($G_{\text{D}}$ and $G_{\text{A}}$) and the cross-correlation function ($G_{\text{DA}}$) that share the same kinetic parameters. The dynamic contributions to the correlation functions are given by (Felekyan et al., 2013; Torres and Levitus, 2007):

$$G_{\text{dyn,D}}(\tau) = 1 + G_{\text{dyn,D}}(0)\exp(-\tau/\tau_R) \tag{2.60}$$

$$G_{\text{dyn,A}}(\tau) = 1 + G_{\text{dyn,A}}(0)\exp(-\tau/\tau_R) \tag{2.61}$$

$$G_{\text{dyn,DA}}(\tau) = 1 - \sqrt{G_{\text{dyn,D}}(0)G_{\text{dyn,A}}(0)}\exp(-\tau/\tau_R) \tag{2.62}$$

The dynamic interconversion shows as a bunching term in the autocorrelation functions but leads to anticorrelation in the cross-correlation function (Figure 2.13 B). The amplitudes of the kinetic terms are dependent on the brightness of donor or acceptor fluorophore in the different FRET states as well as on the kinetic parameters. Due to the complex relationship, they are not well defined and e.g. extraction of the FRET efficiencies of the states is not possible. If the FRET states are known, one can consider to include the amplitude information in the analysis, but generally it is best to leave the amplitudes as free fit parameters and focus on the time-dependence of the correlation function to extract the relaxation time $\tau_R$. Note, however, that it is not

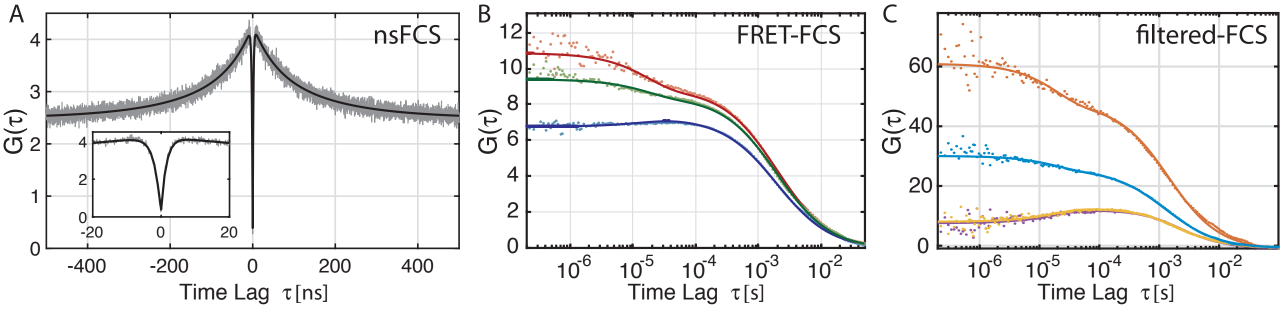

FIGURE 2.13: Studying dynamics with FCS. **(A)** Linear representation of the correlation function shown in Figure 2.12. Inset: Zoom-in to show the photon antibunching. **(B)** FRET-FCS showing matching bunching and anitbunching terms in the auto- cross-correlation functions. **(C)** Filtered-FCS further increases the contrast of the dynamic contribution. Panels B-C are adapted from Barth et al., 2018a.

possible to define the microscopic rates in this case, which would require the amplitude information. Further factors that hamper a quantitative interpretation of the amplitude information are given by contamination with donor-only labeled molecules and experimental artifacts such as spectral cross-talk and cross-excitation. While the latter factor mostly distorts the amplitudes, the presence of a large fraction of donor-only labeled molecules will effectively reduce the contrast by lowering the relative contribution of the kinetic amplitudes, making it difficult to resolve the dynamics. This problem can be avoided if the FRET-FCS analysis is performed selectively on molecules carrying both fluorophores, which is possible in single-molecule experiments with alternating laser excitation (see section 2.10.6). Another approach to increase the contrast in FRET-FCS is filtered fluorescence correlation spectroscopy (fFCS, see Figure 2.13 C), described in more detail in the next section.

### 2.9.6 FLCS and fFCS

The basic idea of filtered fluorescence correlation spectroscopy (fFCS) is to use additional parameters to separate the different species present in a mixture. These additional parameters may hereby be given by the fluorescence lifetime as available in TCSPC measurements (fluorescence lifetime correlation spectroscopy, FLCS, Böhmer et al., 2002), the wavelength or color information (fluorescence spectral correlation spectroscopy, FSCS, Benda et al., 2014; Schrimpf et al., 2018b) or the anisotropy information (Felekyan et al., 2012). The term filtered-FCS generalizes the concept to arbitrary parameters and combinations thereof.

The mathematical formalism of fFCS provides a recipe to define filters or photon weights that depend on the additional parameters to be considered. Here, the method is described based on TCSPC data with a focus on the fluorescence lifetime, but the formalism is transferable to arbitrary types of data. To derive the filter values, consider that the detected TCSPC histogram is a linear combination of the contributions of all species present in the mixture. If the TCSPC patterns of the individual species (and the background) are known, one can determine the intensity contributions of each species $w_i$ by describing the decay of the mixture $D(t_{\mathrm{mi}})$ at the time delay $t_{\mathrm{mi}}$ by:

$$D(t_{\mathrm{mi}}) = w_1 d_1(t_{\mathrm{mi}}) + w_2 d_2(t_{\mathrm{mi}}) \tag{2.63}$$

where $d_i$ are the normalized TCSPC patterns of the individual species, i.e. $\sum_j d_i(j) = 1$. The contributions $w_i$ may then be determined by minimizing the squared deviation over all available time delays. Another way to look at the problem (that may seem un-intuitive at first) is to find functions $f_i$ (so-called "filters") that are defined through the following equation:

$$w_i = \sum_{t_{\mathrm{mi}}} f_i(t_{\mathrm{mi}}) D(t_{\mathrm{mi}}) \tag{2.64}$$

This equation effectively defines statistical weighting functions $f_i$ that allow us to obtain the contribution of a species from the weighted sum of the total decay histogram. The usefulness of the filter functions is the following: If we apply the filter function to the total measured data set, we obtain or "filter" the contribution of the respective species. Since the mixture $D$ is just the cumulative histogram of the individual photon detection events, the same holds true if we apply the filter functions to the individual photons. In other words, the time averaged intensity of species $i$ (as used in the calculation of the FCS curves) is obtained by weighting the photon detection events with the respective filter values given by the micro-time information:

$$\lim_{N_p \to \infty} \frac{1}{T} \sum_{n=1}^{N_p} f_i(t_{\mathrm{mi}}(n)) = \langle I_i(t) \rangle \tag{2.65}$$

where $N_p$ is the number of detected photons, $T$ is the measurement time and $\langle\rangle$ denotes time averaging. In other words, if we use the photon weights given by the filter function in the calculation of the correlation function, we obtain the "pure" correlation function of the individual species.

To obtain the filters, one has to simultaneously minimize the following equation for all species:

$$\underset{f_i}{\operatorname{argmin}} \left[ w_i - \sum f_i(t) D(t) \right]^2 \tag{2.66}$$

This is essentially a least-squares curve fitting problem (see also section 2.12.4) that can be solved analytically if the photon counting statistics are Poissonian (which is fulfilled for photon counting data) (Böhmer et al., 2002; Enderlein and Erdmann, 1997). The filter functions for $n$ species can then be calculated using simple matrix calculations by:

$$\begin{bmatrix} \mathbf{f}_1 \\ \mathbf{f}_2 \\ \vdots \\ \mathbf{f}_n \end{bmatrix} = \left( \begin{bmatrix} \mathbf{d}_1 \\ \mathbf{d}_2 \\ \vdots \\ \mathbf{d}_n \end{bmatrix} \cdot \mathbf{D} \cdot \begin{bmatrix} \mathbf{d}_1 \\ \mathbf{d}_2 \\ \vdots \\ \mathbf{d}_n \end{bmatrix}^{\mathrm{T}} \right)^{-1} \cdot \begin{bmatrix} \mathbf{d}_1 \\ \mathbf{d}_2 \\ \vdots \\ \mathbf{d}_n \end{bmatrix} \cdot \mathbf{D} \tag{2.67}$$

where $\cdot$ indicates matrix multiplication, $^T$ denotes the matrix transpose and $^{-1}$ means matrix inversion. The patterns of the individual components $\mathbf{d}_i$ are given by row vectors, i.e. $\mathbf{d}_i = [d_i(1)\, d_i(2) \ldots d_i(N)]$. The same applies to the filters $\mathbf{f}_i$. The matrix $\mathbf{D}$ is given by a diagonal matrix containing the reciprocal values of the decay histogram of the mixtures $D(i)$:

$$\mathbf{D} = \begin{bmatrix} \frac{1}{D(1)} & 0 & 0 & \cdots & 0 \\ 0 & \frac{1}{D(2)} & 0 & \cdots & 0 \\ 0 & 0 & \frac{1}{D(3)} & \cdots & 0 \\ \vdots & \vdots & \vdots & \ddots & \vdots \\ 0 & 0 & 0 & \cdots & \frac{1}{D(N)} \end{bmatrix} \tag{2.68}$$

Using equation 2.67, the minimization of equation 2.66 is performed in one step for all species. This brings along that the sum of all filter values for a given channel is always equal to 1 and ensures orthonormality of the obtained filter functions:

$$\mathbf{f}_i \cdot \mathbf{d}_j = \sum_{k=1}^{N} f_i(k) d_j(k) = \begin{cases} 1, & \text{if } i = j \\ 0, & \text{otherwise} \end{cases} \tag{2.69}$$

### Practical considerations

While the signal-to-noise ratio in FCS is mostly limited by the number of photons, the quality of the filter patterns is an additional factor in fFCS. Since any noise in the TCSPC patterns of the individual species will propagate to the filters, one should make sure that the TCSPC patterns are measured with high statistics. For a good separation of the contributions, it is also required that the parameter used to distinguish the species is significantly different to offer sufficient contrast. As a rule of thumb for fluorescence lifetimes, good separation is achieved for a factor 2 difference.

The effect of a bad contrast between the contributing species may be seen in two ways. The combination of low contrast with small errors in the filter patterns will result in crosstalk between the species, causing a contamination of the correlation functions by the other species. Secondly, even if the filter patterns are correct, low contrast will significantly lower the achievable signal-to-noise ratio of the correlation curves (Schrimpf et al., 2018b). While the correlating signal of the other species is filtered out, their signal still contributes as uncorrelated noise to the correlation function, effectively reducing the "useful" signal of the species of interest.

### Applications of fFCS

The intriguing aspect of fFCS is that interaction studies, which normally require multicolor detection and labeling, are possible using a single detection channels. Additionally, the increased contrast offered by fFCS compared to FRET-FCS enables a more detailed analysis of dynamics. These two aspects will be discussed below.

**Example 1: Using the lifetime information to extract species-selective FCS curves** As an example for an application of FLCS, consider a mixture of the fluorophore Alexa647, freely diffusing in solution, and the fluorophore Atto647N, attached to double-stranded DNA. The two fluorophores are spectrally very similar ($\lambda^{\text{em,max}}_{\text{Alexa647}} = 669\,\text{nm}$, $\lambda^{\text{em,max}}_{\text{Atto647N}} = 664\,\text{nm}$, see Figure 2.14 A), however the fluorescence lifetimes show a difference of a factor of ~3-4 ($\tau_{\text{Alexa647}} \approx 1.0\,\text{ns}$, $\tau_{\text{Alexa647}} \approx 3.5\,\text{ns}$). The normalized TCSPC patterns of the individual species and the mixture are shown in Figure 2.14 B. Based on these patterns, the filters are calculated according to equation 2.67 (Figure 2.14 B). The filters can be interpreted as a measure of the probability that a photon detected in a given TCSPC channel originated from a given species. Due to the short lifetime of Alexa647, the filter has positive values at low lag times but negative values at high lag times, while the filter for Atto647N shows the opposite trend.

Using the filters, the species auto- and cross-correlation functions are calculated (Figure 2.14 C). Indeed, the correlation function for Atto647N reveals much slower diffusion. Additionally, the curve for Alexa647 shows a large bunching term on the microsecond timescale, characteristic for the photophysics of cyanine dyes. Due to the absence of interactions between the species, the cross-correlation curve has zero amplitude. Lastly, the direct comparison of the autocorrelation functions of the pure samples with the species autocorrelation functions (Figure 2.14 D) shows that, indeed, the FLCS analysis recovers the correct curves. However, the noise in the species autocorrelation functions is slightly increased because the useful signal for each species in the mixture is reduced compared to the pure measurements.

**Example 2: Filtered-FCS for the study of conformational dynamics** In fFCS, the orthonormality of the filters (see equation 2.69) results in an ideal contrast of 100% between the different species, considering that the filters

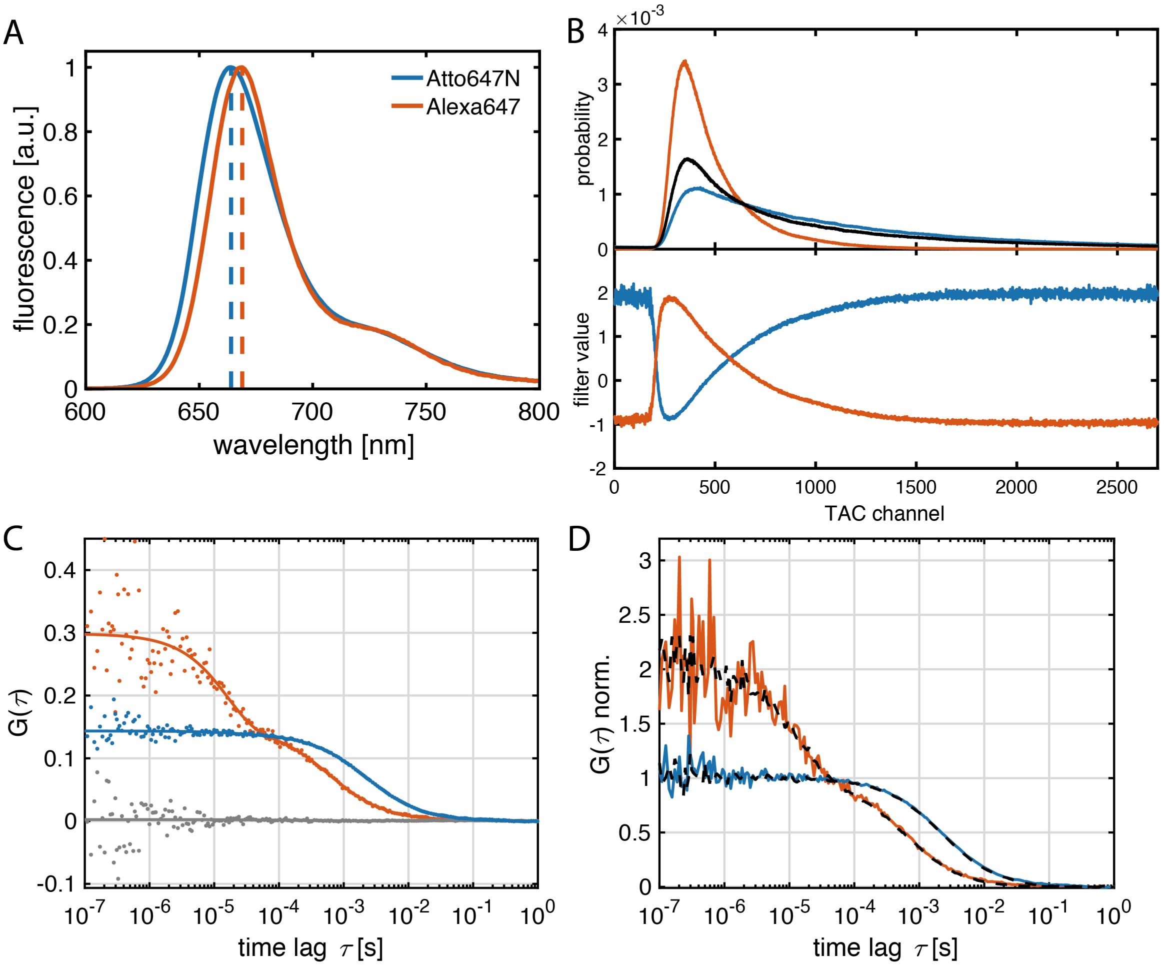

FIGURE 2.14: Fluorescence lifetime correlation spectroscopy to study diffusion of species with different fluorescence lifetimes. Measurements were performed on freely diffusing Alexa647 and Atto647N attached to double-stranded DNA. **(A)** Normalized emission spectra of Atto647N and Alexa647. **(B)** Top: Normalized TCSPC patterns of Alexa647 (red), Atto647N-DNA (blue) and a 1:1 mixture (black). Bottom: Corresponding filter values of the species shown above. **(C)** Species autocorrelation (red: Alexa647, blue: Atto647N-DNA) and cross-correlation (gray) curves calculated using the filters shown in B. **(D)** Comparison of the autocorrelation curves of the pure species determined from separate measurements (dashed lines) with the curves extracted by FLCS analysis as shown in C.

are correct and the species show enough separation in the parameter of interest. Consequently, the cross-correlation between different species results in complete anti-correlation, and the amplitude terms for the autocorrelation functions are equivalent to the formula for PET-FCS introduced in section 2.9.5. The dynamic contributions to the species autocorrelation functions (sACF) and the species cross-correlation function (sCCF) are given by (Felekyan et al., 2012)

$$G_{\text{dyn}}^{\text{sACF1}}(\tau) = 1 + \frac{k_{12}}{k_{21}} \exp\left(-\frac{\tau}{\tau_R}\right) \tag{2.70}$$

$$G_{\text{dyn}}^{\text{sACF2}}(\tau) = 1 + \frac{k_{21}}{k_{12}} \exp\left(-\frac{\tau}{\tau_R}\right) \tag{2.71}$$

$$G_{\text{dyn}}^{\text{sCCF}}(\tau) = 1 - \exp\left(-\frac{\tau}{\tau_R}\right) \tag{2.72}$$

where $\tau_R = (k_{12} + k_{21})^{-1}$. Note that the anticorrelation amplitude in the sCCF is always equal to one since, at time zero, the molecule is found either in state 1 or state 2. Thus, it is not possible to extract the kinetic rates from the sCCF alone which requires the amplitude information from the sACFs.

An example of a filtered-FCS analysis using simulated data of a system transitioning betweeen low and high

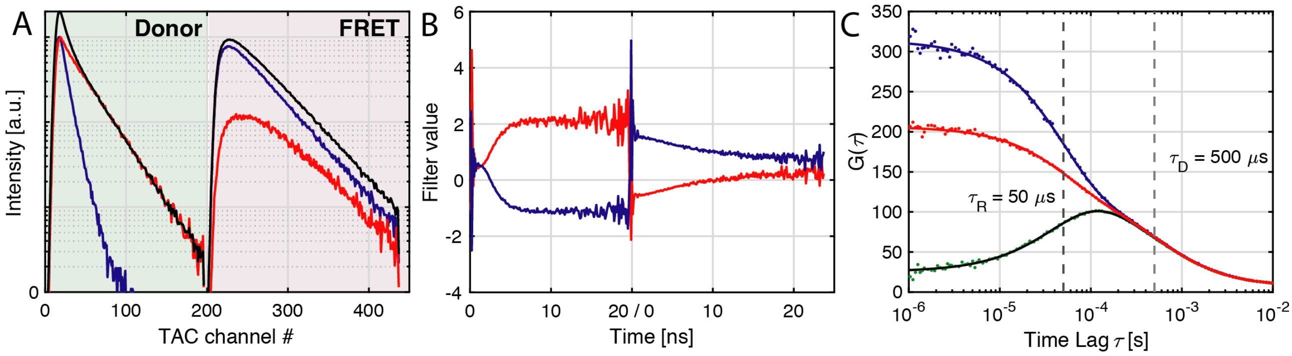

FIGURE 2.15: Studying conformational dynamics with filtered-FCS, illustrated using a simulated dataset. **(A)** TCSPC patterns of the low-FRET species (red), high-FRET species (blue) and the mixture (black). The patterns of the donor and FRET channel (FRET-sensitized acceptor emission) are concatenated to use all available experimental information in the generation of the filters. **(B)** Generated filters for the species shown in A. **(C)** The species autocorrelation functions (red: low-FRET, blue: high-FRET) and cross-correlation function (green) reveal the dynamic interconversion with relaxation time $\tau_R$ and the diffusion time $\tau_D$.

FRET efficiency is shown in Figure 2.15. To include both the information from the donor and the acceptor fluorophore, the donor and FRET detection channels are concatenated (Figure 2.15 A). The low-FRET state is characterized by a long donor fluorescence lifetime and low signal in the FRET detection channel, while the high-FRET state shows a short donor lifetime and a higher signal in the FRET channel. Note that, while the acceptor lifetime is unchanged between the two states, the decay of the FRET-sensitized acceptor emission is dependent the donor lifetime and thus on the FRET state (it is the convolution of the donor and the acceptor fluorescence decay, see Kudryavtsev et al., 2012). This results in an apparent shorter lifetime of the FRET signal for the high-FRET state. Thus, the additional information added by the use of donor and FRET channel is not only given by the signal distribution over the two channels that depends on the FRET efficiency, but also through the shape of the FRET-sensitized acceptor decay.

Based on the concatenated TCSPC patterns, the filters for fFCS analysis are calculated (Figure 2.15 B). The shape of the filters for the donor channel is similar to the filters obtained in the previous example (Figure 2.14 B). Additionally, the effect of the donor lifetime on the FRET-sensitized acceptor emission, as discussed above, results in a time-dependent contribution to the filters for the FRET channel. The FRET efficiency information effectively introduces a constant offset in the filters. For the high-FRET species, where little signal is detected in the donor channel, the donor filter is shifted to negative values, while the FRET filter is positive at all time lags. In contrast, the filter of the low-FRET species, where most signal is detected in the donor channel, shows positive values for the donor channel and negative values for the FRET channel.

Using the filters, the species auto- and cross-correlation functions are calculated (Figure 2.15 C). Note that, in principle, two cross-correlation functions can be calculated (1x2 and 2x1). However, since the dynamic contribution to the cross-correlation function only depends on the relaxation time (see equation 2.72), the two functions contain the same information. Thus, the average of both curves is shown in Figure 2.15 C (compare Figure 2.13 C). Using a global fit of the diffusion and kinetic parameters, the input value for the relaxation and diffusion time ($\tau_R$ and $\tau_D$) are recovered from the correlation functions. In the case of the simulated data set presented here, it is also possible to reliably extract the microscopic rate constants from the amplitudes of the species autocorrelation functions. In experiments, however, amplitudes are often distorted due to non-ideal filters or because the correlation functions are calculated on a subset of bursts (see section 2.10.6). The dynamic information obtained from the relaxation time, however, is unaffected by these artifacts.

## 2.10 Single-molecule FRET by burst analysis

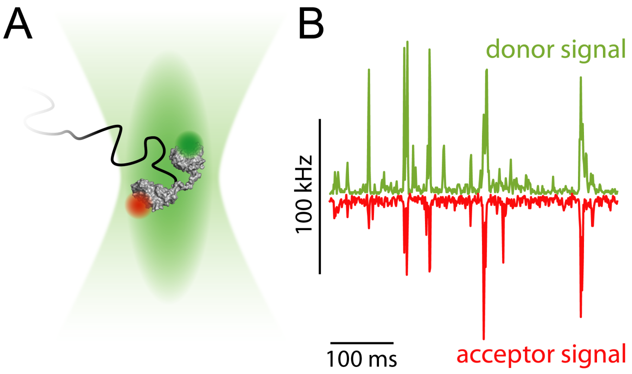

FIGURE 2.16: Measuring single molecules by burst analysis. **(A)** In burst analysis, freely diffusing fluorescently labeled molecules are measured as they diffuse through the observation volume of a confocal microscope. **(B)** Single-molecule events result in bursts of fluorescence that can be identified from the signal trace. Molecules carrying donor and acceptor fluorophores show correlated signal spikes in the donor and acceptor channels. The acceptor channel is inverted. Adapted from Barth et al., 2018a.

There are two fundamental approaches for the measurement of single fluorescent molecules, either immoblized to the surface or freely diffusing in solution. Surface-immobilized molecules can be imaged on a camera using total internal reflection fluorescence microscopy (TIRFM, Schlüsche et al., 2007; Zhuang et al., 2000) or using a confocal microscope (Chung et al., 2009; Heilemann et al., 2004). While surface immobilization allows for long observation times up to several minutes, these approaches also have drawbacks: Camera-based imaging, while allowing a large number of molecules to be measured simultaneously, is limited in the achievable time resolution to ∼10 ms. Confocal imaging using APD detectors and TCSPC electronics, on the other hand, offers picosecond time resolution, but sampling of many molecules is cumbersome as every molecule has to be measured individually.
Solution-based measurements are likewise preformed on a confocal microscope. By simply keeping the confocal volume stationary in solution, single molecules are measured as they freely diffuse through the observation volume, resulting in bursts of fluorescence (commonly called burst analysis, Figure 2.16). The combination of the femtoliter-sized observation volume of the confocal microscope and low (∼ pM) concentrations hereby ensures that the observed bursts originate from single molecules by keeping the average occupancy low. As an example, assuming a confocal volume of 1 fL size and a concentration of 10 pM, the average number of particles in the volume is ∼0.006. Thus, as the occupancy follows a Poisson distribution, the probability to find more than one molecule at any time point is $P(N > 1) = 1 - P(N \leq 1) \approx 0.002\%$ and thus negligible. At a concentration of 100 pM, the multi-molecule probability increases to ∼ 0.2%.
While potential artifacts due to the surface immobilization are avoided in burst analysis, the observation time is ultimately limited by the diffusion time of the molecule of interest. The maximum observable dynamic timescale in burst analysis is thus limited to ∼10 ms. One approach to extend the dynamic timescale is the use of the recurrence of single molecules, taking advantage of the fact that single molecules are often observed multiple times as they randomly diffuse back into the observation volume (Hoffmann et al., 2011). To increase the observation time, it is also recommended not to use a diffraction-limited observation volume, but to increase the excitation volume e.g. through underfilling of the objective lens (see section 2.4). The observation time may additionally be increased by slowing down the diffusion, e.g. by attaching the molecule of interest to large DNA origami nanostructures or by encapsulating it into lipid vesicles.

### 2.10.1 Burst detection

Different approaches have been developed to extract the single-molecule events from the recorded time traces of the fluorescence signal. If the single-photon data is integrated over a given time bin (e.g. if the signal is processed by a multichannel scaler, Zander et al., 1996), single-molecule events can be detected using a simple signal threshold. Consecutive time bins can then be combined if a molecule resided in the detection volume for a time span longer than the integration time. Drawbacks of this simple approach are that unnecessary background signal is included if the bursts are much shorter than the integration time, and that multiple bursts occurring during the integration time will be averaged.

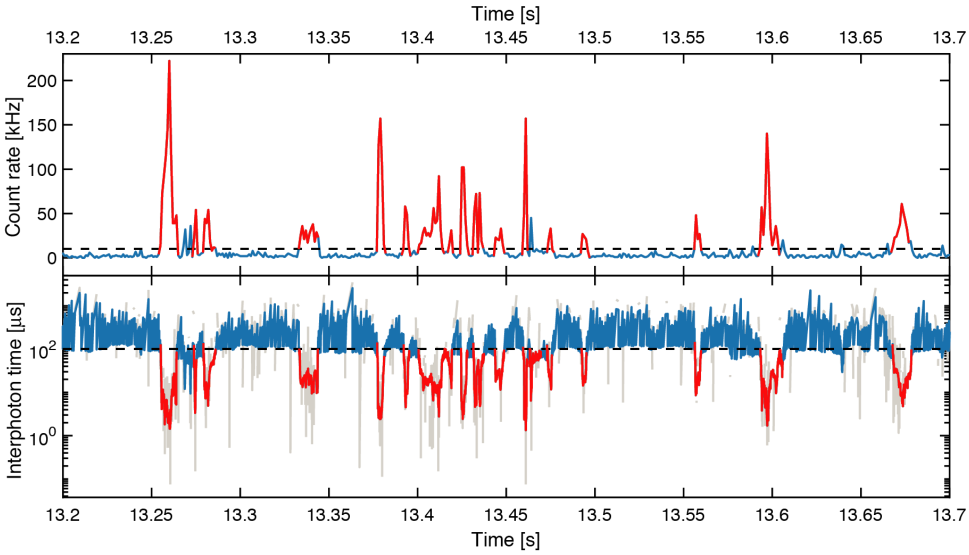

FIGURE 2.17: Overview of burst search methods (top: sliding-time-window method, bottom: interphoton-time method). Selected regions are given red, unselected regions in blue. The dashed lines indicate the effective thresholds (top: count rate 10 kHz using a time windows of 500 µs, bottom: interphoton time of 100 µs, minimum number of photons per event: 100). In the bottom panel, the raw interphoton time trace is given in grey, while the filtered trace, using a smoothing window of 20 photons, is given in blue/red.

These problems can be avoided using a sliding-time-window burst search (Nir et al., 2006). The algorithm computes the local count rate around each detected photon to decide whether the photon belongs to a burst or not. A stream of valid photons is then considered a single-molecule event if the number of photons exceeds a given threshold. The variable parameters are hereby the size of the time window used to estimate the local count rate, the minimum number of photons per time window (or the local count rate) and the minimum required number of photons per event. The choice of the time window size should be tuned to the diffusion time of the molecules of interest. If the time window is chosen too large, the local count rate is underestimated, resulting in a low number of detected molecules. Using smaller time windows, the rise and fall of the burst are detected more accurately, but too small time windows may artificially partition single bursts. See the top panel of Figure 2.17 for an example of the sliding-time-window burst search.

In a similar approach, bursts can also be identified from the interphoton time (Fries et al., 1998; Schaffer et al., 1999). During single-molecule events, short interphoton times are observed, while periods of background signal are characterized by long interphoton times (Figure 2.17, bottom panel). The noisy interphoton time trace is first smoothed using a Lee-filter (Enderlein et al., 1997) before photons originating from bursts are identified using an upper threshold on the interphoton time. Since the two burst search methods are conceptually very similar, they result in nearly identical burst selections. The choice is thus left to the preference of the user.

The burst search is most commonly performed on the sum of all available detection channel, i.e. in PIE experiments on the combined photons after donor excitation and after acceptor excitation (all photon burst search, APBS). This way, all possible labeling combinations (dual-labeled, donor-only, acceptor-only) are detected. It is, however, also possible to perform separate burst searches on different channels (dual channel burst search, DCBS, Nir et al., 2006). By separately searching for bursts on the channel after donor excitation (i.e the donor and FRET signal) and acceptor excitation, donor- and acceptor-only molecules can be excluded if only time intervals are used where both channels detected a single-molecule event.

### 2.10.2 Quantitative single-molecule FRET

The first measurements of single fluorescent molecules in solution have mostly focused on the fluorescence lifetime and anisotropy of environmentally sensitive dyes (Ambrose et al., 1999; Eggeling et al., 2001, 1998). Using two detectors and spectral separation of the emission by means of a dichroic beam splitter (Margittai et al., 2003; Rothwell et al., 2003) the simultaneous measurement of the donor and acceptor signal allows calculation of the FRET efficiency from the photon counts:

$$E = \frac{I_{DA}}{I_{DD} + I_{DA}} \tag{2.73}$$

However, a number of corrections have to be performed to obtain a quantitative FRET efficiency. First, background signal originating from detector dark counts or scattered laser light is subtracted from the measured raw signal $I_{\text{raw}}$:

$$I = I_{\text{raw}} - b \cdot T \tag{2.74}$$

where $b$ is the background count rate (obtained e.g. from a separate measurement of the buffer) and $T$ is the duration of the single-molecule event. Additional corrections are necessary for the spectral crosstalk of the donor fluorophore into the acceptor detection channel and direct excitation of the acceptor fluorophore by the donor excitation laser. The amount of spectral crosstalk is proportional to the detected donor fluorescence, $\text{CT} = \alpha I_{\text{DD}}$. If only donor excitation is employed, the direct excitation of the acceptor is difficult to correct for. It may be treated as a another constant background contribution to the FRET signal (Gansen et al., 2009) or can be corrected for based on the extinction coefficients of the donor and acceptor fluorophore at the excitation wavelength (Schuler, 2007). More commonly nowadays, single-molecule FRET experiments are performed using alternating laser excitation of the donor and acceptor fluorophore on the nanosecond time scale through pulsed interleaved excitation (PIE, Müller et al., 2005, see section 2.6) or on the microsecond time scale through alternating laser excitation (ALEX, Kapanidis et al., 2005). In this case, direct excitation can be corrected for based on the signal of the acceptor fluorophore after acceptor excitation, $\text{DE} = \delta I_{AA}$. Lastly, differences in the detection efficiencies $\eta$ and quantum yields $Q$ of the donor and acceptor fluorophore are corrected for using the $\gamma$-factor that is applied to the corrected donor signal, given by $\gamma = \eta_A Q_A / \eta_D Q_D$. If alternating excitation is employed, the correction factors $\alpha$, $\delta$ and $\gamma$ can be determined from the measurement directly (Hellenkamp et al., 2018; Kudryavtsev et al., 2012). The accurate FRET efficiency is then calculated using:

$$E = \frac{I_{DA} - \alpha I_{DD} - \delta I_{AA}}{\gamma I_{DD} + I_{DA} - \alpha I_{DD} - \delta I_{AA}} \tag{2.75}$$

Additionally, one may also obtain the accurate FRET efficiency from the fluorescence lifetime of the donor fluorophore in the presence and absence of the acceptor fluorophore, $\tau_{D(A)}$ and $\tau_{D(0)}$, which is available if pulsed excitation is used:

$$E = 1 - \frac{\tau_{D(A)}}{\tau_{D(0)}} \tag{2.76}$$

Comparison of the FRET efficiency obtained from photon counts to that obtained from the lifetime information further allows to identify conformational dynamics as described in section 2.10.5.

### 2.10.3 Multiparameter fluorescence detection

Multiparameter fluorescence detection (MFD) describes the method of extracting many parameters simultaneously from the fluorescence experiment, such as spectral information (excitation/emission), the fluorescence intensity (and related brightness and stoichiometry), the fluorescence lifetime and quantum yield, the fluorescence anisotropy, the precise photon arrival time or interdye distances by FRET (Widengren et al., 2006).

All these parameters encode vital information about specific aspects of the studied system. The use of multiple excitation lasers and spectral separation of the detected signal, as employed in pulsed interleaved excitation, provides a mean to distinguish the signal from different fluorophores based on their excitation and emission spectra (see section 2.6). The fluorescence intensity reports on the brightness of the molecules of interest, which may be used to address the stoichiometry of higher order complexes and is most robustly determined using fluorescence correlation spectroscopy as described in section 2.9. For many fluorophores, the related parameters of brightness, fluorescence lifetime and quantum yield are sensitive to the environment. Both quenching (e.g. through PET, see section 2.3) or enhancement (Hwang et al., 2011) have been extensively used to investigate molecular interactions. The assessment of the rotational freedom of the fluorescent probes is an important control in FRET measurements to support the assumption of isotropic averaging of dipole orientation (see also section 2.2.1). The anisotropy may also be used to address the rotation of the biomolecule, rendering it a sensitive parameter to detect e.g. the binding of interaction partners. The precise measurement of the photon arrival time by TCSPC (see section 2.5) is a prerequisite for the study of fast dynamic processes through correlation spectroscopy, especially when combined with the distance-sensitivity provided by FRET (see section 2.9.5).

All these parameters can be measured simultaneously on a confocal microscope (see section 2.7 for a description of the setups used in this work), opening up the whole parameter space to the single-molecule analysis (Figure 2.18). In the following, different aspects of the MFD analysis are described.

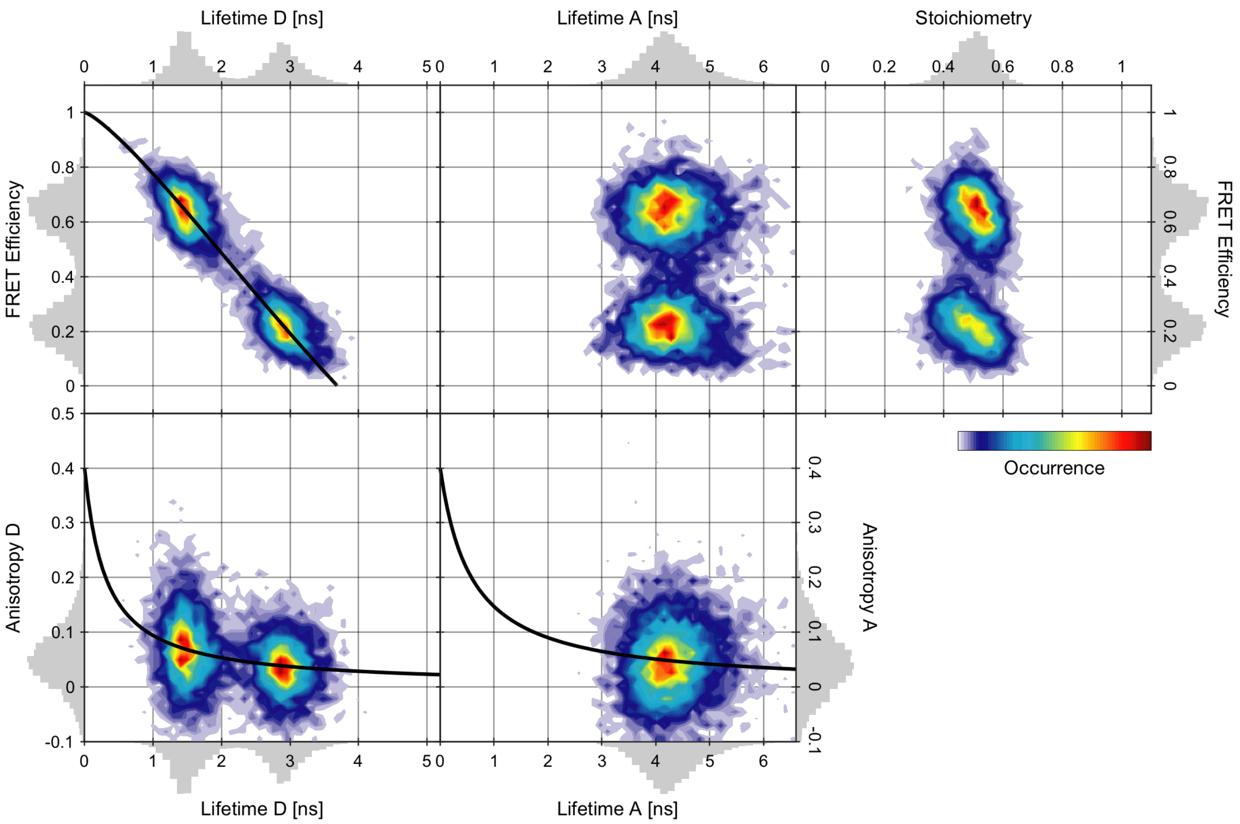

FIGURE 2.18: The full parameter space of fluorescence measured on the single-molecule level. Shown is a measurement of an equimolar mixture of two double-stranded DNA constructs labeled with the dyes Atto532 and Atto647N. **Top:** Two-dimensional histograms of the FRET efficiency from photon counts versus the fluorescence lifetime of the donor (left) and acceptor (center) fluorophores and versus the labeling stoichiometry (right). **Bottom:** Two-dimensional histograms of the anisotropy of the donor (left) and acceptor (center) fluorophores versus the respective fluorescence lifetime. Donor- and acceptor-only molecules have been removed using thresholds on the stoichiometry and ALEX-2CDE parameters.

### Molecule-wise fluorescence lifetimes

The fluorescence lifetimes of the donor and acceptor fluorophores are valuable parameters in single-molecule FRET. The accurate determination of fluorescence lifetime from the low amount of photons available per single-molecule event requires that the statistics of photon detection are correctly accounted for (Kudryavtsev et al., 2012; Maus et al., 2001). The molecule-wise lifetime is estimated by optimizing the parameter $2I^*$, which is the equivalent of the $\chi^2$ goodness-of-fit estimator for maximum likelihood estimation (see section 2.12), given by:

$$2I^* = 2\sum_{i=1}^{k} n_i \ln\left(\frac{M_i}{n_i}\right) \tag{2.77}$$

where $k$ is the number of data points of the TCSPC histogram, and $n_i$ and $M_i$ are the measured and predicted values of data point $i$. Due to the limited amount of data available, the analysis is generally restricted to the extraction of average lifetimes by means of a single-exponential decay model. The fluorescence lifetime of the acceptor fluorophore directly reports on the quantum yield and thus allows one to detect and correct for acceptor quenching (Barth et al., 2014; Kudryavtsev et al., 2012). The donor lifetime may be used as an additional readout of the FRET efficiency, which can be used to identify conformational dynamics (see section 2.10.5).

### Perrin equation

The Perrin equation is used to relate the steady-state anisotropy to the fluorescence lifetime of the fluorophore (see section 2.1.3 for details). It is given by:

$$\langle r \rangle = \frac{r_0}{1 + \tau/\rho} \tag{2.78}$$

where $r_0$ is the fundamental anisotropy, $\tau$ is the fluorescence lifetime and $\rho$ is the rotational correlation time. In single-molecule spectroscopy, the Perrin equation is used in a molecule-wise plot of the anisotropy against the fluorescence lifetime. All species that possess the same rotational properties will fall onto a single Perrin line, regardless of differences in the fluorescence lifetime, allowing one to e.g. verify that the rotational properties of the donor fluorophore are not different between low and high FRET efficiency states.

Examples of Perrin lines are given in the bottom row of Figure 2.18 for a mixture of double-stranded DNA with different separation distances between the fluorophores. For the acceptor fluorophore, a single population is observed in the plot of anisotropy versus lifetime. Due to the different FRET efficiencies, two populations with different lifetimes are observed for the donor fluorophore. While the shorter fluorescence lifetime results in an increased anisotropy, both populations fall onto a single Perrin line defined by a common rotational correlation time of ∼0.3 ns, showing that the rotational properties of the donor are identical for the two constructs.

### Stoichiometry

The labeling stoichiometry is an important parameter to filter donor- and acceptor-only molecules from the analysis. It is only available if alternating excitation is employed and is defined as the fraction of signal after donor excitation with respect to the total detected signal:

$$S = \frac{I_{\mathrm{DD}} + I_{\mathrm{DA}}}{I_{\mathrm{DD}} + I_{\mathrm{DA}} + I_{\mathrm{AA}}} \tag{2.79}$$

A molecule carrying only the donor fluorophore thus has a stoichiometry of ∼1, while a stoichiometry close to 0 is observed for acceptor-only molecules. Double-labeled molecules show an intermediate stoichiometry. Analogous to the corrections applied to the photon counts to obtain accurate FRET efficiencies, the corrected stoichiometry is defined by:

$$S_{\mathrm{cor}} = \frac{\gamma I_{\mathrm{DD}} + I_{\mathrm{DA}} - \alpha I_{\mathrm{DD}} - \delta I_{\mathrm{AA}}}{\gamma I_{\mathrm{DD}} + I_{\mathrm{DA}} - \alpha I_{\mathrm{DD}} - \delta I_{\mathrm{AA}} + \beta I_{\mathrm{AA}}} \tag{2.80}$$

Here, the correction factor $\beta$ has been introduced that corrects for the different extinction coefficients $\varepsilon$ and excitation intensities $I_{\mathrm{ex}}$ of the donor and acceptor fluorophore at their respective excitation wavelengths, $\beta = \varepsilon_{\mathrm{D}}^{\lambda_{\mathrm{D}}} I_{\mathrm{ex,D}} / \varepsilon_{\mathrm{A}}^{\lambda_{\mathrm{A}}} I_{\mathrm{ex,A}}$ (Kapanidis et al., 2005). The use of the corrected stoichiometry has the advantage that it directly corresponds to the true stoichiometry of the fluorescent labels. Double-labeled molecules then show $S = 1/2$, while 2:1 or 1:2 stoichiometries are given by $S = 2/3$ and $S = 1/3$, respectively. This makes the stoichiometry $S$ a useful parameter to elucidate the stoichiometry of complexes (Orte et al., 2010), with the caveats that identical $S$ values may be observed for different complexes (e.g. 1:1 and 2:2 are not distinguishable without performing a more complex brightness analysis) and that the broadness of the stoichiometry distribution makes it difficult to distinguish exact stoichiometries in higher-order complexes (e.g. 1:4 and 1:5 result in the close values of $S = 0.25$ and $S = 0.20$). In three-color FRET experiments, the stoichiometry parameter proves even more vital as it allows the selection of triple-labeled molecules by combination of all three stoichiometry parameters (N. K. Lee et al., 2007a). Moreover, the double-labeled subpopulations in three-color FRET experiments contain additional information that can be used as intrinsic controls in the analysis (Barth et al., 2018b).

### Species-selective analysis

From the many parameters available in MFD, a detailed picture is obtained about the populations and heterogeneities present in the sample. However, the information obtained from the different parameters is restricted to average population values due to the width of the obtained distributions, which is limited by the number of photons detected per molecule. Any time-resolved information about the fluorescence or anisotropy decay is also discarded. The determination of a molecule-wise lifetime is based on a single-exponential model for the fluorescence decay because the low number of photons is not sufficient to apply more complex models. While part of the time-resolved information of the anisotropy decay, specifically the rotational correlation time, is obtained through application of the Perrin equation, the analysis likewise assumes simple models for the decay of the fluorescence and anisotropy decay.

To take advantage of the full information available in the experiment, it is useful to pool all photons of a given species to construct the cumulative fluorescence and anisotropy decays. This way, it is possible to determine, for example, the number of decay components of the fluorescence decay, or to analyse the anisotropy in more detail (see Nicoli et al., 2017 for an application). Another analysis method that can be performed in a species-selective manner is FCS, described in more detail in section 2.10.6.

### 2.10.4 Photon Distribution Analysis

The FRET efficiency histograms obtained in burst analysis are often interpreted in terms of different populations with defined FRET efficiency values, which can e.g. be determined by fitting Gaussian distribution to the data. Due to the limited number of photons per event, even a population with a defined FRET efficiency results in certain width $\sigma_E$ of the measured FRET efficiency distribution, whose upper bound is given by (Gopich and Szabo, 2005):

$$\sigma_E^2 < \frac{E(1-E)}{N_T} \tag{2.81}$$

where $N_T$ is the minimum number of photons per burst. This effect is commonly referred to as shot-noise, since the apparent width is not of physical origin but a result of the photon statistics. Biomolecules, however, do not only exist in discrete conformational states. Rather, conformational states are often best characterized by an ensemble of substates, resulting in additional heterogeneity that causes the width of the resulting FRET efficiency distributions to exceed the shot-noise limit.

Using the photon distribution analysis (PDA), it is possible to disentangle the shot-noise contribution from other heterogeneities in the FRET efficiency histogram, enabling a quantitative analysis of the data. The fundamental idea of PDA is to provide a complete statistic description of the single-molecule burst analysis experiment. Instead of performing corrections on the experimental photon counts to obtain accurate FRET efficiencies, the analysis is subjected to the distribution of the raw signals, including all needed correction factors in the model function. PDA was first described, using slightly different approaches, in Antonik et al., 2006 and Nir et al., 2006, and further developed to account for conformational dynamics (Kalinin et al., 2010b; Santoso et al., 2010).

The experimental data set is given by a set of photon counts detected in the donor and FRET channels ($N_{GG}$, $N_{GR}$). In the ideal case, the distribution of the detected photon counts over the two detection channels is given by a binomial distribution with a probability to detect a FRET photon that is given by the FRET efficiency $E$:

$$P(N_{GR}|E, N_{GG}+N_{GR}) = \binom{N_{GG}+N_{GR}}{N_{GR}} E^{N_{GR}}(1-E)^{N_{GG}} \tag{2.82}$$

The only free parameter in equation 2.82 is the FRET efficiency, which can be varied to find the most likely value given the measured data. The likelihoods for multiple observations are then multiplied to obtain the total likelihood. Experimentally, correction factors such as spectral crosstalk, cross-excitation and differences in the quantum yields and detection efficiencies modify the probability to detect a photon in the FRET channel. If these correction factors are known, one can calculate the probability to detect a photon in the FRET channel $\epsilon$, which replaces $E$ in equation 2.82, by (Antonik et al., 2006; Sisamakis et al., 2010):

$$\epsilon = 1 - \left(1 + \alpha + \gamma \frac{p_{\mathrm{DE}}(1-p_{\mathrm{DE}})^{-1} + E}{1-E}\right)^{-1} \tag{2.83}$$

Note that the direct excitation probability $p_{\mathrm{DE}}$ is different from the correction factor for direct excitation introduced before in section 2.10.2 and is, in this case, calculated from the extinction spectra of the donor and acceptor fluorophore $\varepsilon_D$ and $\varepsilon_A$ by:

$$p_{\mathrm{DE}} = \frac{\varepsilon_A(\lambda_{\mathrm{ex}}^D)}{\varepsilon_D(\lambda_{\mathrm{ex}}^D) + \varepsilon_A(\lambda_{\mathrm{ex}}^D)} \tag{2.84}$$

where $\lambda_{\mathrm{ex}}^D$ is the donor excitation wavelength.

To account for uncorrelated background signal, the background counts $b$ are modeled by Poisson distributions with mean value $\lambda$:

$$P_{\mathrm{BG}}(b) = \frac{\lambda^b}{b!} e^{-\lambda} \tag{2.85}$$

The photon counts obtained from single-molecule events are generally processed into equal time bins (e.g. of 1 ms length), in which case $\lambda$ is the average number of background counts per time bin.

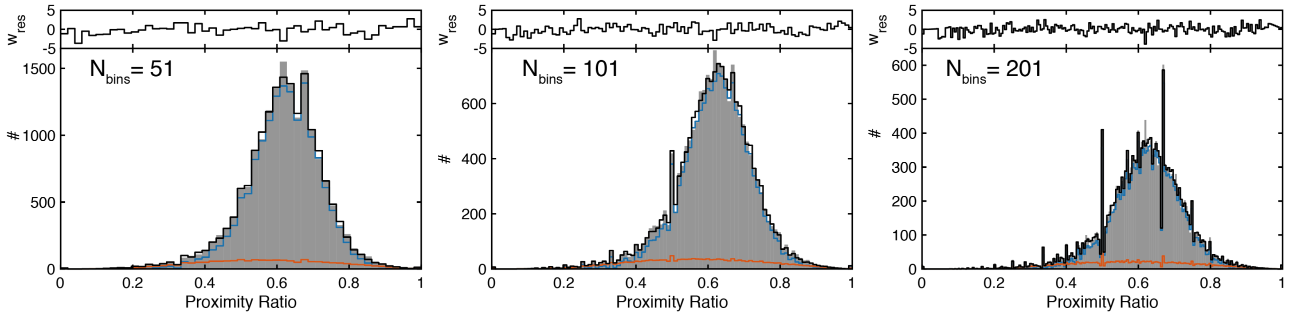

FIGURE 2.19: Photon distribution analysis of double-stranded DNA labeled with the dyes Atto550 and Atto647N, using different number of bins for the proximity ratio histogram. The voids and spikes observed at high number of bins are accurately described by the PDA method. The main population (blue) is described by a center distance of 55 Å and a distribution width of 2 Å.

The probabilities over all combinations of background counts and fluorescence are then summed up:

$$P(N_{GG}, N_{GR}|E) = \sum_{b_{GG}=0}^{N_{GG}} \sum_{b_{GR}=0}^{N_{GR}} P_{\mathrm{BG}}(b_{GG}) P_{\mathrm{BG}}(b_{GR}) P(N_{GR} - b_{GR}|E, N_{GG} - b_{G} + N_{GR} - b_{GR}) \tag{2.86}$$

where the last term in the double sum is given by equation 2.82.

Based on the likelihood, one can derive an analytical description of the proximity ratio histogram $H_{PR}$ by summing up all probabilities of combinations of signal counts that fall into a given bin of the histogram:

$$H_{PR}\left(PR_i < \frac{N_{GR}}{N_{GG}+N_{GR}} < PR_{i+1}\right) = \sum_{\substack{\forall\, N_{GG}, N_{GR} \text{for which} \\ PR_i < \frac{N_{GR}}{N_{GG}+N_{GR}} < PR_{i+1}}} P_{\mathrm{obs}}(N_{GG}+N_{GR}) P(N_{GG}, N_{GR}|E) \tag{2.87}$$

Here, $P_{\mathrm{obs}}(N)$ is the photon count distribution, which is used to weight the probabilities. It describes how often a total number of photons was observed in the experiment and is available from the experiment directly.

In practice, it is never possible to describe the width of the observed proximity ratio histogram by a single value for the FRET efficiency. To account for this broadening beyond the shot-noise limit, a Gaussian distribution of distances is generally assumed. For every distance value, the expected histogram is then calculated according to equation 2.87 and the cumulative histogram is constructed by weighting the individual histogram with the probability of the respective distance value. The continuous distribution of distances is hereby approximated by sampling at distinct distance values. Possible reasons for the excess broadening of FRET efficiency distributions are structural or conformational heterogeneity of the studied biomolecule, sticking of fluorescent dyes to the surface of the biomolecule (resulting in variations of the orientation factor $\kappa^2$), or the existence of multiple photophysical states of the fluorophores (Kalinin et al., 2010a).

A PDA of a double-stranded DNA labeled with the dyes Atto550 and Atto647N is shown in Figure 2.19 for different bin sizes of the proximity ratio histogram. Notice how the shot noise that leads to characteristic voids and spikes (most pronounced at smaller bin sizes) is accounted for by the PDA. The obtained center distance for the main population is 55 Å with a distribution width of 2 Å. Note that a small additional population had to be included in the fit, most likely originating from a long-lived secondary photophysical state of the donor or acceptor fluorophore.

The shot-noise limited proximity ratio histogram can also be approximated using Monte Carlo simulations of the photon emission process (Nir et al., 2006), an approach that is more straightforward to implement than the analytical description presented here. The drawback is that the algorithm is inherently affected by stochastic noise from the random number generator, which may be reduced by oversampling (i.e. averaging of multiple simulations) at the cost of computation time. The analytical histogram as given in equation 2.87, on the other hand, is not affected by sampling noise and does not suffer from long computation times. While the analytical approach requires the use of equal time bins to incorporate the contributions of background noise, the Monte Carlo approach may also be used on the molecule-wise photon counts directly.

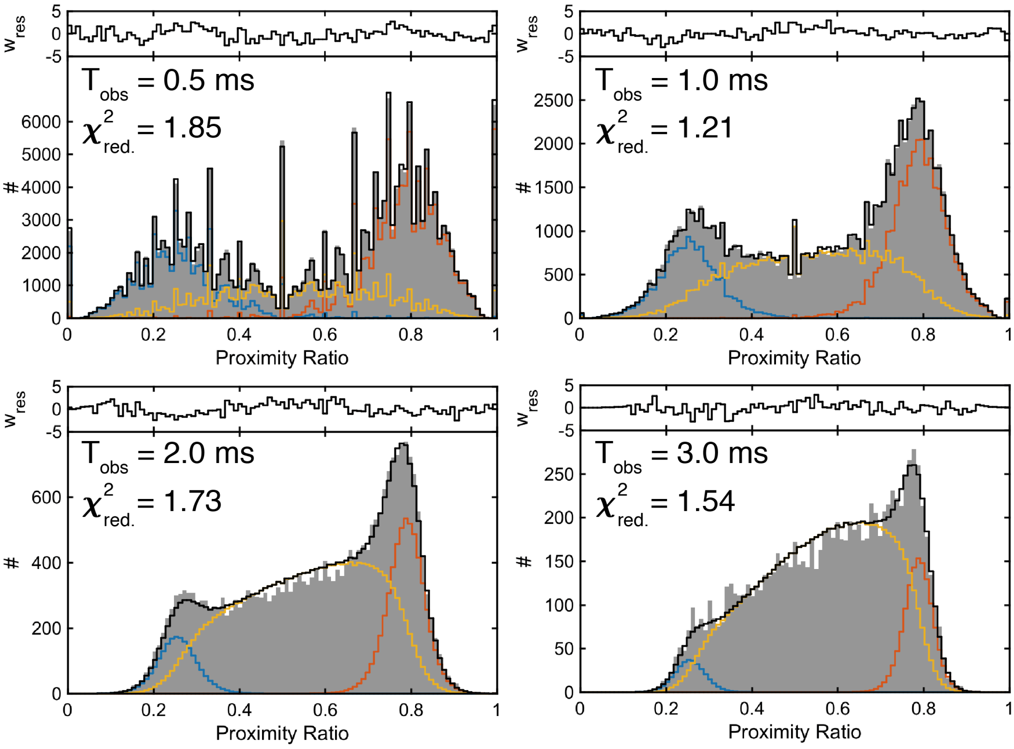

FIGURE 2.20: Dynamic photon distribution analysis of a simulated dataset with $E_1 = 0.25$, $E_2 = 0.80$, $k_1 = 1.0\,\mathrm{ms}^{-1}$ and $k_2 = 0.5\,\mathrm{ms}^{-1}$ at varying time bin sizes $T_{\mathrm{obs}}$. The datasets were globally analyzed.

### Dynamic PDA

Dynamic interconversion during the transit of the molecule through the confocal volume results in mixing of the distinct FRET states. Consider a molecule that interconverts between two FRET states $E_1$ and $E_2$. The average FRET efficiency $\langle E \rangle$ is then determined by the cumulative time $T$ the molecule spent in state 1 and state 2:

$$\langle E \rangle = \frac{T_1 E_1 + T_2 E_2}{T_1 + T_2} \tag{2.88}$$

where $T_2 = T_{\mathrm{obs}} - T_1$ with the total observation time $T_{\mathrm{obs}}$. By sectioning the data set into equal time bins and thus equal observation times (usually of the order of 1 ms), one can find an analytical solution to describe the state mixing by addressing the probability $p(T_1)$ that the molecule spends the cumulative time $T_1$ in state 1 (Kalinin et al., 2010b; Palo et al., 2006):

$$\begin{aligned} p(T_1) = {} & \delta(T_1)\frac{k_1}{k_1+k_2}\exp(-k_2 T_{\mathrm{obs}}) + \delta(T_{\mathrm{obs}} - T_1)\frac{k_2}{k_1+k_2}\exp(-k_1 T_{\mathrm{obs}}) \\ & + \left[\frac{2k_1k_2}{k_1+k_2} I_0(2\sqrt{k_1k_2T_1T_2}) + \frac{k_2T_1 + k_1T_2}{k_1+k_2}\frac{\sqrt{k_1k_2}}{\sqrt{T_1T_2}} I_1(2\sqrt{k_1k_2T_1T_2})\right]\exp(-k_1T_1 - k_2T_2) \end{aligned} \tag{2.89}$$

where $k_1$ and $k_2$ are the interconversion rates from state 1 to state 2 and from state 2 to state 1, respectively, defining the average time the molecule spends in state 1 or 2, $I_0()$ and $I_1()$ are the Bessel functions of order 0 and 1 and the $\delta$-function is defined by:

$$\delta(x) = \begin{cases} 1, & \text{if } x = 0 \\ 0, & \text{otherwise} \end{cases} \tag{2.90}$$

The first and second term in equation 2.89 describe the probability that the molecule stays in state 1 or 2, respectively, while the last term accounts for state mixing. Given a set of interconversion rates $k_1$ and $k_2$, one can then calculate the probability distribution of the time spent in state 1, which is related to the average FRET efficiency by equation 2.88. The resulting proximity ratio histogram is then a superposition of the shot-noise limited proximity ratio histograms given the average FRET efficiencies $\langle E\rangle(T_1)$ weighted by the probability $p(T_1)$:

$$H_{PR} = \sum_{T_1=0}^{T_{\text{obs}}} p(T_1) H_{PR}\left(\langle E\rangle(T_1)\right) \tag{2.91}$$

To increase the robustness of the analysis, one can use the fact that different observation times are available from a single experiment by processing the data into different time bins. An example of a dynamic PDA on a simulated dataset is shown in Figure 2.20. Note how the fraction of molecules showing interconversion (indicated in yellow) increases as the observation time increases.

Before a dynamic model is applied to the data, however, careful controls should be performed to justify the interpretation. The next sections will describe additional parameters and methodologies that allow identification and quantification of conformational dynamics in burst analysis experiments.

### 2.10.5 Detecting dynamics in burst analysis

**FRET efficiency vs. donor fluorescence lifetime**

One of the most important plots in burst analysis using MFD is the plot of the FRET efficiency (calculated from photon counts) versus the donor fluorescence lifetime. While both quantities are a measure of the FRET efficiency and thus the interdye distance, their different averaging characteristics enable the detection of conformational dynamics. First, consider the static case, where both quantities should be related by:

$$E_{\text{static}} = 1 - \frac{\tau_{D(A)}}{\tau_{D(0)}} \tag{2.92}$$

This defines the so-called static-FRET line (see the green line in the left panel of Figure 2.21). Considering the case of dynamic interconversion between distinct FRET states, the mixing will result in an average FRET efficiency as determined from the photon counts that depends on the interconversion rates. The donor fluorescence lifetime, however, shows a different averaging behavior. Since it is determined based on the donor signal only, the low-FRET state has a higher contribution to the fluorescence decay. The maximum-likelihood estimator used to estimate burst-wise lifetimes reports the intensity-average lifetime, which leads to an inherent bias of the extracted lifetime towards the lifetime of the low-FRET state. This shows as a rightward shift away from the static-FRET line.

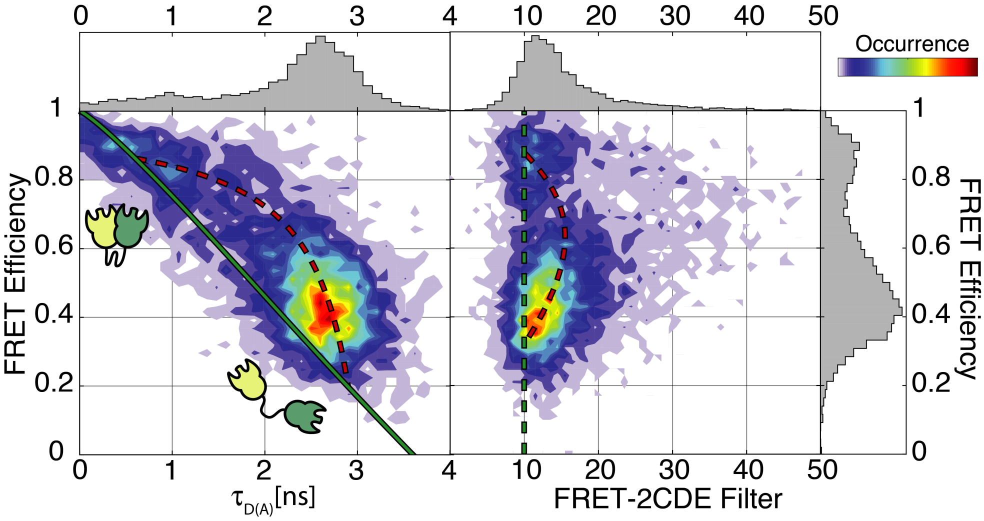

FIGURE 2.21: Dynamic indicators in burst analysis experiments, illustrated using the cohesin dimer CohI$_8$-CohI$_9$ of the cellulosome (adapted from Barth et al., 2018a). The molecule fluctuates between an open conformation with a FRET efficiency of ~0.4 and a closed conformation at a FRET efficiency of ~0.9. Left: In a plot of the FRET efficiency versus the donor fluorescence lifetime $\tau_{D(A)}$, dynamics show as a rightward shift from the static-FRET line (green) and can be described by a dynamic-FRET line (red dashed line). See section 2.10.5 for details. Right: The FRET-2CDE filter detects fluctuations of the FRET efficiency based on the distribution of photon counts.

The mixing between the states can be described analytically to obtain the dynamic-FRET line (see the red dashed line in the left panel of Figure 2.21), given by (Kalinin et al., 2010b):

$$E_{\text{dyn}} = 1 - \frac{\tau_1 \tau_2}{\tau_{D(0)} \left(\tau_1 + \tau_2 - \tau_{D(A)}\right)} \tag{2.93}$$

where $\tau_1$ and $\tau_2$ are the donor fluorescence lifetimes of state 1 and 2 and $\tau_{D(A)} \in [\tau_1, \tau_2]$. Equation 2.93 is obtained by considering that the FRET efficiency from photon counts reports the species-averaged FRET efficiency and is thus related to the species-averaged fluorescence lifetime $\langle\tau\rangle_x$ (which replaces $\tau_{D(A)}$ in equation 2.92) given by:

$$\langle\tau\rangle_x = x_1\tau_1 + (1 - x_1)\tau_2 \tag{2.94}$$

where $x_1$ is the species-fraction of state 1. The donor fluorescence lifetime, however, reports the intensity-weighted average lifetime $\langle\tau\rangle_f$, given by:

$$\langle\tau\rangle_f = \frac{x_1\tau_1^2 + (1 - x_1)\tau_2^2}{x_1\tau_1 + (1 - x_1)\tau_2} \tag{2.95}$$

where the fact was used that the intensity is proportional to the fluorescence lifetime.

In practice, the situation is further complicated due to the flexible linker that connects the fluorophores to the molecule of interest. If the linker dynamics are slower than the fluorescence lifetime, a distribution of donor-acceptor distances is observed even for static molecules which likewise results in an overestimation of the average donor fluorescence lifetime. Assuming a Gaussian distribution of interdye distances, one can numerically calculate a modified static-FRET line in the presence of linker dynamics by integration over the distance distribution at all possible interdye distances. The width of the distribution may hereby be determined from a detailed analysis of the fluorescence decay using a distance distribution model function. Consider a center interdye distance $R_{DA}$ and a distribution width $\sigma_{DA}$, then the weight for the distance $R_i$ is given by:

$$p(R_i) \propto \exp\left[-\frac{(R_i - R_{DA})^2}{2\sigma_{DA}^2}\right] \tag{2.96}$$

Each $R_i$ corresponds to a donor lifetime by:

$$\tau_{D,i} = \tau_{D(0)} \left[1 + \left(\frac{R_0}{R_i}\right)^6\right]^{-1} \tag{2.97}$$

Using equations 2.96 and 2.97, one can then calculate the species- and intensity-averaged fluorescence lifetimes at different center interdye distances $R_{DA}$, e.g. $R_{DA} \in [0...3R_0]$, resulting in a conversion function between the measured intensity-averaged lifetime and the corresponding species-averaged lifetime, $\langle\tau\rangle_x = f(\langle\tau\rangle_f)$. The conversion function is often approximated by a third order polynomial to avoid having to re-calculate the relation. However, the calculation is usually fast (< 1 s), which is why an approximation is not needed. In the case of conformational dynamics, both effects (linker dynamics and dynamic interconversion) have to be considered at the same time. The theory for the static-FRET line has been extended to the three-color FRET case in this work as described in the supporting information of Barth et al., 2018b.

### ALEX-2CDE and FRET-2CDE filter

Photoblinking, -bleaching and FRET dynamics have the common characteristic that they result in brightness fluctations of the donor and/or acceptor fluorophores during the transit of the molecule through the confocal volume. Tomov et al., 2012 developed a robust method to quantify these brightness fluctuations for single-molecule events in the absence of lifetime information, called two-channel kernel density estimation (2CDE). The key idea of the method is the use of kernel density estimation to determine photon densities, which effectively provides a smoothing of the noisy time traces of single-photon events. In general, an exponential kernel is applied, but other functions may be used as well. The FRET-2CDE filter detects FRET dynamics by separately estimating the FRET efficiency around donor photons and acceptor photons, called $(E)_D$ and $(1 - E)_A$.

$$\text{FRET-2CDE} = 110 - 100 \times \left[(E)_D + (1 - E)_A\right] \tag{2.98}$$

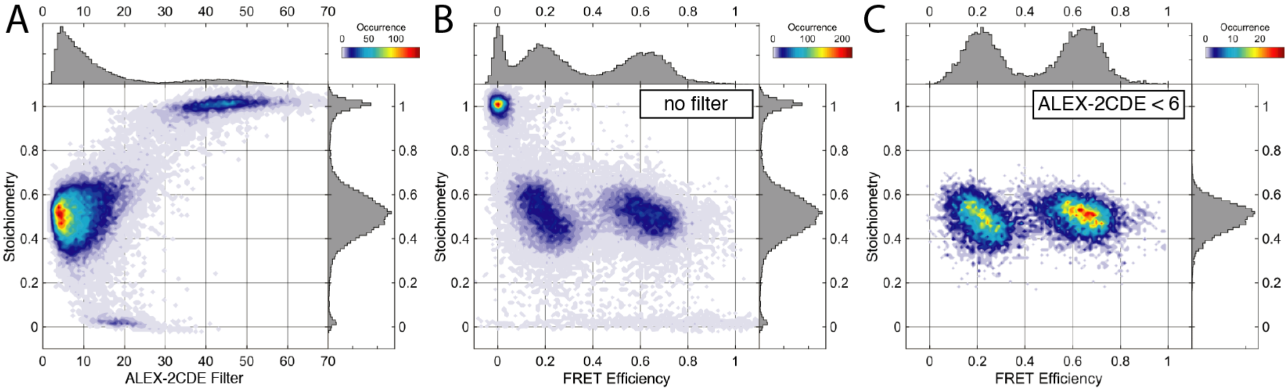

FIGURE 2.22: The ALEX-2CDE filter is an effective tool to remove unwanted contributions of single-labeled or photobleached molecules. **(A)** A plot of the stoichiometry versus the ALEX-2CDE filter is used to determine the required upper threshold to remove donor-only ($S = 1$) and acceptor-only ($S = 0$) molecules. **(B)** Using no filter, the histogram of the stoichiometry versus the FRET efficiency contains significant amounts of single-labeled species. Additionally, photo-bleaching while a molecule passes through the focus is visible as streaking between the double-labeled population at $S = 0.5$ and the single-labeled populations. **(C)** An upper threshold of 6 for the ALEX-2CDE filter allows one to select the molecules suitable for further analysis in a single step.

In the absence of fluctuations, the estimated FRET efficiencies are identical, resulting in a value of 10 for the FRET-2CDE filter. However, the situation changes in the presence of FRET dynamics. Here, donor photons are predominantly emitted during periods of low FRET efficiency, resulting in an underestimation of the FRET efficiency by $(E)_D$. On the other hand, acceptor photons are mainly emitted at high FRET efficiencies, causing an overestimation of the FRET efficiency or an underestimation of $(1 - E)_A$. As a result, the sum in the square brackets in equation 2.98 is smaller than 1, and FRET-2CDE > 10.

A similar logic is applied for the detection of photoblinking and -bleaching by means of the ALEX-2CDE filter. Here, the brightness of the donor (given by the sum of donor and FRET sensitized acceptor signal) and the acceptor (probed using alternating excitation) are compared to detect intensity fluctuations. Since the overall intensities change during the transit through the confocal volume, it is necessary to find a ratiometric quantity, which in this case is the brightness ratio $BR$ of the donor and acceptor brightnesses. It is defined such that it converges to 1 in the absence of fluctuations. The brightness ratio is then separately estimated around the photons detected after donor and acceptor excitation ($BR_{D_{EX}/A_{EX}}$) to compute the ALEX-2CDE filter:

$$\text{ALEX-2CDE} = 100 - 50 \times \left[BR_{D_{EX}} + BR_{A_{EX}}\right] \tag{2.99}$$

In the absence of brightness fluctuations, both brightness ratios return 1 and ALEX-2CDE = 0. In the presence of brightness fluctuations of either channel, the brightness ratios return values < 1, resulting in increased values for the filter. Since both brightness ratios $BR_{D_{EX}}$ and $BR_{A_{EX}}$ are sensitive to fluctuations in either channel, it is not possible to selectively detect fluctuations of the donor or acceptor fluorophore.

The ALEX-2CDE filter provides a convenient way to remove both single-labeled molecules and photoblinking and -bleaching in one step. Figure 2.22 A shows a typical distribution of the ALEX-2CDE filter plotted against the stoichiometry parameter. Both donor- and acceptor-only molecules exhibit high values for the filter. Likewise, the trailing that is evident between the population of double-labeled molecules ($S = 0.5$) and donor- and acceptor-only populations, caused by photobleaching, shows values $> 10$, while the double-labeled population converges to a value of $\sim 5$. By setting an upper threshold for the ALEX-2CDE filter of 6, one can select double-labeled molecules that showed stable emission of both fluorophores in one step (Figure 2.22 B-C).

An example of the use of the FRET-2CDE filter is given in Figure 2.21. The system shows dynamic interconversion on the millisecond timescale between an intermediate FRET state at $E \approx 0.4$ and a high-FRET state at $E \approx 0.9$. Bursts of intermediate FRET efficiency show higher values for the FRET-2CDE filter and are thus found to be dynamic. A closely related method is burst variance analysis (BVA, Torella et al., 2011), which quantifies the standard deviation of the FRET efficiency of single-molecule events to detect broadening beyond the shot noise limit caused by structural dynamics.

### 2.10.6 Species-selective FCS

Another dimension can be added to the MFD toolset through correlation analysis of single-molecule events. Using species-selective FCS (Eggeling et al., 1998, also called purified FCS, Laurence et al., 2007), it is possible to detect differences in diffusion time (and thus e.g. binding interactions) or to quantify fast conformational dynamics on the sub-millisecond timescale.

When calculating correlation functions on time scales similar to the length of the recorded signal, sampling artifacts need to be accounted for. In the time traces of the single-molecule events, long time lags (e.g. on the timescale of diffusion) are sampled less frequently than short time lags. For a given time lag $\tau$ and burst duration $T$, the time lag can only be sampled for photons detected in the range $[0, T-\tau]$. In practice, individual correlation functions are calculated for every contributing burst and subsequently averaged while accounting for the uneven sampling of time lags:

$$G_{\text{species}}(\tau) = \frac{\sum_k n_k\left(\Delta t = \tau\right)\sum_k\left(T_k - \tau\right)}{\sum_k n_k\left(t \leq T_k - \tau\right)\sum_k n_k\left(t \geq \tau\right)} \tag{2.100}$$

Here, the sums go over the number of bursts $k$, $n_k\left(\Delta t = \tau\right)$ is the number of photon pairs in burst $k$ with time lag $\tau$, $T_k$ is the burst duration, and $n_k\left(t \leq T_k - \tau\right)$ and $n_k\left(t \geq \tau\right)$ are the number of photons in the interval $[0, T_k - \tau]$ and $[0, \tau]$, respectively.

The apparent diffusion time determined by species-selective FCS is strongly dependent on the chosen burst search parameters, i.e. higher photon count thresholds will terminate the burst earlier, leading to a shorter burst duration and an underestimation of the diffusion time. Effectively, one observes the burst length distribution in the correlation function. As a consequence, the correlation functions are usually not well described by the diffusion model, but may be fit assuming anomalous diffusion (Laurence et al., 2007). This effect can be diminished by adding a time window around the bursts, enabling a more accurate determination of the diffusion part of the FCS curve. Another effect of the burst selection is that regions of high count rate are selected from the measurements, resulting in reduced fluctuations and thus lower FCS amplitudes since the average intensity is overestimated. Additionally, since only the time intervals containing correlated signal are selected from the measurement, the correlation function usually does not diminish to 0 at large time lags, requiring a significant offset to be considered in the model function.

Figure 2.23 illustrates the effect of the size of the chosen time window on the shape and amplitude of the obtained species-selective FCS curves. A larger time window results in higher amplitudes of the correlation function. The species-selective FCS curve underestimates the diffusion time, which is asymptotically increased with increasing time window. Obviously, also the maximum available time lag scales with the chosen time window. Since the time window is added both to the start and end of the bursts, the maximum lag time is approximately twice the time window size.

When adding a time window, it is possible that adjacent single molecule events fall into the region around the respective burst, leading to contamination of the species-selective correlation function. If another single

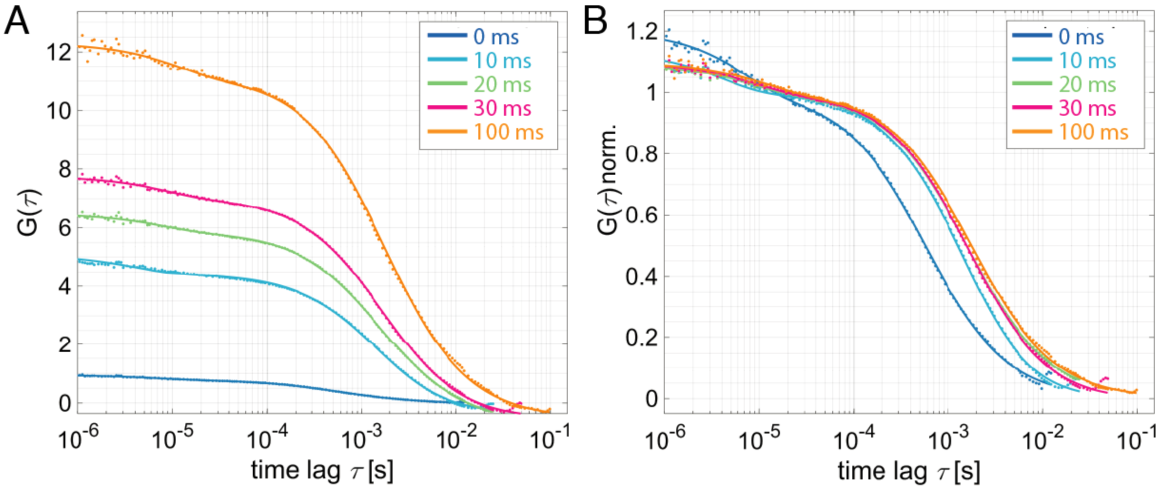

FIGURE 2.23: Artifacts in species-selective FCS. **(A)** Species-selective FCS curves of a single-molecule measurement of labeled double-stranded DNA were computed using different time window sizes. **(B)** Species-selective FCS curves as shown in A, normalized to the apparent particle number.

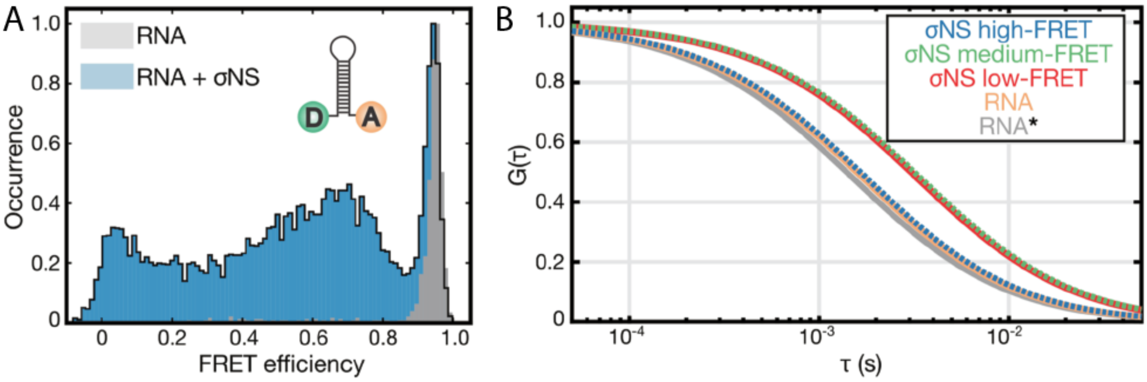

FIGURE 2.24: Studying RNA-protein interactions using species-selective FCS. **(A)** FRET efficiency histograms of the RNA hairpin alone (gray) and in the presence of the RNA-binding protein σNS (blue). **(B)** Comparison of FCS curves calculated from the signal of the acceptor fluorophore after acceptor excitation. Shown are the species-selective FCS curves of the hairpin alone (yellow) and different species from the measurement in presence of σNS (red: $E < 0.15$, green: $0.3 < E < 0.8$, blue: $E > 0.9$), calculated using a time window of 50 ms. The ensemble correlation function of the hairpin in the absence of σNS is additionally given in gray (RNA*). Adapted from Bravo et al., 2018.

molecule event that was detected by the burst search falls into the time window around a contributing burst, the burst is not included in the correlation function. This ensures that the obtained correlation function is specific to the selected species. Contributions of contaminating signal that was not detected as a burst, however, will not be filtered out.

#### Example 1: RNA-binding proteins

An example analysis of diffusion is shown in Figure 2.24, adapted from Bravo et al., 2018. A stable RNA hairpin (see inset in panel A) is labeled with a donor and acceptor dye, resulting in a high FRET efficiency ($E \approx 0.95$) for the hairpin alone (grey histogram). Upon addition of the RNA-unwinding protein σNS, a broad distribution of FRET efficiencies is observed (blue histogram), indicating that the protein unfolds the hairpin structure. However, also a high-FRET peak persists in the presence of the protein (c = 25 nmol). Species-selective FCS was used to answer the question whether the high-FRET peak in the presence of the protein is given by unbound hairpin structures, or whether the hairpin may bind to the protein in the closed from. Species-selective FCS curves were calculated using the signal obtained from direct excitation of the acceptor fluorophore through PIE to avoid influences of different FRET efficiencies on the correlation functions (panel B). Comparison of the ensemble FCS curve of the RNA alone (gray line) with the species-selective FCS curves obtained from the single-molecule measurements of the RNA alone (yellow) and the high-FRET species in the presence of σNS (blue) shows nearly identical diffusion behavior, while the medium- (green) and low-FRET species (red) show significantly slower diffusion indicative of protein binding. Thus, binding of the hairpin to σNS always results in unwinding of the RNA double-helix.

#### Example 2: Analysis of conformational dynamics

In the analysis of conformational dynamics by FRET-FCS, difficulties are encountered due to contaminating donor-only labeled molecules (see section 2.9.5). This problem can be avoided by species-selective FCS. In fact, the correlation curve shown in Figure 2.13 B was calculated from double-labeled molecules only.
For filtered-FCS, it is required to obtain the TCSPC patterns of the different species. From the single-molecule analysis, these are easily obtained using a simple FRET efficiency threshold (see Figure 2.25 A) or by separating molecules that show no dynamic interconversion e.g. through the FRET-2CDE filter (see section 2.10.5). In the example shown in Figure 2.25, the inclusion of a time window of 100 ms around the bursts led to a significant contribution of scattered laser light to the total TCSPC pattern (panel B, black), requiring the addition of the TCSPC pattern of scattered light (grey) in the calculation of the filter functions (panel C). The resulting filtered-FCS curves reveal dynamics with a relaxation time of ~10 µs (panel D). Note that the amplitudes in species-selective FCS are distorted due to the bias of selecting correlating regions (compare Figure 2.23 A). While the relaxation time of the dynamics is unaffected by this issue, the amplitude information should generally not be used in the quantitative analysis of the dynamics.

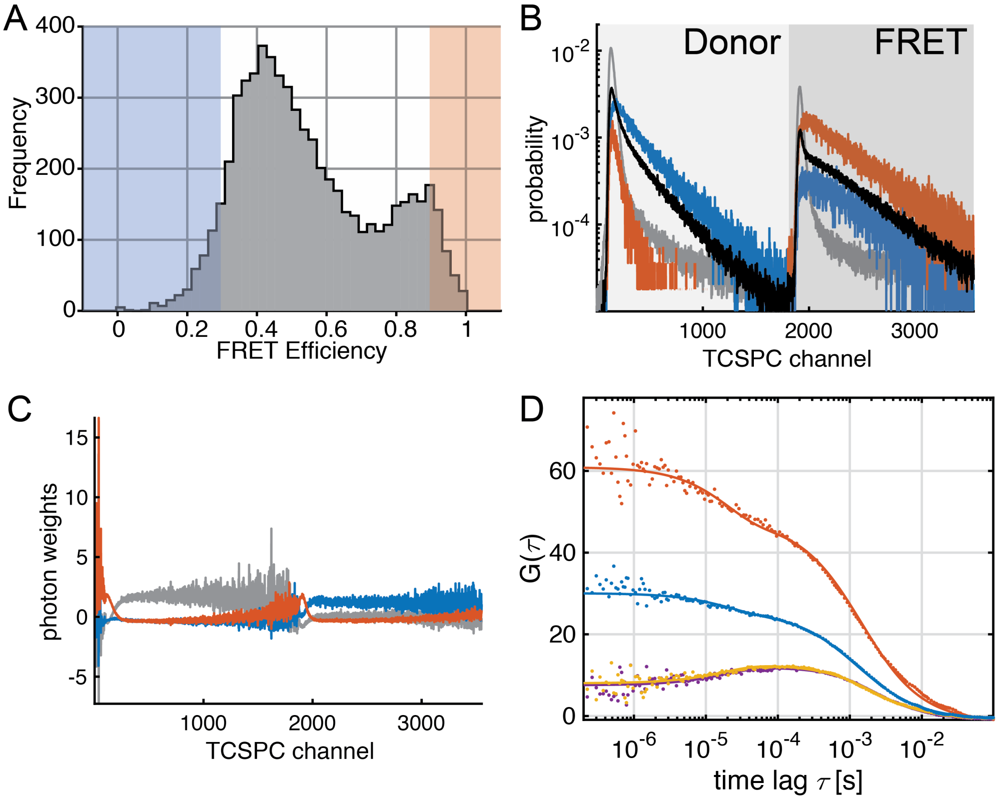

FIGURE 2.25: Species-selective filtered-FCS analysis of conformational dynamics of the cohesin dimer CohI$_8$-CohI$_9$ of the cellulosome, using the dataset shown in Figure 2.21. The molecule fluctuates between an open and a closed conformation on the micro- to millisecond timescale. **(A)** FRET efficiency histogram shows two peaks at FRET efficiencies of ∼0.4 and ∼0.9. **(B)** The TCSPC patterns of the open and closed conformations are extracted from the measurement using thresholds on the FRET efficiency as indicated by the shaded regions in A (blue: low-FRET, red: high-FRET). The TCSPC patterns of all molecules and of the scattered laser light are given in black and gray. **(C)** Filters calculated from the TCSPC patterns in B for the low-FRET (blue) and high-FRET (red) species and the scatter contribution (gray). **(D)** Correlation functions calculated using the filters in C. Species autocorrelation functions are given in blue and red, and the two species cross-correlation functions (1x2/2x1) are given in yellow and purple. Adapted from Barth et al., 2018a.

## 2.11 Computational Biology

With advances in computation power, especially through the wide-spread availability of powerful graphics processing units (GPUs), it has become feasible and affordable to study larger and larger system computationally. In several projects in this work, molecular dynamics (MD) simulations have been applied to obtain atomistic insights.

### 2.11.1 Newton's laws of motion on the molecular scale

The basic idea of molecular dynamics is the use of classical mechanics, i.e. Newton's equations of motion, to numerically compute the time evolution of the system based on the interatomic forces.

$$m_i \ddot{\mathbf{r}}_i = \mathbf{f}_i \qquad \mathbf{f}_i = -\frac{\partial}{\partial \mathbf{r}_i} U(\mathbf{r}) \tag{2.101}$$

An efficient approach for the numeric integration is the velocity Verlet algorithm (Swope et al., 1982), which, starting from the positions $\mathbf{r}$, the initial forces $\mathbf{f}$ (and associated accelerations $\mathbf{a} = \mathbf{f}/m$) and the initial velocities $\mathbf{v}$, updates the atom positions using the following set of instructions:

1. Update the position of the atoms:

$$\mathbf{r}(t + \Delta t) = \mathbf{r}(t) + \mathbf{v}(t)\Delta t + \frac{1}{2}\mathbf{a}(t)\Delta t^2$$

2. Recalculate the force based on the updated atom positions to obtain the acceleration:

$$\mathbf{a}(t + \Delta t) = \frac{\mathbf{f}(t + \Delta t)}{m}$$

3. Update the velocities:

$$\mathbf{v}(t + \Delta t) = \mathbf{v}(t) + \frac{1}{2}\left[\mathbf{a}(t) + \mathbf{a}(t + \Delta t)\right]\Delta t$$

The calculation of the position-dependent potential $U(\mathbf{r})$, used to calculate the forces, is hereby the computationally most expensive step.

The potential term $U(\mathbf{r})$ is a function of the inter-atomic distances, split up into non-bonded and bonded (or intramolecular) contributions. The non-bonded contributions are given by van-der-Waals-type forces, described by the Lennard-Jones potential $v_{\mathrm{LF}}$, and electrostatic Coulomb interactions $v_{\mathrm{Coulomb}}$, which are summed up over all pairs of atoms:

$$U_{\mathrm{non-bonded}}(\mathbf{r}) = \sum_i \sum_{j>i} v_{\mathrm{LJ}}(r_{ij}) + v_{\mathrm{Coulomb}}(r_{ij}) \tag{2.102}$$

$$v_{\mathrm{LJ}}(r) = 4\varepsilon \left[\left(\frac{\sigma}{r}\right)^{12} - \left(\frac{\sigma}{r}\right)^{6}\right] \qquad v_{\mathrm{Coulomb}}(r) = \frac{Q_1 Q_2}{4\pi\epsilon_0 r} \tag{2.103}$$

Bonded interactions are given by stretching and bending of bonds, which are described by spring-like potentials, and torsion-angle twisting:

$$U_{\mathrm{bonded}}(\mathbf{r}) = \frac{1}{2}\sum_{\text{bonds}} k^r_{ij}(r_{ij} - r_{\mathrm{eq}})^2 + \frac{1}{2}\sum_{\substack{\text{bend}\\ \text{angles}}} k^\theta_{ijk}(\theta_{ijk} - \theta_{\mathrm{eq}})^2 + \sum_{\substack{\text{torsion}\\ \text{angles}}} v_{\mathrm{torsion}}(\phi_{ijkl}) \tag{2.104}$$

Given the potential energy function $U(\mathbf{r})$, one can then calculate the force acting on the individual atoms analytically from the derivative with respect to the coordinates (equation 2.101).

The parameters used in the equations to describe the potential $U(\mathbf{r})$ depend on the chemistry of the molecule. They are commonly referred to as "force fields" which are derived from quantum chemical calculations and structural experimental data. An increasing number of force fields are available nowadays, making it difficult to choose. While different force fields have been developed with specific applications in mind, the standard force fields for proteins of many molecular dynamics software suites (such as the AMBER, GROMOS or CHARMM force fields) can generally be assumed to accurately describe most structured protein systems. To

exclude that the MD results are biased by the force field choice, it is advisable to compare the results of different force fields for the studied system. The choice of the correct force field, however, is more difficult for simulations of structurally flexible proteins (such as intrinsically disordered peptides, IDP) or other biomolecules such as lipids or polysaccharides, for which improved force fields are continuously being developed.
The computation time of the all-atom approach mainly depends on the number of atoms in the system. For large systems, the computation time per MD step becomes too large to sample relevant biological time scales in a reasonable amount of computation time. Many coarse-grained approaches have been developed to circumvent this problem, making it possible to simulate larger systems (Marrink et al., 2007; Šulc et al., 2012). By combining multiple atoms (i.e. amino acid side chains or nucleobases) into a single entity, the number of particles is reduced and the computation is sped up at the cost of accuracy. While thus the all-atom information is lost, it is still possible to study large scale conformational transitions or predict thermodynamic quantities.

### 2.11.2 Molecular dynamic simulations of biomolecules

To accurately predict the structural dynamics of biomolecules by MD simulations, it is necessary to account for the effect of solvent molecules and ions. While these effects can be treated implicitly through average potentials, the current state-of-the-art is to embed the molecule in a box of water molecules (Figure 2.26). Depending on the size of the box, the explicit treatment of the solvent adds a large number of molecules and thus degrees of freedom to the system, increasing the computation time significantly. In fact, most of the time is spent on computing the movement of the solvent, which is reduced to some extent by using a simpler model for the water molecules than is employed for the biomolecule. To mimic a continuous system, periodic boundary conditions are applied to the box that reinserts molecules that exit the box on the opposite side. The box should be chosen large enough to eliminate interactions of the molecule with its shadow through the walls of the box, but as small as possible to reduce computation time. Here, an octagonal geometry is more efficient, allowing a smaller volume to be used while minimizing unwanted interactions.

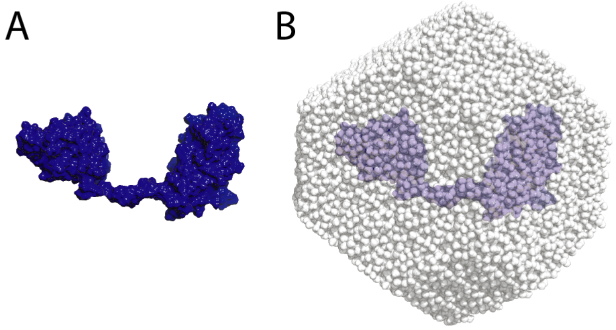

FIGURE 2.26: The scaffoldin fragment CohI$_8$-CohI$_9$ (see Barth et al., 2018a) without solvent (**A**) and embedded in an octagonal box of water (**B**). The spacing between the molecule and the boundaries was set to 15 Å, resulting in the addition of ∼27000 water molecules compared to the ∼5000 atoms in the protein molecule.

### 2.11.3 Analysis of molecular dynamics simulations

The informational content obtained from a molecular dynamics simulations is tremendous. It contains the atom coordinates at every time step of the simulation, referred to as the MD trajectory. While the simulation result may first be investigated visually by exploring a movie of the molecule motion, there are a number of useful parameters and analysis methodologies that enable a quantitative analysis of the trajectory. The simplest quantities obtainable from the trajectory are purely geometrical such as distances between select atoms, residues, domains or molecules, or angles to monitor the relative orientation of e.g. amino acid side chains, nucleobases or domains. More advanced parameters for the analysis are presented in the following section and illustrated using two examples.

#### Root-mean-square deviation

The most important quantity that one should first investigate is the root-mean-square deviation (RMSD). It describes the average displacement of atoms with respect to a reference structure (usually the initial or the average structure) and is thus a measure for the similarity between the structures:

$$RMSD(t) = \sqrt{\frac{1}{N}\sum_{i=1}^{N}(\mathbf{r}_i(t) - \mathbf{r}_{\mathrm{ref},i})^2} \tag{2.105}$$

where $t$ is the frame (time) and $N$ is the number of particles. To counteract translational or rotational diffusion of the molecule during the simulation, the structures are first aligned by minimizing the RMSD with respect to the reference structure at every time step. In that way, the RMSD is only sensitive to conformational changes of the biomolecule. An example RMSD trajectory is shown in Figure 2.27.

A related quantity is the root-mean-square fluctuation, which is computed for a given atom $i$ over the total trajectory:

$$RMSF_i = \sqrt{\frac{1}{T}\sum_{t=1}^{T}(\mathbf{r}_i(t) - \bar{\mathbf{r}}_i)^2} \tag{2.106}$$

where $\bar{\mathbf{r}}$ is the average position. The RMSF quantifies the structural flexibility of atoms or residues, thus allowing one to identify flexible regions in the structure.

### Cluster analysis

Another useful method is cluster analysis. The frames of the trajectory are grouped into clusters based on a distance metric, usually the RMSD between the frames (but other metrics may be used as well). As such, a cluster analysis starts with a calculation of the pairwise RMSD matrix. From there, clustering may be performed using different approaches such as k-means clustering (Lloyd, 1982) or the hierarchical agglomerative clustering algorithm (Sibson, 1973). Briefly, the k-means algorithm aims to group the observations into a given number of sets by minimizing the variance within each cluster. Initially, each observation is assigned to the cluster with the closest centroid. The cluster centroids and assignments of the observations are then iteratively updated until convergence. The hierarchical agglomerative clustering algorithm is a "bottom up" approach that initially assigns each observation to its own cluster. At each iteration, clusters are then merged with their closest neighbor until the desired number of clusters is reached. The result of the analysis depends on the choice of the algorithm and the number of clusters that the data should be partitioned into. A cluster analysis is useful to extract average structures that are frequently populated during the simulation.

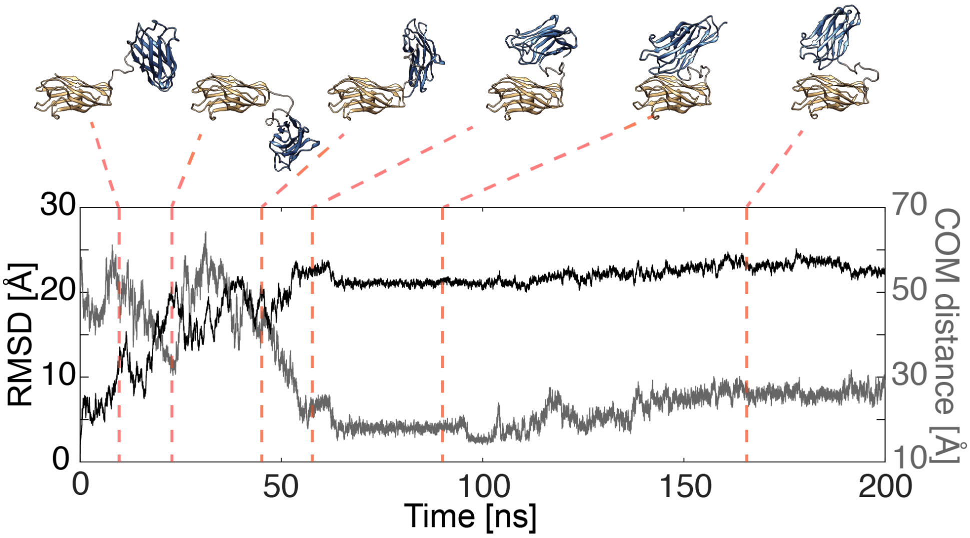

FIGURE 2.27: Analysis of a molecular dynamics trajectory by means of the root-mean-square displacement (RMSD) and center-of-mass distance (COM) between the two domains of a tandem cohesin of the cellulosome. The structures at the indicated time points are given above. Adapted from Barth et al., 2018a.

### Example 1: Intramolecular interactions in the cellulosome

The cellulosome is a large extracellular multi-enzyme complex utilized by selected bacteria for the efficient degradation of plant cell wall material. The smallest unit of the central scaffolding protein are cohesin modules. A tandem of cohesins, connected by a flexible peptide linker, was studied by molecular dynamics simulations (Figure 2.27). Starting from the extended conformation, the two cohesin domains contact each other after $\sim$50 ns. The trajectory was analyzed by means of the root mean square deviation with respect to the starting structure and the center-of-mass distance between the two domains. The RMSD reports on the overall structural fluctuations, plateauing once the domains contact each other. On the other hand, the COM distance more directly reports on the interaction between the domains. While both quantities correlate, the COM distance is more sensitive to the small structural changes observed after contact formation after 100 ns where the RMSD only shows minor changes. The simulation was repeated multiple times by resampling the initial velocities, resulting in different evolutions of the system from the starting configuration. All repeats, however, showed binding of the domains. To obtain a detailed picture of the different binding modes from the simulations, a global cluster analysis identified the main binding geometries that were found throughout the simulations. This allowed e.g. the identifaction of key residues involved in the formation of salt bridges between the domains. For details, see Barth et al., 2018a.

### Example 2: Unfolding of the maltose-binding protein

The maltose-binding protein (MBP, Figure 2.28 A) has previously served as a model system for chaperone-assisted protein folding (Chakraborty et al., 2010; Sharma et al., 2008). While the wild-type protein folds within seconds, two mutations have been identified (V8G/Y283D) that slow down the folding process to the minute time scale due to the formation of kinetically trapped intermediates along the folding pathway. Experimentally, protein unfolding is most commonly induced through the additon of denaturants such as guanidine hydrochlorid or urea. For simulations, the simplest approach for unfolding is to increase the temperature and thus the kinetic energy. To decrease the unfolding time to timescales accessible by molecular dynamics simulations, MBP was simulated at a temperature of 450 K for 1 µs. Note that, while this temperature is above the boiling point of water, no vaporization is observed (Walser et al., 2000), most likely because the parameters for the water model (here TIP3P) are optimized for liquid phase properties. Inspection of the RMSD (Figure 2.28 B) indicates the structural changes occurring during the simulation. A more direct measure of the loss of structure is given by the fraction of native contacts $Q(X)$ (Figure 2.28 C and Best et al., 2013). Native contacts between heavy atoms are hereby determined from the starting structure, and the loss thereof directly reports on the unfolding process. To obtain a structurally resolved picture, the secondary structure was assigned for every residues at every frame of the trajectory using the DSSP algorithm (Kabsch and Sander, 1983), allowing structural changes to be followed with time (Figure 2.28 D). While most regions of the protein lose their native structure within the first 500 ns, the protein maintains its structure in the regions around the residues 8 and 283 that are mutated in the slow-folding double mutant. This indicates that these regions assume their native structure first during the folding process and thus serve as folding nuclei that are disturbed by the mutations.

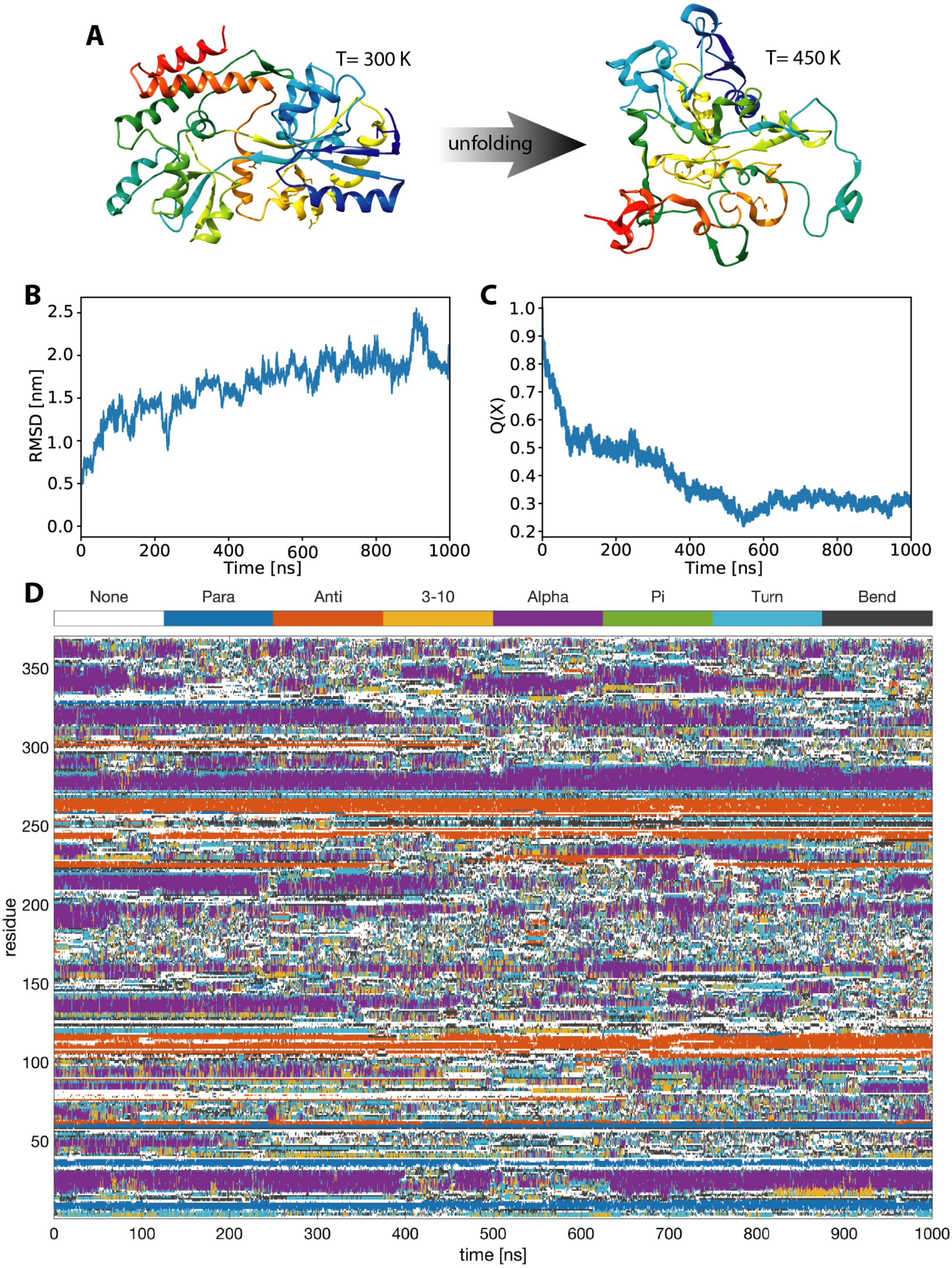

FIGURE 2.28: Molecular dynamics simulations of the unfolding of the maltose-binding protein (MBP). **(A)** The initial and final structure of MBP after 1 μs simulation time at a 450 K. **(B-C)** The root mean square displacement (RMSD) and fraction of native contacts $Q(X)$ along the trajectory. **(D)** Residue-wise assignment of the secondary structure of the trajectory. The secondary structure motifs are *Para*: parallel $\beta$-sheet, *anti*: anti-parallel $\beta$-sheet, *3-10*: $3_{10}$ helix, *Alpha*: $\alpha$-helix, *Pi*: $\pi$-helix.

## 2.12 Data analysis

This section provides a description of the key concepts of model-based data analysis, many of which are used within the *PAM* software suite developed as part of this work (Schrimpf et al., 2018a).

### 2.12.1 Goodness-of-fit

To compare the measured data with the prediction of a model and thus find the best description of the experiments, one first requires a metric that quantifies the goodness of fit. An often used metric is the sum of the squared deviation between measured and predicted values, being used in linear and non-linear least squares analysis. In this metric, every data point is weighted equally. In practice, however, one might know some outcomes with higher certainty than others. It is then advantageous to use the $\chi^2$ value defined by:

$$\chi^2 = \sum_{i=1}^{N} \frac{(M_i - O_i)^2}{\sigma_i^2} = \sum_{i=1}^{N} \frac{(M_i - O_i)^2}{\max(O_i, 1)} \tag{2.107}$$

By normalizing the squared deviations by their uncertainty $\sigma$, data points with low uncertainty are given a higher weight in the evaluation of the goodness-of-fit. In counting experiments, the data follow a Poisson distribution. In this case, the expected variance is equal to the mean, i.e $\sigma^2 = \mu$, which was used in equation 2.107. To avoid division by zero, $\sigma^2$ is set to one if no data were detected. While the variance is hereby estimated by assuming a Poisson distribution, the $\chi^2$ statistic assumes that the error is normally distributed. This assumption is justified by the fact that the Poisson distribution is similar to the normal distribution for mean values $\mu \geq 10$. Assuming normally distributed errors, the expected value for the normalized squared error (i.e. the summands in equation 2.107), is 1, and thus the expected value for $\chi^2$ is equal to the number of degrees of freedom given by the number of data points minus the number of model parameters, $\nu = N - k$. As a consequence, the interpretation of the $\chi^2$ value is simplified by using the reduced $\chi^2$ value given by:

$$\chi^2_{\text{red.}} = \frac{1}{N-k} \chi^2 \tag{2.108}$$

$\chi^2_{\text{red.}}$ is independent of the number of degrees of freedom and has an expected value of 1. Generally, a fit with $\chi^2_{\text{red.}} \approx 1$ can be assumed to adequately describe the data, while $\chi^2_{\text{red.}} \gg 1$ indicates a bad fit due to an inappropriate model function. On the other hand, $\chi^2_{\text{red.}} < 1$ is indicative of overfitting, meaning that the model has too many parameters and that the data is over-interpreted. In addition, $\chi^2_{\text{red.}} < 1$ may also arise if the uncertainty of the data points is overestimated.

### 2.12.2 Maximum Likelihood Estimation

Maximum likelihood estimation (MLE) is another approach to model-based data analysis. Given the observed data, the parameters of a statistical model are optimized using a likelihood function that describes the probability that the observed data are generated by the model. The statistical model may hereby be based on an error model or provide a complete probabilistic description of the experiment. The latter approach is realized for three-color FRET experiments in paper 1 (see section 3.1 and Barth et al., 2018b). For the former approach, consider again normally distributed errors. The mean value of the normal distribution $\mathcal{N}(x|\mu,\sigma)$is then given by the predicted value from the model function $M_i$, while the width is again estimated from the counting statistics as $\sigma = \sqrt{O_i}$. Then, the likelihood $\mathcal{L}$ is the product over the individual probabilities of the observation $O_i$ given the model function:

$$\mathcal{L} = \prod_{i=1}^{N} \mathcal{N}(O_i|M_i, \sqrt{O_i}) = \prod_{i=1}^{N} \frac{1}{\sqrt{2\pi O_i}} \exp\left(-\frac{(O_i - M_i)^2}{2O_i}\right) \tag{2.109}$$

It is often convenient to work with the negative logarithm of the likelihood to avoid small numbers. The negative log-likelihood is then minimized by the fit routine, and is given by:

$$-\log \mathcal{L} = \frac{1}{2} \sum_{i=1}^{N} \frac{(O_i - M_i)^2}{O_i} + \frac{1}{2} \sum_{i=1}^{N} \log(2\pi O_i) \propto \frac{1}{2}\chi^2 \tag{2.110}$$

In other words, using the $\chi^2$ estimator is equivalent to performing a maximum likelihood estimation for normally distributed errors. At low statistics, the assumption of normally distributed errors is no longer valid. In this case, the correct distribution is the Poisson distribution, which only depends on the expected value $\lambda$:

$$P(k|\lambda) = \frac{\lambda^k}{k!} e^{-\lambda} \tag{2.111}$$

where $k$ is an integer value. For a Poisson distribution, the negative log-likelihood is given by:

$$-\log \mathcal{L} = -\sum_{i=1}^{N} \log P(O_i|M_i) = -\sum_{i=1}^{N} O_i \log M_i - \log O_i! - M_i \tag{2.112}$$

Using Stirling's approximation ($\log n! \approx n \log n - n$), one obtains:

$$-\log \mathcal{L} = -\sum_{i=1}^{N} O_i \log M_i - O_i \log O_i + O_i - M_i = \sum_{i=1}^{N} O_i \log \frac{O_i}{M_i} + M_i - O_i \tag{2.113}$$

This is the MLE for Poissonian counting statistics. It applies to all quantities that are processed into histograms, such as the fluorescence intensity decay in a TCSPC experiment (Laurence and Chromy, 2010), the FRET efficiency histogram or the proximity ratio histogram in PDA. For the low counting statistics encountered in burst analysis, the use of the MLE for the estimation of burst-wise fluorescence lifetimes is even required to avoid systematic errors that occur when using the $\chi^2$ statistic (Maus et al., 2001).

### 2.12.3 Model selection and comparison

While the introduced metrics address the question of how to quantify the goodness-of-fit, they offer no information about the choice of the model function. It is always possible to achieve a higher goodness-of-fit by using a more complex model with more free parameters, which can lead to overfitting. A first indication of overfitting is generally given by a $\chi^2_{\text{red.}} < 1$. The $\chi^2$ goodness-of-fit estimator, however, is itself a random variable - it is the sum of squares of $N - k$ independent normally distributed random variables. It follows the $\chi^2$-distribution that depends only on the degrees of freedom $\nu = N - k$.

$$P_{\chi^2}(x|\nu) = \frac{1}{2^{\nu/2}\Gamma(\nu/2)} x^{\nu/2-1} e^{-x/2} \tag{2.114}$$

where $\Gamma$ is the gamma function that generalizes the concept of the factorial to real numbers. Based on the $\chi^2$-distribution, one can calculate the probability of observing a given $\chi^2_{\text{obs}}$ value:

$$P(\chi^2 \geq \chi^2_{\text{obs}}) = 1 - \int_0^{\chi^2_{\text{obs}}} P_{\chi^2}(x|\nu) \mathrm{d}x \tag{2.115}$$

One can then reject a model based on a threshold for the probability (Pearson's chi-squared test, Pearson, 1900). As an example, for 10 degrees of freedom, there is a probability of 95% that $\chi^2 < 18.3$ (or $\chi^2_{\text{red.}} = \chi^2/\nu < 1.83$) if the deviation is purely random. Thus, based on a $p$-value of 0.05, one might reject the model if a larger value is observed.

More advanced concepts are given by the Akaike information criterion (AIC, Akaike, 1974) and the Bayesian information criterion (BIC, Schwarz, 1978). Both require the likelihood at the optimum value of the parameter $\mathcal{L}_{\text{max}}$, but have different ways of introducing a penalty for the usage of more parameters.

$$\text{AIC} = -2 \log \mathcal{L}_{\text{max}} + 2k \qquad \text{BIC} = -2 \log \mathcal{L}_{\text{max}} + k \ln N \tag{2.116}$$

In both cases, the model with the lowest value is to be preferred. Both criteria are derived for the asymptotic case of $N \to \infty$ and are thus only valid if the number of data points is much larger than the number of model parameters ($N \gg k$). The choice between the two criteria is mostly subjective. The AIC is derived from information theory, while the BIC is obtained by Bayesian inference (see also 2.12.5). A fundamental difference in the derivation is that the BIC assumes that the true model is in the set of candidates, while the AIC tries to find the model that most closely resembles the true (unknown) model. This might lead to the (philosophical) conclusion that the BIC is not adequate because every model is only an approximation of a much more complex reality. In practice, the penalty for additional parameters is larger for the BIC than for the AIC (considering that $N > e^2 \approx 7.4$). As a consequence, the AIC is more likely to overfit the data, while the BIC selects a less complex model. Given the ongoing debate in scientific literature, the best advice would be to use both criteria and check for agreement.

### 2.12.4 Optimization algorithms

To find the optimal set of parameters, it is important to have an efficient optimization algorithm. The available algorithms can be grouped into gradient-based and derivative-free methods. To find the optimal parameters, one needs to find the minimum (or maximum) of an objective function that quantifies the goodness-of-fit, such as the introduced $\chi^2_{\mathrm{red.}}$ or the likelihood function $\mathcal{L}$, with respect to the parameters of the model $\theta$. The first (and second) order derivatives of the objective function with respect to the model parameters hereby guide the optimization algorithm on its iterative search of the optimum. If the objective function is given by an explicit mathematical expression, the derivatives can also be expressed analytically. However, often the objective function is not given in closed form or is too complicated to obtain expression for the derivatives. In these cases, the gradient has to be approximated by sampling points in the vicinity of the current parameters values. This step can be computationally costly especially for models with many parameters since the objective function has to be evaluated many times per iteration to approximate the gradient. In these cases, it is important to choose an optimization routine that is efficient. Examples of such algorithms are given by the gradient descent, Gauss-Newton and Levenberg-Marquardt algorithms (Levenberg, 1944; Marquardt, 1963), which are applicable if the sum of the squared deviation are to be minimized (least squares curve fitting). On the other hand, algorithms such as the Nelder-Mead method (also called simplex method, Nelder and Mead, 1965) avoid the need to compute the gradient, but usually take longer to converge than gradient-based methods.

If the optimization surface is rough, i.e. has many local minima, the algorithm is at risk of getting stuck. This can be avoided by running the optimization from different starting values for the parameters or by global search routines such as pattern search (Hooke and Jeeves, 1961). Another family of algorithms adds random fluctuations to avoid the termination in local minima, effectively performing a random walk that explores the parameter space. Examples are given by simulated annealing (Kirkpatrick et al., 1983) or the Metropolis-Hastings algorithm (Hastings, 1970; Metropolis et al., 1953), the latter of which will be described in the following section.

#### Estimating confidence intervals

The $\chi^2$ (or the likelihood function) allows to one to find the optimal parameters of the model function, but contains no information on how well they are defined. To probe the sensitivity of the $\chi^2$ with respect to the individual model parameters, one can vary them systematically to construct the $\chi^2$ surface. For models with many parameters, this approach becomes unfeasible. Instead, one can use the fact that the sensitivity of the $\chi^2$ with respect to the individual parameters is encoded in the curvature of the $\chi^2$ surface, which is given by the second derivative. The matrix of the second order derivatives is called the Hessian matrix and is given by:

$$H_{ij} = \frac{\partial^2 \chi^2(\theta)}{\partial\theta_i \partial\theta_j} \tag{2.117}$$

The Hessian matrix is used during nonlinear regression where it can be obtained from the fit routine at no additional cost. The higher the diagonal element of the Hessian is, the higher is the curvature and the more sharply is the $\chi^2$ surface defined. Thus, one obtains the variances (and thus confidence intervals) by inverting the Hessian matrix. Additionally, the off-diagonal elements contain information about the correlation of fit parameters.

### 2.12.5 Bayesian inference

Bayes' theorem (Bayes, 1763) is a useful tool for data analysis that provides a recipe to update the belief or hypothesis when new evidence is acquired. The probability to observe two outcomes $A$ and $B$, $p(A \cap B)$ relates to the conditional probabilities $p(A|B)$ and $p(B|A)$:

$$p(A \cap B) = p(A)p(B|A) = p(B)p(A|B) \tag{2.118}$$

In data analysis, Bayes' theorem is used in Bayesian inference. The analysis starts with a hypothesis which in model-based analysis is the model function $M$ that depends on a set of parameters $\theta$. Potentially, we have some background knowledge (called $I$) about our system (i.e. from previous experiments or literature) that is described by the prior probability function $p(\theta|I)$. We also require a likelihood function that describes the probability to obtain the observed data $D$ given the parameters $\theta$, $p(D|I)$. We can then rearrange equation 2.118 by substituting outcome $A$ with the data $D$ and outcome $B$ with the parameters $\theta$, and by including the background information $I$, to obtain the posterior probability distribution of the parameters given the measured data:

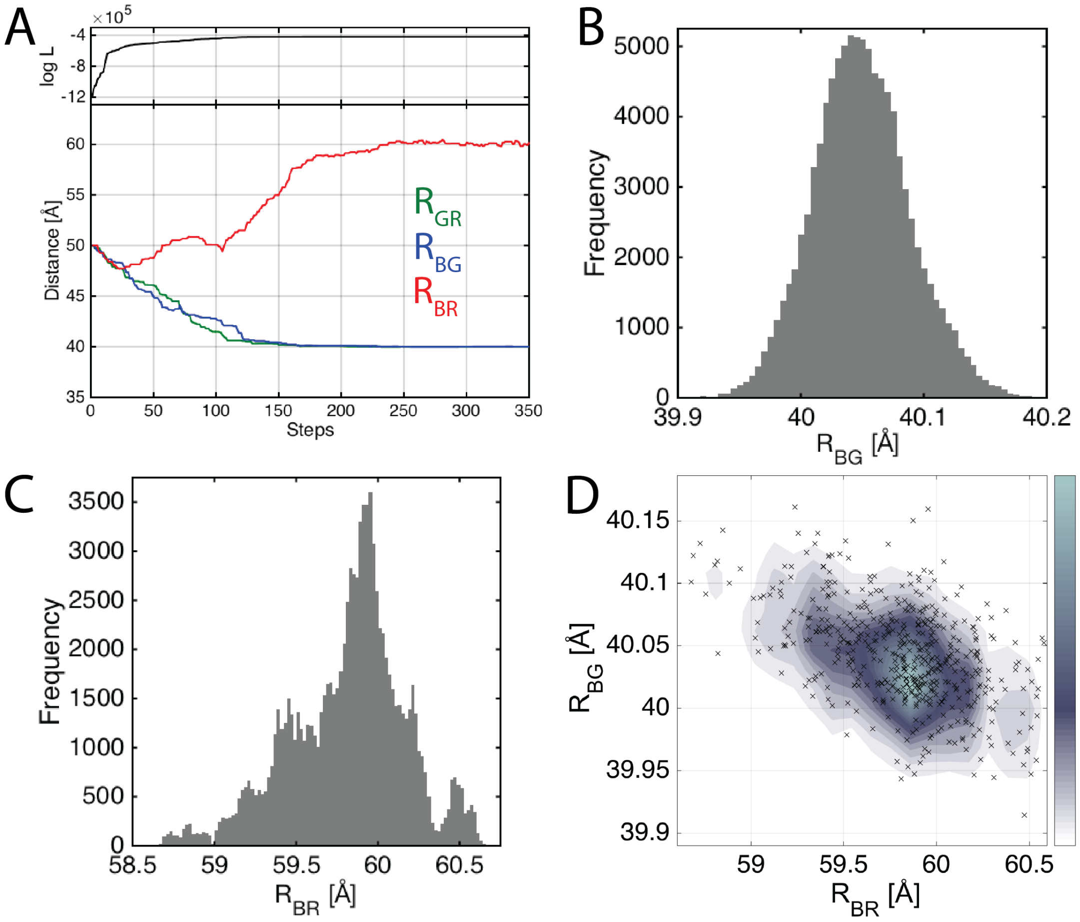

FIGURE 2.29: Markov chain Monte Carlo sampling using the Metropolis-Hastings algorithm to explore the posterior probability density of the parameter space. Shown is a three-color photon distribution analysis (3C-PDA) of a simulated dataset. Using 3C-PDA, the distances between the blue, green and red dyes ($\mathrm{R_{BG}}$, $\mathrm{R_{BR}}$ and $\mathrm{R_{GR}}$) can be extracted from a three-color FRET experiment by maximizing the likelihood of the recorded data with respect to the three interdye distances. **(A)** Starting from the initial guess of the interdye distances of 50 Å, the algorithm quickly moves to a region of high likelihood and finds the correct interdye distances. **(B-D)** From a long run of the sampling algorithm (100.000 steps), the marginal distributions of the distances $\mathrm{R_{BG}}$ (B) and $\mathrm{R_{BR}}$ (C), as well as of the joint distribution of both distances (D) are constructed, revealing the posterior probability distribution of the parameters. Adapted from Barth et al., 2018b.

$$p(\theta|D,I) = \frac{p(\theta|I)p(D|\theta)}{p(D|I)} \tag{2.119}$$

The key idea in Bayesian inference is thus that the model parameters itself are considered random variables whose distribution is defined by the data and background information. Equation 2.119 provides instructions on how to update the knowledge about the model parameters upon acquisition of new data. If no prior information is available for the model parameters, the use of a flat or uniform prior distribution effectively reduces equation 2.119 to the likelihood function, in which case the most probable Bayesian estimate coincides with the maximum likelihood estimate. However, in a Bayesian analysis, one would still consider the full probability distribution of the model parameters to address their uncertainty.

The denominator in equation 2.119 describes the likelihood that the data are observed given the background information, independent of the model parameters. This quantity (also called the "evidence") is often difficult to obtain since it requires integration over the whole parameter space:

$$p(D|I) = \int_\theta p(\theta|I)p(D|\theta)d\theta \tag{2.120}$$

However, since it does not depend on the chosen values for the parameters and serves only as a normalization constant, it can be neglected for the analysis. On the other hand, the evidence is a useful parameter to compare different models. Through the integration over the parameter space, it expresses the total likelihood of the model itself, thus providing an intrinsic measure to compare different model functions, e.g. to decide on the number of components.

Often, the likelihood function $p(D|I)$ has no closed analytic form. It would then be required to to evaluate the likelihood function over the whole parameter space to address the posterior distribution, which is not feasible if the evaluation of the likelihood function is costly. Instead, one would like to evaluate the posterior only in regions of high probability. This is achieved by sampling algorithms such as the Metropolis-Hastings algorithm or Nested Sampling (Skilling, 2004).

The Metropolis-Hastings (MH) algorithm revolves around a Markov chain Monte Carlo (MCMC) sampler that explores the parameter space by a memory-less (Markovian) random walk (Hastings, 1970; Metropolis et al., 1953). At every step, a new parameter vector $\theta \rightarrow \theta'$ is proposed based on a proposal distribution (usually a normal distribution). Steps are accepted or rejected based on the likelihood ratio $r$:

$$r = \frac{p(\theta'|D,I)}{p(\theta|D,I)} \tag{2.121}$$

If the likelihood increases, the step is always accepted, otherwise it is accepted with probability $r$. This way, the algorithm samples from regions of high likelihood of the posterior probability distribution.

An example of Bayesian inference using the Metropolis-Hastings algorithm is given in Figure 2.29 for the analysis of a three-color FRET experiment using a three-color photon distribution analysis. The likelihood function for three-color photon distribution analysis is derived in paper 1. The model function depends on the three interdye distances $R_{GR}$, $R_{BG}$ and $R_{BR}$, whose initial values are set to 50 Å. The MH algorithm quickly moves to the region of high likelihood (panel A, top) after $\sim$ 200 steps, after which it explores the posterior probability distribution. From the samples of a long run of the algorithm (100.000 steps), one can inspect the marginal distributions of the model parameters to address the uncertainty by means of confidence intervals (panels B and C), or investigate correlations of the model parameters (panel D).

# Chapter 3

# Overview of published work

This chapter aims to give an overview over the main work published during this thesis. In these publications, different aspects of the toolbox of confocal single-molecule spectroscopy, as presented in the previous chapter, have been applied. Paper 1 introduces the method three-color photon distribution analysis for the quantitative analysis of single-molecule three-color FRET experiments by burst analysis, and shows its application to study coordinated conformational changes in a protein system. In Paper 2, three-color FRET is used to study long-range energy transfer over a total distance of 16 nm by a combination of hetero- and homo-FRET. The possibility to study dynamic systems by single-molecule FRET is demonstrated in Paper 3, wherein the complex conformational dynamics of a small fragment of the cellulosome on the micro- to millisecond timescale are investigated. Even faster dynamics on the nanosecond timescale are present in intrinsically disordered peptides, which were addressed by PET-FCS in combination with molecular dynamics simulations in Paper 4. Lastly, Paper 5 presents the software framework *PAM*, short for PIE analysis with MATLAB, which makes the methods implemented and developed during this thesis freely available as open-source code.

## 3.1 Paper 1: Quantitative Single-Molecule Three-Color Förster Resonance Energy Transfer by Photon Distribution Analysis

In this paper, a new statistical method for the quantitative analysis of single-molecule three-color FRET experiments by burst analysis, called three-color photon distribution analysis (3C-PDA), is presented.

### 3.1.1 Motivation and key results

Single-molecule three-color FRET is a promising approach to elucidate complex conformational changes in biomolecules. The unique feature of three-color FRET is the possibility to address coordinated movements through the simultaneous measurement of three distances, which can be detected from correlations in the three-dimensional distribution of interdye distances. Using surface-immobilized molecules, a number of three-color FRET studies on the surface have been performed (Chung et al., 2017; Hohng et al., 2004; S. Lee and Hohng, 2013; Wortmann et al., 2017). Ever since its initial realization by Clamme and Deniz, 2005 and N. K. Lee et al., 2007a, however, applications of solution-based single-molecule three-color FRET have been scarce. The limited number of photons available in burst analysis results in broad distributions of distance-related quantities, which has limited most studies to the extraction of average FRET efficiency values (Jung et al., 2012; N. K. Lee et al., 2007b). Through the averaging, however, any information about the distribution of distances and thus the conformational heterogeneity is discarded. While this information is retained when distance-related three-color FRET efficiencies are calculated (see section 2.2.3), the limited number of photons results in broad distribution with nonsensical FRET efficiencies outside the interval $[0, 1]$. This shot-noise problem is illustrated using a simulated dataset in Figure 3.1 A-B. In addition to the broadness and skewness of the distributions, the input values are also not reliably recovered from the obtained distributions (see dashed red lines in panels A and B), and artificial correlations are observed (panel C). These problems complicate a quantitative analysis of the conformational heterogeneity and make it practically impossible to extract information about the coordination of conformational changes.

To solve these issues, a three-color photon distribution analysis (3C-PDA) has been developed in this work. Instead of correcting and converting experimental photon counts, the raw data is left untouched in the analysis. Rather, the method is based on a maximum likelihood estimator that includes the distances and correction factors to find the parameters of the model function that most likely explain the observed photon counts. From the extracted model parameters, the three-color FRET efficiency distribution can be reconstructed and are found in excellent agreement with the measured data (Figure 3.1, black lines). The method is benchmarked using simulated datasets and double-stranded DNA model systems, and applied to the Hsp70 chaperone BiP which undergoes coordinated conformational changes during its nucleotide-dependent conformational cycle.

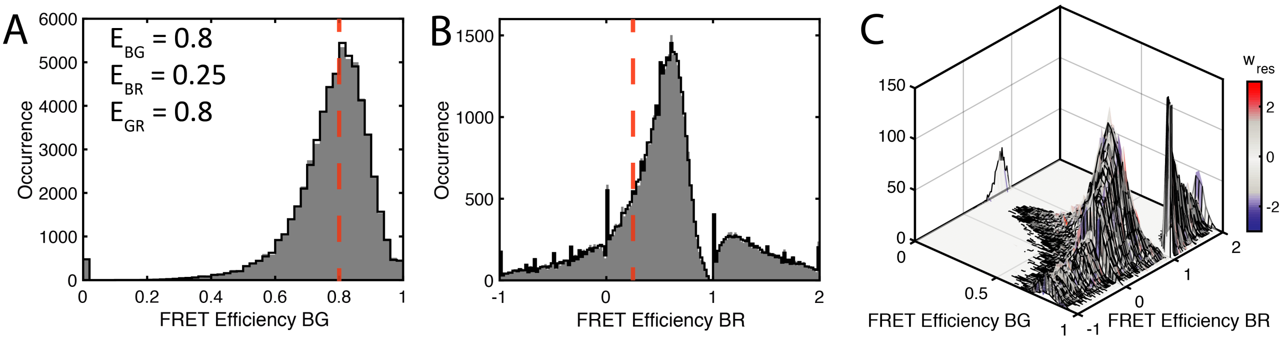

FIGURE 3.1: Illustration of the shot-noise problem in three-color FRET using a simulated dataset. The conversion of photon counts into the three-color FRET efficiencies between the blue and green **(A)** and blue and red **(B)** dyes results in broad distributions and artificial correlations **(C)**. The input parameters of the simulation are given as the equivalent two-color FRET efficiencies in the inset in A. The data is given as grey bars in A-B and as a surface plot in C. Reconstructed theoretical histograms based on the parameters determined from 3C-PDA are given as black lines in A-B and as a black mesh in C. In C, the surface is additionally colored according to the weighted residuals of the fit (see colorbar). Adapted from Barth et al., 2018b.

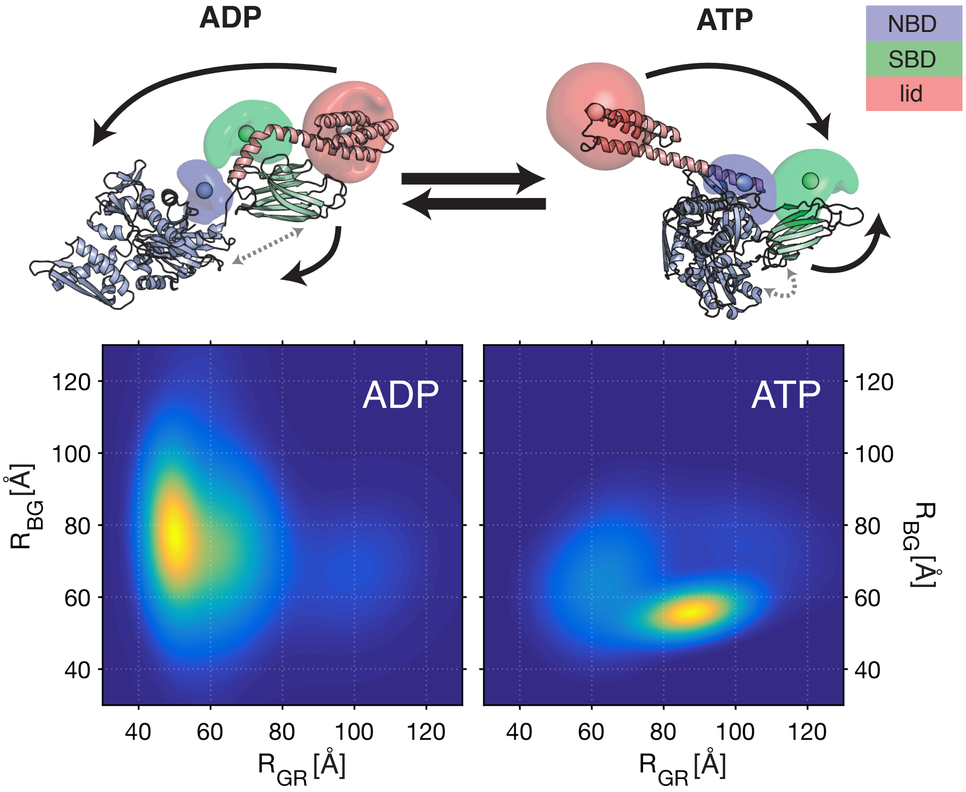

FIGURE 3.2: Coordinated domain motions revealed by 3C-PDA. **(Top)** The Hsp70 chaperone BiP undergoes coordinated domain motions during its nucleotide-dependent conformational cycle. The blue dye is attached to the nucleotide-binding domain (NBD), the green dye to the substrate-binding domain (SBD) and the red dye to the lid. Average dye positions are given as spheres. Clouds indicate the space that the dyes can access based on the length of the connecting linker. **(Bottom)** Distance distributions obtained from 3C-PDA analysis. The distance between the green and red dye labels $R_{GR}$ reports on the separation between the lid and the substrate-binding domain, while the distance between the blue and green dye labels $R_{BG}$ measures the distance between the domains. Adapted from Barth et al., 2018b.

### 3.1.2 Brief description of the method

Following up on the theory of two-color photon distribution analysis (2C-PDA) as described in section 2.10.4, the three-color experiment requires a description of the photon emission after excitation of the donor (blue) dye, which transfers some of its energy to the two acceptor dyes (green and red). The distribution of photon counts in 2C-PDA is given by a binomial distribution. Analogously, the three-color system can be described by a trinomial distribution given by:

$$P(N_{BB}, N_{BG}, N_{BR}|\epsilon_{BG}, \epsilon_{BR}) = \frac{(N_{BB}+N_{BG}+N_{BR})!}{N_{BB}!N_{BG}!N_{BR}!}\left(1-\epsilon_{BG}-\epsilon_{BR}\right)^{N_{BB}}\epsilon_{BG}^{N_{BG}}\epsilon_{BR}^{N_{BR}} \tag{3.1}$$

where $N$ indicates the photon numbers in the respective PIE channels and $\epsilon_{BG}$ and $\epsilon_{BR}$ are the probabilities to detect a green or red photon after excitation of the blue dye, which depend on the interdye distances and the experimental correction factors. Since the three-color FRET efficiencies depend on the FRET efficiency between the green and red dye (see section 2.2.3), alternating excitation e.g. through PIE is required. The probing of the distance between the green and red fluorophores by interleaved excitation of the green dye can be treated independently as described in section 2.10.4, thus the probabilities can be multiplied to obtain the total likelihood:

$$P(N_{BB}, N_{BG}, N_{BR}, N_{GG}, N_{GR}) = P(N_{BB}, N_{BG}, N_{BR}|\epsilon_{BG}, \epsilon_{BR})P(N_{GG}, N_{GR}|\epsilon_{GR}) \tag{3.2}$$

### 3.1.3 Studying coordinated motion in biomolecules

The unique aspect of 3C-PDA is the possibility to study coordinated structural changes during conformational transitions. The Hsp70 chaperone BiP was used as an example to illustrate the capabilities of 3C-PDA to extract information that is otherwise not accessible in single-molecule FRET experiments. BiP is composed of two primary domains called the nucleotide-binding domain (NBD) and substrate-binding domain (SBD) as illustrated in Figure 3.2. While nucleotide hydrolysis occurs in the NBD, the induced conformational change mostly affects the SBD where the flexible lid domain opens or closes upon the substrate-binding pocket. The details of this allosteric mechanism are still not entirely understood (Kityk et al., 2015).

Using three dye labels on the protein, the coordinated conformational change can be followed by 3C-PDA (Figure 3.2, bottom). Based on the labeling scheme, the distance between the green and red fluorophores reports on the opening and closing of the lid in the SBD, while the distance between the blue and green fluorophores monitors the interdomain distance between the NBD and SBD. In agreement with the structural data, the lid is found to be closed in the ADP-bound state while a broad distribution is observed for the interdomain distance $R_{BG}$. The ATP-bound state, on the other hand, shows a large distance $R_{GR}$ and thus an open lid, while a shorter interdomain distance with a narrower distribution is obtained.

### 3.1.4 Outlook: Quantitative multicolor FRET

Three colors is certainly not the end of the line. In fact, a number of single-molecule four-color FRET studies have been performed using surface immobilization (DeRocco et al., 2010; J. Lee et al., 2010; Ratzke et al., 2014) and in solution (Stein et al., 2011; Yim et al., 2012). Most of these studies, however, have focused on a qualitative read-out of the fluorescence signal to detect e.g. the direction of energy transfer or the presence of interaction partners. While a quantitative four-color FRET analysis for solution-based single-molecule measurements has not yet been developed, many promising aspects of four-color FRET can also be realized in simpler schemes. For example, the use of two independent FRET pairs allows to study the coordination of well-separated domains in larger systems. Moreover, for any multi-color experiment, the additional colors may be used to probe the presence of binding partners together with the distance information provided by FRET. By using the most blue-shifted fluorophores to probe the binding interaction, the FRET system is not disturbed by the additional labels and can be probed by alternating excitation. The main limitation for moving to more colors, however, remains the lack of suitable dyes in the UV or NIR region of the spectrum. In the three-color experiments presented here, the use of dyes with absorption in the range of 480 nm, 560 nm and 640 nm provided the best compromise of spectral separation and photophysical properties. Available dyes in the UV region, however, suffer from low extinction coefficients, while NIR dyes have low quantum yields.

At the moment, there is a significant push towards structural FRET in the community (Hellenkamp et al., 2018, 2016; Kalinin et al., 2012; Muschielok et al., 2008). By combining the distance information provided by many FRET sensors with structural modeling, it becomes possible to derive e.g. the precise positioning and arrangements of domains or the binding geometry of nucleic acids to protein surfaces. While three-color FRET is capable of measuring three distances at once, the reduction in the number of measurements required does certainly not offset the increased experimental complexity of fluorescent labeling and data analysis in three-color FRET. However, since biomolecules are often found in equilibrium between different conformations, the coordinated information provided by 3C-PDA may prove vital to correctly assign the distances of the different FRET sensors in complex systems. Lastly, 3C-PDA may be readily extended to account for dynamic interconversion as described for 2C-PDA in section 2.10.4, which will enable the study of complex conformational dynamics. Since the specific labeling of nucleic acids with multiple fluorophores is less difficult than for proteins (Liu et al., 2015), one promising application of 3C-PDA would be e.g. the study of RNA secondary and tertiary structure formation and dynamics (Stephenson et al., 2013).

**Quantitative Single-Molecule Three-Color Förster Resonance Energy Transfer by Photon Distribution Analysis.** by Barth, A., Voith von Voithenberg, L. & Lamb, D. C. *bioRxiv* doi:10.1101/372730 (2018)

## 3.2 Paper 2: Directional Photonic Wire Mediated by Homo-Förster Resonance Energy Transfer on a DNA Origami Platform

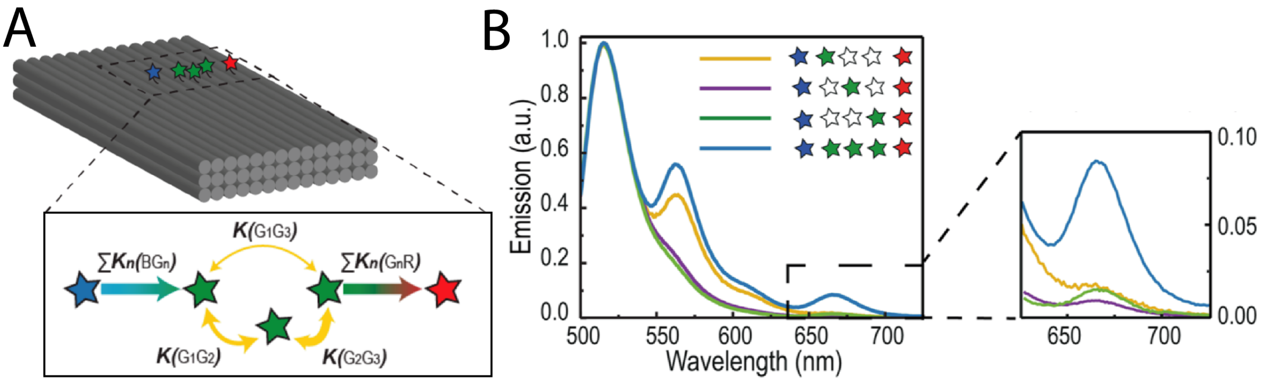

FIGURE 3.3: A homoFRET-mediated photonic wire on a DNA origami platform. **(A)** Schematic of the DNA origami platform and transition pathways in the multi-fluorophore system. The thickness of the arrows corresponds to the efficiency of energy transfer between the green transmitter dyes. The fluorophores are Alexa488 (blue), Cy3 (green) and Cy5 (red). **(B)** Ensemble fluorescence emission spectra of different DNA origami constructs with a single transmitter dye (yellow, purple and green) and all three transmitter dyes (blue) after excitation of the blue donor dye. Significant energy transfer to the red acceptor is only observed if all transmitters are present. Adapted from Nicoli et al., 2017.

In this paper, ensemble fluorescence spectroscopy is combined with single-molecule two- and three-color PIE-MFD experiments to study the energy transfer through a combined hetero- and homo-FRET cascade on a DNA origami structure, enabling energy transfer over a total distance of 16 nm.

### 3.2.1 Motivation and key results

In photosynthetic organisms, light-harvesting complexes rely on energy transfer cascades to channel the energy of the absorbed photons to the reaction center of the complex to convert it into chemical energy. While energy transfer on the sub-nanometer length scale occurs mainly through coupled excitons, long range transfer (> 1 nm) is mediated by dipole-dipole interactions through resonance energy transfer. To understand the role of long-range energy transfer in these systems, artificial linear arrangements of spectrally different fluorophores were created using DNA origami nanotechnology (Rothemund, 2006), allowing precise control over the positioning with sub-nanometer accuracy. The designed energy transfer cascade or "photonic wire" is shown in Figure 3.3 A. The energy is transfer from the blue donor dye (Alexa488) to the red acceptor dye (Cy5) through homo-FRET between three identical green transmitter dyes (Cy3). The efficiency of energy transfer is first evaluated using ensemble fluorescence spectroscopy (Figure 3.3 B). The observation of significant acceptor emission after excitation of the donor dye shows that the photonic wire is capable of energy transfer over a distance of ∼16 nm. The contributions of the individual pathways in the multi-fluorophore system to the overall energy transfer were systematically investigated through analysis of all possible subsystems of the BGGGR cascade.

A major hurdle in DNA origami nanotechnology is the manufacturing cost, making it unfeasible to produce large amounts of material. As a consequence, ensemble methods, which rely on measuring a large number of molecules, are limited in their achievable signal-to-noise ratio, making single molecule methods the perfect tool to study DNA origami constructs. Moreover, while ensemble methods inherently report only an average value and thus hide potential heterogeneity of the sample, single-molecule methods make it possible to investigate the functionality and efficiency of individual nano-machines. Using species-selective analysis of subpopulations in the single-molecule analysis, time-resolved information about the fluorescence and anisotropy decays was obtained. In the measurements of two-color photonic wires carrying only the acceptor dye and two or three transmitter dyes, species-selective analysis allowed us to simultaneously address the efficiency of hetero-FRET from the double-labeled population and homo-FRET from the donor-only population. The efficiency of homo-FRET between Cy3 fluorophores was addressed from the residual fluorescence anisotropy, which is reduced by the occurrence of homo-FRET (see section 2.2.4). Interestingly, the overall energy transfer to the acceptor dye originating from direct excitation of the Cy3 homo-FRET system was found to be enhanced compared to the average efficiency of systems carrying only a single Cy3 fluorophore as donor. Since the energy transfer by homo-FRET lacks directionality, the excitation energy is effectively delocalized over the homo-FRET system and depleted by the acceptor acting as an energy sink. Energy transfer in the complete photonic wire from the blue donor dye to the red acceptor was only efficient if all three transmitter dyes were present (Figure 3.3 B).

### 3.2.2 Outlook: Artificial light harvesting systems

DNA origami as a molecular breadboard is an ideal tool to study energy transfer in complex dye assemblies. While in this work a simple linear dye arrangement was studied, the presented approach may also be applied to study different geometries such as a planar circular arrangement of donor dyes (Hemmig et al., 2016) or more complex, three-dimensional geometries through the use of three-dimensional origami structures (Douglas et al., 2009; Dutta et al., 2011), or to probe the effect of the density of the dyes on the efficiency of the energy cascade. Moreover, it would be interesting to increase the number of spectrally different fluorophores or to combine multiple homo-FRET networks. Moving closer to biological systems, the use of naturally-occurring fluorophores from the pigments of light-harvesting complexes, such as carotenoids or chlorophylls, for the analysis presented here should in principle also be possible based on previous single-molecule studies (J.-E. Lee et al., 2010; Squires and Moerner, 2017; Wörmke et al., 2007).

**Directional Photonic Wire Mediated by Homo-Förster Resonance Energy Transfer on a DNA Origami Platform.** by Nicoli, F.*, Barth, A.*, Bae, W., Neukirchinger, F., Crevenna, A. H., Lamb, D. C., & Liedl, T. *ACS Nano* 11(11), 11264-11272 (2017)

* These authors contributed equally.

## 3.3 Paper 3: Dynamic interactions of type I cohesin modules fine-tune the structure of the cellulosome of *Clostridium thermocellum*

In this work, the structural dynamics of a small fragment of the cellulosome are analyzed quantitatively using dynamic photon distribution analysis and filtered fluorescence correlation spectroscopy.

### 3.3.1 Motivation and key results

Cellulosomes are extra-cellular multimodular protein macro-complexes that digest plant cell walls with high efficiency. Their central module is the protein scaffoldin which consists of nine type I cohesin domains, a cellulose-binding domain and a type II cohesin domain that connects with the cell wall. The individual components of scaffoldin are connected by flexible linkers of variable length. Scaffoldin alone has no catalytic activity, but serves as a scaffold to recruit different enzymatic modules that bind to the type I cohesin domains through dockerin domains. The cohesin-dockerin interaction is one of the strongest non-covalent interactions found in nature (Stahl et al., 2012). Due to the highly dynamic structural organization of the cellulosome, conventional structural approaches such as X-ray crystallography are not suited to characterize their conformation. Structural characterization of fragments of the cellulosome has thus mostly relied on low-resolution structural methods such as nuclear magnetic resonance (NMR) and small angle X-ray scattering (SAXS), revealing a highly dynamic picture of the individual components of the cellulosome.
In this work, the conformational dynamics of the cohesins 8 and 9, connected by their flexible wild type linker, are investigated using four separate FRET sensors to probe four different interdomain distances. To obtain a complete understanding of the structural dynamics of the system, the complementary methods of dynamic photon distribution analysis (PDA, see section 2.10.4) and filtered fluorescence correlation spectroscopy (fFCS, see section 2.9.6) are combined with the atomistic information obtained from molecular dynamics simulations. The CohI$_8$-CohI$_9$ fragment is found to form transient interdomain contacts on the millisecond timescales, while structural fluctuations of the non-interacting states occur on the microsecond timescale (Figure 3.4). Surprisingly, shortening of the linker peptide by half does not impair the conformational dynamics. The addition of dockerin-bearing enzymes did also not inhibit formation of interdomain contacts, but increased the average separation distance in the non-interacting state. Molecular dynamics simulations likewise showed the formation of stable interdomain contacts. As none of the different binding modes observed in the simulations obstructed the dockerin-binding interfaces, the biological function of the cohesin domains is thus not exclusive with the structural dynamics. This indicates that cohesin-cohesin interactions may serve to fine-tune the structure of the cellulosome to optimize the catalytic efficiency, while providing flexibility to adapt to rapidly changing environments.

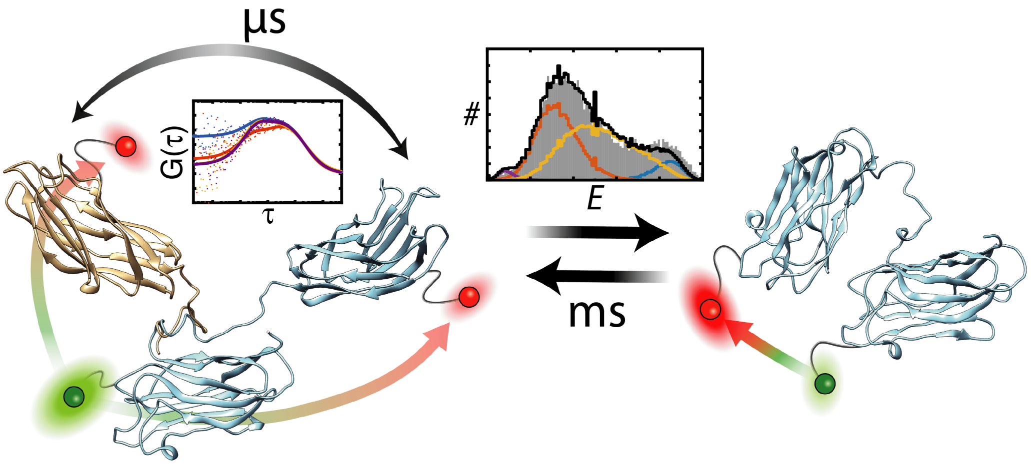

FIGURE 3.4: Conformational dynamics of the CohI$_8$-CohI$_9$ fragment of the cellulosome. **Left:** The CohI$_8$-CohI$_9$ fragment of the scaffoldin is found to be freely fluctuating in the open state on the timescale of ∼10 µs as quantified by filtered-FCS analysis (inset). **Right:** Stable contacts between the two CohI modules persist on the millisecond timescale and were analyzed by dynamic photon distribution analysis (inset above arrow).

### 3.3.2 Outlook: Structural dynamics of the cellulosome

There are still a lot of open questions about the structural organization of the cellulosome. In a next step, the study of larger fragments of the scaffoldin could answer the question of interactions between non-neighboring cohesin modules. Here, three-color FRET could be used to study multiple interactions simultaneously and thus reveal the coordination of intermodular contacts. Similar to the cohesin dyad studied here, the dockerin domains of the enzymatic units are connected to the enzyme through long flexible linkers, and similar interactions might play a role in these systems. Another interesting aspect of the cohesin-dockerin interaction is its dual binding mode, whereby the dockerin may bind in two orientations that are rotated by 180° (Carvalho et al., 2007). The two orientations should be distinguishable by single-molecule FRET, which could be used to measure the distribution over the two configurations under different conditions.

**Dynamic interactions of type I cohesin modules fine-tune the structure of the cellulosome of *Clostridium thermocellum*.** by Barth, A., Hendrix, J., Fried, D., Barak, Y., Bayer, E., & Lamb, D. C. *Proceedings of the National Academy of Sciences* 116(48), E11274–E11283 (2018)

## 3.4 Paper 4: Covalent Dye Attachment Influences the Dynamics and Conformational Properties of Flexible Peptides

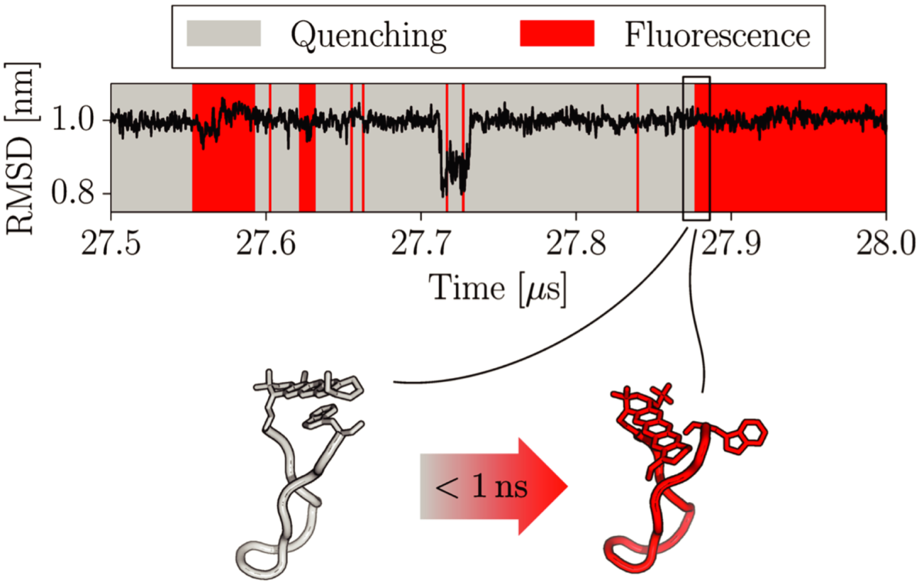

FIGURE 3.5: The dynamics of PET-quenching in the S-peptide studied by PET-FCS and molecular dynamics simulations. Shown is a zoom-in of the root mean square deviation (RMSD) of the peptide residues calculated from the molecular dynamics trajectory. Red-shaded areas indicate times when the dye (Atto655) was fluorescent, while gray shaded errors indicated quenching. Structural dynamics of the peptide and quenching are decoupled. Transitions between quenched and unquenched states occurs on timescales less than 1 ns, as illustrated below the plot. Adapted from Luitz et al., 2017.

In this combined experimental and theoretical study, the dynamics of PET quenching of the fluorophore Atto655 by tryptophan were investigated in a small intrinsically disordered peptide, revealing the detrimental effect that covalently attached moieties can have on the structure of small biomolecules.

### 3.4.1 Motivation and key results

Fluorescence correlation spectroscopy offers the unique possibility to study conformational dynamics of biomolecules from the timescale of minutes down to picoseconds. The high achievable temporal resolution is especially useful for dynamic systems that elude commonly used structural biology tools such as X-ray crystallography or NMR. One example of such a system is the family of intrinsically disordered proteins (IDP). Using fluorescence labels, one can monitor the conformational dynamics of IDPs through FRET or, more commonly used, photoinduced electron transfer (PET, H. Neuweiler and M. Sauer, 2004). However, since these proteins lack stable structure and are thus characterized by a flat energy surface with many possible conformations, it is important to consider the effect of the covalent attachment of fluorophores and quenchers on the conformational space of the molecule of interest. In this study, the timescales of the conformational dynamics of a short IDP were measured by nanosecond-FCS using PET and compared to the results obtained from all-atom molecular dynamics (MD) simulations.

The MD simulations revealed that the conformational space of the peptide is heavily influenced by the covalent modification. $\pi$-stacking interactions between the fluorophore Atto655 and the quencher tryptophan lock the peptide into a stable backbone conformation (see Figure 3.5). In this conformation, quenching/unquenching transitions occur decoupled from the conformational dynamics of the peptide. The timescale of the quenching process extracted from MD agrees very well with the experimental value, indicating that the experimental result does, in fact, not report on the conformational dynamics of the peptide.

### 3.4.2 Outlook

In this study, only a single model system has been tested. To derive general guidelines, it would be interesting to study other combination of dyes and quenchers. Specifically, dye-quencher interactions could be minimized by choosing a pair that shows less attractive interactions or by modifying the moieties to induce charge repulsion. However, artifacts of the introduced labels may also occur through direct interactions with the peptide residues. From the side of the simulations, more accurate force fields for fluorescent dyes are continuously being developed, for which the presented approach may be used to address their viability for disordered systems.

**Covalent Dye Attachment Influences the Dynamics and Conformational Properties of Flexible Peptides.** by Luitz, M. P.*, Barth, A.*, Crevenna, A. H., Bomblies, R., Lamb, D. C. & Zacharias, M. *PLoS ONE* 12(5), e0177139 (2017)

* These authors contributed equally.

## 3.5 Paper 5: PAM: A Framework for Integrated Analysis of Imaging, Single-Molecule, and Ensemble Fluorescence Data

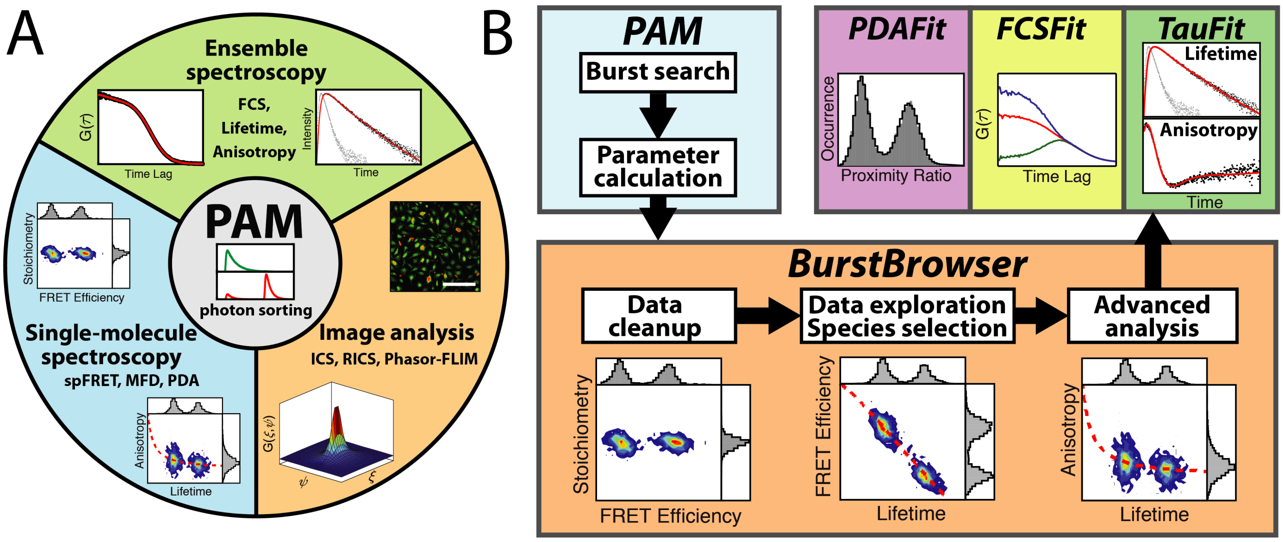

FIGURE 3.6: Overview of the *PAM* software package. **(A)** The three main applications of PAM are ensemble spectroscopy, single-molecule spectroscopy and image analysis. **(B)** The workflow for single-molecule spectroscopy by burst analysis in *PAM*. The data is sorted into PIE channels and processed using a burst search in the main module *PAM*. Data exploration and further analysis is performed in the *BurstBrowser* module. Species-selective analysis methods can be accessed from *BurstBrowser* using the modules *PDAFit* for photon distribution analysis, *FCSFit* for analysis of species-selective correlation functions and *TauFit* for quantitative analysis of fluorescence and anisotropy decays. Adapted from Schrimpf et al., 2018a.

In this paper, the software package *PAM*, short for "PIE Analysis with MATLAB", is introduced. To make the methodologies implemented and developed in this thesis available to a wider audience, many efforts have been undertaken to make *PAM* user-friendly and easily accessible.

### 3.5.1 Motivation

In the field of fluorescence microscopy and spectroscopy, many novel analysis methods have been developed over the past century, while the modalities for data acquisition have remained largely unchanged. As a consequence, an extensive toolbox of analyses is available to researchers, each sensitive to different properties of the studied system. However, publications of new methods have not always included the source code for the analysis, leaving researchers interested in trying out the method with the non-trivial task of writing their own implementation. Arguably, the situation is currently improving as publishers now generally require that all tools and datasets associated with a publication are also made available. However, even if software is provided with the publication, it is often not user-friendly or well documented, difficult to run and potentially written in a programming language that the user is not familiar with. Combining different analysis methods also requires the use of different software suites and programming languages, and data transfer between these is often not trivial. On the other side, closed-source software suites from microscope manufacturers are costly and often lack support for newly developed methods or are slow to implement them.

### 3.5.2 The PAM software package

*PAM* provides an integrated framework for the processing of fluorescence data and implements many cutting-edge analysis methods for the analysis of ensemble, single-molecule or imaging data (Figure 3.6 A). The *PAM* project aims to provide an easy-to-use software package with a high degree of automation that is compatible with a variety of measurement schemes and setups, allowing the user to combine a variety of different quantitative fluorescence analysis techniques on the same data set.
The central module of the software is used to sort the photons into PIE channels. From there, the sorted data is transferred to specialized modules for further processing. The main areas are ensemble spectroscopy by

fluorescence correlation spectroscopy and time-resolved fluorescence decay analysis, single-molecule spectroscopy by burst analysis, and image analysis including fluorescence lifetime imaging and image correlation spectroscopy (Hendrix et al., 2013).
As an example, the workflow for single-molecule spectroscopy by burst analysis is illustrated in Figure 3.6 B. After the photon sorting step, bursts are identified by a burst search routine (see section 2.10.1) and basic parameters such as the FRET efficiency and stoichiometry are computed. Advanced parameters which are more time consuming to compute (such as the fluorescence lifetime and the ALEX-2CDE or FRET-2CDE filters, see section 2.10.5) may be calculated on demand. The burst dataset is then explored using the *BurstBrowser* module. *BurstBrowser* offers extensive capabilities for sorting, filtering and comparison of different datasets or subpopulations. Quantitative analysis of parameter distribution is possible by fitting to two-dimensional Gaussian functions. Additionally, all necessary corrections to the photon counts for the calculation of quantitative FRET efficiencies and stoichiometries can be performed (see section 2.10.2). If PIE is used, the correction factors can additionally be extracted from the dataset automatically. Advanced analysis of selected species is performed using other modules of *PAM*. Filtered-FCS and species-selective FCS curves (see section 2.10.6) are calculated in *BurstBrowser* and subsequently analyzed using *FCSFit*. For photon distribution analysis (see section 2.10.4), single-molecule events are processed into equal time bins in *BurstBrowser* and fit using the *PDAFit* module. Lastly, for species-selective analysis of the fluorescence and anisotropy decays, the photons of the selected species are pooled and histogrammed before being sent to the *TauFit* module for quantitative analysis by reconvolution fitting (see section 2.8).

### 3.5.3 Outlook

The *PAM* software package is continually being developed through improvements of existing functionalities or the implementation of new methods such as three-color photon distribution analysis in the module *tcPDA* (see section 3.1). Nowadays, the publication of new analysis methods is also routinely accompanied by the source code (often written in MATLAB), making their implementation into the software straightforward. The ongoing development aims at improving the handling of multiple datasets within the software for convenient parallel or global analysis of large amounts of data. Within the community, there is a also a push for standardization of experimental protocols (Hellenkamp et al., 2018) and data storage. A common file format for single-photon counting data facilitates the interchange between different laboratories and allows one to append the raw data associated with a publication in a defined format. To this end, *PAM* includes full support for import and export of the Photon-HDF5 file format (Ingargiola et al., 2016).

**Contributions** Besides work on the main module *PAM*, in this work the modules for burst analysis (*BurstBrowser*), including further the modules *PDAFit* and functionality for filtered-FCS analysis and quantitative fluorescence decay analysis (*TauFit*) were developed. As part of Paper 1, functionality for three-color photon distribution analysis is implemented in the module *tcPDA*.

**Availability** The *PAM* software package is hosted at GitLab in a *Git* repository for version control and collaborative development: http://www.gitlab.com/PAM-PIE/PAM.

**PAM: A Framework for Integrated Analysis of Imaging, Single-Molecule, and Ensemble Fluorescence Data.**
by Schrimpf, W.*, Barth, A.*, Hendrix, J., & Lamb, D. C. *Biophysical Journal* 114, 1518-1528 (2018)

* These authors contributed equally.

## 3.6 Other papers and book chapters

**Stability of local secondary structure determines selectivity of viral RNA chaperones.** by Bravo, J. P. K., Borodavka, A., **Barth, A.**, ..., Lamb, D. C. & Tuma, R., *Nucleic Acids Research*, doi:10.1093/nar/gky394 (2018)

This work presents structural and functional data for two RNA-binding proteins from different viruses. The author performed and analyzed single-molecule FRET experiments to investigate the RNA-unwinding capabilities of the proteins σNS and NSP2. Part of the work is presented in section 2.10.6.

**Recognition of the 3′ splice site RNA by the U2AF heterodimer involves a dynamic population shift.** by Voith von Voithenberg, L., Sanchez-Rico, C., ..., **Barth, A.**, ..., Sattler, M., & Lamb, D. C., *Proceedings of the National Academy of Sciences* 113(46), E7169–E7175 (2016)

The interaction of the spliceosomal protein U2AF with different RNA sequences is investigated using nuclear magnetic resonance and single-molecule FRET. The author contributed new analytical tools to the analysis of the single-molecule FRET experiments, namely filtered fluorescence correlation spectroscopy (see section 2.9.6), and assisted in the analysis and interpretation.

**Bap (Sil1) regulates the molecular chaperone BiP by coupling release of nucleotide and substrate.** by Rosam, M., Krader, D., Nickels, C., ..., **Barth, A.**, ..., Lamb, D. C. & Buchner, J., *Nature Structural & Molecular Biology* 25, 90–100 (2018)

In this work, the role of the nucleotide exchange factor Bap on the function and conformation of the Hsp70 chaperone BiP is studied using a combination of single-molecule FRET by burst analysis, analytical ultracentrifugation, hydrogen deuterium exchange and ensemble biochemical techniques. The author contributed analytical tools and assisted in the analysis and interpretation of the single-molecule FRET data.

**MFD-PIE and PIE-FI: Ways to Extract More Information with TCSPC** by **Barth, A.**, Voith von Voithenberg, L. & Lamb, D. C. in *Advanced Photon Counting: Applications, Methods, Instrumentation* (Springer International Publishing, 2014)

This book chapter gives an overview of the advantages of combining pulsed interleaved excitation (PIE) with single-molecule FRET analysis and fluctuation imaging.

**Evaluation of Blue and Far-Red Dye Pairs in Single-Molecule FRET Experiments.** by Vandenberk, N., **Barth, A.**, Borrenberghs, D., Hofkens, J. & Hendrix, J. *J. Phys. Chem. B* (2018)

To provide guidelines for choosing the right pair of dyes for single-molecule FRET experiments, this paper compares the performance of the blue dyes Atto488 and Alexa488 as FRET donors and the dyes Alexa647, Atto647N, Atto655 and StarRed as FRET acceptors. The author developed tools for the analysis and assisted in the interpretation of the single-molecule FRET data.

**Precision and Accuracy of Single-Molecule FRET Measurements—a Multi-Laboratory Benchmark Study.** by Hellenkamp, B., Schmid, S., ..., **Barth, A.**, ..., Michaelis, J., Seidel, C. A. M., Craggs, T. D. & Hugel, T., *Nature Methods* 15 (2018)

The author participated in this worldwide benchmark study on single-molecule FRET measurements.

**Phosphorylation decelerates conformational dynamics in bacterial translation elongation factors.** by Talavera, A., Hendrix, J., ..., **Barth, A.**, ..., Loris, R. & Garcia-Pino, A., *Sci Adv* 4, eaap9714 (2018)

In this study, the combinations of structural and ensemble biochemical methods with single-molecule FRET revealed the conformational dynamics of the ribosomal elongation factor EF-Tu. The author develop new analytical tools, namely dynamic photon distribution analysis (see section 2.10.4), and assisted in the analysis of the single-molecule FRET experiments.

**Excited-state annihilation reduces power dependence of single-molecule FRET experiments.** by Nettels, D., ..., **Barth, A.**, ... Schuler, B. *Phys. Chem. Chem. Phys.* 17, 32304–32315 (2015)

In this work, the photophysical transitions in FRET systems are studied using nanosecond FCS (see section 2.9.3). The contribution of the author to this work was done before the start of the doctoral thesis in the group of Prof. Christian Hübner at the University of Lübeck and may be found in the supporting information of the paper.

## Chapter 4

# Summary and Conclusions

In this thesis, many different aspects of single-molecule spectroscopy have been used to study various systems ranging from artificial assemblies to biological complexes. The fast dynamics of an unstructured peptide on the nanosecond timescale could be addressed by the combination of correlation spectroscopy and photoinduced electron transfer. A detailed characterization of the dynamic conformational space of a tandem fragment of the cellulosome revealed micro- and millisecond dynamics mediated by previously unknown interactions. Species-selective analysis of the fluorescence lifetime and anisotropy was applied to elucidate the energy transfer pathways in a homo-FRET photonic wire, whose efficiency was also evaluated by three-color single-molecule fluorescence spectroscopy. Lastly, the toolbox of single-molecule burst analysis was extended to three colors through the development of three-color photon distribution analysis, providing a framework for the quantitative analysis of three-color FRET experiments.

The standard analysis of single-molecule burst analysis experiments is often limited to a comparison of FRET efficiency histograms, while other valuable parameters of the fluorescence signal are often either not available, disregarded or only used as controls. The analyses presented in this thesis largely go beyond this simple picture and make wide use of additional parameters and dimensions in combination with the sorting capabilities offered by the single-molecule approach. Through species-selective analysis of the fluorescence decay, quantitative information is obtained about the photophysics of the fluorescent probe. The time-resolved anisotropy likewise is a valuable parameter to address the rotational properties of the dye or macromolecule. By combining burst analysis with fluorescence correlation spectroscopy it is possible to connect the diffusion properties of the molecule with its conformational state. Lastly, conformational dynamics can be studied with high sensitivity through the combination of lifetime, anisotropy and color information in filtered-FCS.

An approach that has been used in multiple studies in this thesis is the combination of experiments with molecular simulations, either for cross-validation or to obtain additional insights. While the distance-information obtained through FRET is often compared to expected distances estimated from crystal structures, this approach was not applicable to the dynamic systems studied here. To this end, protocols were established for the comparative evaluation of PET-FCS and single-molecule FRET experiments. Examples are the extraction of the timescales of quenching dynamics in the S-peptide, and the estimation of dynamically-averaged distances of the extended state of the cohesin dyad. Even in the case of thought-to-be static systems, relaxation of the crystal structure, which is potentially affected by the crystal packing, through MD simulations can provide a more accurate structural model that should be preferred for the validation of experimentally obtained distances.

One of the central aims of this work was to set a foundation for future applications and developments of single-molecule spectroscopy. By providing an integrated analysis framework through the *PAM* software package, the first step is taken towards a collaborative development of new methodologies that will be directly available to the user base. In addition to the implementation of several published methodologies during this thesis, such as photon distribution analysis and filtered fluorescence correlation spectroscopy, the new method of three-color photon distribution analysis enables a quantitative analysis of single-molecule three-color FRET experiments, opening up the unique possibility to investigate coordinated conformational changes by measuring three distances simultaneously. Researchers in possession of a microscope capable of measuring single-molecule three-color FRET can readily use the developed software to extract quantitative distance information from the recorded fluorescence signal, allowing to address new questions in established systems through more complex experimental schemes.

# Appendix A

# Homo-FRET

## A.1 Homo-FRET and fluorescence lifetime

The lack of any effect of homo-FRET on the fluorescence lifetime can be understood by considering multiple energy transfer steps between identical fluorophores. The quenched fluorescence lifetime in the presence of homo-FRET is given by:

$$\tau = (1 - E)\tau_0 \tag{A.1}$$

However, since the emission of the donor and acceptor fluorophore is indistinguishable, the unquenched lifetime is measured experimentally. After energy transfer, the acceptor fluorophore may either fluoresce, or transfer the energy back to the identical donor fluorophore. The decay of either fluorophore follows an exponential distributions with the reduced lifetime as given in equation A.1. The expected value of the sum of random variables is the sum of the individual expected values. Thus, the average decay time after $n$ transfer steps is given by $\tau_n = (n+1)\tau$. The average lifetime over all possible transfer sequences is then given by:

$$\begin{aligned}\langle \tau \rangle &= (1-E)\tau + E(1-E)2\tau + E^2(1-E)3\tau + E^3(1-E)4\tau + ... \\ &= (1-E)\tau \sum_{i=1}^{\infty} iE^{i-1}\end{aligned} \tag{A.2}$$

We can find an expression for the infinite sum by using the identity:

$$\sum_{k=1}^{\infty} kz^k = \frac{z}{(1-z)^2} \tag{A.3}$$

$$\langle \tau \rangle = \frac{1-E}{E}\tau \sum_{i=1}^{\infty} i * E^i = \frac{1-E}{E}\tau \frac{E}{(1-E)^2} = \frac{\tau}{1-E} \tag{A.4}$$

Using equation A.1, the average lifetime is thus equivalent to the unquenched lifetime:

$$\langle \tau \rangle = \frac{\tau}{1-E} = \frac{(1-E)\tau_0}{1-E} = \tau_0 \tag{A.5}$$

## A.2 Homo-FRET and anisotropy

Energy transfer between identical fluorophores (homo-FRET) cannot be measured spectrally or by the fluorescence lifetime (see previous section). However, in the presence of homo-FRET, the measured fluorescence anisotropy is decreased. Energy transfer can occur over a wide range of angles between the donor and acceptor dipole moments and thus results in a significant amount of depolarization.

Consider a fluorophore with a steady-state anisotropy $\langle r \rangle_0$ in the absence of homo-FRET, undergoing homo-FRET to an identical fluorophore with FRET efficiency $E$, upon which the emission is depolarized by the factor $d$. The fluorophores may undergo repeated energy transfer steps back and forth, upon which the signal is further depolarized. The measured average anisotropy is then given by:

$$\langle r \rangle = \langle r \rangle_0 (1 - E) + \langle r \rangle_0 (1 - E) Ed + \langle r \rangle_0 (1 - E) E^2 d^2 + \ldots \tag{A.6}$$

We can simplify the infinite sum and obtain:

$$\langle r \rangle = \langle r \rangle_0 \frac{1 - E}{1 - Ed} \tag{A.7}$$

Thus, if the depolarization of a single transfer step $d$ is known, the homo-FRET efficiency can be calculated from the decrease of the steady-state anisotropy by:

$$E = \frac{\langle r \rangle_0 - \langle r \rangle}{\langle r \rangle_0 - d \langle r \rangle} \tag{A.8}$$

Assuming that a single transfer step is sufficient to depolarize the emission completely (i.e. $d \approx 0$), the formula simplifies to:

$$E = 1 - \frac{\langle r \rangle}{\langle r \rangle_0} \tag{A.9}$$

This equation is similar to the relation between the donor lifetime and the FRET efficiency.

# Bibliography

G. B. Airy (1835). "On the Diffraction of an Object-glass with Circular Aperture". *Transactions of the Cambridge Philosophical Society* 5, p. 283.

H. Akaike (1974). "A new look at the statistical model identification". *IEEE Transactions on Automatic Control* 19.6, pp. 716–723.

W. Patrick Ambrose, Peter M. Goodwin, James H. Jett, Alan Van Orden, James H. Werner, and Richard A. Keller (1999). "Single Molecule Fluorescence Spectroscopy at Ambient Temperature". *Chemical Reviews* 99.10, pp. 2929–2956.

Matthew Antonik, Suren Felekyan, Alexander Gaiduk, and Claus A. M. Seidel (2006). "Separating Structural Heterogeneities from Stochastic Variations in Fluorescence Resonance Energy Transfer Distributions via Photon Distribution Analysis". *The Journal of Physical Chemistry B* 110.13, pp. 6970–6978.

Daniel S. Banks, Charmaine Tressler, Robert D. Peters, Felix Höfling, and Cécile Fradin (2016). "Characterizing anomalous diffusion in crowded polymer solutions and gels over five decades in time with variable-lengthscale fluorescence correlation spectroscopy." *Soft Matter* 12.18, pp. 4190–4203.

Anders Barth (2013). "Three-color Multiparameter Fluorescence Detection with Pulsed Interleaved Excitation". Master's thesis. München: Ludwig-Maximilians-Universität. URL: `https://www.cup.uni-muenchen.de/pc/lamb/pdf/Anders_Barth_Thesis.pdf`.

Anders Barth, Jelle Hendrix, Daniel Fried, Yoav Barak, Edward A. Bayer, and Don C. Lamb (2018a). "Dynamic interactions of type I cohesin modules fine-tune the structure of the cellulosome of Clostridium thermocellum". *Proceedings of the National Academy of Sciences* 115.48, E11274.

Anders Barth, Lena Voith von Voithenberg, and Don C. Lamb (2014). "MFD-PIE and PIE-FI: Ways to Extract More Information with TCSPC". *Advanced Photon Counting: Applications, Methods, Instrumentation*. Springer International Publishing.

Anders Barth, Lena Voith von Voithenberg, and Don C. Lamb (2018b). "Quantitative single-molecule three-color Förster resonance energy transfer by photon distribution analysis". *bioRxiv*, p. 372730.

T. Bayes (1763). "A Letter from the Late Reverend Mr. Thomas Bayes, F. R. S. to John Canton, M. A. and F. R. S." *Philosophical Transactions (1683-1775)*.

Aleš Benda, Peter Kapusta, Martin Hof, and Katharina Gaus (2014). "Fluorescence spectral correlation spectroscopy (FSCS) for probes with highly overlapping emission spectra". *Optics express* 22.3, p. 2973.

Robert B. Best, Gerhard Hummer, and William A. Eaton (2013). "Native contacts determine protein folding mechanisms in atomistic simulations." *Proceedings of the National Academy of Sciences* 110.44, pp. 17874–17879.

Martin Böhmer, Michael Wahl, Hans-Jürgen Rahn, Rainer Erdmann, and Jörg Enderlein (2002). "Time-resolved fluorescence correlation spectroscopy". *Chemical Physics Letters* 353.5-6, pp. 439–445.

Jack P. K. Bravo, Alexander Borodavka, Anders Barth, Antonio N. Calabrese, Peter Mojzes, Joseph J. B. Cockburn, Don C. Lamb, and Roman Tuma (2018). "Stability of local secondary structure determines selectivity of viral RNA chaperones". *Nucleic Acids Research*.

E. Brooks Shera, Newton K. Seitzinger, Lloyd M. Davis, Richard A. Keller, and Steven A. Soper (1990). "Detection of single fluorescent molecules". *Chemical Physics Letters* 174.6, pp. 553–557.

Ana Luísa Carvalho, Fernando M. V. Dias, Tibor Nagy, José A. M. Prates, Mark R. Proctor, Nicola Smith, Edward A. Bayer, Gideon J. Davies, Luís M. A. Ferreira, Maria J. Romão, Carlos M. G. A. Fontes, and Harry J. Gilbert (2007). "Evidence for a dual binding mode of dockerin modules to cohesins". *Proceedings of the National Academy of Sciences* 104.9, pp. 3089–3094.

Kausik Chakraborty, Manal Chatila, Jyoti Sinha, Qiaoyun Shi, Bernhard C. Poschner, Martin Sikor, Guoxin Jiang, Don C. Lamb, F. Ulrich Hartl, and Manajit Hayer-Hartl (2010). "Chaperonin-catalyzed rescue of kinetically trapped states in protein folding." *Cell* 142.1, pp. 112–122.

Hoi Sung Chung, John M. Louis, and William A. Eaton (2009). "Experimental determination of upper bound for transition path times in protein folding from single-molecule photon-by-photon trajectories." *Proceedings of the National Academy of Sciences* 106.29, pp. 11837–11844.

Hoi Sung Chung, Fanjie Meng, Jae-Yeol Kim, Kevin McHale, Irina V. Gopich, and John M. Louis (2017). "Oligomerization of the tetramerization domain of p53 probed by two- and three-color single-molecule FRET." *Proceedings of the National Academy of Sciences* 114.33, E6812–E6821.

Jean-Pierre Clamme and Ashok A. Deniz (2005). "Three-Color Single-Molecule Fluorescence Resonance Energy Transfer". *ChemPhysChem* 6.1, pp. 74–77.

Edward Condon (1926). "A Theory of Intensity Distribution in Band Systems". *Physical Review* 28.6, pp. 1182–1201.

— (1928). "Nuclear Motions Associated with Electron Transitions in Diatomic Molecules". *Phys. Rev.* 32.6, pp. 858–872.

Paul C. Cross, John Burnham, and Philip A. Leighton (1937). "The Raman Spectrum and the Structure of Water". *Journal of the American Chemical Society* 59.6, pp. 1134–1147.

Vanessa DeRocco, Trevor Anderson, Jacob Piehler, Dorothy A. Erie, and Keith Weninger (2010). "Four-color single-molecule fluorescence with noncovalent dye labeling to monitor dynamic multimolecular complexes." *BioTechniques* 49.5, pp. 807–816.

Thomas Dertinger, Anastasia Loman, Benjamin Ewers, Claus B. Müller, Benedikt Kramer, and Jörg Enderlein (2008). "The optics and performance of dual-focus fluorescence correlation spectroscopy." *Optics Express* 16.19, pp. 14353–14368.

D. L. Dexter (1953). "A Theory of Sensitized Luminescence in Solids". *The Journal of Chemical Physics* 21.5, pp. 836–850.

Michelle A. Digman, Claire M. Brown, Parijat Sengupta, Paul W. Wiseman, Alan R. Horwitz, and Enrico Gratton (2005). "Measuring Fast Dynamics in Solutions and Cells with a Laser Scanning Microscope". *Biophysical Journal* 89.2, pp. 1317–1327.

Michelle A. Digman and Enrico Gratton (2009). "Imaging Barriers to Diffusion by Pair Correlation Functions". *Biophysical Journal* 97.2, pp. 665–673.

Sören Doose, Hannes Neuweiler, and Markus Sauer (2009). "Fluorescence quenching by photoinduced electron transfer: a reporter for conformational dynamics of macromolecules." *ChemPhysChem* 10.9-10, pp. 1389–1398.

Shawn M. Douglas, Hendrik Dietz, Tim Liedl, Björn Högberg, Franziska Graf, and William M. Shih (2009). "Self-assembly of DNA into nanoscale three-dimensional shapes". *Nature* 459.7245, pp. 414–418.

Palash K. Dutta, Reji Varghese, Jeanette Nangreave, Su Lin, Hao Yan, and Yan Liu (2011). "DNA-Directed Artificial Light-Harvesting Antenna". *Journal of the American Chemical Society* 133.31, pp. 11985–11993.

C. Eggeling, S. Berger, L. Brand, J. R. Fries, J. Schaffer, A. Volkmer, and C. A. M. Seidel (2001). "Data registration and selective single-molecule analysis using multi-parameter fluorescence detection." *Journal of Biotechnology* 86.3, pp. 163–180.

C. Eggeling, J. R. Fries, L. Brand, R. Günther, and C. A. M. Seidel (1998). "Monitoring conformational dynamics of a single molecule by selective fluorescence spectroscopy." *Proceedings of the National Academy of Sciences* 95.4, pp. 1556–1561.

Jörg Enderlein and Rainer Erdmann (1997). "Fast fitting of multi-exponential decay curves". *Optics Communications*, pp. 1–8.

Jörg Enderlein, David L. Robbins, W. Patrick Ambrose, Peter M. Goodwin, and Richard A. Keller (1997). "The statistics of single molecule detection: An overview". *Bioimaging* 5, pp. 88–98.

D. F. Evans (1957). "257. Perturbation of singlet-triplet transitions of aromatic molecules by oxygen under pressure". *Journal of the Chemical Society*, pp. 1351–1357.

Lord Rayleigh F.R.S (1879). "XXXI. Investigations in optics, with special reference to the spectroscope". *The London, Edinburgh, and Dublin Philosophical Magazine and Journal of Science* 8.49, pp. 261–274.

Suren Felekyan, Stanislav Kalinin, Hugo Sanabria, Alessandro Valeri, and Claus A. M. Seidel (2012). "Filtered FCS: species auto- and cross-correlation functions highlight binding and dynamics in biomolecules." *ChemPhysChem* 13.4, pp. 1036–1053.

Suren Felekyan, Hugo Sanabria, Stanislav Kalinin, Ralf Kühnemuth, and Claus A. M. Seidel (2013). *Analyzing Förster Resonance Energy Transfer with Fluctuation Algorithms*. Vol. 519. Single Molecule Tools, Part B:Super-Resolution, Particle Tracking, Multiparameter, and Force Based Methods. Elsevier Inc.

Th. Förster (1948). "Zwischenmolekulare Energiewanderung und Fluoreszenz". *Annalen der Physik* 437.1-2, pp. 55–75.

J. Franck and E. G. Dymond (1926). "Elementary processes of photochemical reactions". *Transactions of the Faraday Society* 21, pp. 536–542.

J. R. Fries, L. Brand, C. Eggeling, M. Köllner, and Claus A. M. Seidel (1998). "Quantitative identification of different single molecules by selective time-resolved confocal fluorescence spectroscopy". *The Journal of Physical Chemistry A* 102, pp. 6601–6613.

Alexander Gansen, Alessandro Valeri, Florian Hauger, Suren Felekyan, Stanislav Kalinin, Katalin Tóth, Jörg Langowski, and Claus A. M. Seidel (2009). "Nucleosome disassembly intermediates characterized by single-molecule FRET". *Proceedings of the National Academy of Sciences* 106.36, pp. 15308–15313.

Irina Gopich and Attila Szabo (2005). "Theory of photon statistics in single-molecule Förster resonance energy transfer." *The Journal of Chemical Physics* 122.1, p. 14707.

Ingo Gregor, Digambara Patra, and Jörg Enderlein (2005). "Optical Saturation in Fluorescence Correlation Spectroscopy under Continuous-Wave and Pulsed Excitation". *ChemPhysChem* 6.1, pp. 164–170.

T. Ha, T. Enderle, D. F. Ogletree, D. S. Chemla, P. R. Selvin, and S. Weiss (1996). "Probing the interaction between two single molecules: fluorescence resonance energy transfer between a single donor and a single acceptor." *Proceedings of the National Academy of Sciences* 93.13, pp. 6264–6268.

W. K. Hastings (1970). "Monte Carlo sampling methods using Markov chains and their applications". *Biometrika* 57.1, pp. 97–109.

Mike Heilemann, Philip Tinnefeld, Gabriel Sanchez Mosteiro, Maria Garcia Parajo, Niek F. Van Hulst, and Markus Sauer (2004). "Multistep Energy Transfer in Single Molecular Photonic Wires". *Journal of the American Chemical Society* 126.21, pp. 6514–6515.

Björn Hellenkamp, Sonja Schmid, Olga Doroshenko, Oleg Opanasyuk, Ralf Kühnemuth, Soheila Rezaei Adariani, Benjamin Ambrose, Mikayel Aznauryan, Anders Barth, Victoria Birkedal, Mark E. Bowen, Hongtao Chen, Thorben Cordes, Tobias Eilert, Carel Fijen, Christian Gebhardt, Markus Götz, Giorgos Gouridis, Enrico Gratton, Taekjip Ha, Pengyu Hao, Christian A. Hanke, Andreas Hartmann, Jelle Hendrix, Lasse L. Hildebrandt, Verena Hirschfeld, Johannes Hohlbein, Boyang Hua, Christian G. Hübner, Eleni Kallis, Achillefs N. Kapanidis, Jae-Yeol Kim, Georg Krainer, Don C. Lamb, Nam Ki Lee, Edward A. Lemke, Brié Levesque, Marcia Levitus, James J. McCann, Nikolaus Naredi-Rainer, Daniel Nettels, Thuy Ngo, Ruoyi Qiu, Nicole C. Robb, Carlheinz Röcker, Hugo Sanabria, Michael Schlierf, Tim Schröder, Benjamin Schuler, Henning Seidel, Lisa Streit, Johann Thurn, Philip Tinnefeld, Swati Tyagi, Niels Vandenberk, Andrés Manuel Vera, Keith R. Weninger, Bettina Wünsch, Inna S. Yanez-Orozco, Jens Michaelis, Claus A. M. Seidel, Timothy D. Craggs, and Thorsten Hugel (2018). "Precision and accuracy of single-molecule FRET measurements—a multi-laboratory benchmark study". *Nature Methods* 15.9, p. 669.

Björn Hellenkamp, Philipp Wortmann, Florian Kandzia, Martin Zacharias, and Thorsten Hugel (2016). "Multidomain structure and correlated dynamics determined by self-consistent FRET networks". *Nature Methods* 14.2, pp. 174–180.

Elisa A. Hemmig, Celestino Creatore, Bettina Wünsch, Lisa Hecker, Philip Mair, M. Andy Parker, Stephen Emmott, Philip Tinnefeld, Ulrich F. Keyser, and Alex W. Chin (2016). "Programming Light-Harvesting Efficiency Using DNA Origami". *Nano Letters* 16.4, pp. 2369–2374.

Jelle Hendrix, Waldemar Schrimpf, Matthias Höller, and Don C. Lamb (2013). "Pulsed Interleaved Excitation Fluctuation Imaging". *Biophysical Journal* 105.4, pp. 848–861.

Samuel T. Hess and Watt W. Webb (2002). "Focal volume optics and experimental artifacts in confocal fluorescence correlation spectroscopy." *Biophysical Journal* 83.4, pp. 2300–2317.

Armin Hoffmann, Daniel Nettels, Jennifer Clark, Alessandro Borgia, Sheena E. Radford, Jane Clarke, and Benjamin Schuler (2011). "Quantifying heterogeneity and conformational dynamics from single molecule FRET of diffusing molecules: recurrence analysis of single particles (RASP)". *Physical Chemistry Chemical Physics* 13.5, p. 1857.

Sungchul Hohng, Chirlmin Joo, and Taekjip Ha (2004). "Single-Molecule Three-Color FRET". *Biophysical Journal* 87.2, pp. 1328–1337.

Robert Hooke and T. A. Jeeves (1961). ""Direct Search"' Solution of Numerical and Statistical Problems". *Journal of the ACM* 8.2, pp. 212–229.

Helen Hwang, Hajin Kim, and Sua Myong (2011). "Protein induced fluorescence enhancement as a single molecule assay with short distance sensitivity." *Proceedings of the National Academy of Sciences* 108.18, pp. 7414–7418.

Antonino Ingargiola, Ted Laurence, Robert Boutelle, Shimon Weiss, and Xavier Michalet (2016). "Photon-HDF5: An Open File Format for Timestamp-Based Single-Molecule Fluorescence Experiments". *Biophysical Journal* 110.1, pp. 26–33.

Vassili Ivanov, Min Li, and Kiyoshi Mizuuchi (2009). "Impact of emission anisotropy on fluorescence spectroscopy and FRET distance measurements." *Biophysical Journal* 97.3, pp. 922–929.

A. Jabłoński (1935). "Über den Mechanismus der Photolumineszenz von Farbstoffphosphoren". *Zeitschrift für Physik* 94.1, pp. 38–46.

Jiwon Jung, Kyu Young Han, Hye Ran Koh, Jihyun Lee, Yoon Mi Choi, Christine Kim, and Seong Keun Kim (2012). "Effect of single-base mutation on activity and folding of 10-23 deoxyribozyme studied by three-color single-molecule ALEX FRET." *The Journal of Physical Chemistry B* 116.9, pp. 3007–3012.

Wolfgang Kabsch and Christian Sander (1983). "Dictionary of protein secondary structure: Pattern recognition of hydrogen-bonded and geometrical features". *Biopolymers* 22.12, pp. 2577–2637.

Stanislav Kalinin, Thomas Peulen, Simon Sindbert, Paul J. Rothwell, Sylvia Berger, Tobias Restle, Roger S. Goody, Holger Gohlke, and Claus A. M. Seidel (2012). "A toolkit and benchmark study for FRET-restrained high-precision structural modeling." *Nature Methods* 9.12, pp. 1218–1225.

Stanislav Kalinin, Evangelos Sisamakis, Steven W. Magennis, Suren Felekyan, and Claus A. M. Seidel (2010a). "On the origin of broadening of single-molecule FRET efficiency distributions beyond shot noise limits." *The Journal of Physical Chemistry B* 114.18, pp. 6197–6206.

Stanislav Kalinin, Alessandro Valeri, Matthew Antonik, Suren Felekyan, and Claus A. M. Seidel (2010b). "Detection of structural dynamics by FRET: a photon distribution and fluorescence lifetime analysis of systems with multiple states." *The Journal of Physical Chemistry B* 114.23, pp. 7983–7995.

Achillefs N. Kapanidis, Ted A. Laurence, Nam Ki Lee, Emmanuel Margeat, Xiangxu Kong, and Shimon Weiss (2005). "Alternating-Laser Excitation of Single Molecules". *Accounts of Chemical Research* 38.7, pp. 523–533.

Michael Kasha (1950). "Characterization of electronic transitions in complex molecules". *Discussions of the Faraday Society* 9.0, pp. 14–19.

S. Kirkpatrick, C. D. Gelatt, and M. P. Vecchi (1983). "Optimization by Simulated Annealing". *Science* 220.4598, p. 671.

Roman Kityk, Markus Vogel, Rainer Schlecht, Bernd Bukau, and Matthias P. Mayer (2015). "Pathways of allosteric regulation in Hsp70 chaperones." *Nature Communications* 6, p. 8308.

Volodymyr Kudryavtsev, Martin Sikor, Stanislav Kalinin, Dejana Mokranjac, Claus A. M. Seidel, and Don C. Lamb (2012). "Combining MFD and PIE for accurate single-pair Förster resonance energy transfer measurements." *ChemPhysChem* 13.4, pp. 1060–1078.

Joseph R. Lakowicz, Józef Kuśba, Henryk Szmacinski, Michael L. Johnson, and Ignacy Gryczynski (1993). "Distance-dependent fluorescence quenching observed by frequency-domain fluorometry". *Chemical Physics Letters* 206.5-6, pp. 455–463.

Ted A. Laurence and Brett A. Chromy (2010). "Efficient maximum likelihood estimator fitting of histograms". *Nature Methods* 7.5, pp. 338–339.

Ted A. Laurence, Youngeun Kwon, Eric Yin, Christopher W. Hollars, Julio A. Camarero, and Daniel Barsky (2007). "Correlation spectroscopy of minor fluorescent species: signal purification and distribution analysis." *Biophysical Journal* 92.6, pp. 2184–2198.

Ji-Eun Lee, Jaesung Yang, Victoria L. Gunderson, Michael R. Wasielewski, and Dongho Kim (2010). "Fluorescence Dynamics of Chlorophyll Trefoils in the Solid State Studied by Single-Molecule Fluorescence Spectroscopy". *The Journal of Physical Chemistry Letters* 1.1, pp. 284–289.

Jinwoo Lee, Sanghwa Lee, Kaushik Ragunathan, Chirlmin Joo, Taekjip Ha, and Sungchul Hohng (2010). "Single-molecule four-color FRET." *Angewandte Chemie (International ed. in English)* 49.51, pp. 9922–9925.

Nam Ki Lee, Achillefs N. Kapanidis, Hye Ran Koh, You Korlann, Sam On Ho, Younggyu Kim, Natalie Gassman, Seong Keun Kim, and Shimon Weiss (2007a). "Three-Color Alternating-Laser Excitation of Single Molecules: Monitoring Multiple Interactions and Distances". *Biophysical Journal* 92.1, pp. 303–312.

Nam Ki Lee, Hye Ran Koh, Kyu Young Han, and Seong Keun Kim (2007b). "Folding of 8-17 deoxyribozyme studied by three-color alternating-laser excitation of single molecules." *Journal of the American Chemical Society* 129.50, pp. 15526–15534.

Sanghwa Lee and Sungchul Hohng (2013). "An optical trap combined with three-color FRET." *Journal of the American Chemical Society* 135.49, pp. 18260–18263.

Kenneth Levenberg (1944). "A method for the solution of certain non-linear problems in least squares". *Quarterly of Applied Mathematics* 2.2, pp. 164–168.

Marcia Levitus and Suman Ranjit (2011). "Cyanine dyes in biophysical research: the photophysics of polymethine fluorescent dyes in biomolecular environments". *Quarterly Reviews of Biophysics* 44.1, pp. 123–151.

Yu Liu, Erik Holmstrom, Jinwei Zhang, Ping Yu, Jinbu Wang, Marzena A. Dyba, De Chen, Jinfa Ying, Stephen Lockett, David J. Nesbitt, Adrian R. Ferré-D'Amaré, Rui Sousa, Jason R. Stagno, and Yun-Xing Wang (2015). "Synthesis and applications of RNAs with position-selective labelling and mosaic composition". *Nature* 522.7556, pp. 368–372.

S. Lloyd (1982). "Least squares quantization in PCM". *IEEE Transactions on Information Theory* 28.2, pp. 129–137.

Manuel P. Luitz, Anders Barth, Alvaro H. Crevenna, Rainer Bomblies, Don C. Lamb, and Martin Zacharias (2017). "Covalent dye attachment influences the dynamics and conformational properties of flexible peptides." *PLoS ONE* 12.5, e0177139.

Douglas Magde, Elliot Elson, and W. W. Webb (1972). "Fluorescence Correlation Spectroscopy". *Physical Review Letters* 25.12, pp. 17–18.

M. Margittai, J. Widengren, E. Schweinberger, G. F. Schröder, S. Felekyan, E. Haustein, M. König, D. Fasshauer, H. Grubmuller, R. Jahn, and C. A. M. Seidel (2003). "Single-molecule fluorescence resonance energy transfer reveals a dynamic equilibrium between closed and open conformations of syntaxin 1." *Proceedings of the National Academy of Sciences of the United States of America* 100.26, pp. 15516–15521.

Donald W. Marquardt (1963). "An Algorithm for Least-Squares Estimation of Nonlinear Parameters". *Journal of the Society for Industrial and Applied Mathematics* 11.2, pp. 431–441.

Siewert J. Marrink, H. Jelger Risselada, Serge Yefimov, D. Peter Tieleman, and Alex H. de Vries (2007). "The MARTINI Force Field: Coarse Grained Model for Biomolecular Simulations". *The Journal of Physical Chemistry B* 111.27, pp. 7812–7824.

Michael Maus, Mircea Cotlet, Johan Hofkens, Thomas Gensch, Frans C. De Schryver, J. Schaffer, and C. A. M. Seidel (2001). "An Experimental Comparison of the Maximum Likelihood Estimation and Nonlinear Least-Squares Fluorescence Lifetime Analysis of Single Molecules". *Analytical Chemistry* 73.9, pp. 2078–2086.

Nicholas Metropolis, Arianna W. Rosenbluth, Marshall N. Rosenbluth, Augusta H. Teller, and Edward Teller (1953). "Equation of State Calculations by Fast Computing Machines". *The Journal of Chemical Physics* 21.6, p. 1087.

M. Minsky (1961). "Microscopy apparatus".

W. E. Moerner and L. Kador (1989). "Optical detection and spectroscopy of single molecules in a solid". *Physical Review Letters* 62.21, pp. 2535–2538.

Barbara K. Müller, Evgeny Zaychikov, Christoph Bräuchle, and Don C. Lamb (2005). "Pulsed interleaved excitation." *Biophysical Journal* 89.5, pp. 3508–3522.

Adam Muschielok, Joanna Andrecka, Anass Jawhari, Florian Brückner, Patrick Cramer, and Jens Michaelis (2008). "A nano-positioning system for macromolecular structural analysis". *Nature Methods* 5.11, pp. 965–971.

Nikolaus Naredi-Rainer, Jens Prescher, Achim Hartschuh, and Don C. Lamb (2013). "Confocal Microscopy". *Fluorescence Microscopy: From Principles to Biological Applications*. Ed. by Ulrich Kubitscheck. Weinheim, Germany: Wiley-VCH Verlag GmbH & Co. KGaA, pp. 175–214.

J. A. Nelder and R. Mead (1965). "A Simplex Method for Function Minimization". *The Computer Journal* 7.4, pp. 308–313.

Daniel Nettels, Irina V. Gopich, Armin Hoffmann, and Benjamin Schuler (2007). "Ultrafast dynamics of protein collapse from single-molecule photon statistics." *Proceedings of the National Academy of Sciences* 104.8, pp. 2655–2660.

H. Neuweiler and M. Sauer (2004). "Using photoinduced charge transfer reactions to study conformational dynamics of biopolymers at the single-molecule level." *Current Pharmaceutical Biotechnology* 5.3, pp. 285–298.

Francesca Nicoli, Anders Barth, Wooli Bae, Fabian Neukirchinger, Alvaro H. Crevenna, Don C. Lamb, and Tim Liedl (2017). "Directional Photonic Wire Mediated by Homo-Förster Resonance Energy Transfer on a DNA Origami Platform". *ACS Nano* 11.11, pp. 11264–11272.

Eyal Nir, Xavier Michalet, Kambiz M. Hamadani, Ted A. Laurence, Daniel Neuhauser, Yevgeniy Kovchegov, and Shimon Weiss (2006). "Shot-noise limited single-molecule FRET histograms: comparison between theory and experiments." *The Journal of Physical Chemistry B* 110.44, pp. 22103–22124.

M. Orrit and J. Bernard (1990). "Single pentacene molecules detected by fluorescence excitation in a p-terphenyl crystal". *Physical Review Letters* 65.21, pp. 2716–2719.

Angel Orte, Richard Clarke, and David Klenerman (2010). "Single-molecule two-colour coincidence detection to probe biomolecular associations". *Biochemical Society Transactions* 38.4, p. 914.

Kaupo Palo, Ülo Mets, Vello Loorits, and Peet Kask (2006). "Calculation of Photon-Count Number Distributions via Master Equations". *Biophysical Journal* 90.6, pp. 2179–2191.

Karl Pearson (1900). "X. On the criterion that a given system of deviations from the probable in the case of a correlated system of variables is such that it can be reasonably supposed to have arisen from random sampling". *The London, Edinburgh, and Dublin Philosophical Magazine and Journal of Science* 50.302, pp. 157–175.

Francis Perrin (1926). "Polarisation de la lumière de fluorescence. Vie moyenne des molécules dans l'etat excité". *Journal de Physique et le Radium* 7.12, pp. 390–401.

Christoph M. Pieper and Jörg Enderlein (2011). "Fluorescence correlation spectroscopy as a tool for measuring the rotational diffusion of macromolecules". *Chemical Physics Letters* 516.1-3, pp. 1–11.

C. Ratzke, B. Hellenkamp, and T. Hugel (2014). "Four-colour FRET reveals directionality in the Hsp90 multicomponent machinery." *Nature Communications* 5, p. 4192.

Dieter Rehm and Albert Weller (1970). "Kinetics of Fluorescence Quenching by Electron and H-Atom Transfer". *Israel Journal of Chemistry* 8.2, pp. 259–271.

Paul W. K. Rothemund (2006). “Folding DNA to create nanoscale shapes and patterns”. *Nature* 440.7082, pp. 297–302.

P. J. Rothwell, S. Berger, O. Kensch, S. Felekyan, M. Antonik, B. M. Wöhrl, T. Restle, R. S. Goody, and C. A. M. Seidel (2003). “Multiparameter single-molecule fluorescence spectroscopy reveals heterogeneity of HIV-1 reverse transcriptase:primer/template complexes.” *Proceedings of the National Academy of Sciences* 100.4, pp. 1655–1660.

Yusdi Santoso, Joseph P. Torella, and Achillefs N. Kapanidis (2010). “Characterizing Single-Molecule FRET Dynamics with Probability Distribution Analysis”. *ChemPhysChem* 11.10, pp. 2209–2219.

Markus Sauer and Hannes Neuweiler (2014). “PET-FCS: Probing Rapid Structural Fluctuations of Proteins and Nucleic Acids by Single-Molecule Fluorescence Quenching”. *Fluorescence Spectroscopy and Microscopy*. Ed. by Yves Engelborghs and Antonie J.W.G. Visser. Vol. 1076. Totowa, NJ: Humana Press, pp. 597–615.

J. Schaffer, A. Volkmer, C. Eggeling, V. Subramaniam, G. Striker, and C. A. M. Seidel (1999). “Identification of Single Molecules in Aqueous Solution by Time-Resolved Fluorescence Anisotropy”. *The Journal of Physical Chemistry A* 103.3, pp. 331–336.

Peter Schlüsche, Gertraud Stelzer, Elisa Piaia, Don C. Lamb, and Michael Meisterernst (2007). “NC2 mobilizes TBP on core promoter TATA boxes.” *Nature Structural & Molecular Biology* 14.12, pp. 1196–1201.

Waldemar Schrimpf, Anders Barth, Jelle Hendrix, and Don C. Lamb (2018a). “PAM: A Framework for Integrated Analysis of Imaging, Single-Molecule, and Ensemble Fluorescence Data”. *Biophysical Journal* 114, pp. 1518–1528.

Waldemar Schrimpf, Veerle Lemmens, Nick Smisdom, Marcel Ameloot, Don C. Lamb, and Jelle Hendrix (2018b). “Crosstalk-free multicolor RICS using spectral weighting.” *Methods* 140-141, pp. 97–111.

Benjamin Schuler (2007). “Application of single molecule Förster resonance energy transfer to protein folding.” *Methods in Molecular Biology* 350, pp. 115–138.

Gideon Schwarz (1978). “Estimating the Dimension of a Model”. *The Annals of Statistics* 6.2, pp. 461–464.

P. Schwille, F. J. Meyer-Almes, and R. Rigler (1997). “Dual-color fluorescence cross-correlation spectroscopy for multicomponent diffusional analysis in solution.” *Biophysical Journal* 72.4, pp. 1878–1886.

Shruti Sharma, Kausik Chakraborty, Barbara K. Müller, Nagore Astola, Yun-Chi Tang, Don C. Lamb, Manajit Hayer-Hartl, and F. Ulrich Hartl (2008). “Monitoring protein conformation along the pathway of chaperonin-assisted folding.” *Cell* 133.1, pp. 142–153.

R. Sibson (1973). “SLINK: An optimally efficient algorithm for the single-link cluster method”. *The Computer Journal* 16.1, pp. 30–34.

Alain Sillen and Yves Engelborghs (1998). “The Correct Use of “Average” Fluorescence Parameters”. *Photochemistry and Photobiology* 67.5, pp. 475–486.

Simon Sindbert, Stanislav Kalinin, Hien Nguyen, Andrea Kienzler, Lilia Clima, Willi Bannwarth, Bettina Appel, Sabine Müller, and Claus A. M. Seidel (2011). “Accurate distance determination of nucleic acids via Förster resonance energy transfer: implications of dye linker length and rigidity.” *Journal of the American Chemical Society* 133.8, pp. 2463–2480.

Evangelos Sisamakis, Alessandro Valeri, Stanislav Kalinin, Paul J. Rothwell, and Claus A. M. Seidel (2010). *18-Accurate Single-Molecule FRET Studies Using Multiparameter Fluorescence Detection*. Vol. 475. Single Molecule Tools, Part B:Super-Resolution, Particle Tracking, Multiparameter, and Force Based Methods. Elsevier Inc.

John Skilling (2004). “Nested Sampling”. *AIP Conference Proceedings* 735.1, pp. 395–405.

Allison H. Squires and W. E. Moerner (2017). “Direct single-molecule measurements of phycocyanobilin photophysics in monomeric C-phycocyanin.” *Proceedings of the National Academy of Sciences*, p. 201705435.

Stefan W. Stahl, Michael A. Nash, Daniel B. Fried, Michal Slutzki, Yoav Barak, Edward A. Bayer, and Hermann E. Gaub (2012). “Single-molecule dissection of the high-affinity cohesin-dockerin complex.” *Proceedings of the National Academy of Sciences* 109.50, pp. 20431–20436.

Ingo H. Stein, Christian Steinhauer, and Philip Tinnefeld (2011). “Single-molecule four-color FRET visualizes energy-transfer paths on DNA origami.” *Journal of the American Chemical Society* 133.12, pp. 4193–4195.

Florian Steiner, John M. Lupton, and Jan Vogelsang (2017). “Role of Triplet-State Shelving in Organic Photovoltaics: Single-Chain Aggregates of Poly(3-hexylthiophene) versus Mesoscopic Multichain Aggregates”. *Journal of the American Chemical Society* 139.29, pp. 9787–9790.

Elana M. S. Stennett, Monika A. Ciuba, Su Lin, and Marcia Levitus (2015). “Demystifying PIFE: The Photophysics Behind the Protein-Induced Fluorescence Enhancement Phenomenon in Cy3.” *The Journal of Physical Chemistry Letters* 6.10, pp. 1819–1823.

James D. Stephenson, Haitao Li, Julia C. Kenyon, Martyn Symmons, Dave Klenerman, and Andrew M.L. Lever (2013). “Three-Dimensional RNA Structure of the Major HIV-1 Packaging Signal Region”. *Structure* 21.6, pp. 951–962.

Otto Stern and Max Volmer (1919). “Über die Abklingungszeit der Fluoreszenz”. *Phys. Z.* 20, pp. 183–188.

George Gabriel Stokes (1852). "XXX. On the change of refrangibility of light". *Philosophical Transactions of the Royal Society of London* 142, pp. 463–562.

L. Stryer and R. P. Haugland (1967). "Energy transfer: a spectroscopic ruler." *Proceedings of the National Academy of Sciences* 58.2, pp. 719–726.

Petr Šulc, Flavio Romano, Thomas E. Ouldridge, Lorenzo Rovigatti, Jonathan P. K. Doye, and Ard A. Louis (2012). "Sequence-dependent thermodynamics of a coarse-grained DNA model". *The Journal of Chemical Physics* 137.13, p. 135101.

William C. Swope, Hans C. Andersen, Peter H. Berens, and Kent R. Wilson (1982). "A computer simulation method for the calculation of equilibrium constants for the formation of physical clusters of molecules: Application to small water clusters". *The Journal of Chemical Physics* 76.1, pp. 637–649.

Mariusz Szabelski, Douglas Ilijev, Pabak Sarkar, Rafal Luchowski, Zygmunt Gryczynski, Peter Kapusta, Rainer Erdmann, and Ignacy Gryczynski (2009). "Collisional Quenching of Erythrosine B as a Potential Reference Dye for Impulse Response Function Evaluation". *Applied Spectroscopy* 63.3, pp. 363–368.

Toma E. Tomov, Roman Tsukanov, Rula Masoud, Miran Liber, Noa Plavner, and Eyal Nir (2012). "Disentangling Subpopulations in Single-Molecule FRET and ALEX Experiments with Photon Distribution Analysis". *Biophysical Journal* 102.5, pp. 1163–1173.

Joseph P. Torella, Seamus J. Holden, Yusdi Santoso, Johannes Hohlbein, and Achillefs N. Kapanidis (2011). "Identifying Molecular Dynamics in Single-Molecule FRET Experiments with Burst Variance Analysis". *Biophysical Journal* 100.6, pp. 1568–1577.

Tedman Torres and Marcia Levitus (2007). "Measuring Conformational Dynamics: A New FCS-FRET Approach". *The Journal of Physical Chemistry B* 111.25, pp. 7392–7400.

Niels Vandenberk, Anders Barth, Doortje Borrenberghs, Johan Hofkens, and Jelle Hendrix (2018). "Evaluation of Blue and Far-Red Dye Pairs in Single-Molecule FRET Experiments." *The Journal of Physical Chemistry B*.

Regula Walser, Alan E. Mark, and Wilfred F. van Gunsteren (2000). "On the Temperature and Pressure Dependence of a Range of Properties of a Type of Water Model Commonly Used in High-Temperature Protein Unfolding Simulations". *Biophysical Journal* 78.6, pp. 2752–2760.

Jerker Widengren, Volodymyr Kudryavtsev, Matthew Antonik, Sylvia Berger, Margarita Gerken, and Claus A. M. Seidel (2006). "Single-Molecule Detection and Identification of Multiple Species by Multiparameter Fluorescence Detection". *Analytical Chemistry* 78.6, pp. 2039–2050.

Jerker Widengren and Rudolf Rigler (1996). "Mechanisms of photobleaching investigated by fluorescence correlation spectroscopy". *Bioimaging*.

Jerker Widengren, Rudolf Rigler, and Ülo Mets (1994). "Triplet-state monitoring by fluorescence correlation spectroscopy". *Journal of Fluorescence* 4.3, pp. 255–258.

Jerker Widengren and Petra Schwille (2000). "Characterization of Photoinduced Isomerization and Back-Isomerization of the Cyanine Dye Cy5 by Fluorescence Correlation Spectroscopy". *The Journal of Physical Chemistry A* 104.27, pp. 6416–6428.

S. Wörmke, S. Mackowski, T.H.P. Brotosudarmo, C. Jung, A. Zumbusch, M. Ehrl, H. Scheer, E. Hofmann, R.G. Hiller, and C. Bräuchle (2007). "Monitoring fluorescence of individual chromophores in peridinin–chlorophyll–protein complex using single molecule spectroscopy". *Biochimica et Biophysica Acta (BBA) - Bioenergetics* 1767.7, pp. 956–964.

Philipp Wortmann, Markus Götz, and Thorsten Hugel (2017). "Cooperative Nucleotide Binding in Hsp90 and Its Regulation by Aha1." *Biophysical Journal* 113.8, pp. 1711–1718.

Seok W. Yim, Taiho Kim, Ted A. Laurence, Steve Partono, Dongsik Kim, Younggyu Kim, Shimon Weiss, and Armin Reitmair (2012). "Four-color alternating-laser excitation single-molecule fluorescence spectroscopy for next-generation biodetection assays." *Clinical Chemistry* 58.4, pp. 707–716.

C. Zander, M. Sauer, K. H. Drexhage, D. S. Ko, A. Schulz, J. Wolfrum, L. Brand, C. Eggeling, and C. A. M. Seidel (1996). "Detection and characterization of single molecules in aqueous solution". *Applied Physics B: Lasers and Optics* 63.5, pp. 517–523.

Ming Zhao, Lei Jin, Bo Chen, Yao Ding, Hui Ma, and Dieyan Chen (2003). "Afterpulsing and its correction in fluorescence correlation spectroscopy experiments". *Applied Optics* 42.19, pp. 4031–4036.

Xiaowei Zhuang, Laura E. Bartley, Hazen P. Babcock, Rick Russell, Taekjip Ha, Daniel Herschlag, and Steven Chu (2000). "A Single-Molecule Study of RNA Catalysis and Folding". *Science* 288.5473, p. 2048.

# List of Figures

# List of Abbreviations

| | |
|---|---|
| **2CDE** | two-channel kernel density estimator |
| **3C-PDA** | three-color photon distribution analysis |
| **ACF** | autocorrelation function |
| **ADC** | amplitude-to-digital converter |
| **ADP** | adenosine diphosphate |
| **AIC** | Aikaike information criterion |
| **ALEX** | alternating laser excitation |
| **APBS** | all photon burst search |
| **APD** | avalanche photodiode |
| **ATP** | adenosine triphosphate |
| **BIC** | Bayesian information criterion |
| **BiP** | binding immunoglobulin protein |
| **BVA** | burst variance analysis |
| **CCD** | charge-coupled device |
| **CCF** | cross-correlation function |
| **CFD** | constant fraction discriminator |
| **CohI$_8$-CohI$_9$** | cohesin tandem subunit 8-9 of the scaffoldin protein of the cellulosome |
| **COM** | center of mass |
| **Cy3** | cyanine 3 |
| **DCBS** | dual channel burst search |
| **DNA** | deoxyribonucleic acid |
| **FCS** | fluorescence correlation spectroscopy |
| **FLCS** | fluorescence lifetime correlation spectroscopy |
| **fFCS** | filtered fluorescence correlation spectroscopy |
| **FRET** | Förster resonance energy transfer |
| **FSCS** | fluorescence spectral correlation spectroscopy |
| **FWHM** | full width at half maximum |
| **GPU** | graphics processing unit |
| **Hsp70** | heat-shock protein 70 |
| **IDP** | intrinsically disordered peptide |
| **IRF** | instrument response function |
| **LUMO** | lowest unoccupied molecular orbital |
| **MATLAB** | *matrix laboratory*, computing environment and programming language developed by MathWorks, Inc. |
| **MBP** | maltose-binding protein |
| **MCMC** | Markov chain Monte Carlo |
| **MD** | molecular dynamics |
| **MFD** | multiparameter fluorescence detection |
| **MH** | Metropolis-Hastings algorithm |
| **MLE** | maximum likelihood estimator |
| **NA** | numerical aperture |
| **NBD** | nucleotide-binding domain |
| **NIR** | near-infrared |
| **NMR** | nuclear magnetic resonance |
| **nsFCS** | nanosecond fluorescence correlation spectroscopy |
| **PALM** | photo-activated localization microscopy |
| **PAM** | PIE analysis with MATLAB |
| **PBS** | polarizing beam splitter |
| **PET** | photoinduced electron transfer |
| **PDA** | photon distribution analysis |

| | |
|---|---|
| **PIE** | pulsed interleaved excitation |
| **PIFE** | protein-induced fluorescence enhancement |
| **PMT** | photomultiplier tubes |
| **PSF** | point spread function |
| **RMSD** | root-mean-square deviation |
| **RMSF** | root-mean-square fluctuation |
| **RNA** | ribonucleic acid |
| **sACF** | species autocorrelation function |
| **SAXS** | small-angle X-ray scattering |
| **SBD** | substrate-binding domain |
| **sCCF** | species cross-correlation function |
| **σNS** | non-structural protein σNS |
| **STED** | stimulated emission depletion microscopy |
| **STORM** | stochastic optical reconstruction microscopy |
| **TAC** | time-to-amplitude converter |
| **TCSPC** | time-correlated single photon counting |
| **TIRFM** | total internal reflection fluorescence microscopy |
| **UV** | ultraviolet |

# *Acknowledgements*

The value of this thesis is not measured by its results alone. It was a long journey to get here, and what a ride it's been! So here's to all the people that guided, helped, encouraged and supported me, that brightened my days, cheered me up and softened the fall when things didn't go the way they were supposed to go.

Don, I'll put you first so I don't forget to mention the person that made all of this possible in the first place. Thank you for taking me in when I was but an inexperienced master's student with an interest in single-molecule fluorescence. (Albeit the first two months of my master's thesis were probably the most stressful time in the lab, what with you having submitted an abstract on three-color single-molecule FRET to the Biophysical Society Meeting 2013 with no data, or even a setup to measure it on.) Thank you for all the ideas which led me into new directions, for always finding money, and your patience (and thoroughness) when it comes to writing manuscripts. I have learned a lot thanks to you and the environment you provide in the lab.

I would also like to thank Prof. Christoph Bräuchle for his support and motivation during my PhD, and for his contagious enthusiasm for science in general. Many thanks as well to the members of my thesis committee, Prof. Achim Hartschuh, Prof. Philip Tinnefeld, Prof. Martin Zacharias and Prof. Ralf Jungmann.

I gratefully acknowledge the support and networking opportunities provided by CeNS, NIM and SFB1032 and SFB1035. I would also like to thank Prof. Tim Liedl, Prof. Martin Zacharias and Prof. Edward Bayer for the exciting and successful collaborations. For the photonic wire, I would like to thank Francesca Nicoli and Wooli Bae from the Liedl group. For the S-peptide project, many thanks go to Manuel Luitz and Rainer Bomblies. Lastly, for the cellulosome project, I would like to thank Yoav Barak, Avital Artan-Forman and Daniel Fried for their hard work and contributions to the success of the project, especially during the revision stage.

Thanks to all the members of AK Lamb that have helped and supported me over the years. Jelle, thank you for all the input, discussion and the projects that we shared. It was a joy working with you, and I took a lot with me from those initial months when we shared an office. Lena, it was a pleasure to work with you on the different projects, and I hope our paths will cross again sometime. Waldi, thank you for all your input and the many discussion we had (and the shared vacation through the vast landscapes of Iceland). Let's hope that *PAM* lives on forever! Alex, thank you for being a friend, colleague and mentor at the same time, and for always having some Cheddar, ales and wine around when the time calls for it. Alvaro, thank you for your support and ideas, and for jump-starting several of my projects. Vanessa, now that I am leaving you may have my lamp. Handle it with care. Ganesh, thank you for all the thorough discussion we had, for your biochemical perspectives, and just for being you. It was a pleasure working with you. Niko, I very much appreciate your help during my Master's thesis.

Thanks to the whole of AK Lamb and AK Bräuchle for all the fun times we had at all the various dinners, movie nights and other outings, and for all the interesting discussion during coffee breaks. Specifically, thanks to the coffee crew for taking coffee making to the next level and making it a proper science. Moritz, thank you for all the life advice and perspectives, some useful and some maybe not so much.

Last but not least, I would like to thank my parents for their support all these years. Ohne euch wäre all dies nicht möglich gewesen. Finally, I want to thank my much better half Kira for bringing out the best in me and for keeping me company throughout this journey and the many adventures to come.

# Curriculum Vitae

## Education

| | |
|---|---|
| 10/2013 - 12/2018 | PhD in Physical Chemistry<br>Ludwig-Maximilians-Universität München, Germany<br>Supervisor: Prof. Don C. Lamb |
| 10/2010 - 09/2013 | Studies in Chemistry, Master of Science<br>Ludwig-Maximilians-Universität München, Germany<br>Final grade: 1.13 |
| 01/2013 - 09/2013 | Master's thesis<br>Subject: "Three-color Multiparameter Fluorescence Detection with Pulsed Interleaved Excitation"<br>Supervisor: Prof. Don C. Lamb |
| 10/2007 - 09/2010 | Studies in Chemistry, Bachelor of Science<br>Ludwig-Maximilians-Universität München, Germany<br>Final grade: 1.23 |
| 05/2010 - 09/2010 | Bachelor's thesis<br>Subject: "Determination of anisotropies of fluorescently labeled RNA polymerase II elongation complexes"<br>Supervisor: Prof. Jens Michaelis |
| 09/1998 - 06/2007 | Secondary school, Thomas-Mann-Gymnasium Lübeck, Germany |

## Professional Experience

| | |
|---|---|
| 10/2013 - 12/2018 | PhD candidate in Prof. Don C. Lamb's lab<br>Ludwig-Maximilians-Universität München, Germany |
| 03/2012 - 06/2012 | Research internship at Prof. Bert Weckhuysen's lab<br>University of Utrecht, Netherlands<br>Subject: "Study of Temperature Stability of Supported Ag Nanoparticle Catalysts for Propylene Epoxidation by Scanning Probe Microscopy and Nanoplasmonic Spectroscopy" |
| 09/2011 - 02/2011 | Research internship at Prof. Christian Hübner's lab<br>University of Lübeck, Germany<br>Subject: "Photon statistics of FRET coupled dyes linked to a polyproline peptide" |

## Honors and Prizes

| | |
|---|---|
| 12/2018 | Price for the Doctoral thesis of the Römer-Stiftung |
| 12/2013 | Price for the Master's thesis of the Römer-Stiftung |
| 06/2009 - 09/2013 | Scholarship of the Studienstiftung des deutschen Volkes |

## Appendix B

# Appended Papers

## B.1 Paper 1: Quantitative Single-Molecule Three-Color Förster Resonance Energy Transfer by Photon Distribution Analysis

# Quantitative single-molecule three-color Förster resonance energy transfer by photon distribution analysis

Anders Barth, Lena Voith von Voithenberg and Don C. Lamb*

Department of Chemistry, Center for Integrated Protein Science Munich, Nanosystems Initiative
Munich and Center for Nanoscience, Ludwig-Maximilians-Universität München, Butenandtstr. 5-13,
81377 Munich, Germany

* Corresponding author: d.lamb@lmu.de

## Abstract

Single-molecule Förster resonance energy transfer (FRET) is a powerful tool to study conformational dynamics of biomolecules. Using solution-based single-pair FRET by burst analysis, conformational heterogeneities and fluctuations of fluorescently labeled proteins or nucleic acids can be studied by monitoring a single distance at a time. Three-color FRET is sensitive to three distances simultaneously and can thus elucidate complex coordinated motions within single molecules. While three-color FRET has been applied on the single-molecule level before, a detailed quantitative description of the obtained FRET efficiency distributions is still missing. Direct interpretation of three-color FRET data is additionally complicated by an increased shot noise contribution when converting photon counts to FRET efficiencies. However, to address the question of coordinated motion, it is of special interest to extract information about the underlying distance heterogeneity, which is not easily extracted from the FRET efficiency histograms directly. Here, we present three-color photon distribution analysis (3C-PDA), a method to extract distributions of inter-dye distances from three-color FRET measurements. We present a model for diffusion-based three-color FRET experiments and apply Bayesian inference to extract information about the physically relevant distance heterogeneity in the sample. The approach is verified using simulated data sets and experimentally applied to triple-labeled DNA duplexes. Finally, 3C-FRET experiments on the Hsp70 chaperone BiP reveal conformational coordinated changes between individual domains. The possibility to address the co-occurrence of intramolecular distances makes 3C-PDA a powerful method to study the coordination of domain motions within biomolecules during conformational changes.

## Significance:

In solution-based single-molecule Förster resonance energy transfer (FRET) experiments, biomolecules are studied as they freely diffuse through the observation volume of a confocal microscope, resulting in bursts of fluorescence from single molecules. Using three fluorescent labels, one can concurrently measure three distances in a single molecule but the experimentally limited number of photons is not sufficient for a straight-forward analysis. Here, we present a probabilistic framework, called three-color photon distribution analysis (3C-PDA), to extract quantitative information from single-molecule three-color FRET experiments. By extracting distributions of inter-dye distances from the data, the method provides a three-dimensional description of the conformational space of biomolecules, enabling the detection of coordinated movements during conformational changes.

## Introduction:

Förster resonance energy transfer (FRET) is a powerful tool to measure intra- or intermolecular distances in the range of 2-10 nm on the single-molecule level. It has been widely applied on the single-molecule level to study the conformational landscape of proteins and nucleic acids using surface-immobilization (1-4) or in solution (5-9). In the latter case, molecules are studied at picomolar concentrations as they diffuse through the observation volume of a confocal microscope, resulting in bursts of fluorescence signal from single molecules (Figure 1A-B) (10-13). The photons from a single molecule burst are analyzed and the molecule-wise distribution of FRET efficiencies provides information regarding the conformational states and dynamics of the biomolecules. Extensions of this method have included lifetime and polarization information (9) as well as direct probing of the acceptor fluorophore using alternating excitation schemes (14, 15) to increase sorting capabilities and informational content of the measurements. Accurate FRET measurements require carefully determined correction factors for spectral crosstalk, direct excitation of the acceptor fluorophore, and differing photon detection efficiencies and quantum yields (16). Using the methods of alternating laser excitation (ALEX) or pulsed interleaved excitation (PIE), these correction factors can be determined from the experiment directly (14, 17). Diffusion-based FRET measurements avoid possible artifacts related to surface immobilization. This advantage comes at the cost of a limited detection time of a few milliseconds per molecule, restricted by the diffusion time through the observation volume as well as fewer photons and thus increased shot noise. The shot-noise contribution can be accounted for in the analysis. Thus, it is possible to elucidate the contributions of physically relevant broadening of the FRET efficiency histogram (18, 19) to study static conformational heterogeneity as well as dynamical interconversion between distinct states (20, 21). This method, named the photon distribution analysis (PDA), has been widely applied in the field (22-29).

Two-color FRET is limited to the observation of a single distance at a time. Multiple distance readouts are thus only available in separate experiments. Three-color FRET enables the monitoring of three distances in one experiment (30-34). While the same distance distributions are obtainable from three two-color FRET experiments, information about the correlation of distance changes and thus the coordination of molecular movements is only obtained using three-color FRET. This is possible since three-color FRET experiments contain information about the co-occurrence of distances for the individual FRET sensors. During the last decade, a number of single-molecule multicolor FRET studies have been performed both in solution and using surface immobilization (35-41). Proof-of-principle experiments showing the possibility to extract accurate distances from solution-based experiments, however, have been limited to the extraction of average values (35, 36), while a complete description of the shape of the FRET efficiency histogram is still missing. Three-color FRET using surface immobilization has been applied to study coordinated motion in different nucleic acid systems (36-39) and the oligomerization state of proteins (42). With the development of new strategies for protein labeling (43-46), it is becoming more feasible to site-specifically label proteins with three or more fluorophores, opening up the possibility to study coordinated movements within single proteins during their conformational cycle.

However, the extension of two-color FRET to three-color FRET is not as straightforward as it appears and there are many challenges that limit the quantitative analysis of three-color FRET data. First of all, the signal fractions in a three-color FRET experiment are not easily interpreted in terms of distances, as is the case in a two-color FRET experiment. Moreover, any heterogeneity observed for these quantities is difficult to relate to physically relevant distance heterogeneity of the studied system. To complicate the issue, shot noise is a larger problem in three-color FRET measurements because signal after excitation of the donor dye is distributed among three channels, lowering the achievable signal-to-noise ratio. Fluorophores, detectors and optics have been optimized for the visual region of the spectra, which minimizes the obtainable spectral separation of the three channels used for three-color FRET. Hence, larger corrections need to be applied to account for spectral crosstalk and direct excitation of the fluorophores. Thus, extracting accurate distances from three-color FRET experiments remains challenging. To this end, a detailed statistical analysis of the experiment with respect to the underlying three-dimensional distance distribution is needed, which opens up the possibility to study coordinated movements within single biomolecules by analyzing correlations between measured distances.

Here, we present three-color photon distribution analysis (3C-PDA), an extension of the framework of photon distribution analysis to three-color FRET systems. The method is based on a likelihood function for the three-color FRET process in diffusion-based experiments. We apply model-based Bayesian inference using the Metropolis-Hastings algorithm (47, 48) to infer the model parameters. The method is tested using synthetic data and applied experimentally to triple-labeled double-stranded DNA as a model system and to investigate the coordinated motions with the Hsp70 chaperone BiP.

**Theory:**

*Three-color FRET*

FRET is the non-radiative energy transfer from a donor fluorophore $D$ to an acceptor fluorophore $A$ mediated by dipole-dipole interactions with a strong dependence on distance (49):

$$E = \frac{1}{1+\left(\frac{R}{R_0}\right)^6} \tag{1}$$

where $R$ is the interdye distance and $R_0$ is the Förster distance which depends on the quantum yield of the donor fluorophore $\Phi_D$, the spectral overlap integral $J$, the orientation of the donor and acceptor fluorophore through the factor $\kappa^2$ and the refractive index of the surrounding medium $n$:

$$R_0 \propto \sqrt[6]{\Phi_D J \kappa^2 n^{-4}} \tag{2}$$

In the experiment, the amount of energy transfer can be measured by separating the fluorescence signal according to the emission spectra of the donor and acceptor fluorophore. A qualitative measure of the FRET efficiency can be obtained from the raw signal fractions in the donor and acceptor channels after donor excitation ($I_D^{D_{\mathrm{ex}}}$, $I_A^{D_{\mathrm{ex}}}$), which we call the proximity ratio $PR$:

$$PR = \frac{I_A^{D_{\mathrm{ex}}}}{I_D^{D_{\mathrm{ex}}} + I_A^{D_{\mathrm{ex}}}} \tag{3}$$

When alternating laser excitation is employed using PIE or ALEX (17, 50), accurate intensity-based FRET efficiencies can be determined when appropriate corrections are applied to the photon counts (17):

$$E = \frac{I_A^{D_{\mathrm{ex}}} - \alpha I_D^{D_{\mathrm{ex}}} - \delta I_A^{A_{\mathrm{ex}}}}{\gamma I_D^{D_{\mathrm{ex}}} + I_A^{D_{\mathrm{ex}}} - \alpha I_D^{D_{\mathrm{ex}}} - \delta I_A^{A_{\mathrm{ex}}}} \tag{4}$$

where $\alpha$ is the correction factor for spectral crosstalk of the donor in the acceptor channel, $\delta$ is the correction factor for direct excitation of the acceptor at the wavelength of the donor, $\gamma$ is the correction factor for different quantum yields and detection efficiencies of the fluorophores, and $I_A^{A_{\mathrm{ex}}}$ is the signal in the acceptor channel after acceptor excitation.

In three-color FRET, energy can be transferred from a donor fluorophore $D$ to two spectrally different acceptor fluorophores $A_1$ and $A_2$ (see Figure 1C-D). One of the acceptors, which we define as $A_1$, may also transfer energy to the lower energy acceptor $A_2$. Thus, the signal observed for $A_2$ contains contributions from two possible pathways, either from direct energy transfer from $D$, or from two-step energy transfer mediated by $A_1$. The signal fractions after excitation of the donor dye are defined by:

$$PR_{DA_1} = \frac{I_{A_1}^{D_{\mathrm{ex}}}}{I_D^{D_{\mathrm{ex}}} + I_{A_1}^{D_{\mathrm{ex}}} + I_{A_2}^{D_{\mathrm{ex}}}}; \quad PR_{DA_2} = \frac{I_{A_2}^{D_{\mathrm{ex}}}}{I_D^{D_{\mathrm{ex}}} + I_{A_1}^{D_{\mathrm{ex}}} + I_{A_2}^{D_{\mathrm{ex}}}} \tag{5}$$

It should be noted that, contrary to two-color FRET, these quantities are not directly related to distances.

The FRET efficiency is defined as the fraction of transitions from the excited donor dye to the acceptor dye, given by:

$$E = \frac{k_T}{k_F + k_T + k_{\mathrm{nr}}} \tag{6}$$

where $k_T$ is the rate of energy transfer, $k_F$ is the intrinsic radiative decay rate of the donor, and $k_{\mathrm{nr}}$ is the sum over all non-radiative relaxation pathways of the donor. In three-color FRET systems, energy transfer may occur from the donor dye to either acceptor. The efficiency of energy transfer to one acceptor dye is thus modified by the quenching effect of the second acceptor dye, effectively reducing the Förster radius of the dye pair. In analogy to equation 6, one can define apparent FRET efficiencies from the donor dye to either acceptor $E'_{DA_i}$, which describe the transition probabilities in the three-color FRET system as shown in Figure 1C.

$$E'_{DA_i} = \frac{k_T^{D\to A_i}}{k_F^D + k_T^{D\to A_i} + k_T^{D\to A_j} + k_{\mathrm{nr}}^D} \tag{7}$$

The total FRET efficiency from the donor dye to both acceptor dyes is then given by:

$$E_{D\to A_1A_2} = E'_{DA_1} + E'_{DA_2} = 1 - \frac{\tau_{D(A_1A_2)}}{\tau_{D(0)}} \tag{8}$$

where $\tau_{D(0)}$ is donor lifetime in the absence of either acceptor, and $\tau_{D(A_1A_2)}$ is the donor lifetime in the presence of both acceptors.

The conversion of apparent FRET efficiencies to physical distances is more involved than for two-color FRET due to the additional quenching of the donor by the second acceptor. To define the equivalent of a single-pair FRET efficiency, we ignore the presence of the other acceptor in the rate equation:

$$E_{DA_i} = \frac{k_T^{D\to A_i}}{k_F^D + k_T^{D\to A_i} + k_{\mathrm{nr}}^D} \tag{9}$$

From the definition of the single-pair FRET efficiencies, we calculate the apparent FRET efficiencies for three-color FRET as defined in equation 7:

$$E'_{DA_1} = \frac{E_{DA_1}\left(1 - E_{DA_2}\right)}{1 - E_{DA_1}E_{DA_2}} \tag{10}$$

$$E'_{DA_2} = \frac{E_{DA_2}\left(1 - E_{DA_1}\right)}{1 - E_{DA_1}E_{DA_2}} \tag{11}$$

Thus, when the distances are known, the transition probabilities in the three-color FRET system can be calculated by means of equations 1, 10 and 11.

Excitation of the donor dye yields three signal streams and thus two independent intensity ratios, which is insufficient to solve the three-color FRET system for the three inter-dye distances. Thus, to calculate distance-related three-color FRET efficiencies, the FRET efficiency between the two acceptor dyes $E_{A_1A_2}$ needs to be determined independently. In the experiment, this information is obtained by alternating the excitation of the blue and green dye (Figure 1C-D and Supplementary Figures S1-2). The FRET efficiencies in the three-color FRET system are then calculated using:

$$E_{A_1A_2} = \frac{I_{A_2}^{A_1,\mathrm{ex}}}{I_{A_1}^{A_1,\mathrm{ex}} + I_{A_2}^{A_1,\mathrm{ex}}} \tag{12}$$

$$E_{DA_1} = \frac{I_{A_1}^{D\mathrm{ex}}}{I_D^{D\mathrm{ex}}\left(1 - E_{A_1A_2}\right) + I_{A_1}^{D\mathrm{ex}}} \tag{13}$$

$$E_{DA_2} = \frac{I_{A_2}^{D\mathrm{ex}} - E_{A_1A_2}\left(I_{A_1}^{D\mathrm{ex}} + I_{A_2}^{D\mathrm{ex}}\right)}{I_D^{D\mathrm{ex}} + I_{A_2}^{D\mathrm{ex}} - E_{A_1A_2}\left(I_D^{D\mathrm{ex}} + I_{A_1}^{D\mathrm{ex}} + I_{A_2}^{D\mathrm{ex}}\right)} \tag{14}$$

A detailed derivation of equations 10-14 is given in Supplementary Note 1 and may be found in ref.

(33). Extensions of equations 13 and 14 with correction factors for real experimental conditions are given in Supplementary Note 2.

In our experiments, a blue, green and red dye are used. Hence, we change the notation from the general case of one donor dye with two acceptor dyes ($D$, $A_1$, $A_2$) to the specific notation indicating the dye colors ($B$, $G$, $R$). The emission probabilities $\varepsilon$ in the three-color FRET system can be calculated according to:

$$\varepsilon_{BB} = 1 - E'_{BG} - E'_{BR} \tag{15}$$

$$\varepsilon_{BG} = E'_{BG}(1 - E_{GR}) \tag{16}$$

$$\varepsilon_{BR} = E'_{BG}E_{GR} + E'_{BR} \tag{17}$$

where $\varepsilon_{ij}$ describes the probability to detect a photon in channel $j$ after excitation of dye $i$.

These expressions hold true only for an ideal system. As also is the case for two-color FRET, a number of correction factors have to be considered. Additional signal in the FRET channels occurs due to spectral crosstalk of the shorter wavelength dyes into the detection channels of the longer wavelength dyes and direct excitation of dyes by shorter wavelength lasers. Additionally, the different detection efficiencies and quantum yields of the dyes need to be considered. Modified emission probabilities in the non-ideal case are calculated as described in Supplementary Note 3 and 4.

*A likelihood expression for three-color FRET*

To extract detailed information about the system in terms of distance heterogeneity, it is necessary to sufficiently sample the FRET efficiency histogram. For three-color FRET, the histogram spans three independent dimensions, requiring the cube of the number of data points as compared to two-color FRET (see Figure S4). In practice, this amount of sampling is usually not accessible. When using the reduced chi-squared ($\chi^2_{\text{red}}$) as a determinate for the goodness-of-fit, large counting errors can result in misleadingly small values of $\chi^2_{\text{red}}$ and lead to an over-interpretation of insufficient or bad quality data (see Supplementary Note 5). In such cases, it is advisable to use a maximum likelihood estimator (MLE) to subject the analysis to the likelihood that the observed data was generated by a given model. The MLE approach generally performs better at low statistics and does not require binning of the data (51).

In a three-color FRET experiment, the registered data is a time series of photons in the different detection channels, which are processed into a time-binned set of photon counts $\{I\}_i = \{I_{BB}, I_{BG}, I_{BR}, I_{GG}, I_{GR}\}_i$ with a typical time interval of 1 millisecond. The total likelihood $\mathcal{L}$ is then the product over the probabilities for all observations that yield the given combination of photon counts $\{I\}_i$ for a given model $M$:

$$\mathcal{L} = \prod_{\text{all bins } i} P(\{I\}_i | M) \tag{18}$$

Since excitation of the blue and green dyes is performed alternatingly, both photon emission processes are statistically independent. However, the underlying parameters of the two probability distributions are linked (see equations 15-17). The probability of observing a combination of photon counts after green excitation and after blue excitation is then the product of the individual probabilities:

$$P(I_{BB}, I_{BG}, I_{BR}, I_{GG}, I_{GR}|M) = P(I_{BB}, I_{BG}, I_{BR}|M)P(I_{GG}, I_{GR}|M) \tag{19}$$

The model $M$, in its simplest form, is described by a triple of distances $\boldsymbol{R} = (R_{BG}, R_{BR}, R_{GR})$, which are converted into a set of emission probabilities after blue and green excitation $\boldsymbol{\varepsilon} = (\varepsilon_{BG}, \varepsilon_{BR}, \varepsilon_{GR})$ according to equations 1, 16 and 17. To model the FRET processes, a binomial distribution is applied for two-color FRET after green excitation. Analogously, a trinomial distribution is used to describe the three-color FRET process after blue excitation:

$$P(I_{GR}, I_{GG}|\varepsilon_{GR}) = B(I_{GR}, I_{GG}|\varepsilon_{GR}) = \frac{(I_{GG} + I_{GR})!}{I_{GR}!\, I_{GG}!}\varepsilon_{GR}^{I_{GR}}(1 - \varepsilon_{GR})^{I_{GG}} \tag{20}$$

$$P(I_{BB}, I_{BG}, I_{BR}|\varepsilon_{BG}, \varepsilon_{BR}) = T(I_{BB}, I_{BG}, I_{BR}|\varepsilon_{BG}, \varepsilon_{BR}) = \frac{(I_{BB} + I_{BG} + I_{BR})!}{I_{BB}!\, I_{BG}!\, I_{BR}!}(1 - \varepsilon_{BG} - \varepsilon_{BR})^{I_{BB}}\varepsilon_{BG}^{I_{BG}}\varepsilon_{BR}^{I_{BR}} \tag{21}$$

Experimental correction factors are accounted for in the calculation of emission probabilities from distances as described in Supplementary Note 3. Constant background signal in the different detection channels, originating from scattered laser light or detector dark counts, can have a substantial influence on the determined FRET efficiencies, especially in the case of high or low FRET efficiencies where the fluorescence signal in the donor or acceptor channel is low. Since the data is processed into time windows of equal length, background count distributions are assumed to be Poissonian with a mean value of $\lambda$:

$$P(b|\lambda) = \frac{\lambda^b}{b!}e^{-\lambda} \tag{22}$$

Background contributions are included into the model by summing over all combinations of photon and background counts, whereby the fluorescence signal used to evaluate the FRET processes is reduced by the respective number of background counts.

$$P(\{I_{GG}, I_{GR}\}|\varepsilon_{GR}) = \sum_{b_{GG}=0}^{I_{GG}}\sum_{b_{GR}=0}^{I_{GR}} P(b_{GG}|\lambda_{GG})P(b_{GR}|\lambda_{GR})B(I_{GR} - b_{GR}, I_{GG} - b_{GG}|\varepsilon_{GR}) \tag{23}$$

$$\begin{aligned} P(\{I_{BB}, I_{BG}, I_{BR}\}|\varepsilon_{BG}, \varepsilon_{BR}) = \sum_{b_{BB}=0}^{I_{BB}}\sum_{b_{BG}=0}^{I_{BG}}\sum_{b_{BR}=0}^{I_{BR}} P(b_{BB}|\lambda_{BB})\, P(b_{BG}|\lambda_{BG})P(b_{BR}|\lambda_{BR}) * \dots \\ T(I_{BB} - b_{BB}, I_{BG} - b_{BG}, I_{BR} - b_{BR}|\varepsilon_{BG}, \varepsilon_{BR}) \end{aligned} \tag{24}$$

The observed FRET efficiency or proximity ratio histograms usually show broadening beyond the shot noise limit. It has been shown that photophysical artifacts of the acceptor dye can cause additional broadening, which can be described by a Gaussian distribution of distances instead of a single distance with widths of approximately 4-8% of the center distance (18, 52). Broadening beyond this width is typically attributed to conformational heterogeneity of the sample, e.g. due to the existence of conformational substates. To describe additional broadening, a trivariate normal distribution is used to describe a distribution of distances.

$$P(\boldsymbol{R}) = (2\pi)^{-\frac{3}{2}}|\Sigma|^{-\frac{1}{2}}\exp\left(-\frac{1}{2}(\boldsymbol{R}-\overline{\boldsymbol{R}})^T\Sigma^{-1}(\boldsymbol{R}-\overline{\boldsymbol{R}})\right) \tag{25}$$

Here, $\boldsymbol{R} = (R_{BG}, R_{BR}, R_{GR})$ is the column vector of distances, $\overline{\boldsymbol{R}}$ is the column vector of center distances and $\Sigma$ is the covariance matrix given by:

$$\Sigma_{ij} = \mathrm{COV}(R_i, R_j) = \mathrm{E}\left[(R_i - \overline{R}_i)(R_j - \overline{R}_j)\right] = \int_{\boldsymbol{R}} P(\boldsymbol{R})(R_i - \overline{R}_i)(R_j - \overline{R}_j)\mathrm{d}\boldsymbol{R} \tag{26}$$

where $\mathrm{E}[X]$ is the expected value of $X$.

By normalizing the covariance with respect to the individual variances $\sigma_i^2$, one obtains the Pearson correlation coefficient that quantifies the observed correlation in the interval [-1,1]:

$$\mathrm{COR}(R_i, R_j) = \frac{\mathrm{COV}(R_i, R_j)}{\sigma_i \sigma_j} \tag{27}$$

This quantity is a more direct measure of the correlation between the observed distances. The implementation of a Gaussian distribution of distances is achieved by constructing a linearly spaced grid of distances with a given number of bins $G$ and width of $2\sigma$, thus covering more than 95 % of the probability density, and numerically integrating over the three dimensions:

$$\begin{aligned} P(\{I\}_i|M) &= \int P(\boldsymbol{R})P(\{I\}_i|\boldsymbol{R})\,\mathrm{d}\boldsymbol{R} \\ &= \sum_{j=1}^{G}\sum_{k=1}^{G}\sum_{l=1}^{G} P(\boldsymbol{R}_{jkl})P(\{I\}_i|\boldsymbol{R}_{jkl}) \end{aligned} \tag{28}$$

Generally, a grid with $G = 5$ sample points at $\overline{R} + [-2\sigma, -1\sigma, 0, 1\sigma, 2\sigma]$ is employed to implement the distance distribution.

Proteins or nucleic acids can exist in multiple conformational states, each of which may show different degrees of static heterogeneity described by a distribution of distances through model $M_j$. When $N_s$ species are present, the individual likelihoods are summed up and weighted by the normalized contributions $A_j$ of the respective species:

$$P(\{I\}_i|M) = \sum_{j=1}^{N_s} A_j P(\{I\}_i|M_j), \text{ with } \sum A_j = 1 \tag{29}$$

Since the overall likelihood $\mathcal{L}$ is generally very small, it is necessary to work with the logarithm of the likelihood function to avoid underflow problems:

$$\log\mathcal{L} = \sum_{\text{all bins } i} \log[P(\{I\}_i|M)] \tag{30}$$

For comparison of the model to the experimental photon count distribution, we use a Monte Carlo approach that simulates the photon emission process to generate expected photon count distributions for the extracted model parameters (for details, see Supplementary Note 6) (19). The Monte Carlo approach is also initially used to find the region of high likelihood (see Supplementary Note 7).

With the likelihood expression for the proposed model of the three-color FRET process, one can find the most likely parameters having generated an observed data set using standard optimization methods. However, since a complex model is applied to a usually limited amount of noisy data, it is of special interest to get a precise idea of how accurately the different parameters are defined given the data at hand. In other words, not only do we want to know the most likely parameters, but also their respective probability distributions, which describe the precision with which we can determine individual parameters. This is a typical problem addressed by Bayesian inference. Using Bayes' theorem (53), one can relate the probability of certain parameters $\theta_i$, given the observed data $\{I\}$ and background information $\alpha$, to the above derived likelihood by addressing the posterior distribution:

$$P(\theta_i|\{I\},\alpha) = \frac{P(\{I\}|\theta_i)P(\theta_i|\alpha)}{\int_\theta P(\{I\}|\theta)P(\theta|\alpha)\mathrm{d}\theta} \tag{31}$$

Here, $P(\theta_i|\alpha)$ describes prior information about the parameters derived from the background information $\alpha$. The denominator is a normalization factor, also called the evidence, expressed as the integral of the likelihood over the whole parameter space. Evaluation of the evidence is not feasible in our case as there is no analytical expression available and numerical integration over the whole parameter space is computationally too costly. In Bayesian statistics, however, a number of tools have been developed to estimate the posterior distribution without having to address the evidence. One approach is the Metropolis-Hastings algorithm (47, 48), which samples the posterior distribution by performing random walks over the parameter space using a Markov chain Monte Carlo algorithm. Using independent samples from long random walks (Figure S5A), one can estimate the joint posterior distribution over all parameters and examine marginal posterior distributions to compute the mean and variance of individual parameters (Figure S5B-D). The custom implementation of the Metropolis-Hastings algorithm is outlined in Supplementary Note 8. In the Bayesian inference framework, prior information about the parameters, which may be known from previous experiments, or from the analysis of double-labeled subpopulations, can be incorporated into the analysis. In this way, previous information known about one-dimensional distance distributions can be updated in the Bayesian sense using the triple-labeled molecules to infer additional information regarding the correlation of distances. If no prior information is available, usually a flat prior assigning equal probability over the whole parameter space is used.

## Results and Discussion:

### Verification of 3C-PDA using simulations

To test the analysis method, we first applied it to synthetic datasets. Freely diffusing molecules were simulated using a Monte Carlo approach (see Materials and Methods) assuming a molecular brightness of 200 kHz for all fluorophores, similar to what is experimentally observed for our setup. The resulting photon stream was analyzed in the same manner as the experimental data. The simulation assumes fixed distances between the fluorophores resulting in a FRET efficiency of 80% between the green and red dye, 80% between the blue and red dye, and 25% between the blue and red dye. From the photon counts, we calculated three-color FRET efficiencies according to equations 12-14 (Figure 2A-B, grey bars). The conversion of burst-wise photon counts to distance-related three-color FRET efficiencies leads to very broad FRET efficiency distributions with nonsensical values outside the interval [0,1] for the FRET efficiency between blue and red dye. Furthermore, the input value of $\mathrm{E_{BR}}$ = 0.25 does not coincide with the peak value in the respective distribution (Figure 2B) and inherent correlations due to stochastic variations in the distribution of photons over the three detection channels are apparent (Figure 2C and S6). Using 3C-PDA, we can determine the underlying inter-dye distances (Table 1) and compare the measured distributions of the FRET efficiencies with expected distributions given by the fitted values (black lines in Figure 2A-C), determined by Monte Carlo simulations (see Supplementary Notes 6 and 7). 3C-PDA accounts for the observed shot-noise broadening of the histograms and accurately captures the apparent correlations in the distributions. To avoid these inherent artifacts, we represent the three-color FRET dataset using the proximity ratios (or signal fractions) $\mathrm{PR_{BG}}$, $\mathrm{PR_{BR}}$ and $\mathrm{PR_{GR}}$ as defined in equations 3 and 5 (Figure 2D-I). To visualize the three-dimensional distribution of occurrences, we show the one- and two-dimensional projections. In this parameter space, the data shows a single population that is well described by the extracted distances. Thus, compared to the transformation into FRET efficiency space, it poses a more natural way of displaying the three-color FRET data. In fact, most single-molecule three-color FRET studies have been analyzed by determining mean values of signal fractions or similar quantities, which are then used to calculate FRET efficiencies and thus distances (35, 36, 40). Using this approach, however, the extracted distances can be very sensitive to errors in the determined mean values (Figure S3), and any information about sample heterogeneity is discarded.

To accurately reflect the experimental system, we assumed a normal distribution of distances in the simulations with a width of 2 Å around the center values (Table 1). Using the distance distribution model, we were able to recover the input distances as well as the additional broadening with high accuracy. To map the sensitivity of the method at various inter-dye distance combinations, we simulated different combinations of distances with a constant distance distribution width of 2 Å and a Förster radius of 50 Å for all FRET pairs. To judge the performance at the sampled distances, we determined the precision given by 95% confidence intervals and the accuracy given by the deviation of the inferred values from the input. The precision and accuracy of the analysis depend on the gradient of the signal distribution with respect to the distances. When a change in distance invokes a large change in the distribution of the photon counts over the three detection channels, the inferred values will be well defined. On the other hand, when the photon count distribution is not sensitive to distance changes, the confidence intervals will increase and inaccuracies may occur. To illustrate this effect and to map the sensitive range of 3C-PDA, we plot the fraction of green and red photons after blue excitation as a function of the distances $R_{BG}$ and $R_{BR}$ at a fixed distance $R_{GR}$ of 40 Å (Figure 3A-B). Generally, the sensitivity for the distances $R_{BG}$ and $R_{BR}$ will be optimal when the FRET efficiency between the green and red dye is 0, and worst when the FRET efficiency between green and red is high. In the latter case, the majority of fluorescence signal after excitation of the blue dye is detected in the red channel while only a minor fraction is seen in the green channel, resulting in reduced sensitivity. Mapping the uncertainty at different distance combinations confirms the trend of the signal distributions (Figure 3A-B and Figure S7). The highest uncertainty is observed for the distance $R_{BR}$ in the case of a small distance $R_{BG}$ and a large distance $R_{BR}$, where neither the red nor the green signal fraction shows high sensitivity to a change in the distance $R_{BR}$. However, for the case of $R_{BG} = 40$ Å and $R_{BR} = 60$ Å (Table 1), the input values are still recovered with high accuracy and precision.

To address the minimum amount of data needed to accurately infer all three distances, we randomly picked subsets of increasing number of time bins from the simulation using input values of $R_{GR} = 40$ Å, $R_{BG} = 60$ Å and $R_{BR} = 60$ Å, and performed 3C-PDA (Figure 3C). Using 500 time bins, the inferred distances already deviate by less than 2 % from the target values, however the uncertainty is large, especially for the distance $R_{BR}$. At 1000 time bins, the relative error is well below 1 % and the distance uncertainty is reduced to ≤ 2 %, further improving upon inclusion of more time bins. For a simple 3C-PDA including a single population, 1000 time bins are thus sufficient to infer accurate distances. Note that, depending on the duration of the single-molecule observations, one burst can contribute multiple time bins to the 3C-PDA, so the number of sampled molecules can be lower.

To test the sensitivity of our approach with respect to correlated distance broadening, we simulated a static distance distribution with a single non-zero covariance element, using a correlation coefficient of 0.5 between $R_{BG}$ and $R_{GR}$. This corresponds to a system where the blue and red dye are fixed with respect to each other, but the green dye position is flexible, leading to static heterogeneity in the distances with respect to the green dye (Table 1 and Figure S8A-B). When all covariance elements are set to zero, no satisfactory fit could be achieved (Figure S8C). By introducing the covariance matrix as a fit parameter, there is indeed a correlation detected between $R_{BG}$ and $R_{GR}$, while the other distance combinations show no correlation. The analysis yields an inferred correlation coefficient of 0.53 ± 0.01, close to the input value of 0.5 (Table 1 and Figure S8D). Thus, in the ideal case, all input values can be recovered with high confidence, showing that our method is capable of extracting quantitative values for the separation of the three fluorophores as well as the correlation between them.

Experimental systems often coexist in different conformational states. To test to what limit small subpopulations can be detected, we simulated a 9:1 mixture of molecules with a difference in center distance of 2 Å and 5 Å for all distances and a distance distribution width of 2 Å (Figure S9-10). By eye, both datasets can be fit reasonably well using a single population. However, in both cases addition of a second population increases the log-likelihood. To test whether this increase is justified or just caused by the increased number of model parameters, we applied the Bayesian information criterion (BIC) (54) to decide between the two models. The BIC is defined as:

$$\mathrm{BIC} = -2\ln\mathcal{L}_M + k\ln N \tag{32}$$

where $\mathcal{L}_M$ is the maximum value of the likelihood function, $k$ is the number of parameters of the model and $N$ is the number of data points (here time bins). When comparing different models, the model with the lowest value of the BIC is to be preferred. In this case, the number of model parameters increases from 6 (three center distances and three distribution widths) to 13 (six center distances, six distribution widths and one fractional amplitude). Indeed, the BIC is lower for the two-population model for a separation of 5 Å (Table 2). However, if the distance difference is only 2 Å, the use of the more complex model is not justified by the BIC.

In real experiments, a number of experimental artifacts have to be accounted for. Background noise can lead to an error in the extracted distances, especially if the signal is low. In three-color FRET, this situation can easily occur for the blue channel due to the presence of two FRET acceptors. To test the robustness of our analysis with respect to background noise, we performed simulations using a brightness of 200 kHz for all fluorophores at increasing Poissonian background signal (Figure 3D-F). We define the signal-to-noise ratio (SNR) as the ratio of the average burst-wise count rate over the total background count rate of all detection channels. Typical burst-wise count rates are above 100 kHz and the background count rate per color channel is usually below 2 kHz, resulting in a SNR of 15-20 over all detection channels for our setup. The fitted distances deviate from the input value at low SNR, however at SNR ≥ 10, the relative error is below 1% (Figure 3D-E). The uncertainty of the extracted distances, on the other hand, is independent of the SNR (Figure 3F), since it is primarily limited by the amount of data available.

Additional experimental artifacts are given by crosstalk, direct excitation, and differences in detection efficiency and quantum yield. To test whether we could still infer correct distances in the presence of these artifacts, we included them into the simulations, choosing values close to those encountered in the experiment (Table S1). We were able to still recover the correct center distances for the case of a high FRET efficiency between the blue and green as well as the green and red dyes, and a low FRET efficiency between the blue and red dyes (Table 1). There is, however, a deviation for the inferred value of $\sigma_{\mathrm{BR}}$ and a larger uncertainty associated with both $\mathrm{R}_{\mathrm{BR}}$ and $\sigma_{\mathrm{BR}}$, likely due to the reduced sensitivity of the red channel caused by the smaller simulated detection efficiency. We then simulated a system showing coordinated broadening of the distance distribution in all dimensions in the presence of experimental artifacts. Mean distances and distribution widths are again accurately recovered, although some deviations can be observed (Table 1). The inferred covariance matrix elements can deviate from simulated values but are within the confidence interval. Revisiting the case of a small distance between blue and green dye and large distance between red and green dye, the existence of substantial coordination can cause deviation of inferred distance values exceeding the inference uncertainty. In this case, the distance $\mathrm{R}_{\mathrm{BR}}$ is inferred to be 57.5 ± 1.9 Å, while the input value was 60 Å. Likewise, the covariance elements for $\mathrm{R}_{\mathrm{BR}}$ also deviated from the simulated values, resulting in an underestimation of the anti-correlation between $\mathrm{R}_{\mathrm{BR}}$ and $\mathrm{R}_{\mathrm{BG}}$, and an overestimation for the correlation between $\mathrm{R}_{\mathrm{BR}}$ and $\mathrm{R}_{\mathrm{GR}}$. Even in this extreme case, the method can thus still recover the correct trend of coordination, albeit the absolute values for the elements of the covariance matrix may deviate from the input values to some extent.

*The likelihood approach to photon distribution analysis*

The 3C-PDA method is an extension of previous work on the statistics of photon emission in solution-based two-color FRET experiments (18, 19). By using a likelihood approach, 3C-PDA can be performed without the need of processing the data into histograms. As a result, the Bayesian inference approach is more stable at low statistics, which is of special importance for three-color FRET experiments. We note, however, that our analysis is subjected to pre-processing of the data through burst detection. Thus, determined population sizes will be biased when species differ in brightness because bright bursts are preferentially selected by the burst search algorithm (55). The likelihood analysis presented here may also be applied to two-color FRET experiments. Although acquiring sufficient statistics to sample the proximity ratio histogram usually is not a problem in two-color FRET experiments, we still find that using the likelihood estimator presented here, instead of a $\chi^2$ goodness-of-fit estimator, yields a smoother optimization surface, leading to a faster convergence of the optimization algorithm and generally more accurate results at low statistics. Furthermore, data from two-color FRET measurements of the same distances can be incorporated into the three-color photon distribution analysis to perform a global analysis over many data sets. The two-color FRET data may be taken from incompletely labeled subpopulations, which are available in the three-color FRET measurement, or from independent two-color FRET measurements. In such a global analysis, distances are linked between two- and three-color experiments, however, the dye pairs or setup parameters do not need to be identical for all included datasets. Since the covariance matrix is unique to the three-color FRET dataset, the inclusion of additional two-color FRET datasets increases the robustness of the extracted correlation coefficients between distances. Furthermore, the Bayesian framework presented here allows the natural incorporation of additional information (available e.g. from structural methods such as X-ray crystallography, NMR, cryo-EM or SAXS) into the model by means of the prior probability distribution of the model parameters (see equation 31).

**Application of 3C-PDA to triple labeled DNA**

As an experimental benchmark, we measured double stranded DNA labeled with three dyes as a static model system. To see if we could quantitatively detect small changes in a three-color FRET system, we arranged the dyes Alexa488, Alexa568 and Alexa647 such that significant FRET could occur between all dye pairs. The green and red dyes were positioned on one strand of the double helix at a distance of 27 bp, while the blue dye was positioned on the complementary strand between the two acceptor dyes. Two constructs were designed where the position of the blue dye was shifted by 3 bp, resulting in distances of 17 bp to the green dye and 10 bp to the red dye for construct 1 (DNA-Alexa1), and 14 bp to the green dye and 13 bp to the red dye for construct 2 (DNA-Alexa2) (Figure 4G). The 3C-PDA fit of DNA-Alexa1 is shown in Figure 4A-F. While not directly apparent from the photon count distributions, a second population with ~20% contribution was required to describe the data. DNA-Alexa2 more visibly showed a second population with a lower value for $\mathrm{PR}_{\mathrm{BG}}$, accounting for ~15% of the measured data (Figure S11B). Here, we focus the analysis on the main population (Table 3 and Figure 4H) and attribute the minor secondary population to a photophysical artifact of the dyes, discussed further below. As expected, the distance between the green and red dye is unchanged for both arrangements at 94.9 Å and 96.4 Å for DNA-Alexa1 and DNA-Alexa2, respectively. Changing the position of the blue dye results in a distance change for $\mathrm{R_{BG}}$ from 64.4 Å to 52.3 Å, and for $\mathrm{R_{BR}}$ from 62.2 Å to 72.6 Å, resulting in a difference of $\Delta\mathrm{R_{BG}}$= -12.1 Å and $\Delta\mathrm{R_{BR}}$= 10.4 Å. To investigate whether we could infer correct distances, we compare our result with expected distances as determined by accessible volume (AV) simulations (56). When comparing the relative distance differences between the two constructs, we find very good agreement between measurement and AV simulations, which yield $\Delta\mathrm{R_{BG}}$= -13.5 Å and $\Delta\mathrm{R_{BR}}$= 10.8 Å (Table 3). The absolute inter-dye distances for $\mathrm{R_{GR}}$ and $\mathrm{R_{BG}}$ also match reasonably well with the AV-derived distances, while a large deviation is observed for $\mathrm{R_{BR}}$ ($R_{\mathrm{exp}} - R_{\mathrm{AV}}$ = 13/18 Å for DNA-Alexa1/2, Table S3). We separately analyzed double-labeled subpopulations of the same measurement using 2C-PDA (Table S3 and Figure S12) and performed measurements on DNA molecules carrying two of the three dyes (Table S3 and Figures S13 A-D). The results agree well with the distances determined by 3C-PDA, showing that the deviation of absolute distances from expected values for $\mathrm{R_{BR}}$ is not an artifact of the 3C-PDA method (see Supplementary Notes 9 and 10 for further discussion of potential photophysical and structural artifacts).

We then tested another combination of fluorophores by arranging the dyes Atto488, Atto565 and Atto647N first in a cascade geometry (Figure 4I). This arrangement (DNA-Atto1) is expected to show a high FRET efficiency from the blue to green dye and the green to red dye, while the FRET efficiency from the blue to red dye will be very low, similar to the situation studied using simulated datasets in the previous section. This resulted in similar distributions of the three-color FRET efficiencies as observed for the simulated data, including the occurrence of false correlations (Figure S14). A single population was again not sufficient to describe the data. Therefore, a second population was included in our fit, accounting for approximately 15% of the data (Figure S15A and Table S4). For the main population, we find a large distance of 74 Å between the blue and red dye and shorter distances between the green and red dye (46 Å) as well as the blue and green dye (61 Å) (Table 3 and Figure 4J). We then switched the positions of the blue and green dye such that substantial energy transfer could occur between all dyes (DNA-Atto2). Again, inclusion of a small secondary population was necessary, accounting for 20% of the data (Table S4 and Figure S15B). As expected, the distance between the green and red dye is now similar to the distance between the blue and red dye in the cascade arrangement (74 Å). Likewise, the distance between the blue and red dye in DNA-Atto2 is close to the distance measured between the green and red dye in DNA-Atto1 (44 Å). Surprisingly, we find a significant disagreement for the distance between the blue and green dye at 48 Å, which should be identical in both arrangements (indicated by a * in Figure 4J). We analyzed separate measurements of the same constructs carrying only two of the three dyes by 2C-PDA, which resulted in similar distances for DNA-Atto2 as compared to the 3C-PDA results (Figure S13 E-H and Table S4). In DNA-Atto1, however, the dye Atto565 showed position-dependent quenching causing the observed deviation for the distance $\mathrm{R_{BG}}$. The quenching likely occurs due to photoinduced electron transfer to nearby guanine residues, as has previously been reported for rhodamine-based fluorophores (61) (see Supplementary Note 11 for a detailed discussion). By selective analysis of the unquenched population using 2C-PDA, we can recover comparable values for $\mathrm{R_{BG}}$ for both constructs, yielding a corrected value for DNA-Atto1 of ~50 Å (black diamond in Figure 4J). Such a selective analysis was not possible for the three-color FRET data because the fluorescence lifetime of Atto565 was already significantly reduced due to the high FRET efficiency to the red dye ($E_{GR} > 0.9$, $\tau_G < 1$ ns), making it difficult to separate quenched and unquenched populations.

In our model function, we assumed a Gaussian distribution of inter-dye distances. A Gaussian distance distribution model has been standard for almost all PDA studies so far, even for systems that are expected to be rigid such as dsDNA (18, 19). A detailed discussion of the origin of the broadening of the FRET efficiency histograms beyond the shot-noise in the absence of conformational heterogeneity is given by in reference (52) and is attributed to the existence of different photophysical states of the acceptor leading to an apparent distribution width that is proportional to the mean inter-dye distance. The observed distribution widths in the 3C-PDA of dsDNA are in the range of 8.4 ± 3.1% of the center distances (averaged over all dye combination). This value is comparable to previously reported results for two-color PDA analyses of dsDNA labeled with Alexa488 and Cy5, yielding a value of 7.6% (52). Here, we did not consider the covariances in the analysis of the DNA constructs. When artifacts due to dye photophysics are the main contribution to the width of the observed distance distribution, e.g. the existence of multiple photophysical states, 3C-PDA will reveal apparent false correlations. Considering, for example, a quenched state of the red dye, the distances to both the green and the blue dye would be affected, which would result in a false-positive covariance for these distances. While it is in principle possible to use the off-diagonal elements of the covariance matrix to investigate the correlation between distances, special care has to be taken when investigating the covariance matrix in terms of physically relevant conformational broadening. Moreover, whereas artifacts originating from the presence of multiple photophysical states can usually still be described by a single population with an increased distribution width in 2C-PDA, 3C-PDA is more sensitive to these artifacts. In this case, the covariance matrix of the distance distribution would be required to describe the correlated broadening of the apparent distribution of distances. As such, it is not unexpected that two populations were required to describe the three-color FRET data in all cases. Indeed, the minor secondary population observed in the DNA measurements most likely originates from photophysical artifacts such as spectral shifts of the fluorophores reported for Atto647N (62, 63) and Alexa488 (64, 65) or sticking interactions of the dyes to the DNA surface (52, 60).

### Towards quantitative three-color FRET in proteins

To test 3C-PDA on a protein system, we labeled the Hsp70 chaperone BiP (binding immunoglobulin protein) with the dyes Atto488, Atto565 and Atto647N (Figure 5A). During its nucleotide-dependent conformational cycle, BiP undergoes a large conformational change whereby the lid of the substrate binding domain assumes an open conformation when ATP is bound but is closed in the ADP-bound state (23, 29). By positioning the green and red dyes on the flexible lid and the substrate-binding domain (SBD), we can monitor the state of the lid (open/closed). The blue dye is specifically attached to the nucleotide-binding domain (NBD) through introduction of an unnatural amino acid. The labeling of the green and red dye, however, was performed stochastically using two site-specifically introduced cysteines, resulting in a random distribution of the green and red dye labels between the two possible configurations BGR and BRG. Under the assumption that the environment of the dyes is similar at both labeling positions, the measured distance between the green and red dyes should not be affected. In 3C-FRET, however, a superposition of the two configurations is observed. The model function can be extended to account for the stochastic labeling using only one additional parameter, which is the relative population of the two configurations BGR and BRG. Considering that a permutation of the positions of green and red dye is equivalent to adding a second population with interchanged distances BG and BR, the total likelihood per time bin is then given by:

$$P(\{I\}) = F_{BGR} * P\left(\{I\}|M(\mathbf{R}_{\mathrm{BGR}})\right) + (1 - F_{BGR}) * P\left(\{I\}|M(\mathbf{R}_{\mathrm{BRG}})\right) \tag{33}$$

where $F_{BGR}$ is the fraction of molecules with labeling scheme BGR. When the labeling positions are not equally accessible for the two acceptor dyes, the resulting distribution will be uneven. In such cases, where $F_{BGR}$ significantly differs from 0.5, it can be extracted from the fit as a free fit parameter. A more robust analysis can be performed when $F_{BGR}$ is determined by other methods (e.g. by mass spectrometry).

Here, we performed 3C-PDA on BiP in the presence of ADP and ATP. The conformational cycle of BiP has previously been studied by single-pair FRET using the identical labeling positions (23, 29). We determined the degree of labeling for the individual dyes using absorption spectroscopy, yielding an upper estimate for the triple-labeling efficiency of ~25 %. However, after filtering for photobleaching and -blinking, the fraction of usable single-molecule events for 3C-PDA was reduced to less than 5% of all detected molecules. For the ADP-state, the obtained proximity ratio histograms show a broad distribution with a peak at high proximity ratio GR and low proximity ratio BG and BR (Figure 5B). The ATP-state, on the other hand, is characterized by a main population at low proximity ratio GR and BR, whereas the proximity ratio BG shows a bimodal distribution (Figure S16). Inspection of the one-dimensional projections does, however, not reveal the full complexity of the data, which is more evident in the two-dimensional projections. As such, it is not straightforward to assign the number of populations based on the one-dimensional projections alone. To fit the data, we assumed the occupancy of the two cysteine labeling positions to be equal between the green and red dye ($F_{BGR} = 0.5$). At a minimum, we required three components to describe the data. However, since inclusion of a fourth component increased the likelihood and decreased the BIC (Table S5), we fit the data using a total of 4 populations (Figure 5B, S16 and Table S6). Without further knowledge about the distribution of the green and red labels, the three-color FRET distances $R_{BG}$ and $R_{BR}$ cannot be assigned to physical distances in the molecule. However, by reducing the analysis to the main population (colored blue in the figures), we can assign the three-color FRET derived distances by simple comparison with the previously determined values using single-pair FRET (Figure 5C) (29). Reasonable agreement is obtained between two-color and three-color FRET experiments for all distances, showing that we can follow the conformational cycle of BiP with three-color FRET.

Previously, the observed two-color FRET efficiency distributions for the NBD-lid and NBD-SBD FRET sensors (i.e. the distances between the blue/red and the blue/green labels in Figure 5A) were found to be very similar (23, 29). Based on this observation, we also performed a simplified analysis using a four-component model without accounting for the stochasticity of the fluorescent labeling (Figure S17). Indeed, also the inferred distributions from 3C-PDA for $R_{BG}$ and $R_{BR}$ are very similar (Figure S18 and Table S7), indicating that both distances may be used interchangeably to address the interdomain distance. The inferred two-dimensional distribution of the SBD-lid ($R_{GR}$) and SBD-NBD (here $R_{BG}$) distances are shown in Figure 5D (see Figure S18 for all distance pairs). From the main populations of the distance distribution, we can confirm the picture obtained from the crystal structures (Fig. 5A), showing that the protein indeed undergoes a coordinated conformational change. In the presence of ADP, the lid-domain is closed ($R_{GR} \approx 50$ Å, $\sigma_{GR} \approx 5$ Å), while the interdomain distance shows a broad distribution indicating conformational heterogeneity ($R_{BG} \approx 80$ Å, $\sigma_{BG} \approx 15$ Å, Fig. 5D, left). In the ATP-state the lid opens up ($R_{GR} \approx 89$ Å, $\sigma_{GR} \approx 10$ Å), while the domains come into closed contact, resulting in a narrower distribution width for the interdomain distance ($R_{BG} \approx 56$ Å, $\sigma_{BG} \approx 5$ Å, Fig. 5D, right). The simplified model thus allowed us to characterize the conformational space of BiP using three-color FRET and investigate correlated distance changes from the inferred multidimensional distance distributions.

While we generally expected broad distributions for the three-color FRET data, we also observed large conformational heterogeneity for the sensor between the substrate-binding domain and the lid, which previously was found to adopt more defined conformations (23, 29). A possible explanation for the excess heterogeneity might be given by the contribution of contaminations. Through the filtering for triple-labeled molecules that showed no photo-bleaching, we are subjecting our analysis to a small fraction of generally less than 5% of all detected molecules. Thus, it is expected that fluorescent impurities, which by chance pass the filtering process, may have a higher contribution compared to two-color FRET experiments. Although BiP was still functional after the triple-labeling step with respect to its ATPase activity (see Figure S19), we also cannot exclude that the labeling with three dyes might slightly destabilize the structure of the protein.

Biomolecules generally often show complex conformational landscapes. Here, we required a total of four populations to describe our data. Due to the sensitivity of 3C-PDA to correlations in the data, it is expected that more states are necessary to fully describe the data as compared to two-color FRET experiments. On the other hand, the sensitivity of 3C-PDA is also what makes it possible to reliably extract more information from the data. Using the example of the Hsp70 chaperones, previous studies suggested that the opening and closing of the lid correlates with the distance between substrate-binding and nucleotide-binding domains (66, 67). However, each state of the lid (open/closed), might show multiple states of the interdomain sensor. Thus, while two-color experiments on the SBD-lid sensor could be well described by two states, and the interdomain sensor fit well to a broad distance distribution, three-color experiments naturally require a larger number of states due to the multidimensional and correlated information available. With respect to the Hsp70 chaperones, the question of the allosteric communication between the nucleotide-binding and substrate-binding domains is a key question to understand their function (66, 68). 3C-PDA is a promising method to elucidate the coordination between substrate binding and nucleotide hydrolysis within these proteins. Fundamentally, our results on the conformational changes of BiP are limited by the lack of specific labeling for the two acceptor dyes in the experiment. We describe how this limitation can be overcome when the labeling efficiencies of the acceptor positions are different and known *a priori*. Promisingly, many novel approaches for the specific labeling of proteins have been developed in the past years (44-46), enabling the attachment of three or more fluorophores to single proteins through a combination of orthogonal labeling approaches. Moreover, it is worth noting that 3C-PDA is, of course, not limited to the study of intramolecular distances in single proteins. Rather, it has promising applications in the study of interactions between proteins and/or nuclei acids, whereby the interaction partners may be labeled with a single or two fluorophores each.

## Summary and Conclusions:

Here, we presented 3C-PDA, a statistical method for the analysis of single-molecule three-color FRET burst analysis experiments. The method incorporates the underlying physical distance heterogeneity into the model function, enabling a detailed description of the conformational space of biomolecules by three distances simultaneously. The need to apply statistical methods to the analysis of three-color FRET data arises due to the inherent noise that occurs when converting the limited number of photons per molecule to three-color FRET efficiencies. Our model-based Bayesian inference approach describes the observed data with a distance distribution model that includes all needed experimental correction factors, thus presenting an effective way to de-noise three-color FRET experiments and extract information about the underlying distance heterogeneity. The experimental results can be directly interpreted in terms of distance changes, using the three-color FRET information to reveal the existence of coordinated conformational changes. The theory described here applies to systems that show no conformational dynamics on the millisecond time scale. The framework can, however, be extended to account for dynamic interconversion between distinct conformational states, which will enable the study of complex dynamic processes within single biomolecules.

## Materials and Methods:

### *Simulations:*

Simulations of single-molecule three-color FRET experiments were performed using a Monte Carlo approach. Diffusion of molecules in a box of size 7 µm x 7 µm x 12 µm was simulated by drawing normally distributed random numbers for the displacement at each time step $\Delta t$ of 1 µs with a width given by $\sigma_{x/y/z} = \sqrt{2D\Delta t}$. Molecules exiting the box were re-inserted on the opposite side (periodic boundary condition). The observation volume was represented by a 3D Gaussian function with lateral and axial width of 500 nm and 1500 nm at $1/e^2$ of the maximum intensity, respectively. Photons for each excitation channel were generated randomly at each time step with a probability proportional to the excitation intensity at the current position. FRET and experimental artifacts were evaluated on photon emission as described in Supplementary Note 3. Simulation parameters were chosen to approximately represent experimental conditions with a diffusion coefficient of 125 µm$^2$/s and a brightness of 200 kHz at the center of the confocal volume. To simulate static broadening of distance distributions, a new set of distances was drawn according to the distance distribution for each molecule every 10 ms.

### *Experimental Setup:*

Three-color FRET experiments with pulsed interleaved excitation (PIE) (15, 69) and multiparameter fluorescence detection (MFD) (8) were performed on a homebuilt confocal three-color dual-polarization detection setup (Figure S1) based on a Nikon Eclipse Ti-DH inverted microscope. For pulsed interleaved excitation, the three lasers (LDH-D-C-485, LDH-D-TA-560, LDH-D-C-640, PicoQuant, Berlin, Germany) are synchronized by a laser driver (Sepia II, PicoQuant) at a frequency of 16.67 MHz with 20 ns delay between consecutive pulses to minimize temporal crosstalk between PIE channels. The lasers are combined into a polarization maintaining single-mode fiber (QPMJ-A3A 405/640, OZ Optics, Ottawa, Canada), collimated (60SMS-1-4-RGBV11-47, Schäfter+Kirchhoff, Hamburg, Germany) and focused into the sample by a 60x 1.27 NA water immersion objective (Plan Apo IR 60x 1.27 WI, Nikon, Düsseldorf, Germany). The average excitation power measured before the objective was 100 µW, 90 µW and 70 µW for the blue, yellow and red lasers, respectively. Fluorescence was separated from the excitation light by a polychroic mirror (zt405/488/561/633, AHF Analysentechnik, Tübingen, Germany) and focused through a 50 µm pinhole. The signal was then split into parallel and perpendicular polarization with respect to the excitation by a polarizing beam splitter (Thorlabs, Dachau, Germany) and spectrally separated into the three spectral channels by two dichroic mirrors (BS560 imaging, 640DCXR, AHF Analysentechnik) and three emission filters per polarization (ET525/50, ET607/36, ET670/30, AHF Analysentechnik). Photons were detected using six single-photon-counting avalanche photodiodes (2x COUNT-100B, LaserComponents, Olching, Germany, and 4x SPCM-AQR14, Perkin Elmer, Waltham, Massachusetts) and registered by TCSPC electronics (HydraHarp400, PicoQuant), which was synchronized with the laser driver.

*DNA sample preparation and measurement:*

Single- and double-labled ssDNA was purchased from IBA GmbH (Göttingen, Germany). DNA was labeled either with Atto488, Atto565 and Atto647N (Atto-Tec, Siegen, Germany) or Alexa488, Alexa568 and Alexa647 (Thermofisher Scientific). DNA sequences and labeling positions are given in the SI. Single-stranded DNA was annealed in TE buffer (10 mM Tris, 1 mM EDTA, 50 mM NaCl, pH 8.0) by heating to 95 °C for 5 min and then gradually cooling down at a rate of 1 °C per minute to a final temperature of 4 °C. The sample was diluted to a final concentration of 20 pM in PBS buffer (Thermofisher Scientific) containing 1 mM Trolox (Sigma Aldrich) to reduce photobleaching and -blinking of the dyes(70).

*Data analysis:*

Data processing was performed using the software package *PAM* written in MATLAB (The MathWorks, Natick, Massachusetts), which is freely available (see Code Availability) (71). Bursts were selected as described previously using a sliding time window approach on the total signal, requiring at least 5 photons per time window of 500 µs and at least 100 photons in total per burst (19). Triple-labeled bursts were selected based on stoichiometry thresholds ($S_{BG}$, $S_{BR}$ and $S_{GR}$) (35) using a lower boundary of 0.15 and an upper boundary of 0.9. To additionally remove photobleaching and blinking events, the ALEX-2CDE filter (72) was applied, which was calculated pairwise for the three excitation channels. Fluorescence lifetimes and anisotropies for the PIE channels BB, GG and RR were determined as described previously (17). For the photon distribution analysis, burstwise data was processed into time bins of 1 ms length. Using three-color MFD-PIE, we can determine all necessary correction factors directly from the experiment, with the exception of the direct excitation probability for the PDA, which is different from the direct excitation correction factor used to correct photon counts. Direct excitation correction of FRET photon counts was performed based on the signal from the alternating acceptor excitation (see Supplementary Note 2), whereas, for the PDA, one requires the relative probability that the donor excitation laser excites the acceptor dye (see Supplementary Note 4). Crosstalk is determined from single-dye species, which are isolated using the sorting capabilities available in three-color PIE-MFD. $\gamma$-factors, accounting for the differences in quantum yield and detection efficiency for the different dyes, can be determined using the lifetime information by plotting the FRET efficiency as determined from photon counts versus the donor lifetime and minimizing the deviation from the theoretical static FRET line (20). This method is applicable only when the measured system shows no dynamics. For two-color FRET, the static FRET line is given by:

$$E = 1 - \frac{\tau_{D(A)}}{\tau_{D(0)}} \tag{34}$$

where $\tau_{D(0)}$ and $\tau_{D(A)}$ are the donor dye lifetimes in the absence and in the presence of the acceptor dye. An analogous relation is found for the total FRET efficiency from the blue dye to both acceptor dyes as shown in equation 8. In the case of flexible linkers, the static FRET line has to be modified to account for the distance averaging occurring over the burst duration (20). To apply this method to three-color FRET, we extended the theory to determine the static FRET line in the case of linker fluctuations as described by Kalinin et al. (20) for a three-color FRET system (see Supplementary Note 12). Since the systems discussed here are static, $\gamma$-factors can be extracted directly from the experiment. For three-color FRET, three $\gamma$-factors have to be considered, defined as the ratio of quantum yield $\Phi$ and detection efficiency $g$ of the two dyes by $\gamma_{XY} = \frac{\Phi_Y g_Y}{\Phi_X g_X}$. The three $\gamma$ -factors are approximately related by $\gamma_{BR} = \gamma_{BG} * \gamma_{GR}$. To determine the $\gamma$-factors for a three-color FRET measurement, first $\gamma_{GR}$ is determined by minimizing the deviation from the static FRET line as described above. Subsequently, the deviation of $E_{B\rightarrow G+R}$ from the static FRET line with respect to the lifetime of the blue dye is minimized by varying either $\gamma_{BG}$ or $\gamma_{BR}$. The third $\gamma$-factor is then calculated using the above-mentioned relation between the $\gamma$-factors. We verified this approach by separate measurements on double-labeled DNA constructs with two FRET species, where we determined the $\gamma$-factor using the relation between FRET efficiency and stoichiometry, which, within error, yielded equivalent values (Table S2).

*Determination of confidence intervals:*

Inference uncertainties are given by 95% confidence intervals determined from long runs of the Metropolis-Hastings algorithm to estimate the posterior probability density (> 10.000 steps). Statistically independent samples are drawn with a spacing of 500 steps and parameter uncertainties are determined from the distribution of samples.

*Protein constructs:*

For expression and purification of BiP, the BiP-PrK-pProEX and pEvol tRNA$^{Pyl}$ PylRS$^{WT}$ plasmids(73) were co-expressed in *E. coli* BL21-AI as described previously (23) with the following modifications: 1 mM N-propargyl-lysine was added after an initial incubation at 37°C for approximately 30 min (OD$_{600nm}$(*E.coli*)=0.2). Induction was achieved by the combined addition of IPTG and 0.02% L-(+)-arabinose.

*Protein labeling:*

Atto488 dyes were attached to propargyl-lysine by copper-catalyzed Click reactions of 5 nmol BiP-PrK and 25 nmol Atto488-azide in the presence of 2 mM $CuSO_4$, 4 mM TBTA, 0.02 mM TCEP, 10 mM fresh sodium ascorbate and protease inhibitor cocktail at room temperature for 2 hours. Centrifugal filters with a cutoff of 10 kDa were used to remove excess dye. The attachment of Atto532-maleimide and Atto647N-maleimide to cysteine residues was performed according to the protocol of the manufacturer (Atto-Tec, Siegen, Germany). Cysteines were reduced by incubation with 1 mM DTT followed by buffer exchange into oxygen-free buffer containing 50 µM TCEP and labeling with two- to threefold molar excess of dye at room temperature for two hours. Unbound fluorophores were removed by a size-dependent filtration. The labeling efficiency was determined via fluorophore absorption and the protein concentration using a bicinchoninic acid assay.

*Protein measurements:*

Triple labeled BiP was diluted to concentrations of 20-100 pM in 50 mM Hepes, pH7.5, 150 mM KCl, and 10 mM $MgCl_2$. Measurements were performed in the absence or in the presence of 1 mM ADP or 1 mM ATP.

## Code availability

Source code for three-color photon distribution analysis is available through the open-source software package *PAM,* freely available under http://www.gitlab.com/PAM-PIE/PAM (71). The module *tcPDA.m* is tightly integrated with PAM, but also supports a text-based file format for direct loading of three-color FRET datasets.

## Acknowledgements

We thank Jelle Hendrix for helpful discussions and Johannes Meyer zum Alten Borgloh for help with implementing computational routines on GPUs. Our thanks belong to Edward Lemke, Swati Tyagi, and Christine Koehler for the introduction to protein expression using non-natural amino acids. We thank Mathias Rosam and Johannes Buchner for providing the BiP plasmid. L.V. acknowledges funding by P-CUBE: The research leading to these results has received funding from the European Community's Seventh Framework Programme (FP7/2007-2013) under grant agreement n° 227764 (P-CUBE). We gratefully acknowledge the financial support by the Deutsche Forschungsgemeinschaft via the Collaborative Research Consortium on Conformational Switches (SFB1035, Project A11), and by the Ludwig-Maximilians-Universität through the Center for NanoScience (CeNS) and the BioImaging Network (BIN).

## Author contributions

A.B. built the experimental setup, developed and programmed the analysis method, and performed the analysis and measurements of DNA samples. L.V. expressed and labeled proteins and performed the protein measurements. A.B. and D.C.L. wrote the manuscript.

**References:**

1. Ha T, et al. (1996) Probing the interaction between two single molecules: fluorescence resonance energy transfer between a single donor and a single acceptor. *Proc Natl Acad Sci USA* 93(13):6264–6268.

2. Myong S, Rasnik I, Joo C, Lohman TM, Ha T (2005) Repetitive shuttling of a motor protein on DNA. *Nature* 437(7063):1321–1325.

3. Ha T (2001) Single-Molecule Fluorescence Resonance Energy Transfer. *Methods* 25(1):78–86.

4. Schluesche P, Stelzer G, Piaia E, Lamb DC, Meisterernst M (2007) NC2 mobilizes TBP on core promoter TATA boxes. *Nature Structural & Molecular Biology* 14(12):1196–1201.

5. Weiss S (1999) Fluorescence spectroscopy of single biomolecules. *Science* 283(5408):1676–1683.

6. Zander C, et al. (1996) Detection and characterization of single molecules in aqueous solution. *Applied Physics B: Lasers and Optics* 63(5):517–523.

7. Brooks Shera E, Seitzinger NK, Davis LM, Keller RA, Soper SA (1990) Detection of single fluorescent molecules. *Chemical Physics Letters* 174(6):553–557.

8. Eggeling C, et al. (2001) Data registration and selective single-molecule analysis using multi-parameter fluorescence detection. *Journal of Biotechnology* 86(3):163–180.

9. Widengren J, et al. (2006) Single-Molecule Detection and Identification of Multiple Species by Multiparameter Fluorescence Detection. *Anal Chem* 78(6):2039–2050.

10. Tellinghuisen J, Goodwin PM, Ambrose WP, Martin JC, Keller RA (1994) Analysis of fluorescence lifetime data for single Rhodamine molecules in flowing sample streams. *Anal Chem* 66(1):64–72.

11. Eggeling C, Fries JR, Brand L, Günther R, Seidel CA (1998) Monitoring conformational dynamics of a single molecule by selective fluorescence spectroscopy. *Proc Natl Acad Sci USA* 95(4):1556–1561.

12. Fries JR, Brand L, Eggeling C, Köllner M (1998) Quantitative identification of different single molecules by selective time-resolved confocal fluorescence spectroscopy. *The Journal of …*.

13. Schaffer J, et al. (1999) Identification of Single Molecules in Aqueous Solution by Time-Resolved Fluorescence Anisotropy. *J Phys Chem A* 103(3):331–336.

14. Kapanidis AN, et al. (2005) Alternating-Laser Excitation of Single Molecules. *Acc Chem Res* 38(7):523–533.

15. Müller BK, Zaychikov E, Bräuchle C, Lamb DC (2005) Pulsed interleaved excitation. *Biophys J* 89(5):3508–3522.

16. Hellenkamp B, et al. (2017) Precision and accuracy of single-molecule FRET measurements - a worldwide benchmark study. doi:arXiv:1710.03807v2 [q-bio.QM].

17. Kudryavtsev V, et al. (2012) Combining MFD and PIE for accurate single-pair Förster resonance energy transfer measurements. *ChemPhysChem* 13(4):1060–1078.

18. Antonik M, Felekyan S, Gaiduk A, Seidel CAM (2006) Separating Structural Heterogeneities from Stochastic Variations in Fluorescence Resonance Energy Transfer Distributions via Photon Distribution Analysis. *J Phys Chem B* 110(13):6970–6978.

19. Nir E, et al. (2006) Shot-noise limited single-molecule FRET histograms: comparison between theory and experiments. *J Phys Chem B* 110(44):22103–22124.

20. Kalinin S, Valeri A, Antonik M, Felekyan S, Seidel CAM (2010) Detection of structural dynamics by FRET: a photon distribution and fluorescence lifetime analysis of systems with multiple states. *J Phys Chem B* 114(23):7983–7995.

21. Tsukanov R, Tomov TE, Berger Y, Liber M, Nir E (2013) Conformational Dynamics of DNA Hairpins at Millisecond Resolution Obtained from Analysis of Single-Molecule FRET Histograms. *J Phys Chem B* 117(50):131126115511008–16109.

22. Rothwell PJ, et al. (2013) dNTP-dependent conformational transitions in the fingers subdomain of Klentaq1 DNA polymerase: insights into the role of the “nucleotide-binding” state. *Journal of Biological Chemistry* 288(19):13575–13591.

23. Marcinowski M, et al. (2011) Substrate discrimination of the chaperone BiP by autonomous and cochaperone-regulated conformational transitions. *Nature Structural & Molecular Biology* 18(2):150–158.

24. Gansen A, et al. (2009) Nucleosome disassembly intermediates characterized by single-molecule FRET. *Proceedings of the National Academy of Sciences* 106(36):15308–15313.

25. Cristovao M, et al. (2012) Single-molecule multiparameter fluorescence spectroscopy reveals directional MutS binding to mismatched bases in DNA. *Nucleic Acids Research* 40(12):5448–5464.

26. Santoso Y, Torella JP, Kapanidis AN (2010) Characterizing Single-Molecule FRET Dynamics with Probability Distribution Analysis. *ChemPhysChem* 11(10):2209–2219.

27. Krainer G, et al. (2017) Ultrafast protein folding in membrane-mimetic environments. *Journal of Molecular Biology*. doi:10.1016/j.jmb.2017.10.031.

28. Hellenkamp B, Wortmann P, Kandzia F, Zacharias M, Hugel T (2016) Multidomain structure and correlated dynamics determined by self-consistent FRET networks. *Nat Meth* 14(2):174–180.

29. Rosam M, et al. (2018) Bap (Sil1) regulates the molecular chaperone BiP by coupling release of nucleotide and substrate. *Nature Structural & Molecular Biology* 25(1):90–100.

30. Horsey I, Furey WS, Harrison JG, Osborne MA, Balasubramanian S (2000) Double fluorescence resonance energy transfer to explore multicomponent binding interactions: a case study of DNA mismatches. *Chem Commun* 0(12):1043–1044.

31. Ramirez-Carrozzi VR, Kerppola TK (2001) Dynamics of Fos-Jun-NFAT1 complexes. *Proc Natl Acad Sci USA* 98(9):4893–4898.

32. Liu J, Lu Y (2002) FRET study of a trifluorophore-labeled DNAzyme. *J Am Chem Soc* 124(51):15208–15216.

33. Watrob HM, Pan C-P, Barkley MD (2003) Two-step FRET as a structural tool. *J Am Chem Soc* 125(24):7336–7343.

34. Haustein E, Jahnz M, Schwille P (2003) Triple FRET: A tool for Studying Long-Range Molecular Interactions. *ChemPhysChem* 4(7):745–748.

35. Lee NK, et al. (2007) Three-Color Alternating-Laser Excitation of Single Molecules: Monitoring Multiple Interactions and Distances. *Biophys J* 92(1):303–312.

36. Person B, Stein IH, Steinhauer C, Vogelsang J, Tinnefeld P (2009) Correlated movement and bending of nucleic acid structures visualized by multicolor single-molecule spectroscopy. *ChemPhysChem* 10(9-10):1455–1460.

37. Hohng S, Joo C, Ha T (2004) Single-Molecule Three-Color FRET. *Biophys J* 87(2):1328–1337.

38. Lee J, et al. (2010) Single-molecule four-color FRET. *Angew Chem Int Ed Engl* 49(51):9922–9925.

39. Lee S, Lee J, Hohng S (2010) Single-Molecule Three-Color FRET with Both Negligible Spectral Overlap and Long Observation Time. *PLoS ONE* 5(8):e12270.

40. Clamme J-P, Deniz AA (2005) Three-Color Single-Molecule Fluorescence Resonance Energy Transfer. *ChemPhysChem* 6(1):74–77.

41. Stein IH, Steinhauer C, Tinnefeld P (2011) Single-molecule four-color FRET visualizes energy-transfer paths on DNA origami. *J Am Chem Soc* 133(12):4193–4195.

42. Chung HS, et al. (2017) Oligomerization of the tetramerization domain of p53 probed by two- and three-color single-molecule FRET. *Proceedings of the National Academy of Sciences* 114(33):E6812–E6821.

43. Milles S, Koehler C, Gambin Y, Deniz AA, Lemke EA (2012) Intramolecular three-colour single pair FRET of intrinsically disordered proteins with increased dynamic range. *Mol BioSyst* 8(10):2531–2534.

44. Milles S, et al. (2012) Click strategies for single-molecule protein fluorescence. *J Am Chem Soc* 134(11):5187–5195.

45. Shi X, et al. (2012) Quantitative fluorescence labeling of aldehyde-tagged proteins for single-molecule imaging. *Nat Meth* 9(5):499–503.

46. Antos JM, et al. (2009) Site-specific N- and C-terminal labeling of a single polypeptide using sortases of different specificity. *J Am Chem Soc* 131(31):10800–10801.

47. Hastings WK (1970) Monte Carlo sampling methods using Markov chains and their applications. *Biometrika* 57(1):97–109.

48. Metropolis N, Rosenbluth AW, Rosenbluth MN, Teller AH, Teller E (1953) Equation of State Calculations by Fast Computing Machines. *J Chem Phys* 21(6):1087.

49. Förster T (1948) Zwischenmolekulare Energiewanderung und Fluoreszenz. *Annalen der Physik* 437(1-2):55–75.

50. Lee NK, et al. (2005) Accurate FRET Measurements within Single Diffusing Biomolecules Using Alternating-Laser Excitation. *Biophys J* 88(4):2939–2953.

51. Hauschild T, Jentschel M (2001) Comparison of maximum likelihood estimation and chi-square statistics applied to counting experiments. *Nuclear Instruments and Methods in Physics Research Section A: Accelerators, Spectrometers, Detectors and Associated Equipment* 457(1-2):384–401.

52. Kalinin S, Sisamakis E, Magennis SW, Felekyan S, Seidel CAM (2010) On the origin of broadening of single-molecule FRET efficiency distributions beyond shot noise limits. *J Phys Chem B* 114(18):6197–6206.

53. Bayes T (1763) A Letter from the Late Reverend Mr. Thomas Bayes, F. R. S. to John Canton, M. A. and F. R. S. on JSTOR. *Philosophical Transactions (1683-1775)*. doi:10.2307/105732.

54. Schwarz G (1978) Estimating the Dimension of a Model. *The Annals of Statistics* 6(2):461–464.

55. Kalinin S, Felekyan S, Antonik M, Seidel CAM (2007) Probability distribution analysis of single-molecule fluorescence anisotropy and resonance energy transfer. *J Phys Chem B* 111(34):10253–10262.

56. Kalinin S, et al. (2012) A toolkit and benchmark study for FRET-restrained high-precision structural modeling. *Nat Meth* 9(12):1218–1225.

57. Woźniak AK, Schröder GF, Grubmüller H, Seidel CAM, Oesterhelt F (2008) Single-molecule FRET measures bends and kinks in DNA. *Proceedings of the National Academy of Sciences* 105(47):18337–18342.

58. Höfig H, Gabba M, Poblete S, Kempe D, Fitter J (2014) Inter-dye distance distributions studied by a combination of single-molecule FRET-filtered lifetime measurements and a weighted accessible volume (wAV) algorithm. *Molecules* 19(12):19269–19291.

59. Stelzl LS, Erlenbach N, Heinz M, Prisner TF, Hummer G (2017) Resolving the Conformational Dynamics of DNA with Ångstrom Resolution by Pulsed Electron–Electron Double Resonance and Molecular Dynamics. *J Am Chem Soc* 139(34):11674–11677.

60. Vandenberk N, Barth A, Borrenberghs D, Hofkens J, Hendrix J (2018) Evaluation of Blue and Far-Red Dye Pairs in Single-Molecule FRET Experiments. *J Phys Chem B*. doi:10.1021/acs.jpcb.8b00108.

61. Doose S, Neuweiler H, Sauer M (2009) Fluorescence quenching by photoinduced electron transfer: a reporter for conformational dynamics of macromolecules. *ChemPhysChem* 10(9-10):1389–1398.

62. Vogelsang J, et al. (2008) A Reducing and Oxidizing System Minimizes Photobleaching and Blinking of Fluorescent Dyes. *Angew Chem Int Ed Engl* 47(29):5465–5469.

63. Wang Q, Moerner WE (2013) Lifetime and spectrally resolved characterization of the photodynamics of single fluorophores in solution using the anti-Brownian electrokinetic trap. *J Phys Chem B* 117(16):4641–4648.

64. Chung HS, Louis JM, Eaton WA (2009) Experimental determination of upper bound for transition path times in protein folding from single-molecule photon-by-photon trajectories. *Proceedings of the National Academy of Sciences* 106(29):11837–11844.

65. Chung HS, Louis JM, Eaton WA (2010) Distinguishing between protein dynamics and dye photophysics in single-molecule FRET experiments. *Biophys J* 98(4):696–706.

66. Kityk R, Vogel M, Schlecht R, Bukau B, Mayer MP (2015) Pathways of allosteric regulation in Hsp70 chaperones. *Nature Communications* 6:8308.

67. Sikor M, Mapa K, Voithenberg von LV, Mokranjac D, Lamb DC (2013) Real-time observation of the conformational dynamics of mitochondrial Hsp70 by spFRET. *The EMBO Journal* 32(11):1639–1649.

68. Kityk R, Kopp J, Sinning I, Mayer MP (2012) Structure and dynamics of the ATP-bound open conformation of Hsp70 chaperones. *Molecular Cell* 48(6):863–874.

69. Kapanidis AN, et al. (2004) Fluorescence-aided molecule sorting: analysis of structure and interactions by alternating-laser excitation of single molecules. *Proc Natl Acad Sci USA* 101(24):8936–8941.

70. Cordes T, Vogelsang J, Tinnefeld P (2009) On the mechanism of Trolox as antiblinking and antibleaching reagent. *J Am Chem Soc* 131(14):5018–5019.

71. Schrimpf W, Barth A, Hendrix J, Lamb DC (2018) PAM: A Framework for Integrated Analysis of Imaging, Single-Molecule, and Ensemble Fluorescence Data. *Biophys J*. doi:10.1016/j.bpj.2018.02.035.

72. Tomov TE, et al. (2012) Disentangling Subpopulations in Single-Molecule FRET and ALEX Experiments with Photon Distribution Analysis. *Biophys J* 102(5):1163–1173.

73. Chatterjee A, Sun SB, Furman JL, Xiao H, Schultz PG (2013) A versatile platform for single- and multiple-unnatural amino acid mutagenesis in Escherichia coli. *Biochemistry* 52(10):1828–1837.

## Tables:

**Table 1: Results of 3C-PDA of simulated data sets with and without experimental correction factors.** Distances (R) and distributions widths (σ**)** are given in Å, while the covariances (COV) are given in Å$^2$. Inferred values are shown together with 95 % confidence intervals. Simulation input values are given in brackets. The values used for the experimental correction factors were chosen similar to those obtained experimentally (Table S2). Each analysis was performed on a total number of 10,000 time bins.

| | **Ideal** | | **+ experimental corrections** | | |
|---|---|---|---|---|---|
| **$R_{GR}$** | 40.00 ± 0.05 (40) | 50.00 ± 0.02 (50) | 40.15 ± 0.08 (40) | 49.90 ± 0.06 (50) | 40.09 ± 0.11 (40) |
| **$R_{BG}$** | 39.96 ± 0.06 (40) | 40.03 ± 0.03 (40) | 39.57 ± 0.08 (40) | 49.77 ± 0.13 (50) | 40.11 ± 0.16 (40) |
| **$R_{BR}$** | 60.18 ± 0.88 (60) | 59.95 ± 0.19 (60) | 60.13 ± 1.00 (60) | 49.89 ± 0.12 (50) | 57.50 ± 1.88 (60) |
| **$\sigma_{GR}$** | 1.97 ± 0.04 (2) | 2.03 ± 0.02 (2) | 3.98 ± 0.06 (4) | 2.02 ± 0.07 (2) | 3.99 ± 0.09 (4) |
| **$\sigma_{BG}$** | 1.98 ± 0.06 (2) | 3.98 ± 0.02 (4) | 2.99 ± 0.08 (3) | 3.82 ± 0.19 (4) | 3.05 ± 0.34 (3) |
| **$\sigma_{BR}$** | 1.89 ± 2.44 (2) | 3.02 ± 0.33 (3) | 1.28 ± 1.56 (2) | 3.08 ± 0.21 (3) | 4.52 ± 1.81 (5) |
| **$COV_{BG,BR}$** | - | -0.11 ± 0.66 (0) | - | 4.62 ± 0.98 (4.8) | -1.54 ± 4.36 (-4.8) |
| **$COV_{BG,GR}$** | - | 4.22 ± 0.09 (4) | - | -3.98 ± 0.48 (-4) | 3.77 ± 0.86 (4.5) |
| **$COV_{BR,GR}$** | - | -0.30 ± 0.43 (0) | - | 1.57 ± 0.36 (1.8) | 13.86 ± 4.78 (10) |

**Table 2: Testing the detection limit for a minor subpopulation.** The main population is defined by center distances of $R_{GR}$ = 60 Å, $R_{BG}$ = 55 Å and $R_{BR}$ = 45 Å with a distribution width of 2 Å. A second population is added at a fraction of 10% with specified distance difference ΔR for all interdye distances. Using the Bayesian information criterion (BIC, see equation 32), the 3C-PDA of the data with one or two populations are compared. For ΔR = 2 Å, the BIC does not justify the use of the model with more parameters (13 versus 6 for a single population). However, a difference of 5 Å justifies the use of the two-population model as indicated by the lower value of the BIC. For a table of all parameters of the analysis, see the Table S1.

| **BIC** | **Δ*R* = 2 Å** | **Δ*R* = 5 Å** |
|---|---|---|
| **1 population** | $1.3072 \cdot 10^5$ | $1.4853 \cdot 10^5$ |
| **2 populations** | $1.3075 \cdot 10^5$ | $1.4782 \cdot 10^5$ |
| **ΔBIC** | $0.0003 \cdot 10^5$ | $-0.0071 \cdot 10^5$ |

**Table 3: Results of the 3C-PDA of DNA constructs.** Distances determined by 3C-PDA of the DNA constructs labeled with Alexa488, Alexa568 and Alexa647 (DNA-Alexa1/2) or with Atto488, Atto565 and Atto647N (DNA-Atto1/2). The inferred distances for the major population (>80% contribution) are listed with associated inference uncertainties given as 95% confidence intervals. For DNA-Alexa measurements, experimental distance changes, $\Delta R(\text{meas.})$, are compared to theoretical distance changes as determined from accessible volume (AV) calculations, $\Delta R(\text{AV})$. For a complete list of all inferred model parameters, comparison to two-color control constructs and theoretical distances estimated from accessible volume calculations, see Table S3-4.

| | $R_{GR}$ | $R_{BG}$ | $R_{BR}$ | $\sigma_{GR}$ | $\sigma_{BG}$ | $\sigma_{BR}$ |
|---|---|---|---|---|---|---|
| **DNA-Alexa1** | 94.9 ± 0.2 | 64.4 ± 0.2 | 62.2 ± 0.2 | 11.2 ± 0.2 | 6.1 ± 0.2 | 7.3 ± 0.2 |
| **DNA-Alexa2** | 96.4 ± 0.4 | 52.3 ± 0.2 | 72.6 ± 1.0 | 9.1 ± 0.4 | 3.3 ± 0.2 | 10.4 ± 0.6 |
| $\boldsymbol{\Delta R}(\textbf{meas.})$ | 1.5 | -12.1 | 10.4 | - | - | - |
| $\boldsymbol{\Delta R}(\textbf{AV})$ | 0 | -13.5 | 10.8 | - | - | - |
| **DNA-Atto1** | 46.0 ± 0.2 | 60.5 ± 0.2 | 73.7 ± 2.1 | 3.2 ± 0.2 | 4.9 ± 0.2 | 2.6 ± 1.7 |
| **DNA-Atto2** | 74.1 ± 0.2 | 48.5 ± 0.2 | 44.1 ± 0.2 | 4.5 ± 0.2 | 2.9 ± 0.2 | 3.4 ± 0.2 |

**Figures:**

**Figure 1:**

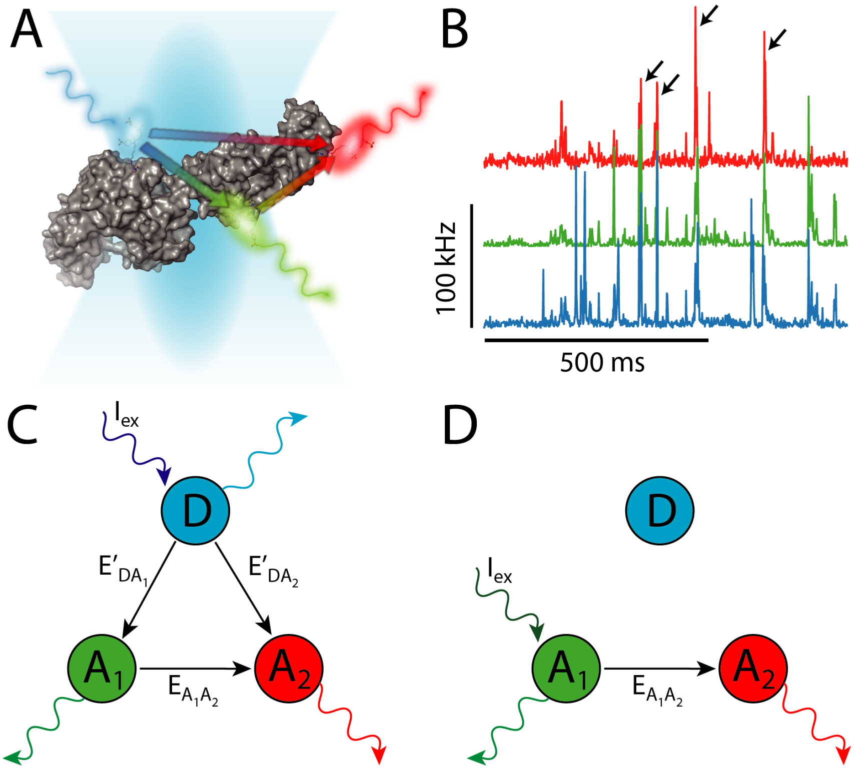

**Single-molecule three-color FRET.** (A) In a solution-based three-color FRET experiment, single-molecules are measured as they diffuse through the observation volume of a confocal microscope. Possible transition pathways in the three-color FRET system after excitation of the blue dye are schematically shown on a two-domain protein (DnaK, PDB: 2KHO). (B) Single-molecule events result in bursts of fluorescence. Shown are the fluorescence time traces of the combined signal after excitation of the blue, green and red dyes, which are alternatingly excited using pulsed-interleaved excitation (PIE, see Figure S2). Coinciding bursts in all three channels, belonging to triple labeled molecules, are indicated by arrows. (C) Scheme of the possible transition pathways in a three-color FRET system following excitation of the donor dye (blue). Energy can be transferred to either acceptor A1 or A2 (green and red, respectively) with transition probabilities $E'_{DA_1}$ and $E'_{DA_2}$. Acceptor A1 may further transfer the energy to A2 with the FRET efficiency $E_{A_1A_2}$. (D) Possible transition pathways following direct excitation of acceptor A1. Excitation of A1 reduces the complexity of the system to independently determine the FRET efficiency between the two acceptors $E_{A_1A_2}$. Experimentally, blue and green excitation are alternated on the nanosecond timescale using pulsed interleaved excitation (PIE, see Figure S2).

**Figure 2:**

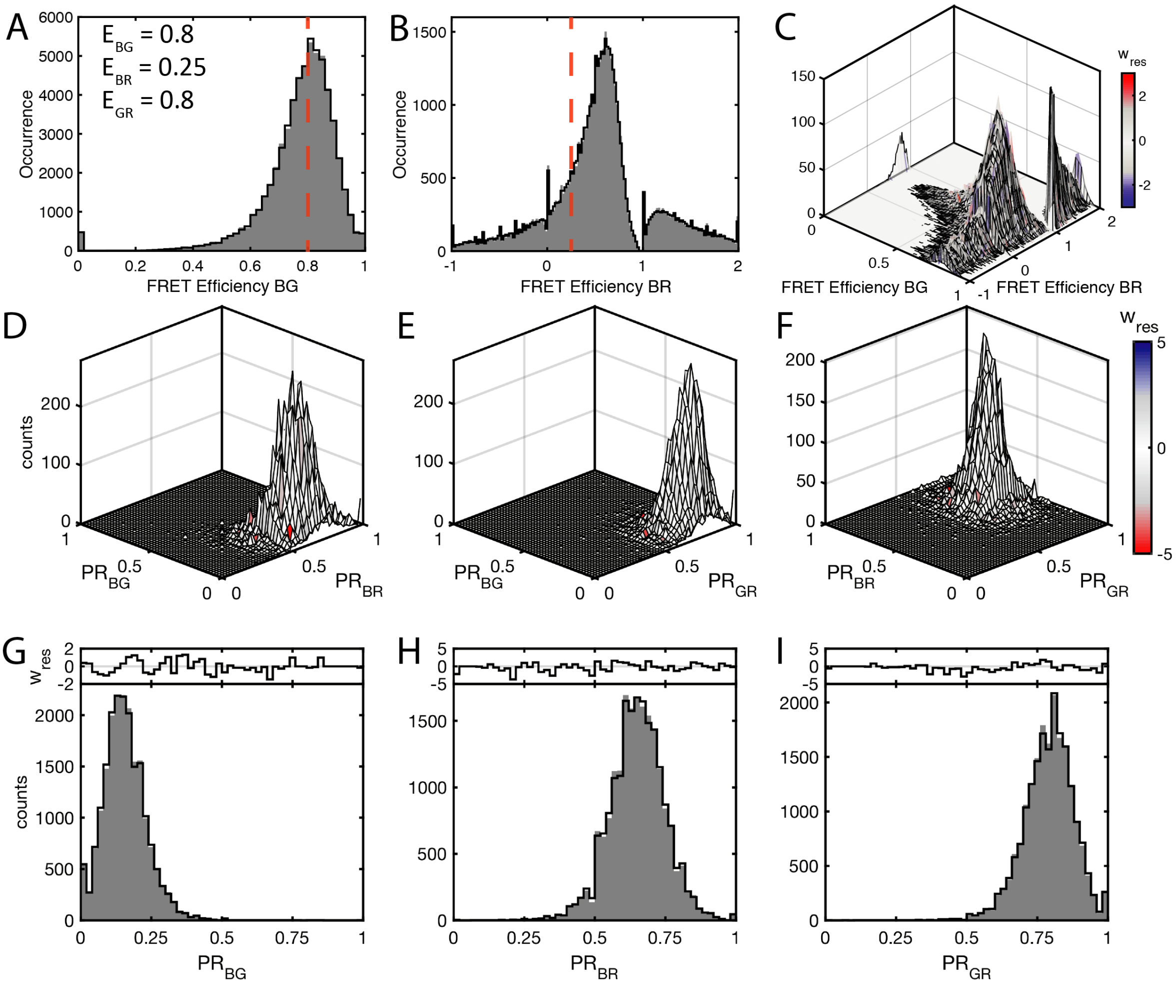

**Stochastic noise in three-color FRET.** (A-C) Three-color FRET efficiency distributions simulated for an ideal system with the respective two-color FRET efficiencies as listed in (A). The input distances are $R_{BG}$ = 40 Å, $R_{BR}$ = 60 Å and $R_{BG}$ = 40 Å using a Förster distance of $R_0$ = 50 Å and a distribution width of $\sigma$ = 2 Å for all dye pairs. FRET efficiencies $E_{BG}$ and $E_{BR}$ show broad and skewed distributions, whereas even values below zero and above one are observed for the FRET efficiency $E_{BR}$. Red dashed lines indicate the expected values of $E_{BG}$ = 0.8 in (A) and $E_{BR}$ = 0.25 in (B). The two-dimensional plot in (C) shows inherent correlations between the two FRET efficiencies due to photon shot noise (compare also Figure S4). Data is shown as grey bars in (A/B) and as a surface plot in (C). Fits are shown as black lines. In (C), the surface used to represent the data is colored according to the weighted residuals. (D-I) Representation of the result of 3C-PDA of the dataset in proximity ratio parameter space. The data is processed into signal fractions after blue excitation ($PR_{BG}$ and $PR_{BR}$) and after green excitation ($PR_{GR}$). Shown are the two-dimensional (D-F) and one-dimensional (G-I) marginal distributions of the three-dimensional frequency distribution. In the two-dimensional projections, the surface representing the data is colored according to the weighted residuals ($w_{res}$). In the one-dimensional projections, the data is shown as grey bars and the 3C-PDA fit as black lines. Weighted residuals are plotted above.

**Figure 3:**

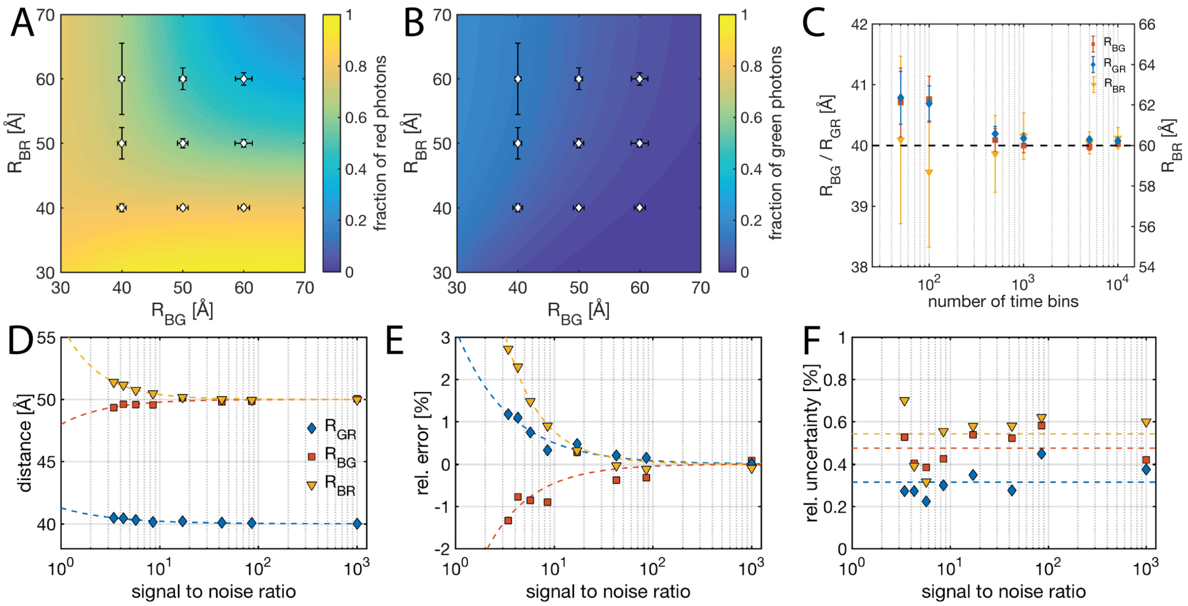

**Characterizing the performance of 3C-PDA.** (A-B) Map of the distribution of signal after blue excitation on the three-color channels (A: red detection channel, B: green detection channel) at a constant distance between the green and red dye of 40 Å ($R_0$ = 50 Å for all dye pairs). Error bars represent the uncertainty at the sampled distance given by the 95% confidence intervals. For better visualization, the absolute uncertainties are multiplied by a factor of 4. Regions where the change in signal is low with respect to distance changes correspond to large uncertainties. See Figure S7 for precision and accuracy maps at different values for $R_{GR}$. (C) Uncertainty of extracted distances given by 95% confidence intervals as a function of the number of time bins used for the analysis. Fitted distance (D), relative error (E) and relative uncertainty (F) as a function of signal-to-noise ratio. To guide the eye, dashed lines, given by power law fits to the data, are shown in D-F.

**Figure 4:**

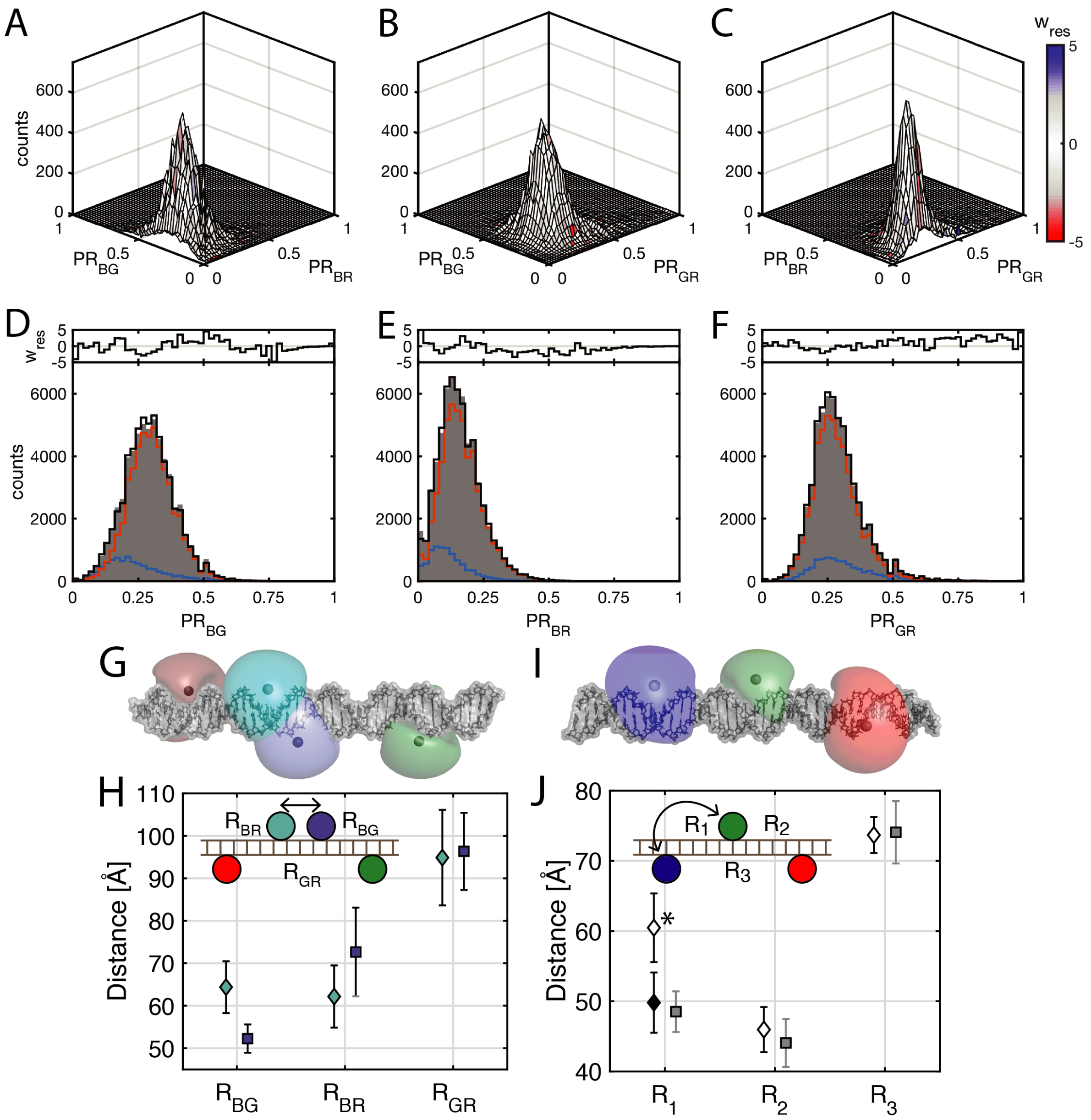

**3C-PDA of triple-labeled DNA.** (A-F) Exemplary fit result of 3C-PDA of DNA-Alexa1, corresponding to the cyan position of the blue dye in the structural model of the dsDNA construct shown in panel G. Shown are the projections of the three-dimensional histogram of signal fractions $PR_{GR}$, $PR_{BG}$ and $PR_{BR}$. Two-dimensional projections are displayed as surface plots in the top row (A-C). The surface is colored according to the weighted residuals as indicated by the color bar. In the bottom row (D-F), one-dimensional projections (grey bars) are plotted together with the fit result (black line). The two components of the model function are shown as red and blue lines. Weighted residuals are shown above. All DNA constructs required the use of two Gaussian distance distributions to describe the data. The 3C-PDA of DNA-Alexa2 and DNA-Atto1/2 are shown in Figure S11 and S15, respectively. (G) Structural model of the DNA-Alexa constructs. The accessible volumes of the dyes Alexa488 (cyan: DNA-Alexa1, blue: DNA-Alexa2), Alexa568 (green) and Alexa647 (red) are shown as clouds.

Spheres with the respective colors indicate the mean positions of the dyes. (H) Fit results for DNA-Alexa measurements. Cyan diamonds show the results with the blue dye in the left position (DNA-Alexa1, cyan cloud in the structure above), whereas blue squares indicate the blue dye in the right position (DNA-Alexa2, blue cloud). Fitted distribution widths are given as error bars. The change of the position of the blue dye by 3 bp results in an anticorrelated change of the distances RBG and RBR. (I) Structural model of the construct DNA-Atto1. The accessible volumes of the dyes Atto488 (blue), Atto565 (green) and Atto647N (red) are shown as clouds. Gray spheres indicate the mean positions of the dyes. In the DNA-Atto2 construct, the positions of the blue and green dyes are switched. (J) Fit results for the DNA-Atto constructs. Diamonds indicate the results of DNA-Atto1, corresponding to the arrangement of dyes as shown in the inset. Gray squares indicated the arrangement where the blue and green dye positions have been exchanged (DNA-Atto2). Switching of the positions of blue and green dye should not affect the recovered distances. This holds true for distances R2 and R3. For the distance R1, however, a large difference is observed (*). This deviation originates from dynamic quenching of Atto565 in construct DNA-Atto1 (see main text and Supplementary Note 9). By accounting for the quenching in the analysis, the correct distance can still be recovered for R1 in DNA-Atto1 (black diamond). Error bars represent the fitted distribution widths.

**Figure 5:**

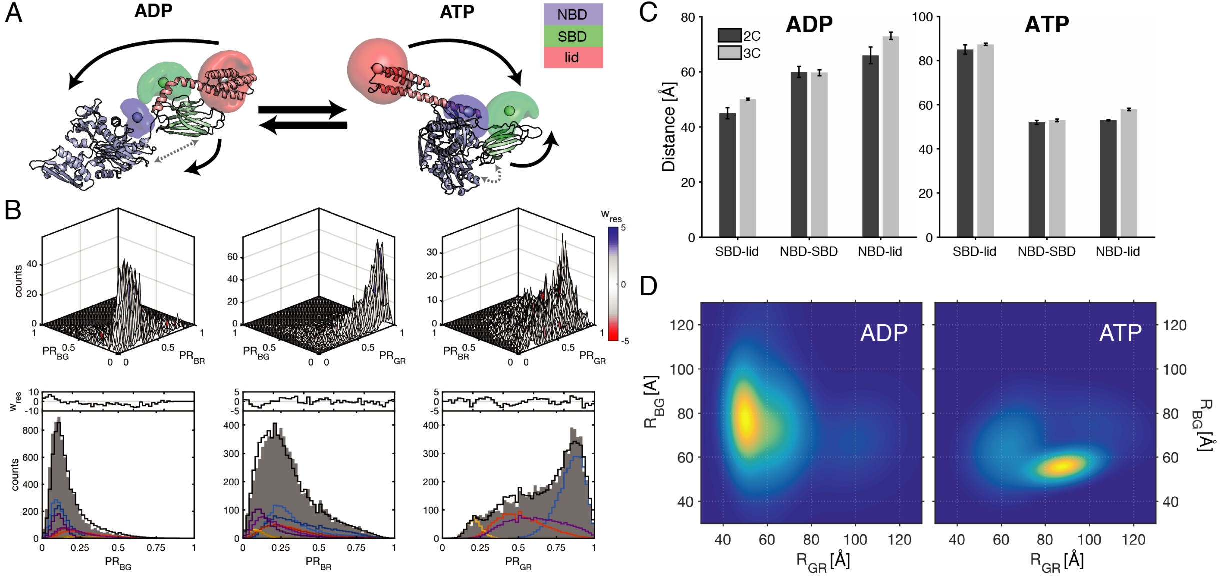

**3C-PDA of the heat shock protein BiP.** (A) Structural representations of the Hsp70 chaperone BiP in the ADP-bound state (left, based on the crystal structure of the homolog DnaK, PDB: 2KHO) and in the ATP-bound state (right, PDB: 5E84). The nucleotide-binding, substrate-binding and lid-domain (NBD, SBD and lid) are color-coded in blue, green and red respectively. Dye positions are indicated by clouds that represent the possible positions determined using accessible volume calculations. The lid of the SBD is closed in the ADP-bound state but opens up in the ATP-bound state. Black arrows indicate the movement of domains during the nucleotide-dependent conformational cycle. The distance between the SBD and NBD is larger in the ADP-bound state, while the two domains directly contact each other in the ATP-bound state (grey arrows). (B) 3C-PDA of BiP in the ADP state. Shown are the projections of the three-dimensional histogram of signal fractions $PR_{GR}$, $PR_{BG}$ and $PR_{BR}$. Two-dimensional projections are displayed as surface plots in the top row. The surface is colored according to the weighted residuals as indicated by the color bar. In the bottom row, one-dimensional projections (grey bars) are plotted together with the fit result. Weighted residuals are shown above the plots. The individual components of the fit are shown in blue, red, yellow and purple in the one-dimensional projections. Additionally, the second population originating from stochastic labeling is shown in darker color (dark blue, dark red, dark yellow, dark purple) in the one-dimensional projections of $PR_{BG}$ and $PR_{BR}$. (C) Comparison of distances extracted from two-color FRET experiments of BiP (dark grey), taken from Rosam et al. (29), and determined using 3C-PDA (light grey). D) Two-dimensional distance distributions extracted from the measurements of BiP in the presence of ADP (left) and ATP (right) using 3C-PDA without correcting for the stochastic labeling. The distance between the green and red fluorophores, $R_{GR}$, reports on the distance between the lid-domain and the substrate-binding domain. The distance between the blue and green fluorophores, $R_{BG}$, monitors the distance between the substrate-binding and the nucleotide-binding domain. The 3C-PDA confirms the picture obtained from the crystal structures (A): In the presence of ADP, the lid is closed and the interdomain distance shows a broad distribution, indicative of conformational heterogeneity; in the presence of ATP, the lid closes and the distribution width of the interdomain distance is narrower, showing a more defined conformation. See Fig. S18 for the associated 3C-PDA fits and Fig. S19 for a complete display of the inferred distance distribution.

## B.2 Paper 2: Directional Photonic Wire Mediated by Homo-Förster Resonance Energy Transfer on a DNA Origami Platform

Reproduced with permission from *ACS Nano* 2017, 11, 11264-11272. Copyright 2017 American Chemical Society.

ACS NANO
Cite This: ACS Nano 2017, 11, 11264-11272
www.acsnano.org
ARTICLE

# Directional Photonic Wire Mediated by Homo-Förster Resonance Energy Transfer on a DNA Origami Platform

Francesca Nicoli,[†,∥] Anders Barth,[‡,∥] Wooli Bae,[†] Fabian Neukirchinger,[†] Alvaro H. Crevenna,[‡,§] Don C. Lamb,[*,‡] and Tim Liedl[*,†]

[†]Department of Physics and Center for Nanoscience and [‡]Department of Chemistry and Biochemistry and Center for Nanoscience, Ludwig-Maximilians-Universität, 80539 Munich, Germany

*Supporting Information*

**ABSTRACT:** **Elaborating efficient strategies and deepening the understanding of light transport at the nanoscale is of great importance for future designs of artificial light-harvesting assemblies and dye-based photonic circuits. In this work, we focus on studying the phenomenon of Förster resonance energy transfer (FRET) among fluorophores of the same kind (homo-FRET) and its implications for energy cascades containing two or three different dye molecules. Utilizing the spatial programmability of DNA origami, we arranged a chain of cyanine 3 (Cy3) dyes flanked at one end with a dye of lower excitation energy, cyanine 5 (Cy5), with or without an additional dye of higher excitation energy, Alexa488, at the other end. We characterized the response of our fluorophore assemblies with bulk and single-molecule spectroscopy and support our measurements by Monte Carlo modeling of energy transfer within the system. We find that, depending on the arrangement of the fluorophores, homo-FRET between the Cy3 dyes can lead to an overall enhanced energy transfer to the acceptor fluorophore. Furthermore, we systematically analyzed the homo-FRET system by addressing the fluorescence lifetime and anisotropy. Finally, we built a homo-FRET-mediated photonic wire capable of transferring energy through the homo-FRET system from the blue donor dye (Alexa488) to the red acceptor fluorophore (Cy5) across a total distance of 16 nm.**

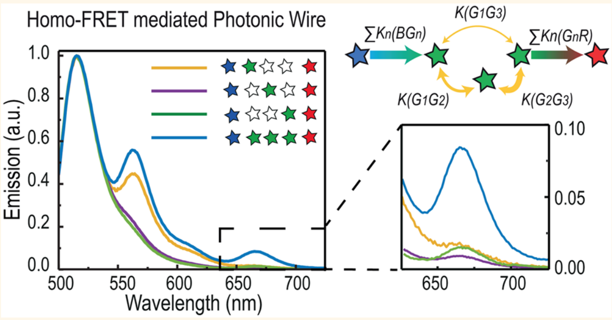

**KEYWORDS:** *artificial light harvesting, homo-FRET, DNA origami, photonic wires, energy transfer, single-molecule FRET*

The phenomenon of light migration *via* resonant energy transfer is of fundamental importance in nature. In photosynthetic organisms,[1−3] light is absorbed by pigments located in the light-harvesting complexes (LHCs) and then transferred through different mechanisms to the reaction center, where the photons' energy is transformed into chemical energy.[1,4,5] Energy transfer on the sub-nanometer length scale between the pigment molecules within the LHC occurs mainly through coupled excitons. Over longer distances (>1 nm), the energy is transferred through dipole−dipole interactions by means of resonance energy transfer.[5−7] To understand and mimic the natural process of light harvesting, it is beneficial to construct artificial systems that efficiently control the transport of light. Great success has already been achieved in creating complex arrangements of dyes and LHCs on different biological platforms such as lipid membranes[8−11] and protein capsids.[12,13] The ability of collecting light with dye clusters is also utilized in dye-sensitized solar cells.[14] Here, inspired by the basic principle of nature's light-harvesting mechanisms, we designed a DNA origami nanostructure to investigate long-range energy transfer by creating a linear arrangement of three spectrally different dyes. The resulting energy landscape allows the energy to be transferred from the excited donor dye through a number of identical transmitter dyes to a single acceptor fluorophore. We investigate the contributions of the different fluorophores to the energy cascade coming from hetero-FRET (Förster resonance energy transfer between two different fluorophores) and homo-FRET (energy transfer between fluorophores of the same kind). Because DNA can be used as a rigid and easily modifiable scaffold for positioning molecules at precise distances and in many different configurations,[15−17] extensive work has been done on constructing photonic networks for light harvesting and photonic circuits on simpler DNA constructs[15,18−26] as well

Received: August 8, 2017
Accepted: October 23, 2017
Published: October 24, 2017

DOI: 10.1021/acsnano.7b05631

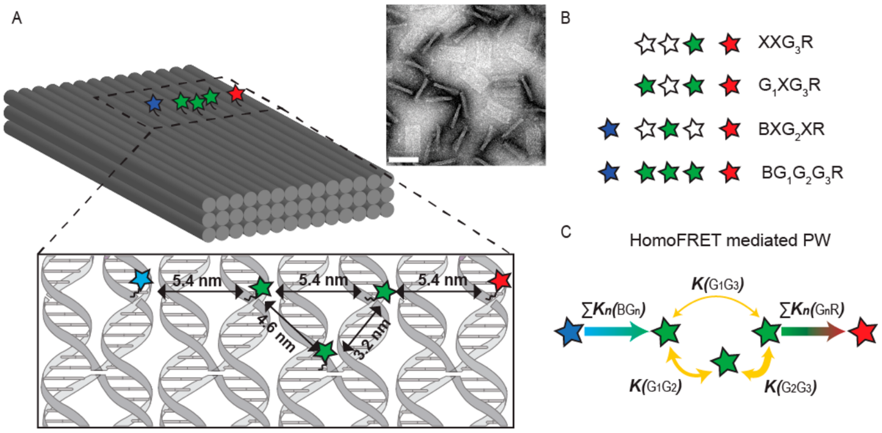

**Figure 1. Homo-FRET-mediated photonic wire. (A) Schematic representation of the three-layered DNA origami block and a TEM image of origami blocks, some of which are lying flat and others standing on their sides (scale bar: 80 nm). In the enlarged region, the scheme indicates the designed locations of the dye molecules with respect to the DNA strands. (B) Examples of wire constructs introducing the nomenclature. Alexa488, Cy3, and Cy5 dyes are depicted as blue, green, and red stars, respectively. Empty stars indicate the absence of a dye at this position. (C) Possible energy pathways of the photonic wire and their corresponding transfer rates. The thickness of the yellow arrows is proportional to the calculated efficiency of the homo-FRET between the two green dyes.**

as more complex DNA origami nanostructures.[16,17,27,28] Previous bulk studies focused on homo-FRET-mediated photonic wires, where the energy is transferred from a high-energy donor to a lower-energy acceptor through a chain of equal energy dyes. Performing FRET studies on DNA origami provides some advantages over simpler double-stranded DNA structure.[18,19,21−23] DNA origami[29−31] offers an efficient and robust way to arrange a large number of dyes in custom-tailored configurations. In fact, by simply exchanging a few specific oligonucleotides, the same nano-breadboard-like structure can be utilized to place different species of dye molecules or other nanocomponents[27,32,33] with nanometer precision in almost arbitrary arrangements in a single plane. Furthermore, the components can be assembled with finely controlled stoichiometry, whereas DNA structures consisting of few strands often require tedious tailoring of DNA strand ratios to achieve a good assembly quality. Another important aspect of using DNA origami for reliable optical characterization is the effectiveness of the purification steps, where it is straightforward to separate large DNA origami objects from individual oligonucleotides or dye molecules.

Here, we assembled a combination of a three-color cascade and a homo-FRET-based photonic wire (PW), achieving energy transfer over a distance of 16 nm from a blue donor dye to a red acceptor dye through three green fluorophores. We focus on the effects of homo-FRET on the overall energy transfer. Specifically, we break down the complex dye cascade into its individual components and, through a systematic analysis of the partial contributions of each dye to the system, we show that the overall energy migration is enhanced by homo-FRET between the donors, as compared to expected transfer efficiency in the absence of homo-FRET. We carried out bulk fluorescence spectroscopy measurements as well as single-molecule (SM) experiments measuring the FRET efficiency, fluorescence lifetime, and fluorescence anisotropy. Finally, Monte Carlo (MC) simulations were performed to obtain a consistent picture of the energy transfer processes.

## RESULTS AND DISCUSSION

**Homo-FRET Wires on DNA Origami.** A schematic drawing of the DNA-origami-supported PW is shown in Figure 1A. The full PW consists of five dyes: one blue donor (Alexa488) with the highest excitation and emission energies, three green dyes (Cy3) of intermediate energies, and one acceptor (Cy5) exhibiting the lowest energies. The dyes are positioned in a quasi-linear arrangement on the upper surface of a three-layered DNA origami block, resembling a 1D wire. The different labeling positions for Cy3 are indicated with a "$G_1$", "$G_2$", or "$G_3$" when the respective dye is present, whereas an "X" indicates the absence of any dye in that position (Figure 1B and Supporting Information 1 Table S1 for the complete list of all constructs). As the blue and red fluorophore are separated by 16 ± 0.6 nm (the distances and corresponding errors are based on the well-known structure of DNA origami objects[34,35] and the flexibility of the linker molecule), energy absorbed from the blue donor to the red acceptor must travel through a multistep energy transfer process *via* one or more intermediate green dyes. Of the multiple possible energy pathways, the most important ones are shown in Figure 1C. The spectral characteristics of the dyes are illustrated in Figure S1 and discussed in Supporting Information 2.

For the homo-FRET system, we determined a Förster radius of 4.6 nm, resulting in expected transfer efficiencies in an isolated system of 90% ($G_2G_3$), 50% ($G_1G_2$), and 27% ($G_1G_3$) between Cy3s in our PW. We assume the dipole−dipole interaction regime, as the minimum separation between the fluorophores is larger than 3 nm.

**Ensemble FRET Experiments.** We first investigate the system with a single acceptor dye and no blue dye, a condition inspired by the energy migration in the LHC from multiple donors to a single acceptor acting as an energy sink, meaning that the chromophore actively depletes the system. To determine the overall energy transfer in this system, we measured bulk fluorescence emission spectra after excitation of the Cy3 fluorophores. Figure 2 shows the spectrum of the construct $G_1G_2G_3R$ with the three homo-FRET green dyes and the red acceptor and the corresponding assembly without acceptor. Clearly, the former spectrum exhibits two emission

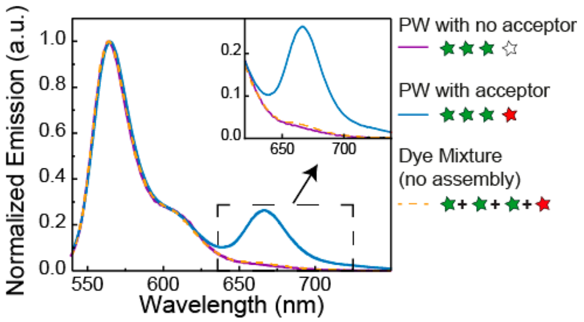

**Figure 2. FRET *vs* non-FRET emission spectra. Bulk emission spectra of the homo-FRET photonic wire with (blue line) and without (purple line) acceptor dye and the mixture of Cy3/Cy5-labeled DNA staples which constitute the photonic wire (orange dashed line), upon 520 nm incident light.**

peaks, one from Cy3 around 560 nm and the second one from Cy5 around 660 nm, indicating the occurrence of FRET, whereas for the latter construct, no red emission is detected. To assess the amount of the direct excitation of Cy5 upon 520 nm incident light, we performed a control where we mixed in a 3:1 ratio the fluorescently labeled DNA staples corresponding to the three green and the one red staple and measured the emission spectrum. A negligible amount of red fluorescence is detected (see inset in Figure 2 and Figure S2 and Supporting Information 3 for the quantification of Cy5 absorption at 520 nm).

To investigate the effect of homo-FRET on the energy transfer, we measured the emission from the single Cy3/Cy5 hetero-FRET pairs ($G_1XXR$, $XG_2XR$, and $XXG_3R$) and $G_1G_2G_3R$. This assembly shows a significant increase in Cy5 fluorescence compared to the constructs with only one donor. The measured increase in absolute fluorescence is expected in hetero-FRET systems from the contribution of multiple donors.[17] To quantify the contribution of multiple donor dyes on the energy transfer, we compared the sum of the individual Cy3/Cy5 pairs to the full construct (Figure 3A, gray spectrum). Overall, we found that this energy delocalization results in a small increase of Cy5 emission compared to the sum of the single contributions of $G_1$, $G_2$, and $G_3$. When calculating the corresponding energy transfer efficiency, we find that the three-donor construct leads to an increase of $\Delta E = 0.01$, compared to the averaged contribution of single hetero-FRET pairs. This increase corresponds to an enhancement of 7.5% (see Table 1 and Supporting Information 3 and 4 for bulk efficiency and enhancement calculations). Due to heterogeneity of samples, this increase falls within variability, but it is consistently present in every sample batch measured. It should be noted that while $G_1G_2G_3R$ has an overall lower FRET efficiency compared to the $XXG_3R$ construct, the overall transfer to the acceptor is enhanced as is evident from the increased Cy5 emission. The decreased FRET efficiency is a consequence of the increasingly larger distance between the additional donors $G_1$ and $G_2$ from the acceptor.

To analyze all the possible energy transfer pathways, we assembled a series of partial constructs with two green dyes (Figure 3B–D). For the $G_1G_2XR$ construct, we observe a slight

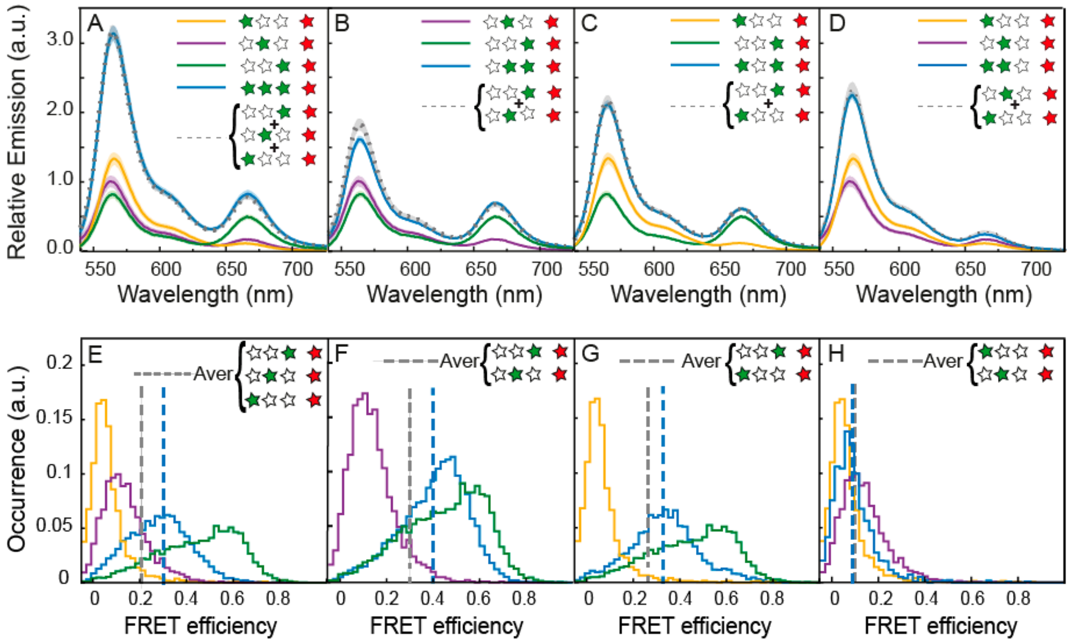

**Figure 3. Two-color cascade. (A–D) Bulk emission spectra of constructs carrying a variable number of Cy3 dyes and a single Cy5 acceptor. The recorded emission intensities are normalized by the intensity of the Cy5 emission after Cy5 excitation in order to account for differences in sample concentration. The shading around the plotted lines indicates the error of the mean (the final spectra are the result of an average of multiple measurements on at least six different sample batches). The comparison between the spectra of the constructs containing two Cy3 dyes (blue lines) and the mathematical sum of the spectra of the respective partial constructs with only one Cy3 (gray lines) is shown for $XG_2G_3R$ (A), $G_1XG_3R$ (B), $G_1G_2XR$ (C), and $G_1G_2G_3R$ (D). (E–H) SM FRET histograms of constructs carrying a variable number of Cy3 dyes and a single Cy5 acceptor. Occurrence values are normalized by the histogram areas. Each histogram contains at least 2000 events. Dashed lines indicate the average efficiency.**

DOI: 10.1021/acsnano.7b05631
*ACS Nano* 2017, 11, 11264–11272

Table 1. FRET Efficiencies with Their Absolute Error from Bulk and SM Measurements and MC Calculations[a]

| | $G_1XXR$ | $XG_2XR$ | $XXG_3R$ | $G_1G_2XR$ | $G_1XG_3R$ | $XG_2G_3R$ | $G_1G_2G_3R$ |
|---|---|---|---|---|---|---|---|
| $E_{bulk}$ | 0.05 ± 0.004 | 0.12 ± 0.009 | 0.36 ± 0.02 | 0.07 ± 0.004 | 0.21 ± 0.009 | 0.29 ± 0.01 | 0.19 ± 0.001 |
| $\Delta E$ | | | | −0.015 ± 0.011 | 0.000 ± 0.025 | 0.040 ± 0.027 | 0.011 ± 0.028 |
| $E_{SM}$ | 0.06 ± 0.002 | 0.13 ± 0.002 | 0.45 ± 0.002 | 0.09 ± 0.002 | 0.33 ± 0.002 | 0.4 ± 0.001 | 0.28 ± 0.002 |
| $\Delta E$ | | | | −0.01 ± 0.003 | 0.07 ± 0.003 | 0.11 ± 0.003 | 0.06 ± 0.004 |
| $E_{MC}$ | 0.03 | 0.10 | 0.28 | 0.07 | 0.15 | 0.22 | 0.15 |
| $\Delta E$ | | | | 0.005 | −0.005 | 0.025 | 0.014 |

[a] The efficiency increment $\Delta E$ is calculated as the difference between the averaged efficiency of single hetero-FRET pairs and their corresponding homo-FRET construct.

decrease in red emission, compared to the sum of $G_1XXR$ and $XG_2XR$, whereas the difference of green emission falls within the sample variability, indicating a slight reduction of the energy transfer efficiency. No consistent difference in energy transfer is observed for $G_1XG_3R$ when compared to the sum of $XXG_3R$ and $G_1XXR$. The construct $XG_2G_3R$, on the other hand, shows an energy transfer increase of $\Delta E = 0.04$ compared to the average contribution of $XXG_3R$ and $XG_2XR$. This result indicates an enhancement of the energy transfer of about 18%, where both hetero- and homo-FRET occur with the highest efficiency. However, in ensemble experiments, an average value is measured, and errors arising from variations in dye−DNA labeling efficiencies and incomplete DNA staple incorporation cannot be easily corrected, limiting our understanding of the system.

**Single-Molecule FRET Experiments.** To address these limitations and to obtain complementary data, we performed single-molecule FRET measurements in solution by burst analysis.[36] Through this tecnique, single molecules are measured at picomolar concentration as they diffuse through the femtoliter-sized observation volume of a confocal microscope on the time scale of a few milliseconds. Fluorescence bursts coming from a single origami are isolated and analyzed. By using pulsed interleaved excitation,[36] we can selectively investigate only those constructs that carry both an active donor and an active acceptor dye (see Supporting Information 6 and Figure S3). The single-molecule FRET results are thus not biased by the efficiency of acceptor strand incorporation into the origami, by the labeling efficiency of the acceptor strand, nor by long-lived dark states of the fluorophore. In fact, we find that the fraction of constructs missing an active acceptor fluorophore varies between 7 and 23%, which affects the ensemble results (see Supporting Information Table S3).

We measured single-molecule distributions of the green to red energy transfer efficiency again for samples with one Cy5 acceptor and one, two, or three Cy3 donors (Figure 3E−H). Generally, we observe broad distributions of FRET efficiencies beyond what is expected from photon shot-noise even for constructs with a single Cy3 dye. This heterogeneity could be caused by interactions of the dyes with the DNA, which can affect the quantum yield and thus lead to a distribution of observed transfer efficiencies. We obtain mean apparent energy transfer efficiencies of $E = 0.06$ for $G_1XXR$, $E = 0.13$ for $XG_2XR$, and $E = 0.45$ for $XXG_3R$, which qualitatively correspond to what we measured in ensemble FRET experiments.

As before, we compare the average transfer efficiency of the individual Cy3/Cy5 pairs to the average transfer efficiency of the constructs with two or three Cy3 dyes. For the single-molecule FRET efficiency histograms, the average FRET efficiencies are given by the dashed lines in Figure 3E−H. SM measurements allows us to obtain a distribution of FRET efficiencies which is not possible through bulk measurements. To compare the contributions of the individual FRET pairs with respect to the full photonic wire, we here have to consider the average value of transfer efficiencies. The increased energy transfer efficiency observed in the bulk measurements for constructs $G_1G_2G_3R$ and $XG_2G_3R$ is seen more clearly by the single-molecule measurements, where, compared to the single Cy3 constructs, we observe an increase in energy transfer of $\Delta E = 0.11$ and $\Delta E = 0.06$, corresponding to an enhancement of 38 and 28% for $XG_2G_3R$ and $G_1G_2G_3R$, respectively. In the ensemble measurements, no enhancement was observed for $G_1XG_3R$. However, in the single-molecule experiments, we measure an energy transfer increase of 27%. This increase in sensitivity in the single-molecule experiments comes from the ability to only select DNA origami structures with both photoactive donor and acceptor fluorophores. Thus, single-molecule experiments are not influenced by the contributions from the donor-only species and are more robust for different sample preparations with varying amounts of fluorescent labeling. By correcting the ensemble FRET efficiencies using knowledge of the fraction of Cy3-only molecules determined from burst analysis experiments, we find that the quantitative agreement between ensemble and single-molecule experiments is increased (see Table S5). The construct $G_1G_2XR$ shows no significant change in both single-molecule and ensemble FRET experiments.

Homo-FRET can be interpreted as a diffusive process between molecules without preferential direction.[13,19,23] If the green fluorophores were acting as independent molecules, the emission of the full construct should be equivalent to the sum of the single components; that is, the ensemble of independent energy pathways should be equal to the sum of the parts. Our observations of enhanced energy transfer in the constructs $XG_2G_3R$ and $G_1G_2G_3R$, however, indicate that the dyes are not acting independently but that homo-FRET is contributing to the increase of energy transfer. Given our experimental conditions, saturation effects are precluded, and only one green dye is excited at any time. Previous studies showed that cyanine dyes linked to DNA exhibit Förster behavior down to a distance of ~8 base pairs,[37] and heterodimer formation was only observed at distances of <6 base pairs.[37−39] We thus rule out the eventuality of contact quenching and dye−dye strong interactions and consider the role homo-FRET is playing in the energy transfer process. The short distance between the green dyes promotes an efficient energy exchange among them, whereas the proximity of $G_3$ to the acceptor dye, which acts as an energy sink, depletes the energy from the homo-FRET system. Here, the hetero-FRET process creates an energy drain on $G_3$, which can subsequently accept more energy from $G_1$ and $G_2$ and again transfer it to the final acceptor. This

DOI: 10.1021/acsnano.7b05631
ACS Nano 2017, 11, 11264−11272

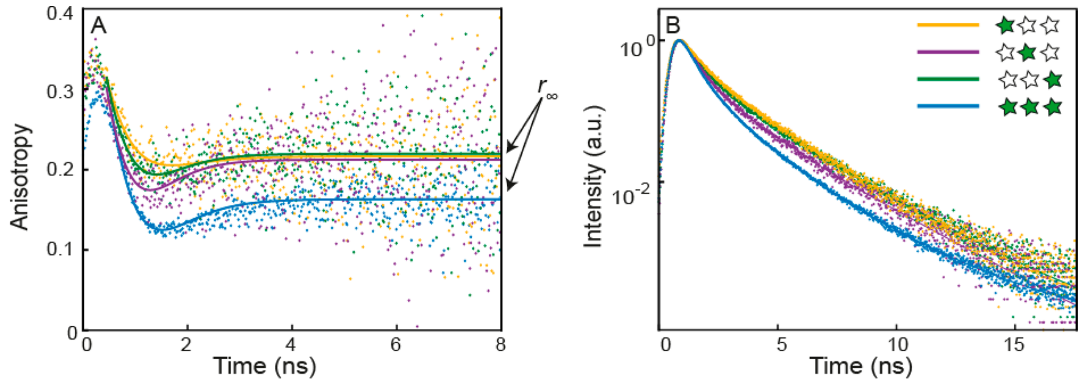

**Figure 4. Single-molecule fluorescence anisotropy and fluorescence lifetimes. (A) Time-resolved fluorescence anisotropy decays of Cy3-labeled DNA origami. The anisotropy decays of the single-labeled constructs, $G_1$, $G_2$, and $G_3$ (orange, purple, and green line, respectively) show similar behavior, whereas the decay of the triple-labeled construct ($G_1G_2G_3$, blue line) shows decreased anisotropy, confirming homo-FRET occurrence. (B) Fluorescence lifetimes of the same constructs. The lifetime decay of $G_1G_2G_3R$ (blue) shows a reduction in lifetime compared to that of the single-labeled constructs.**

**Table 2. Residual Fluorescence Anisotropy ($r_\infty$) and Average Fluorescence Lifetime ($\tau$) of Single- And Triple-Labeled Cy3 Constructs**[a]

| | $G_1XX$ | $XG_2X$ | $XXG_3$ | $G_1G_2G_3$ | $G_1G_2X$ | $G_1XG_3$ | $XG_2G_3$ |
|---|---|---|---|---|---|---|---|
| $r_\infty$ | 0.219 ± 0.007 | 0.216 ± 0.009 | 0.223 ± 0.006 | 0.167 ± 0.004 | 0.203 ± 0.007 | 0.198 ± 0.004 | 0.188 ± 0.006 |
| $\Delta r_\infty$ | | | | 0.052 ± 0.006 | 0.014 ± 0.009 | 0.023 ± 0.006 | 0.032 ± 0.008 |
| $\tau$ (ns) | 1.57 ± 0.04 | 1.34 ± 0.06 | 1.52 ± 0.09 | 1.09 ± 0.03 | 1.20 ± 0.07 | 1.27 ± 0.02 | 1.27 ± 0.05 |
| $\Delta\tau$ (ns) | | | | 0.40 ± 0.05 | 0.27 ± 0.08 | 0.27 ± 0.05 | 0.16 ± 0.07 |

[a] $\Delta r_\infty$ and $\Delta\tau$ indicate the differences of these values for the multiple-dye constructs with respect to the average value of the single-dye constructs. Errors are given as 95% confidence intervals.

mechanism of efficient migration of energy from $G_3$ to R could explain the increased energy transfer of these constructs. In the $G_1XG_3R$ assembly, only a small enhancement was observed in the ensemble experiments, but a clear enhancement is evident from the single-molecule results. Here, the homo-FRET distance is larger than that in the constructs $G_1G_2G_3R$ and $XG_2G_3R$, resulting in a reduced homo-FRET transfer efficiency. In spite of the reduced delocalization of energy over the homo-FRET system, the results indicate that the depletion by $G_3$ still results in an enhancement of energy transfer. On the other hand, for $G_1G_2XR$, the lower efficiency of hetero-FRET diminishes the depletion of the homo-FRET system by the energy sink, resulting in no net enhancement for this construct.

**Monte Carlo Simulations.** As the contribution of a homo-FRET system to energy transfer is not intuitive, we confirmed the enhancement by modeling our photonic wire with MC simulations. The MC simulations were performed using standard theory of Förster-type energy transfer. To better simulate our system, we incorporate the limited rotational freedom of the fluorophores on the origami platform into the calculation. Often, the dipole moments of fluorophores are assumed to rotate freely so that the orientation factor, $\kappa^2$, for the FRET efficiency averages to 2/3. However, the attachment of the fluorophores to the flat surface of our DNA construct limits the accessible volume of the dyes. Additionally, the rotational freedom can be partially hindered by the interaction between the dyes and the DNA.[37,40,41] These considerations can be implemented by sampling different angle configurations for each energy transfer step in the system. Here, we modeled all the partial and the full homo-FRET constructs assuming isotropic dipole orientations within a half-sphere for the different dyes and no preferential directionality for the energy transfer in the homo-FRET part of the wire. We used the experimental values of FRET efficiency from fluorescence bulk measurements of single hetero-FRET pairs to establish the simulations parameters. For the rate of homo-FRET, we used the expected efficiency values calculated from overlap integral and distance between the green dyes. From the simulations, we obtained overall transfer efficiencies in very good agreement with our bulk experimental values (see Table 1). Importantly, the FRET efficiencies from the MC calculation of homo-FRET constructs also show an increased energy transfer of 16% for $XG_2G_3R$ and 10% for $G_1G_2G_3R$ and a negligible change for $G_1XG_3R$ and $G_1G_2XR$ ($\Delta E < 0.01$).

**Fluorescence Lifetime and Anisotropy Measurements Elucidate the Contributions of Homo-FRET.** To investigate homo-FRET in the absence of hetero-FRET, we need to use anisotropy information as the fluorescence lifetime should not change for an ideal homo-FRET system nor can FRET be calculated *via* spectral shifts. Fortunately, anisotropy data are available from the single-molecule multiparameter fluorescence detection experiments with pulsed interleaved excitation.[36] Anisotropy uses the polarization of the excited and emitted photons to measure the orientation of the molecule. The anisotropy decreases due to molecular rotation as well as *via* energy transfer. Figure 4A shows the time-resolved anisotropy decay of the various constructs (for constructs carrying two Cy3 dyes, see Figure S4). The emitted photons preferentially have the same polarization as the excitation light at short times, which quickly decays. The "dip-and-rise" behavior with an initial fast decay of the anisotropy and subsequent rise to the residual anisotropy value occurs in the presence of distinct states of the dye that exhibit different rotational flexibility and different fluorescence lifetimes.[42] Especially for cyanine dyes

DOI: 10.1021/acsnano.7b05631
ACS Nano 2017, 11, 11264−11272

such as Cy3 and Cy5, it is well-known that steric hindrance affects the isomerization rate to the nonfluorescent cis isomer, leading to an increase in brightness and fluorescence lifetime.[41,43,44] At early time lags, the anisotropy decay is dominated by the contribution of the short lifetime species, whereas at long time lags, only the long lifetime species contribute. After the initial decay of the anisotropy due to the fluorophore rotation, the decay levels off to a residual value, $r_\infty$, reporting on the slow rotation of the origami. The model to describe the decay (solid lines in Figure 4A) is outlined in detail in the Supporting Information 8. In the singly labeled constructs, the decay in anisotropy is due to rotation of the fluorophores. For the full construct, a larger drop in anisotropy is observed due to homo-FRET.[45−48] Here, we focus only on the residual anisotropy $r_\infty$ as an indicator of homo-FRET (Table 2).

The triple-labeled construct, $G_1G_2G_3$, showed the largest change in the residual anisotropy ($\Delta r_\infty$ = 0.052), a clear indication for efficient homo-FRET. All double-labeled constructs also exhibited a reduced residual anisotropy compared to the single-labeled constructs. The highest difference is observed for the construct $XG_2G_3$ ($\Delta r_\infty$ = 0.032) and the lowest for $G_1G_2X$ ($\Delta r_\infty$ = 0.014). Surprisingly, $G_1XG_3$ ($\Delta r_\infty$ = 0.023) shows a higher change in residual anisotropy and thus a higher efficiency of homo-FRET than $G_1G_2X$, even though the distance between the dyes is larger (5.4 nm *vs* 4.6 nm). The influence of the dipole−dipole orientation is an important factor in FRET.[49] In the case of homo-FRET, the measured anisotropies for the single-labeled constructs of $r_\infty \approx 0.22$ for donor and acceptor indicate a possible effect of the orientation on the transfer efficiency. Furthermore, the interdependence of the quantum yield and steric hindrance for Cy3 introduces a correlation between the rotational flexibility and the Förster radius. Thus, differences in the local environment or dipole orientation could account for the higher homo-FRET efficiency of $G_1XG_3$ construct with respect to $G_1G_2X$. As a control, we measured a construct with large separation between the three Cy3 dyes, yielding no significant change in the residual anisotropy ($r_\infty$ = 0.226) (see Figure S4 for measurements and details on dyes arrangement).

We additionally investigated the fluorescence lifetime of the different constructs. In all cases, Cy3 showed a complex fluorescence decay, which we analyzed using a three-component exponential model function (see lifetime distributions in Figure S5).[42,44] The three lifetime components of the single-labeled constructs are 0.33 ± 0.08, 1.14 ± 0.20, and 2.60 ± 0.01 ns. In the following, we focus our discussion on the average fluorescence lifetime (see Table 2). Among the single-labeled constructs, $G_2$ shows a shorter average lifetime. We attribute the difference in lifetimes to the position on the origami structure and to the different way the fluorophore is linked to the staple strand. It is well-known that the behavior of dyes, in particular, their quantum yield and rotational flexibility, is influenced both by neighboring DNA bases through stacking interactions and sequence-dependent enhancement and quenching and by the covalent coupling of the dye to DNA.[41,44,50,51] The Cy3 molecule in position $G_2$ is the only one directly linked to a thymine base on a modified DNA strand, whereas the fluorophores in positions $G_1$ and $G_3$ are terminally linked to the 5′-end of the DNA strands, and an extra unpaired thymine base has been added as a spacer to prevent quenching from other DNA bases on the origami surface. Therefore, we attribute the difference in lifetime to the different linker flexibility and local environment surrounding the dyes. Furthermore, the longer lifetime of positions $G_1$ and $G_3$ is likely caused by transient base-stacking interactions with the unpaired thymine.[41,44] Interestingly, looking at the average lifetime per molecule measured in our single-molecule experiments (Figure S5), we observe broad distributions ranging from 0.6 to 2 ns. This observation indicates that the dye−origami interactions persist for time scales longer than the diffusion of origami through the observation volume of ∼10 ms.

In general, all constructs with multiple green dyes show reduced lifetimes compared to the single-labeled ones. Theoretically, homo-FRET should not result in a change of the observed fluorescence lifetimes and the quantum yield.[46] However, this conclusion only holds true when the dyes behave identically. In our case, multiple lifetime components are observed and, although the absolute values of the three lifetime components do not change significantly, a reduction in the fraction of the long lifetime component is observed (see Supporting Information 9 Table S5 and lifetime distribution plots Figures S5 and S6). The observed change of the fluorescence lifetime is larger for the triple-labeled construct, which also exhibits the highest decrease in anisotropy. We speculate that the decrease in lifetime is most likely a consequence of the existence of multiple lifetime components. The longer a molecule remains in the excited state, the higher probability it has to undergo FRET. Thus, the longer lifetime component will contribute more strongly to the homo-FRET system and the shorter lifetime components have a higher probability of dissipating the energy.

**Three-Color Photonic Wire with Localized Excitation.** We have demonstrated that our intermediate dyes can perform homo-FRET and that this phenomenon does lead to higher-energy transfer over the 10.5 nm distance of the dye assembly with respect to the single FRET pairs. However, any one of the three green dyes can be initially excited in the system. To localize the excitation and study directed energy transfer through the homo-FRET system, we investigated the full three-color cascade PW, where a blue primary donor is placed 5.4 nm from $G_1$ (cf. Figure 1). After verifying that no energy transfer occurs between the blue donor and the red acceptor without intermediate green dyes (Supporting Information 10 Figure S8), we separately measured the previous constructs in the presence of the blue fluorophore. To estimate the energy transfer efficiency from the blue donor to the red acceptor dye, we use the percentage of red signal after excitation of the blue dye. This apparent energy transfer efficiency for SM FRET is not corrected for spectral cross-talk or cross-excitation and only serves as an indicator to compare the relative efficiency of the different constructs (see Supporting Information 11). The efficiency calculated for bulk measurements is corrected for spectral cross-talk but not for cross-excitation (see Supporting Information 12). The presence of only one intermediate green dye results in very low or undetectable emission from the red acceptor ranging from 0.6 to 1.3% in bulk measurements and between 3 and 5% in SM measurements (Figure S9 and Table S7 for smFRET experiments and Figure S10 and Table S9 for bulk experiments). Using the fluorescence lifetime of Alexa488, we estimate the FRET efficiency from the blue dye to the individual Cy3 positions to be 52% to position $G_3$, 13% to position $G_2$, and 4% to position $G_1$ (see Table S8). For constructs with two green dyes, we observed an increase in the apparent transfer efficiency from the blue dye to the red fluorophore ranging from 5 to 9% for SM FRET and from 1.3

to 3.3% for bulk measurements. Our full photonic wire with all three Cy3s produces an increase in energy transfer efficiency to 5% measured in bulk (see Supporting Information 12 and Table S9 for efficiency estimation) and 10% in the SM measurements (Table S7). To visualize this increase, we compared the sum of the red emissions of all single Cy3 dye wires, $BXXG_3R$, $BXG_2XR$, and $BG_1XXR$, with the complete wire $BG_1G_2G_3R$ (Figure 5). As exciting the blue donor at 490 nm results in partial excitation of Cy3, we also performed bulk measurements with 460 nm excitation (see Figure S11). The results are consistent with the spectra obtained with 490 nm excitation.

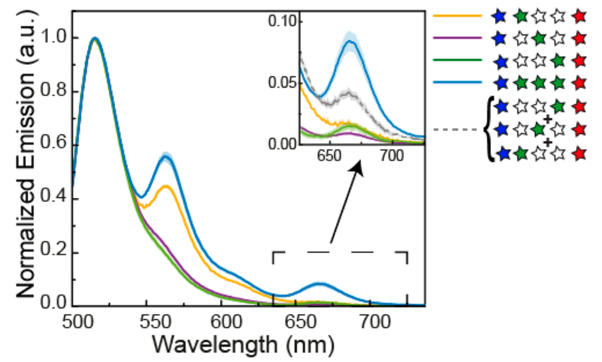

**Figure 5. Three-color cascade. (A) Normalized emission spectra of the three-color cascade after Alexa488 excitation. Due to spectral overlap between Alexa488 and Cy3, the green emission peak around 550 nm becomes only apparent for constructs where the closest dye to the blue donor is present. Inset: Zoomed-in image into the Cy5 emission spectral region. Wires with only one green dye do not show a significant emission of the red acceptor. Cy5 emission appears when all three Cy3 dyes are present. The gray line represents the arithmetic sum of the red signals from $BG_1XXR$, $BXG_2XR$, and $BXXG_3R$, which is significantly lower than the red emission from $BG_1G_2G_3R$.**

Finally, we modeled the three-color energy transfer process with MC simulations. By accounting for the partial direct excitation of Cy3 dyes in the simulation, the calculated values are in very good agreement with our experimental findings (see Table S10). Most importantly, the overall transfer efficiency is 4.4%, which is significantly higher than the arithmetic sum of the constructs with only one intermediated green dye (2%).

## CONCLUSION

In this work, we demonstrated a photonic wire mediated by a homo-FRET chain of three Cy3 fluorophores. Our observations show that homo-FRET among the Cy3 dyes can have an enhancing effect on the overall energy transfer to the acceptor fluorophore. The occurrence of homo-FRET between all Cy3 dyes was confirmed by a decrease of the fluorescence anisotropy. Furthermore, we found that homo-FRET can significantly change the fluorescence lifetime and thus quantum yield of Cy3, an effect that is not predicted from FRET theory alone. Last, we showed that energy can be transferred through the homo-FRET system from a blue donor dye to a red acceptor dye over a distance of 16 nm.

In summary, the energy transfer enhancement and the insights about the homo-FRET process investigated in our work can be utilized as a guide to extract design principles for complex light-harvesting assemblies on biological platforms, such as DNA, protein capsids, and lipid membranes as well as on artificial systems such as dye-sensitized solar cells.

## MATERIALS AND METHODS

**Dyes and DNA Origami.** The DNA origami structure used in our experiments is a square lattice three-layer brick-like structure (for origami design, DNA sequences, and folding conditions, see Supporting Information 14). The dyes were incorporated in the DNA structure during folding by adding the desired dye-labeled DNA strands in the mixture of ssDNA scaffold, staples, and buffer. All the samples were purified with poly(ethylene glycol) precipitation[52,53] before fluorescence measurements were performed.

The dye-functionalized DNA strands were purchased from IBA GmbH (Göttingen, Germany). Both internal (on thymine base) and terminal (on 5′-end) functionalization were carried out through NHS ester coupling. For details on dye-labeled DNA strands, see Table S11.

**Bulk Fluorescence Spectroscopy.** Bulk fluorescence measurements were carried out with a modular spectrofluorometer Fluorolog3 (Horiba Scientific). For the measurements, the sample was transferred into a cuvette with a 2 × 10 mm optical path (Hellma Analytics). The samples consist of 100 $\mu$L of 10 nM DNA origami carrying different dyes combinations in a buffer solution (10 mM Tris, 1 mM EDTA, and 20 mM $MgCl_2$).

Each construct was independently assembled and measured at least six times. Fluorescence emission spectra were recorded, and the FRET efficiency was calculated from the relative intensities of the donor and acceptor fluorescence. To avoid direct excitation of Cy5, Cy3 was excited at 520 nm instead of its absorbance maximum at 555 nm. We normalized the emission spectra with respect to the Cy5 emission after excitation at 640 nm in order to correct for different sample concentrations.

**Single-Molecule Fluorescence.** Single-molecule measurements of FRET efficiency, fluorescence lifetime, and anisotropy were performed on a custom-built confocal microscope. DNA origami samples were diluted to concentrations of 100 pM in 10 mM Tris, 1 mM EDTA, 20 mM $MgCl_2$, and 1 mM Trolox to reduce photoblinking and bleaching. The fluorophores were excited using pulsed interleaved excitation[36] at the laser excitation lines at 482, 561, and 641 nm (LDH-D-C-485, LDH-D-TA-560, LDH-D-C-640, Picoquant, Berlin, Germany). Laser powers of 110 $\mu$W for the blue laser, 80 $\mu$W for the green laser, and 40 $\mu$W for the red laser, as measured before the objective, were used. Fluorescence was collected by a 60× water immersion objective (60×/1.27 WI, Nikon, Düsseldorf, Germany), separated from the excitation light by a polychroic mirror (zt405/488/561/633), and focused through a 50 $\mu$m pinhole. It was then split according to polarization (PBS251, Thorlabs, Dachau, Germany) and wavelength (dichroic mirrors BS560 and 640DCXR) and filtered by the emission filters for blue (ET525/50), green (ET607/36), and red (ET670/30) fluorescence (AHF Analysentechnik, Tübingen, Germany). The signals were detected on six avalanche photodiodes (Count-100B, Laser Components, Olching, Germany; SPCM-AQR-14, SPCM-AQRH-14, PerkinElmer, Hamburg, Germany) and recorded by time-correlated single-photon electronics (HydraHarp 400, Picoquant, Berlin, Germany). Data analysis was performed using custom software written in MATLAB.

**Monte Carlo Simulation on Energy Transfer Efficiency.** The emission from each dye was calculated by using Monte Carlo simulation that samples different orientation of fluorophores. The angles of fluorophore dipole $\theta$ and $\varphi$ were isotropically varied from $-\pi$ to $-\pi$ and $-\pi/2$ to $-\pi/2$, respectively, to take account of fluorophores rotating on the surface of a DNA nanostructure. The transfer rate from each Cy3 to Cy5 was calculated from the control bulk measurement, and homotransfer rate and Alexa488 to Cy3 transfer rate was calculated from the spectral overlap $J$. We assume that a fluorophore in an excited state has three pathways—radiative decay, nonradiative decay, and energy transfer. Radiative decay and nonradiative decay were calculated from the quantum yield of fluorophores. The orientation factor $\boldsymbol{\kappa}^2$ was calculated from $\boldsymbol{\kappa} = \hat{\mu}_D \cdot \hat{\mu}_A - 3(\hat{\mu}_D \cdot \hat{R}_{AD})(\hat{\mu}_A \cdot \hat{R}_{DA})$, where $\hat{\mu}_D$ and $\hat{\mu}_A$ are the normalized dipole moment of each fluorophore, which undergo rotation, and $\hat{R}_{AD}$ and $\hat{R}_{DA}$ denote normalized interfluorophore distance vector. We sampled 4000 configurations of angles over 10 energy transfer cycles, which were enough to acquire a converging value of the emission from each fluorophore.

## ASSOCIATED CONTENT

### Supporting Information

The Supporting Information is available free of charge on the ACS Publications website at DOI: 10.1021/acsnano.7b05631.

> Spectral characteristics of the dyes, control experiments, additional fluorescence spectroscopy data, description of fitting models and parameters, and DNA origami structure design (PDF)

## AUTHOR INFORMATION

### Corresponding Authors

*E-mail: d.lamb@lmu.de.
*E-mail: tim.liedl@physik.lmu.de.

### ORCID

Tim Liedl: 0000-0002-0040-0173

### Present Address

[§]Instituto de Tecnologia Química e Biológica António Xavier, Universidade Nova de Lisboa, 2780-157 Oeiras, Portugal.

### Author Contributions

[‖]F.N. and A.B. contributed equally to this work. F. Nicoli and T.L. designed the study and planned experiments. F. Nicoli and F. Neukirchinger fabricated the samples and performed and analyzed the ensemble measurements. A.B. and D.C.L. planned the single-molecule experiments. A.B. performed and analyzed the single-molecule experiments. F. Nicoli, W.B., and T.L. planned the Monte Carlo simulation, and W.B. performed the simulations. All authors have read and contributed to the manuscript.

### Notes

The authors declare no competing financial interest.

## ACKNOWLEDGMENTS

The authors are grateful for financial support from the European Commission through the ERC Grant Agreement No. 336440, ORCA, from the Volkswagen foundation, from the Deutsche Forschungsgemeinschaft (DFG) through the SFB1032 (Project A6 and B3) and the Ludwig-Maximillians-Universität München *via* the Center for NanoScience Munich (CeNS) and LMUinnovativ initiative BioImaging Network (BIN).

## REFERENCES

(1) Scholes, G. D.; Fleming, G. R.; Olaya-Castro, A.; van Grondelle, R. Lessons from Nature about Solar Light Harvesting. *Nat. Chem.* **2011**, *3*, 763−774.

(2) Hu, X.; Damjanovic, A.; Ritz, T.; Schulten, K. Architecture and Mechanism of the Light-Harvesting Apparatus of Purple Bacteria. *Proc. Natl. Acad. Sci. U. S. A.* **1998**, *95*, 5935−5941.

(3) van Amerongen, H.; Croce, R. Light Harvesting in Photosystem II. *Photosynth. Res.* **2013**, *116*, 251−263.

(4) Cheng, Y.-C.; Fleming, G. R. Dynamics of Light Harvesting in Photosynthesis. *Annu. Rev. Phys. Chem.* **2009**, *60*, 241−262.

(5) Scholes, G. D. Long-Range Resonance Energy Transfer in Molecular Systems. *Annu. Rev. Phys. Chem.* **2003**, *54*, 57−87.

(6) Andrews, D. L.; Crisp, R. G. Theory of Directed Electronic Energy Transfer. *J. Fluoresc.* **2006**, *16*, 191−199.

(7) Daniels, G. J.; Jenkins, R. D.; Bradshaw, D. S.; Andrews, D. L. Resonance Energy Transfer: The Unified Theory Revisited. *J. Chem. Phys.* **2003**, *119*, 2264−2274.

(8) Sumino, A.; Dewa, T.; Kondo, M.; Morii, T.; Hashimoto, H.; Gardiner, A. T.; Cogdell, R. J.; Nango, M. Selective Assembly of Photosynthetic Antenna Proteins into a Domain-Structured Lipid Bilayer for the Construction of Artificial Photosynthetic Antenna Systems: Structural Analysis of the Assembly Using Surface Plasmon Resonance and Atomic Force Microscopy. *Langmuir* **2011**, *27*, 1092−1099.

(9) Nagata, N.; Kuramochi, Y.; Kobuke, Y. Energy Transfer among Light-Harvesting Macrorings Incorporated into a Bilayer Membrane. *J. Am. Chem. Soc.* **2009**, *131*, 10−11.

(10) Nagata, M.; Yoshimura, Y.; Inagaki, J.; Suemori, Y.; Iida, K.; Ohtsuka, T.; Nango, M. Construction and Photocurrent of Light-Harvesting Polypeptides/Zinc Bacteriochlorophyll a Complex in Lipid Bilayers. *Chem. Lett.* **2003**, *32*, 852−853.

(11) Bhosale, S. Photoproduction of Proton Gradients with $\pi$-Stacked Fluorophore Scaffolds in Lipid Bilayers. *Science* **2006**, *313*, 84−86.

(12) Nam, Y. S.; Shin, T.; Park, H.; Magyar, A. P.; Choi, K.; Fantner, G.; Nelson, K. A.; Belcher, A. M. Virus-Templated Assembly of Porphyrins into Light-Harvesting Nanoantennae. *J. Am. Chem. Soc.* **2010**, *132*, 1462−1463.

(13) Park, H.; Heldman, N.; Rebentrost, P.; Abbondanza, L.; Iagatti, A.; Alessi, A.; Patrizi, B.; Salvalaggio, M.; Bussotti, L.; Mohseni, M.; et al. Enhanced Energy Transport in Genetically Engineered Excitonic Networks. *Nat. Mater.* **2015**, *15*, 211−216.

(14) Mishra, A.; Fischer, M. K. R.; Bäuerle, P. Metal-Free Organic Dyes for Dye-Sensitized Solar Cells: From Structure: Property Relationships to Design Rules. *Angew. Chem., Int. Ed.* **2009**, *48*, 2474−2499.

(15) Buckhout-White, S.; Spillmann, C. M.; Algar, W. R.; Khachatrian, A.; Melinger, J. S.; Goldman, E. R.; Ancona, M. G.; Medintz, I. L. Assembling Programmable FRET-Based Photonic Networks Using Designer DNA Scaffolds. *Nat. Commun.* **2014**, *5*, 5615.

(16) Dutta, P. K.; Varghese, R.; Nangreave, J.; Lin, S.; Yan, H.; Liu, Y. DNA-Directed Artificial Light-Harvesting Antenna. *J. Am. Chem. Soc.* **2011**, *133*, 11985−11993.

(17) Hemmig, E. A.; Creatore, C.; Wünsch, B.; Hecker, L.; Mair, P.; Parker, M. A.; Emmott, S.; Tinnefeld, P.; Keyser, U. F.; Chin, A. W. Programming Light-Harvesting Efficiency Using DNA Origami. *Nano Lett.* **2016**, *16*, 2369−2374.

(18) Melinger, J. S.; Khachatrian, A.; Ancona, M. G.; Buckhout-White, S.; Goldman, E. R.; Spillmann, C. M.; Medintz, I. L.; Cunningham, P. D. FRET from Multiple Pathways in Fluorophore-Labeled DNA. *ACS Photonics* **2016**, *3*, 659−669.

(19) Hannestad, J. K.; Gerrard, S. R.; Brown, T.; Albinsson, B. Self-Assembled DNA-Based Fluorescence Waveguide with Selectable Output. *Small* **2011**, *7*, 3178−3185.

(20) Adeyemi, O. O.; Malinovskii, V. L.; Biner, S. M.; Calzaferri, G.; Häner, R. Photon Harvesting by Excimer-Forming Multichromophores. *Chem. Commun.* **2012**, *48*, 9589.

(21) Albinsson, B.; Hannestad, J. K.; Börjesson, K. Functionalized DNA Nanostructures for Light Harvesting and Charge Separation. *Coord. Chem. Rev.* **2012**, *256*, 2399−2413.

(22) Díaz, S. A.; Buckhout-White, S.; Ancona, M. G.; Spillmann, C. M.; Goldman, E. R.; Melinger, J. S.; Medintz, I. L. Extending DNA-Based Molecular Photonic Wires with Homogeneous Förster Resonance Energy Transfer. *Adv. Opt. Mater.* **2016**, *4*, 399−412.

(23) Hannestad, J. K.; Sandin, P.; Albinsson, B. Self-Assembled DNA Photonic Wire for Long-Range Energy Transfer. *J. Am. Chem. Soc.* **2008**, *130*, 15889−15895.

(24) Graugnard, E.; Kellis, D. L.; Bui, H.; Barnes, S.; Kuang, W.; Lee, J.; Hughes, W. L.; Knowlton, W. B.; Yurke, B. DNA-Controlled Excitonic Switches. *Nano Lett.* **2012**, *12*, 2117−2122.

(25) Cannon, B. L.; Kellis, D. L.; Davis, P. H.; Lee, J.; Kuang, W.; Hughes, W. L.; Graugnard, E.; Yurke, B.; Knowlton, W. B. Excitonic

AND Logic Gates on DNA Brick Nanobreadboards. *ACS Photonics* **2015**, *2*, 398−404.

(26) Tinnefeld, P.; Heilemann, M.; Sauer, M. Design of Molecular Photonic Wires Based on Multistep Electronic Excitation Transfer. *ChemPhysChem* **2005**, *6*, 217−222.

(27) Stein, I. H.; Schüller, V.; Böhm, P.; Tinnefeld, P.; Liedl, T. Single-Molecule FRET Ruler Based on Rigid DNA Origami Blocks. *ChemPhysChem* **2011**, *12*, 689−695.

(28) Stein, I. H.; Steinhauer, C.; Tinnefeld, P. Single-Molecule Four-Color FRET Visualizes Energy-Transfer Paths on DNA Origami. *J. Am. Chem. Soc.* **2011**, *133*, 4193−4195.

(29) Rothemund, P. W. K. Folding DNA to Create Nanoscale Shapes and Patterns. *Nature* **2006**, *440*, 297−302.

(30) Douglas, S. M.; Dietz, H.; Liedl, T.; Högberg, B.; Graf, F.; Shih, W. M. Self-Assembly of DNA into Nanoscale Three-Dimensional Shapes. *Nature* **2009**, *459*, 414−418.

(31) Seeman, N. C. Nanomaterials Based on DNA. *Annu. Rev. Biochem.* **2010**, *79*, 65−87.

(32) Zhang, T.; Neumann, A.; Lindlau, J.; Wu, Y.; Pramanik, G.; Naydenov, B.; Jelezko, F.; Schüder, F.; Huber, S.; Huber, M.; et al. DNA-Based Self-Assembly of Fluorescent Nanodiamonds. *J. Am. Chem. Soc.* **2015**, *137*, 9776−9779.

(33) Schreiber, R.; Do, J.; Roller, E.-M.; Zhang, T.; Schüller, V. J.; Nickels, P. C.; Feldmann, J.; Liedl, T. Hierarchical Assembly of Metal Nanoparticles, Quantum Dots and Organic Dyes Using DNA Origami Scaffolds. *Nat. Nanotechnol.* **2013**, *9*, 74−78.

(34) Bai, X. -c.; Martin, T. G.; Scheres, S. H. W.; Dietz, H. Cryo-EM Structure of a 3D DNA-Origami Object. *Proc. Natl. Acad. Sci. U. S. A.* **2012**, *109*, 20012−20017.

(35) Fischer, S.; Hartl, C.; Frank, K.; Rädler, J. O.; Liedl, T.; Nickel, B. Shape and Interhelical Spacing of DNA Origami Nanostructures Studied by Small-Angle X-Ray Scattering. *Nano Lett.* **2016**, *16*, 4282−4287.

(36) Kudryavtsev, V.; Sikor, M.; Kalinin, S.; Mokranjac, D.; Seidel, C. A. M.; Lamb, D. C. Combining MFD and PIE for Accurate Single-Pair Förster Resonance Energy Transfer Measurements. *ChemPhysChem* **2012**, *13*, 1060−1078.

(37) Cunningham, P. D.; Khachatrian, A.; Buckhout-White, S.; Deschamps, J. R.; Goldman, E. R.; Medintz, I. L.; Melinger, J. S. Resonance Energy Transfer in DNA Duplexes Labeled with Localized Dyes. *J. Phys. Chem. B* **2014**, *118*, 14555−14565.

(38) Di Fiori, N.; Meller, A. The Effect of Dye-Dye Interactions on the Spatial Resolution of Single-Molecule FRET Measurements in Nucleic Acids. *Biophys. J.* **2010**, *98*, 2265−2272.

(39) Nicoli, F.; Roos, M. K.; Hemmig, E. A.; Di Antonio, M.; de Vivie-Riedle, R.; Liedl, T. Proximity-Induced H-Aggregation of Cyanine Dyes on DNA-Duplexes. *J. Phys. Chem. A* **2016**, *120*, 9941−9947.

(40) Iqbal, A.; Arslan, S.; Okumus, B.; Wilson, T. J.; Giraud, G.; Norman, D. G.; Ha, T.; Lilley, D. M. J. Orientation Dependence in Fluorescent Energy Transfer between Cy3 and Cy5 Terminally Attached to Double-Stranded Nucleic Acids. *Proc. Natl. Acad. Sci. U. S. A.* **2008**, *105*, 11176−11181.

(41) Spiriti, J.; Binder, J. K.; Levitus, M.; van der Vaart, A. Cy3-DNA Stacking Interactions Strongly Depend on the Identity of the Terminal Basepair. *Biophys. J.* **2011**, *100*, 1049−1057.

(42) Stennett, E. M. S.; Ciuba, M. A.; Lin, S.; Levitus, M. Demystifying PIFE: The Photophysics behind the Protein-Induced Fluorescence Enhancement Phenomenon in Cy3. *J. Phys. Chem. Lett.* **2015**, *6*, 1819−1823.

(43) Stennett, E. M. S.; Ma, N.; van der Vaart, A.; Levitus, M. Photophysical and Dynamical Properties of Doubly Linked Cy3−DNA Constructs. *J. Phys. Chem. B* **2014**, *118*, 152−163.

(44) Sanborn, M. E.; Connolly, B. K.; Gurunathan, K.; Levitus, M. Fluorescence Properties and Photophysics of the Sulfoindocyanine Cy3 Linked Covalently to DNA. *J. Phys. Chem. B* **2007**, *111*, 11064−11074.

(45) Berberan-Santos, M. N.; Valeur, B. Fluorescence Depolarization by Electronic Energy Transfer in Donor−acceptor Pairs of like and Unlike Chromophores. *J. Chem. Phys.* **1991**, *95*, 8048−8055.

(46) Runnels, L. W.; Scarlata, S. F. Theory and Application of Fluorescence Homotransfer to Melittin Oligomerization. *Biophys. J.* **1995**, *69*, 1569−1583.

(47) Lidke, D. S.; Nagy, P.; Barisas, B. G.; Heintzmann, R.; Post, J. N.; Lidke, K. A.; Clayton, A. H. A.; Arndt-Jovin, D. J.; Jovin, T. M. Imaging Molecular Interactions in Cells by Dynamic and Static Fluorescence Anisotropy (rFLIM and emFRET). *Biochem. Soc. Trans.* **2003**, *31*, 1020−1027.

(48) Weber, G. Dependence of the Polarization of the Fluorescence on the Concentration. *Trans. Faraday Soc.* **1954**, *50*, 552.

(49) Ivanov, V.; Li, M.; Mizuuchi, K. Impact of Emission Anisotropy on Fluorescence Spectroscopy and FRET Distance Measurements. *Biophys. J.* **2009**, *97*, 922−929.

(50) Harvey, B. J.; Levitus, M. Nucleobase-Specific Enhancement of Cy3 Fluorescence. *J. Fluoresc.* **2009**, *19*, 443−448.

(51) Kretschy, N.; Sack, M.; Somoza, M. M. Sequence-Dependent Fluorescence of Cy3- and Cy5-Labeled Double-Stranded DNA. *Bioconjugate Chem.* **2016**, *27*, 840−848.

(52) Douglas, S. M.; Chou, J. J.; Shih, W. M. DNA-Nanotube-Induced Alignment of Membrane Proteins for NMR Structure Determination. *Proc. Natl. Acad. Sci. U. S. A.* **2007**, *104*, 6644−6648.

(53) Stahl, E.; Martin, T. G.; Praetorius, F.; Dietz, H. Facile and Scalable Preparation of Pure and Dense DNA Origami Solutions. *Angew. Chem., Int. Ed.* **2014**, *53*, 12735−12740.

## B.3 Paper 3: Dynamic interactions of type I cohesin modules fine-tune the structure of the cellulosome of *Clostridium thermocellum*

# Dynamic interactions of type I cohesin modules fine-tune the structure of the cellulosome of *Clostridium thermocellum*

**Anders Barth[a,b,c,d], Jelle Hendrix[a,b,c,d,1], Daniel Fried[e,2], Yoav Barak[e,3], Edward A. Bayer[e], and Don C. Lamb[a,b,c,d,4]**

[a]Physical Chemistry, Department of Chemistry, Ludwig-Maximilians-Universität München, 81377 Munich, Germany; [b]Center for Integrated Protein Science Munich, Ludwig-Maximilians-Universität München, 81377 Munich, Germany; [c]Nanosystems Initative Munich, Ludwig-Maximilians-Universität München, 81377 Munich, Germany; [d]Center for Nanoscience, Ludwig-Maximilians-Universität München, 81377 Munich, Germany; and [e]Department of Biomolecular Sciences, The Weizmann Institute of Science, Rehovot 7610001, Israel

Edited by Martin Gruebele, University of Illinois at Urbana–Champaign, Urbana, IL, and approved October 19, 2018 (received for review May 30, 2018)

**Efficient degradation of plant cell walls by selected anaerobic bacteria is performed by large extracellular multienzyme complexes termed cellulosomes. The spatial arrangement within the cellulosome is organized by a protein called scaffoldin, which recruits the cellulolytic subunits through interactions between cohesin modules on the scaffoldin and dockerin modules on the enzymes. Although many structural studies of the individual components of cellulosomal scaffoldins have been performed, the role of interactions between individual cohesin modules and the flexible linker regions between them are still not entirely understood. Here, we report single-molecule measurements using FRET to study the conformational dynamics of a bimodular cohesin segment of the scaffoldin protein CipA of *Clostridium thermocellum*. We observe compacted structures in solution that persist on the timescale of milliseconds. The compacted conformation is found to be in dynamic equilibrium with an extended state that shows distance fluctuations on the microsecond timescale. Shortening of the intercohesin linker does not destabilize the interactions but reduces the rate of contact formation. Upon addition of dockerin-containing enzymes, an extension of the flexible state is observed, but the cohesin–cohesin interactions persist. Using all-atom molecular-dynamics simulations of the system, we further identify possible intercohesin binding modes. Beyond the view of scaffoldin as "beads on a string," we propose that cohesin–cohesin interactions are an important factor for the precise spatial arrangement of the enzymatic subunits in the cellulosome that leads to the high catalytic synergy in these assemblies and should be considered when designing cellulosomes for industrial applications.**

single molecule | fluorescence | FRET | molecular dynamics | conformational dynamics

Cellulose from plant cell walls is the most abundant source of renewable carbon (1). As the world reserve of fossil fuels is being depleted, the conversion of plant biomass into bioethanol is a promising approach to solve the global energy problem. The efficient degradation of plant cell wall material, however, remains a challenge due to the hydrolytic stability of cellulosic polysaccharides (2–4). In nature, aerobic bacteria and fungi secrete specialized enzymes to break down cellulose into oligosaccharides. In contrast, anaerobic bacteria utilize a cell-attached extracellular megadalton multienzyme complex, called the cellulosome, to efficiently degrade plant cell walls (5–7). The spatial proximity of cellulases and hydrolases within the cellulosome results in its highly synergetic catalytic activity (8).

The cellulosome of the thermophilic anaerobe *Clostridium thermocellum* contains the extracellular scaffoldin protein CipA that mediates the cell–substrate interactions via the cellulose-binding module (CBM) (Fig. 1*A*) (9–12). Cell wall attachment is achieved through the binding of a type II dockerin (DocII) module in CipA to a type II cohesin (CohII) module in a cell surface-associated protein linked to the cell through a surface layer homology domain (SLH). An X module adjacent to the DocII module has been shown to have an important function for the binding interaction (13). CipA contains a linear array of nine type I cohesin (CohI) modules with the CBM located between CohI 2 and 3. Each CohI module acts as an attachment site for various cellulose-processing enzymes, which bind with high affinity through their type I dockerin (DocI) modules (14–16). The interactions between the CipA CohI and the enzyme-borne DocI modules of different enzymes are nonspecific and thus allow for variability in the composition of the catalytic subunits (17, 18).

Previous X-ray crystallography and NMR spectroscopy studies revealed the structure of many individual components of the cellulosome (19, 20). However, due to the inherently dynamic quaternary structure of the cellulosome (21, 22), the precise arrangement of the components linked by the scaffoldin protein remains poorly understood. Low-resolution structural methods such as small-angle X-ray scattering (SAXS) have revealed a dynamic picture of different artificial (23) and natural scaffoldin

## Significance

**Cellulosomes are large, multienzyme complexes that efficiently degrade plant cell walls. Their central building blocks are cohesin modules that serve as attachment sites for enzymes. We study the dynamic structural organization by investigating a dyad of cohesin modules connected by a flexible linker using a combination of single-molecule FRET experiments and molecular dynamics simulations. We show that cohesin modules engage in intermodular interactions on the submillisecond timescale, which persist in the presence of the catalytic modules of the cellulosome. We propose that cohesin–cohesin interactions are important for the fine-tuning of the structure of cellulosomes for precise positioning of the catalytic enzymes, while their structural flexibility is facilitated by the flexible linkers.**

Author contributions: A.B., J.H., Y.B., E.A.B., and D.C.L. designed research; A.B., J.H., D.F., and Y.B. performed research; A.B. and J.H. analyzed data; and A.B. and D.C.L. wrote the paper.

The authors declare no conflict of interest.

This article is a PNAS Direct Submission.

[1] Present address: Dynamic Bioimaging Lab, Advanced Optical Microscopy Centre and Biomedical Research Institute, Hasselt University, B-3590 Diepenbeek, Belgium.

[2] Present address: Department of Chemistry, Saint Peter's University, Jersey City, NJ 07306.

[3] Present address: Department of Chemical Research Support, Weizmann Institute of Science, Rehovot 7610001, Israel.

[4] To whom correspondence should be addressed. Email: d.lamb@lmu.de.

This article contains supporting information online at www.pnas.org/lookup/suppl/doi:10.1073/pnas.1809283115/-/DCSupplemental.

www.pnas.org/cgi/doi/10.1073/pnas.1809283115

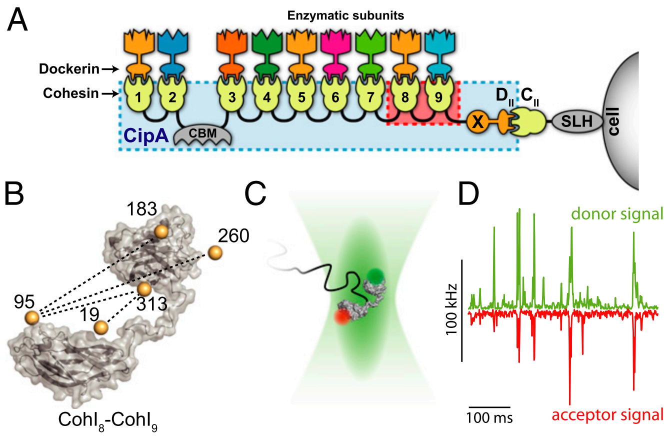

**Fig. 1.** Structure of the cellulosome of *C. thermocellum*. (*A*) The cellulosome complex is composed of the scaffoldin protein (CipA, blue box) that is anchored to the cell surface and the cellulose, offering binding sites for cellulose-processing enzymes. Surface attachment occurs through a surface layer homology domain (SLH) linked to a type II cohesin module ($C_{II}$), that interacts with a type II dockerin module ($D_{II}$) connected to an X module (X) at the C terminus of CipA. Binding to cellulose occurs via the cellulose-binding module (CBM). CipA contains nine type I cohesin modules (1–9) that can each bind to a type I dockerin module on different cellulose-processing enzymes. In this work, the CohI$_8$–CohI$_9$ fragment of CipA is studied (highlighted in red). (*B*) Atomistic model of the CohI$_8$–CohI$_9$ fragment defined from a homology model. Bronze spheres indicate the average fluorophore positions determined from geometrical calculations of the accessible volume (36). Dashed lines show the labeling combinations investigated by smFRET. (*C*) In the experiment, fluorescently labeled molecules are measured as they freely diffuse through the confocal volume. (*D*) Single-molecule events result in coinciding bursts of fluorescence in the donor and acceptor detection channels.

(24–26) fragments. Additional structural insights were obtained by cryo-electron microscopy (cryo-EM) on a fragment of CipA consisting of three consecutive CohI modules, which in contrast showed a compacted structure with outward-pointing catalytic domains (27). The *C. thermocellum* scaffoldin segments are connected by flexible linkers that are 20–40 residues long and rich in proline and threonine residues. These intercohesin linkers were found to be predominantly disordered by molecular-dynamics (MD) (28) and SAXS (24–26) studies, but were proposed to adopt a predominantly extended structure based on recent NMR data (29). The structural flexibility may be essential for the efficient access to the crystalline cellulose substrate within the heterogeneous environment of the plant cell wall containing hemicellulose, lignin, and pectin components. The connection of cohesins by linkers has been reported to enhance the catalytic activity in minicellulosome model systems by a factor of ~2; however, contradictory results have been obtained regarding the effect of linker length and composition (23, 30).

To directly measure the dynamics of scaffoldin and thereby investigate the role dynamics play for the cellulosome, we investigated the conformational dynamics of a tandem fragment of CipA consisting of the cohesin I modules 8 and 9 connected by the 23-residue-long WT linker (Fig. 1*A*, red square, and Fig. 1*B*) using single-molecule Förster resonance energy transfer (smFRET). The CohI$_8$–CohI$_9$ fragment underwent transitions between compacted and extended structures on the millisecond timescale. Quantitative information about the interconversion rates was obtained from dynamic photon distribution analysis (dynamic PDA) (31, 32) and filtered fluorescence correlation spectroscopy (fFCS) (33). The effect of the linker on the structural dynamics was probed by shortening of the linker peptide, and the influence of the CohI–DocI interactions was investigated using the enzymes Cel8A and Cel48S. We also complemented the experimental data with all-atom MD simulations to gain further insights into possible intercohesin binding modes on the atomic level.

## Results and Discussions

**smFRET Identifies Interactions in the CohI$_8$–CohI$_9$ Fragment.** We investigated the intermodular distance fluctuations of the CohI$_8$–CohI$_9$ fragment from CipA using a smFRET analysis (34). In this method, fluorescently labeled single molecules are measured at picomolar concentrations in solution as they diffuse through the observation volume of a confocal fluorescence microscope on the timescale of ~1 ms (Fig. 1 *C* and *D*). For every single-molecule event, the efficiency of energy transfer from a donor fluorophore to an acceptor fluorophore reports on the interdye distance and thus the conformation of the molecule. In contrast to ensemble methods, which report an average value, smFRET is particularly suited to study the conformational heterogeneity of biomolecules by measuring intramolecular distances one molecule at a time. smFRET experiments were performed for different constructs probing a total of four distances between the CohI modules. For fluorescent labeling, we introduced cysteines at positions 19, 95, 183, 260, and 313 in the CohI$_8$–CohI$_9$ fragment to obtain the four combinations of labeling positions 19–313, 95–313, 95–183, and 95–260 (Fig. 1*B*). The attachment sites of the fluorophores were chosen outside of the dockerin-binding interface (*SI Appendix*, Fig. S1) (35). For each CohI$_8$–CohI$_9$ mutant, these positions were stochastically labeled with the dyes Atto532 and Atto647N. No local influence of the labeling position on the photophysical properties of either fluorophore was observed, allowing quantitative analyses without the necessity for site-specific labeling. The results of the smFRET experiments are shown in Fig. 2 *A*–*D*. The molecule-wise FRET efficiency histograms are shown together with the fit to three-component Gaussian distributions. All constructs showed a major FRET population with low-to-intermediate FRET efficiency (red dashed lines) and a high FRET efficiency population ($E$ > 0.8, blue dashed lines). An intermediate FRET efficiency population (yellow dashed lines) connects the two populations. In construct 19–313, no intermediate population was detected by the analysis, but rather a small low FRET efficiency population was observed (purple dashed line).

To estimate expected FRET efficiencies of the dynamic, noninteracting CohI$_8$–CohI$_9$ fragment for all tested mutants, we performed simplified MD simulations in the absence of solvent, treating the CohI modules as rigid bodies. Under the conditions of the simulation, indeed no stable interactions occurred between the CohI modules, as is evident from the root-mean-square deviation (RMSD) of the MD trajectory, which shows vanishing correlation after ~100 ps (*SI Appendix*, Fig. S2 *A* and *B*). From the simulation, average FRET efficiency values are extracted using accessible volume calculations to determine sterically accessible positions for the dyes at every time step (36). We obtained good agreement between smFRET results for the low-FRET conformation and the simulated MD data ($R^2 > 0.98$; Fig. 2*E* and *SI Appendix*, Table S1) with an average deviation of 1.1 Å. The discrepancy is within the absolute experimental error one would expected for smFRET measurements (37). The good agreement between smFRET results and the MD data suggests that the “open” conformation, characterized by the absence of long-lived interactions between the CohI modules, corresponds to the dominant CohI$_8$–CohI$_9$ conformation.

Since previous studies revealed a highly dynamic structure for the related CohI$_1$–CohI$_2$ fragment (26), we expected all CohI$_8$–CohI$_9$ mutants to show a FRET efficiency distribution with a single peak for all constructs, as would be expected from fast dynamic averaging over many conformations on the timescale of diffusion through the confocal volume of ~1 ms. The existence of a high FRET efficiency population in all four constructs suggests

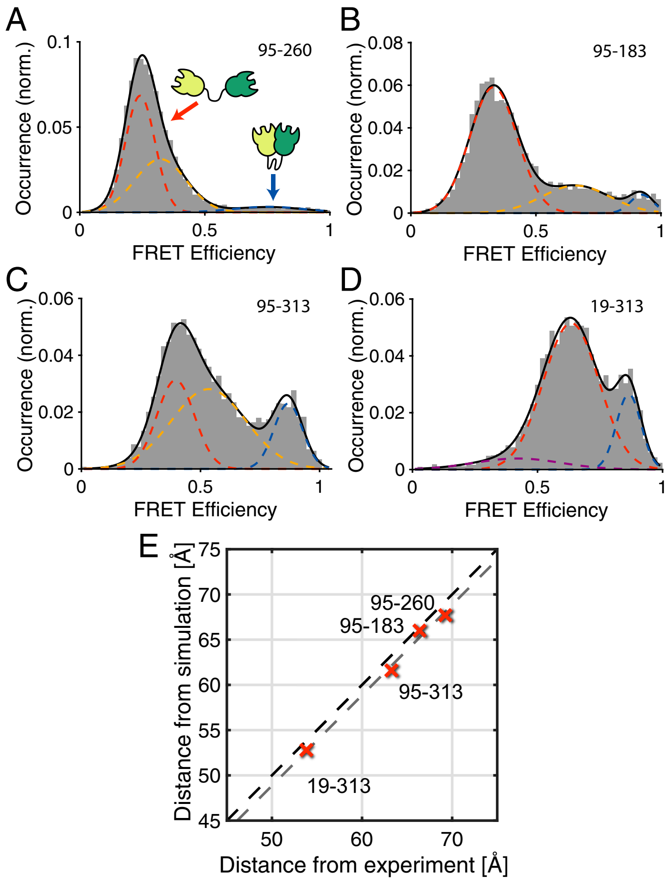

**Fig. 2.** Conformations of the investigated CohI$_8$–CohI$_9$ fragment. (*A*–*D*) SmFRET efficiency histograms for different combinations of labeling positions as indicated in Fig. 1*B*. Respective residues were mutated to cysteines, and labeling was performed stochastically with the dyes Atto532 and Atto647N. Histograms were fit using three Gaussian distributions, revealing low (red), medium (yellow), and high (blue) FRET efficiency populations. In the 19–313 construct (*D*), no medium-FRET efficiency population is observed, but an additional low-FRET efficiency population is detected (purple). (*E*) A comparison of the measured and simulated distances for the different constructs. A linear correlation is observed between the distances determined from the main population (dashed red lines in *A*–*D*) of the smFRET experiments and from rigid-body torsion-angle MD simulations. The experimental FRET efficiencies were converted into distances using a Förster radius of 59 Å. The black dashed line indicates a linear correlation, while the gray dashed line indicates linear correlation with an offset of 1.1 Å, as determined from the average deviation between experimental and theoretical distances.

specific interactions between the two CohI modules that persist on the millisecond timescale. The observation of a characteristic bridge between the high FRET efficiency ("closed") population and the low-to-intermediate FRET efficiency ("open") conformation is additionally indicative of dynamic interconversion between the states. For the 19–313 construct, no intermediate FRET efficiency population is detected, likely because the difference between the FRET efficiencies of the open ($E \sim 0.6$) and closed ($E \sim 0.9$) is not large enough to resolve the conformational dynamics. The rigid-body MD simulations showed no stable interactions between the CohI modules and thus sampled the dynamic state of CohI$_8$–CohI$_9$, agreeing well with the experimentally determined distances of the main population.

**The CohI$_8$–CohI$_9$ Fragment Shows Conformational Dynamics on the Millisecond Timescale.** To further investigate the conformational dynamics of CohI$_8$–CohI$_9$, we employed the FRET-2CDE filter that identifies FRET fluctuations based on anticorrelated changes of the donor and FRET-sensitized acceptor signals (Fig. 3*A*) (38). The FRET-2CDE filter is defined such that a value of 10 signifies no dynamics, while any larger values indicate the presence of conformational transitions on the timescale between 0.1 and 10 ms. The 2D plot of FRET efficiency against FRET-2CDE filter (Fig. 3*A*) revealed a systematic deviation from the static line at a value of 10 for the FRET-2CDE filter for single-molecule events with intermediate FRET efficiency. We also examined the fluorescence lifetime of the donor fluorophore to further investigate the dynamics of the CohI$_8$–CohI$_9$ construct (Fig. 3*B*) (32). The lifetime of the donor fluorophore offers an independent readout of the FRET efficiency. In a plot of the FRET efficiency against the donor fluorescence lifetime, one can define a static FRET line (green line in Fig. 3*B*) that single-molecule events showing no conformational dynamics will lie on. A systematic shift toward longer fluorescence lifetimes results when conformational transitions occur during a single-molecule event. In the case of a two-state dynamic system, the dynamic FRET line can be calculated by considering all mixtures of the two states (dashed red line in Fig. 3*B*). The data clearly showed a systematic deviation from the static FRET line that could be explained by two-state conformational dynamics with lifetime values for the donor fluorophore of 0.6 and 2.9 ns for the two conformations. The same qualitative result was obtained for all four constructs (*SI Appendix*, Fig. S3 and Table S2). Interestingly, the low-FRET state was also shifted from the dynamic FRET line, although it showed a value around 10 for the FRET-2CDE filter. Since the FRET-2CDE filter relies on a kernel density estimator, effectively smoothing over a finite time window (here 100 µs), it is not sensitive to faster fluctuations. The lifetime-based readout, however, is independent of the timescale of the dynamics, since it only relies on the mixing of different conformations during a single-molecule event. This suggests that the extended state is highly dynamic on the microsecond timescale, faster than the averaging window of 100 µs chosen for the calculation of the FRET-2CDE filter. As a control, we measured a construct where both the donor and acceptor dyes were placed on the CohI$_9$ module (*SI Appendix*, Fig. S4). As expected, the control construct showed a single population and exhibits no deviation from the static FRET line.

The qualitative assessment of the conformational dynamics in CohI$_8$–CohI$_9$ confirms the hypothesis of a compacted state, which is in dynamic equilibrium with an open, flexible state or family of states. Additional information is obtained about the timescales of the dynamic processes. Transition to and from the compacted state occur on the millisecond timescale, while the open state exhibits fast fluctuations on the microsecond timescale. In the following sections, we focus on the characterization and quantification of the dynamics.

**PDA Quantifies the Dynamics Between Open and Closed States.** To quantify the timescale of the dynamics, we utilized additional analysis methods. First, we focus on the millisecond dynamics between the open and closed states. PDA is a powerful tool to disentangle the contributions of photon shot noise to the width of the observed FRET efficiency distribution, from physically relevant factors such as static conformational heterogeneity (31). In its simplest form, PDA assumes a Gaussian distribution of distances that is transformed using the known photon statistics of the measurement and the experimental correction factors to obtain the corresponding shot-noise limited proximity ratio (PR) histogram. PDA can also be used to describe the effect of conformational dynamics on the observed PR histogram (32). By sectioning the photon counts into equal time intervals, the resulting PR histogram can be described analytically using a two-state kinetic model, whereby each individual state's heterogeneity is described by a distribution of distances. To increase the

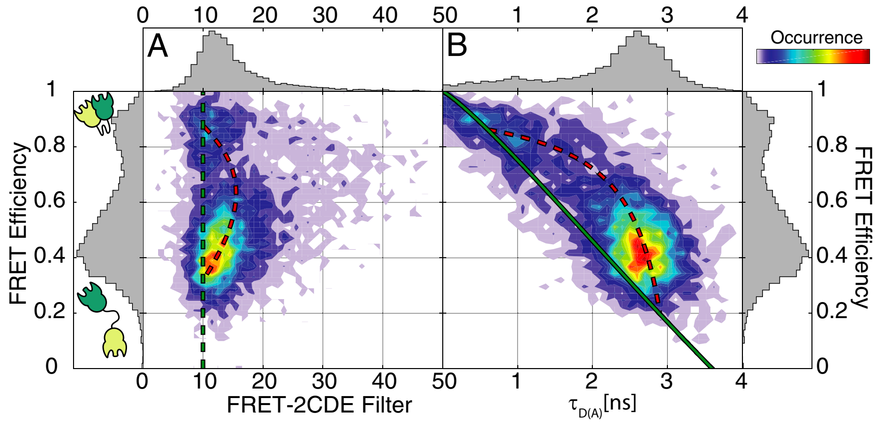

**Fig. 3.** Identification of conformational dynamics in the CohI$_8$–CohI$_9$ construct 95–313. (*A*) Two-dimensional histogram of the FRET-2CDE filter versus FRET efficiency. Values larger than 10, visible for events with intermediate-to-high FRET efficiency, indicate dynamics within the burst. (*B*) Two-dimensional histogram of the donor lifetime versus FRET efficiency. A systematic shift from the static FRET line (green) is observed, consistent with the presence of conformational dynamics. Additionally, the low-to-intermediate FRET efficiency species at ~40% also deviates from the static FRET line, indicating fast dynamics on the microsecond timescale. The dynamic behavior can be described theoretically using the dynamic FRET line (dashed red line). The start and end points were extracted from fluorescence decay analysis of all molecules using a biexponential model function (*SI Appendix*, Table S2).

robustness of the analysis, each dataset was processed using different time window sizes (0.25, 0.5, and 1 ms) and globally fit with respect to the interdye distances and kinetic rates.

We performed dynamic PDA of all different constructs (Fig. 4 and Table 1). In addition to the two interconverting species, a static low-FRET population was needed to account for the contributions of small amounts (1–5%) of low-FRET efficiency species likely caused by acceptor blinking. The kinetic model was successful in describing the observed distributions of FRET efficiencies in all cases (*SI Appendix*, Fig. S5). While for the 19–313 construct no intermediate-FRET population was detected from the analysis of the FRET efficiency distribution (Fig. 2*D*), the global dynamic PDA was successful in recovering kinetic information for this construct (Fig. 4*D*). In all constructs, the extended state was more populated than the closed state, suggesting a fast rate of opening and a slower rate of contact formation. This is confirmed by the extracted rates for closing of $k_{\mathrm{oc}} = 0.5 \pm 0.3\ \mathrm{ms}^{-1}$ and opening of $k_{\mathrm{co}} = 2.0 \pm 0.4\ \mathrm{ms}^{-1}$, corresponding to dwell time of ~2 ms in the open state and ~0.5 ms in the closed state. The determined center distances from PDA are in good agreement with the previous analysis of the FRET efficiency histograms, deviating by less than 3 Å (Table 1 and *SI Appendix*, Table S1).

**Correlation Analysis Identifies a Second Kinetic State on the Microsecond Timescale.** Second, we looked for conformational dynamics on the microsecond timescale. To this end, we applied FCS (39, 40). As a first step, we calculated the autocorrelation and cross-correlation functions of the donor fluorescence and the FRET-induced acceptor signal. In the presence of conformational dynamics, the FRET fluctuations cause an anticorrelation contribution to the cross-correlation function and matching positive contributions to the autocorrelation functions. Representative autocorrelation and cross-correlation functions for construct 95–260 are shown in Fig. 5*A* and for all constructs in *SI Appendix*, Fig. S6. From the FRET-FCS analysis, we obtained a kinetic relaxation time of 24 ± 7 μs across all four constructs (Table 2). To obtain a more detailed picture of these fast dynamics, we applied fFCS (33, 41). fFCS uses the lifetime, anisotropy, and color information available for each photon to assign statistical weights (or filters) with respect to two or more defined species (*SI Appendix*, Fig. S7). To define the open and closed conformation, the characteristic patterns were determined from the measurement directly by pooling data from the low- or high-FRET efficiency events (*SI Appendix*, Fig. S7*B*). The inclusion of additional dimensions and the application of statistical weighting in fFCS leads to increased contrast in comparison with the FRET-FCS analysis. The fFCS cross-correlation functions for the four constructs are shown in Fig. 5*B*. Fitting with a single kinetic term revealed systematic deviations in the residuals, prompting us to include a second kinetic term (*SI Appendix*, Fig. S8). The extracted timescales of the two terms are 15 ± 4 and 600 ± 200 μs for the fast and slow components, respectively (Table 2). The timescale of the slow component overlapped with the timescale of diffusion (~1–2 ms), resulting in the relatively high uncertainty. The amplitude of the fast term was significantly higher, contributing to 72 ± 8% of the observed dynamics. Because the relaxation time of the slow component agrees well with that determined from the dynamic-PDA analysis ($\tau_R = 410 \pm 80$ μs), we assign the slow component

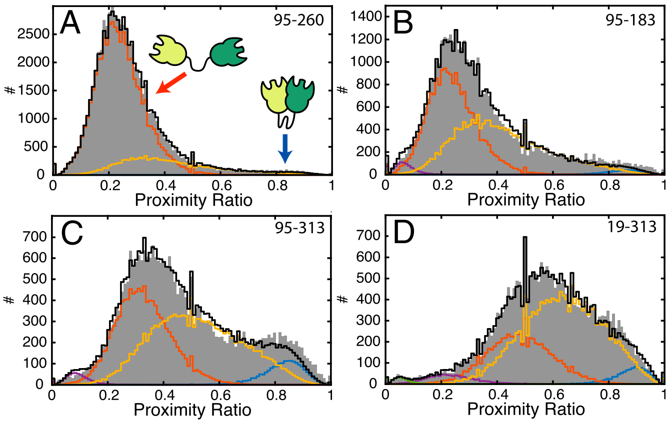

**Fig. 4.** Dynamic photon distribution analysis (PDA) of the WT CohI$_8$–CohI$_9$ fragment. To investigate the timescale of the indicated dynamics, PR histograms for constructs 95–260 (*A*), 95–183 (*B*), 95–313 (*C*), and 19–313 (*D*) were fit using dynamic PDA. Shown are the data for a time window size of 1 ms. The PRs (uncorrected FRET efficiency) are shown as gray bars and the dynamic PDA fits are shown as black lines. In addition, the low (red)- and high (blue)-FRET efficiency populations and the population of molecules showing interconversion during the observation time (yellow) are indicated. Additional static low-FRET efficiency populations are shown in purple and green. See *SI Appendix*, Fig. S5, for the global fit of the data using time windows of $\Delta t$ = 0.25, 0.5, and 1 ms.

**Table 1. Dynamic PDA of the different CohI$_8$–CohI$_9$ constructs with WT linker, Δ17 linker, and Δ11 linker**

| Construct | 95–260 | 95–183 | 95–313 | 19–313 |
|---|---|---|---|---|
| WT linker | | | | |
| $R_{\mathrm{closed}}$, Å | 40.2 ± 0.6 | 40.7 ± 1.0 | 41.3 ± 0.8 | 39.7 ± 1.0 |
| $R_{\mathrm{open}}$, Å | 69.4 ± 0.1 | 68.6 ± 0.3 | 62.8 ± 0.3 | 55.6 ± 0.6 |
| $k_{\mathrm{closed}\rightarrow\mathrm{open}}$, ms$^{-1}$ | 2.09 ± 0.10 | 2.39 ± 0.13 | 1.41 ± 0.09 | 1.92 ± 0.17 |
| $k_{\mathrm{open}\rightarrow\mathrm{closed}}$, ms$^{-1}$ | 0.14 ± 0.01 | 0.51 ± 0.03 | 0.57 ± 0.05 | 0.87 ± 0.13 |
| Δ11 linker | | | | |
| $R_{\mathrm{closed}}$, Å | — | 40.0 ± 0.6 | 39.1 ± 1.6 | 38.5 ± 0.7 |
| $R_{\mathrm{open}}$, Å | — | 66.0 ± 0.2 | 62.6 ± 0.3 | 54.7 ± 0.3 |
| $k_{\mathrm{closed}\rightarrow\mathrm{open}}$, ms$^{-1}$ | — | 1.94 ± 0.10 | 2.14 ± 0.14 | 1.79 ± 0.23 |
| $k_{\mathrm{open}\rightarrow\mathrm{closed}}$, ms$^{-1}$ | — | 0.37 ± 0.02 | 0.67 ± 0.05 | 0.38 ± 0.06 |
| Δ17 linker | | | | |
| $R_{\mathrm{closed}}$, Å | — | 42.9 ± 0.5 | 41.4 ± 0.5 | — |
| $R_{\mathrm{open}}$, Å | — | 66.2 ± 0.3 | 66.1 ± 0.3 | — |
| $k_{\mathrm{closed}\rightarrow\mathrm{open}}$, ms$^{-1}$ | — | 1.39 ± 0.22 | 1.93 ± 0.23 | — |
| $k_{\mathrm{open}\rightarrow\mathrm{closed}}$, ms$^{-1}$ | — | 0.15 ± 0.03 | 0.24 ± 0.04 | — |

The average interdye distances in the closed and open states, $R_{\mathrm{closed}}$ and $R_{\mathrm{open}}$, and the interconversion rates, $k_{\mathrm{closed}\rightarrow\mathrm{open}}$ and $k_{\mathrm{open}\rightarrow\mathrm{closed}}$ are given. Construct 95–260 with the Δ11 linker showed artifacts in the measurement and was thus excluded from the analysis (*SI Appendix*, Fig. S10). Errors are given as 95% confidence intervals as determined from the curvature of the $\chi^2_{red.}$-surface.

to the previously described slow transition between the open and closed state. The fast component identified by fFCS consequently corresponds to the dynamics of the freely fluctuating open state that occur on the timescale of ∼15 μs.

Our observation of a highly dynamic structure in the open state is in agreement with previous studies on artificial chimeric minicellulosomes (23) or the CipA fragments CohI$_1$–CohI$_2$ and CohI$_2$–CBM–CohI$_3$ in complex with the enzyme Cel8A (26). On the other hand, a cryo-EM study on the fragment CohI$_3$–CohI$_4$–CohI$_5$ in complex with Cel8A revealed predominantly compacted structures showing direct interactions between the cohesin modules with outward-pointing enzymes (27), similar to the compacted state observed here. The report of a small fraction of complexes in extended conformations in that study additionally supports our observation of a dynamic equilibrium between extended and compacted structures. Cohesin–cohesin interactions were also observed in the crystal structure of the C-terminal fragment of CipA, CohI$_9$–X–DocII, in complex with a CohII module, showing homodimerization mediated by intermolecular contacts between the CohI$_9$ modules (42), and in the crystal structure of a CohII dyad from *Acetivibrio cellulolyticus* (43).

**Shortening of the Linker Has a Minor Effect on the Observed Dynamics.** After having characterized the structure and dynamics of the WT-linker CohI$_8$–CohI$_9$ fragment, we turned to investigate the role of the linker by designing constructs with shortened linkers. The WT linker is 23 residues long and is mainly composed of polar and aliphatic amino acids with a high content of threonine (39%) and proline (22%) residues (*SI Appendix*, Fig. S1). We deleted 11 residues from the center of the linker, shortening it to 12 residues without significantly altering the peptide properties (Δ11 linker; *SI Appendix*, Fig. S1). The dynamic behavior detected for the WT linker persists in the Δ11 linker constructs (*SI Appendix*, Fig. S9). However, construct 95–260 in combination with the Δ11 linker showed dye-related artifacts in the pulsed interleaved excitation (PIE)–multiparameter fluorescence detection (MFD) analysis and was thus excluded from the discussion (*SI Appendix*, Fig. S10). We again performed dynamic PDA to quantify the dynamics and interdye distance distributions (see Fig. 6*A* and Table 1 for construct 95–313, and *SI Appendix*, Figs. S5 and S11, for all constructs). No significant distance change was detected for the closed conformation. Surprisingly, also no significant shift to shorter distances was evident for the open conformation, although construct 95–183 showed a minor contraction from 69 to 66 Å (Fig. 6*B* and Table 1). The dynamic interconversion rates of the Δ11 linker constructs exhibited no major change with respect to the WT linker with an opening rate of 2.0 ± 0.2 ms$^{-1}$ and a closing rate of 0.5 ± 0.2 ms$^{-1}$. As before, we performed a fFCS analysis (Table 2). In contrast to the dynamic PDA, the correlation analysis detects increased interconversion rates for the Δ11 linker constructs. The slow component showed a relaxation time of 350 ± 200 μs (averaged over all constructs), in good agreement with the dynamic timescale detected by dynamic PDA of 420 ± 60 μs for the Δ11 linker construct, but faster than what we obtained from the correlation analysis for the WT linker (600 ± 200 μs). For the Δ11 linker, the dynamics in the open conformation showed similar interconversion rates (relaxation time of 10 ± 6 μs) compared with the timescales in the WT-linker constructs (relaxation time of 15 ± 4 μs). To test whether further shortening of the linker peptide would disrupt the interactions, we measured the constructs 95–183 and 95–313 with a six-residue-long linker

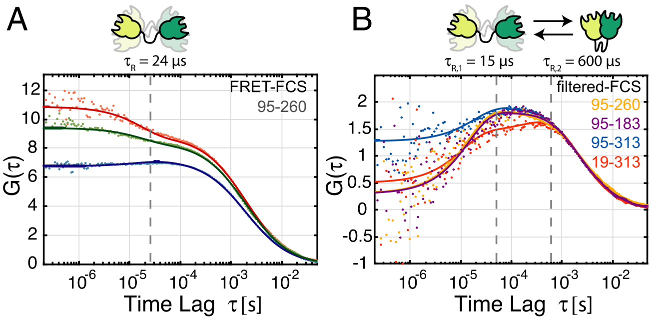

**Fig. 5.** FCS analysis of conformational dynamics. (*A*) FRET-FCS reveals a bunching term in the donor fluorescence and FRET-induced acceptor fluorescence autocorrelation curves (green and red curves, respectively), as well as a corresponding anticorrelation term in the cross-correlation function (blue curve). A global analysis reveals dynamics with a timescale of 24 ± 7 μs. Data are shown for the 95–260 construct. (*B*) The fFCS cross-correlation functions are shown for the constructs 95–260 (yellow), 95–183 (purple), 95–313 (blue), and 19–313 (red). fFCS enhances the contrast of the kinetic contributions to the correlation function. The species cross-correlation curves for the four constructs show similar timescale of dynamics, revealing two terms, one at 15 ± 4 μs and a second at 600 ± 200 μs with contributions of 76 ± 4% and 24 ± 4%, respectively.

**Table 2. Species-selective FCS analysis of the different CohI$_8$–CohI$_9$ constructs with WT linker, Δ11 linker, and Δ17 linker**

| | FRET-FCS | fFCS | | | | Dynamic PDA |
|---|---|---|---|---|---|---|
| Construct | $\tau_R$, µs | $\tau_{R,1}$, µs | $f_1$, % | $\tau_{R,2}$, µs | $f_2$, % | $\tau_R$, µs |
| WT linker | 24 ± 7 | 15 ± 4 | 72 ± 8 | 600 ± 200 | 28 ± 8 | 410 ± 80 |
| Δ11 linker | 30 ± 14 | 10 ± 6 | 68 ± 4 | 350 ± 200 | 32 ± 4 | 420 ± 60 |
| Δ17 linker | 15 ± 2 | 11 ± 3 | 77 ± 15 | 440 ± 260 | 23 ± 15 | 550 ± 130 |

The average and SD of the relaxation times, $\tau_R$, and relative amplitudes, $f$, of independent analyses of the different labeling positions are listed here for the various linker constructs. All three correlation functions in FRET-FCS or four correlation functions in fFCS were globally fit as described in the main text. Relative amplitudes were determined based on amplitudes of the kinetic terms in the species cross-correlation functions. For comparison, the relaxation times from dynamic PDA, calculated by $\tau_R = (k_{c\to o} + k_{o\to c})^{-1}$, are given. For the Δ11 linker, the construct 95–260 was excluded due to dye artifacts (*SI Appendix*, Fig. S10). For the Δ17 linker, constructs 95–313 and 95–163 were measured. For detailed results of the FCS analysis of the different constructs, see *SI Appendix*, Table S3.

(Δ17 linker). Still, no large change was observed for the average distance of the open conformation with respect to the WT linker (Fig. 6*B*, Table 1, and *SI Appendix*, Fig. S11). CohI$_8$–CohI$_9$ remained dynamic with the Δ17 linker; however, a depopulation of the interacting state is apparent (Fig. 6*A* and *SI Appendix*, Figs. S9 and S11). The kinetic analysis revealed that, while the opening rate remains approximately constant, the closing rate is decreased by a factor of 2–3 (Table 1), indicating that the steric restriction caused by the shortened linker increases the barrier for the formation of intermodular contacts. The fluctuations in the open state remained on similar timescales as observed for the WT and Δ11 linker (relaxation time of 11 ± 3 µs; Table 2). Complete removal of the linker of construct 95–183 resulted in a single low-FRET state with no detectable dynamics, abolishing the interaction (*SI Appendix*, Figs. S9 and S11).

In summary, the effect of the Δ11 linker on the conformational states and dynamics of CohI$_8$–CohI$_9$ seems to be minor. As expected, the closed conformation was not affected by the linker length. However, shortening of the linker also had no significant effect on the average distance of the open conformation for both the Δ11 and Δ17 linkers, suggesting that the linker is not fully extended in the WT CohI$_8$–CohI$_9$, but assumes a more compacted structure due to the observed cohesin–cohesin interactions or via the formation of secondary structure. This is consistent with the results of a SAXS study where the linker length of a chimeric cohesin tandem construct (Scaf4) was systematically varied from 4 to 128 residues (23), revealing that the maximum extension of the construct plateaued already at a linker length of 39 residues. A recent NMR study of the isolated CohI$_5$ module with its 24-residue-long linker of similar composition reported a rigid and extended structure of the linker (29). The absence of a second CohI module in that study further indicates that cohesin–cohesin or cohesin–linker interactions may be responsible for the observed compaction of the structure. Interestingly, the stability of the cohesin–cohesin interactions was not affected by the linker length, as the interconversion rates between compacted and extended structures showed no significant change. On the other hand, shortening of the linker overall resulted in reduced rates of contact formation.

**Dockerin Binding Shifts the Conformational Space Toward the Extended State.** The primary in vivo function of the CohI modules is the binding of cellulose-processing enzymes. We investigated the influence of the cellulosomal enzymes Cel8A and Cel48S on the conformational dynamics of CohI$_8$–CohI$_9$. Both enzymes bind with high affinity to a CohI module through their respective DocI modules with $K_D$ values in the range of 10 nM (14). We first confirmed that Cel8A and Cel48S bind to CohI$_8$–CohI$_9$ under the experimental conditions using FCS (*SI Appendix*, Fig. S12*A*). We determined $K_D$ values of 4 nM for Cel8A and 14 nM for Cel48S (*SI Appendix*, Fig. S12*B*). In the presence of binding partners, the dynamic behavior of CohI$_8$–CohI$_9$ persisted (*SI Appendix*, Fig. S13). The dynamic PDAs of CohI$_8$–CohI$_9$ in the presence of Cel8A and Cel48S are shown in Fig. 6*A* for the 95–313 construct. The results for all four constructs are shown in *SI Appendix*, Fig. S14 and Table S4, and summarized in Fig. 6*B*. For construct 95–313 (Fig. 6*A*), the average distance in the extended conformation increases from 63 Å in the absence of binding partners to 73 and 69 Å in the presence of Cel8A and Cel48S, respectively. This extension of the open state was consistently observed for all constructs (Fig. 6*B*). Averaged over all constructs, no significant shift of the dynamic equilibrium toward the extended state was observed, with average rates of opening and closing of 1.9 ± 1.5 and 0.5 ± 0.3 ms$^{-1}$ for Cel8A and 1.7 ± 0.6 and 0.5 ± 0.1 ms$^{-1}$ for Cel48S, similar to the rates observed in the absence of binding partners of 2.0 ± 0.4 and 0.5 ± 0.3 ms$^{-1}$.

In summary, the interaction of CohI$_8$–CohI$_9$ with the cellulosomal enzymes Cel8A and Cel48S resulted in an extension of the open state, while leaving the conformational dynamics largely unaffected. The observed dynamic structure of the CohI$_8$–CohI$_9$ fragment in complex with Cel8A is supported by SAXS studies on CohI$_1$–CohI$_2$ with the same enzyme (26) and enzyme-bound hybrid minicellulosomes (23), which identified a dynamic and extended structure. Likewise, the fragment CohI$_3$–CohI$_4$–CohI$_5$ in complex with Cel8A has been observed to adopt both extended and compacted structures mediated by cohesin–cohesin interactions (27). The persistence of the compacted conformation in the presence of cohesin–dockerin interactions implies that the dockerin-binding interfaces on the cohesins are not involved in cohesin–cohesin interactions.

**All-Atom MD Simulations Provide an Atomistic Picture of the Interactions.** From the smFRET experiments, we could identify a compacted state of the CohI$_8$–CohI$_9$ fragment. To complement the FRET information provided by the four distances, we performed

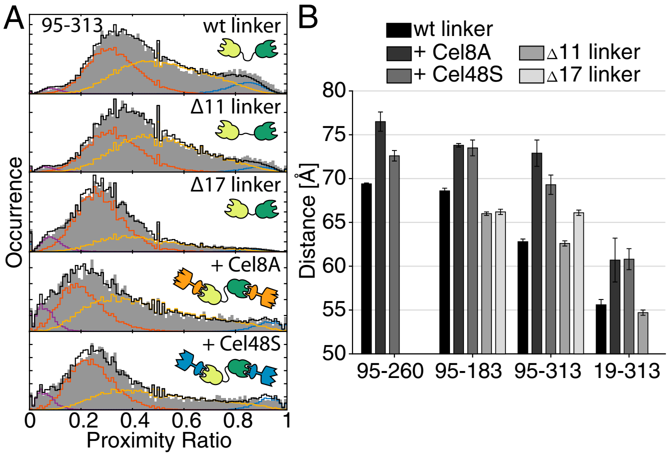

**Fig. 6.** The effect of linker shortening and enzyme binding on the dynamics of CohI$_8$–CohI$_9$. (*A*) Dynamic photon distribution analyses (PDAs) of the 95–313 construct with WT linker, Δ11 and Δ17 linkers, and WT linker with addition of the cellulosomal enzymes Cel8A and Cel48S. The smFRET histograms of the PRs (uncorrected FRET efficiencies) are plotted as gray bars, and the dynamic-PDA fits are shown as black lines. In addition, the low (red)- and high (blue)-FRET efficiency populations and the population of molecules showing interconversion during the observation time (yellow) are shown. Additional static low-FRET efficiency populations are shown in purple. (*B*) Comparison of the interdye distances of the open conformation (red in *A*) for the different constructs with WT linker, in the presence of the cellulosomal enzymes Cel8A and Cel48S and for the Δ11 and Δ17 linker constructs.

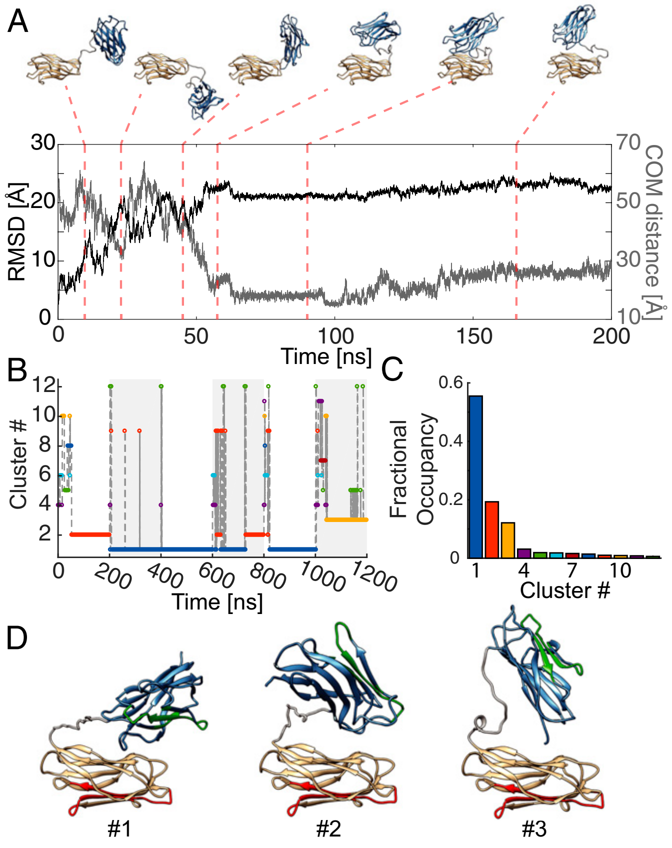

**Fig. 7.** All-atom MD simulations of the CohI$_8$–CohI$_9$ fragment. (*A*) A representative trajectory of a 200-ns MD simulation. (*Top*) Snapshots at the indicated time points of the trajectory. Starting from an extended configuration, the two modules (bronze, CohI$_8$; blue, CohI$_9$) come into close contact after ∼60 ns. After the initial contact formation, only minor movements occur without dissociation. (*Bottom*) The root-mean-square deviation (RMSD) with respect to the starting structure plateaus after ∼60 ns. Analogously, the center-of-mass (COM) distance between the two modules indicates a close contact. From 100 ns onward, slight structural rearrangements in the compacted form are evident. See Movie S1 for an animation of the trajectory. (*B*) A cluster analysis of all six MD simulations of 200 ns each was performed to obtain global structures of the compacted conformation (shading indicates the individual trajectories). Trajectories 2, 3, 4, and 5 are dominated by cluster 1. (*C*) Fractional occupancy of the individual clusters. The top three clusters constitute over 80% of the global trajectory. (*D*) The average structures of clusters 1–3. Regions colored in green and red indicate the binding interfaces for DocI modules as given in *SI Appendix*, Fig. S1 (35).

all-atom MD simulations of CohI$_8$–CohI$_9$ in explicit solvent (*Materials and Methods*). In total, six trajectories of 200-ns length were simulated from the extended starting configuration, resulting in a different evolution of the system despite the use of identical starting coordinates as evidenced by the RMSD of the trajectories (*SI Appendix*, Fig. S15). A detailed display of one of the MD runs is given in Fig. 7*A* and in Movie S1. Snapshots of the trajectory are displayed at the indicated time points above the graph. For the first 50 ns of the simulation, the protein sampled many different open structures without forming intermodular contacts. The two modules then contacted each other and form a stable interaction after ∼60 ns, which persisted for the rest of the simulation, showing little additional change in the RMSD (black line in Fig. 7*A*). As a second parameter for investigating the cohesin–cohesin interactions, we computed the center-of-mass (COM) distance between the two modules (gray line). The COM distance contains more specific information about the interaction between the two modules, revealing a slow conformational readjustment from 100 ns until the end of the simulation. During this period, the modules stay in contact but perform a twisting motion with respect to each other, transitioning from a collinear to a perpendicular orientation. Similar behavior of intermodular docking during the first half of the simulation was observed for all repeats (*SI Appendix*, Fig. S16). In some cases, detachment of the modules was observed, persisting for only ∼10 ns. To obtain an overview of the sampled stable configurations of CohI$_8$–CohI$_9$, we performed a global cluster analysis over all six trajectories (Fig. 7 *B* and *C*). The conformational landscape is dominated by three main clusters, accounting for ∼85% of the trajectories (Fig. 7*D*). Clusters 1 and 2 were found in multiple trajectories, whereas cluster 3 is unique to trajectory 6. The first cluster adopted a structure showing a perpendicular orientation of the modules. The second and third largest clusters both showed structures where one module contacts the other in a "heads-down" orientation, however showing opposite orientation of the top module between cluster 2 and 3. We also performed individual cluster analyses for each trajectory (*SI Appendix*, Fig. S17). Each trajectory was dominated by one or two clusters that accounted for at least 50% of the trajectory. The structures for all major clusters are shown in *SI Appendix*, Fig. S18, for a complete picture of all stable conformations adopted during the simulation. It should be noted that the identified binding modes here are different from the cohesin–cohesin interaction previously observed in crystals (42). To compare the MD simulations with our experimental results on the closed state of CohI$_8$–CohI$_9$, we determined FRET-average distances from the MD trajectories as described before for the open state (*SI Appendix*, Table S5). Given the high FRET efficiency of the closed state and thus increased uncertainty of the experimentally determined distances, we find reasonable agreement; however, the MD-derived distances are consistently larger than the experimental distances by ∼8 Å on average. A possible reason could be transient dye–dye interactions that might occur at the short interdye distances, resulting in deviations of the experimentally derived distances (44).

**The Intermodular Interaction Is Characterized by a Variety of Different Binding Modes.** The experimental results of cohesin–cohesin interactions raised the questions whether specific interactions are present, and what role the cohesin–dockerin binding interfaces play. Overall, the simulations showed a variety of binding modes. While the global cluster analysis revealed three predominant structures, each of the individual clusters still exhibits some degree of internal variance, indicated by average pairwise RMSD distances within the clusters of 7–8 Å and SDs of the RMSD of 2.5–4 Å. This suggests that a multitude of different binding modes are present, and the interaction between the modules is not dominated by one specific conformation. To further investigate the cohesin–cohesin interactions, we quantified the number of intermodular contacts formed per residue. Intriguingly, arginine 6 in CohI$_8$ is found to be involved in intermodular contacts in all three major clusters (*SI Appendix*, Fig. S19 *A*–*C*). Indeed, in the simulations, the observed conformational space changed significantly when R6 is replaced by a glycine, leading to less frequent formation of stable cohesin–cohesin interactions (*SI Appendix*, Figs. S19 *D* and *E* and S20). In construct 95–260, T260 was mutated to a cysteine, placing the fluorescent label in direct vicinity of Q195 and E261. In the experiments, this construct showed the lowest population of the closed state (Fig. 4) due to a reduced rate of closing of 0.14 ms$^{-1}$ compared with 0.5–0.9 ms$^{-1}$ for the other constructs (Table 1), indicating that cohesin–cohesin interactions are hindered in this construct. To further test our hypothesis, we performed experiments on R6G mutants of the constructs 95–183, 95–313, and 19–313 (*SI Appendix*, Fig. S19 *F*–*K* and Table S6). While a slight depopulation of the interacting state was observed for construct 19–313, no clear change is observed for the other two constructs. This indicates that the intermodular contacts are not dominated by a single specific interaction with the arginine at position 6.

Rather, this suggests that many residues in the region are involved in stabilizing the interaction, as supported by the results from the simulation of the R6G mutant (*SI Appendix*, Fig. S19*E*). Based on the high sequence conservation between the different type I cohesins (*SI Appendix*, Fig. S21), other cohesin pairs may exhibit similar intermodular interactions, which potentially serve as a mechanism to fine-tune the quaternary structure of the scaffoldin.

We further tested the stability of the intermodular contacts with respect to salt and denaturant. Even at high salt concentrations above 1 M NaCl, the interactions persisted (*SI Appendix*, Fig. S22*A*), indicating that the interaction is not governed by electrostatics. As cellulosomal subunits and their individual component parts (notably, cohesin and dockerin modules) are known to be remarkably stable to heat, mechanical forces, and denaturing agents, such as guanidine, urea, and SDS (45–49), we could use mild denaturing conditions to investigate the role of hydrogen bonding without denaturing the protein. In the presence of 500 mM GuHCl (*SI Appendix*, Fig. S22*B*), we indeed did observe a decrease in the strength of the interaction, suggesting that hydrogen bonding is important.

With respect to the enzymatic activity of the cellulosome, it is important to consider the formation of cohesin–cohesin interactions in the context of the accessibility of the dockerin-binding sites. To this end, we colored the residues that have previously been identified to be involved in contacts to DocI modules in Fig. 7*D* and in *SI Appendix*, Fig. S18, in red and green (see *SI Appendix*, Fig. S1, for the colored residues) (35). Interestingly, the DocI-binding surfaces on the CohI modules are mostly unobstructed by the cohesin–cohesin interaction in all stable structures. Hence, the binding of enzymes to the cohesins is not expected to be hindered by cohesin–cohesin interactions. Likewise, the dockerin–cohesin interaction should not interrupt the formation of compacted structures, as is confirmed by our experimental results. Regarding the intermodular linker, we observed no significant formation of stable secondary structure or long-lived interactions within the linker or between the linker and the cohesin domains. In agreement with the experimental data, the linker was rarely extended and often assumed compacted conformations.

In summary, the MD simulations reveal that CohI$_8$–CohI$_9$ consistently adopts compacted conformations that are stable on the timescale of the simulations (200 ns). A multitude of different binding modes were identified, indicating that the interaction between the modules is not dominated by one specific conformation. In these stable conformations, the dockerin-binding interfaces of the cohesins are exposed to the solvent and thus accessible for enzyme binding. This suggests that cohesin–cohesin interactions and dockerin binding are not mutually exclusive.

## Conclusions

Herein, we characterized the conformational dynamics of CohI$_8$–CohI$_9$ as a minimal tandem subunit of the scaffoldin protein. Our results show that CohI$_8$–CohI$_9$ transitions on the millisecond timescale between a flexible extended family of structures and compacted states mediated by cohesin–cohesin interactions. The conformational states and dynamic equilibrium are not influenced by shortening of the intercohesin linker. Addition of DocI-containing enzymes preserved the conformational dynamics but showed a higher cohesin–cohesin distance in the extended state. MD simulations identified potential binding modes for the cohesin–cohesin interaction. All stable conformations identified from the MD simulations showed no obstruction of the cohesin–dockerin binding interfaces.

By probing the structural dynamics using four different FRET sensors, we could obtain a detailed understanding of the conformational space of the CohI$_8$–CohI$_9$ fragment. In principle, the different FRET sensors should yield identical results for the kinetic rates. While we obtained good agreement between the different constructs for most parameters, we also observed some deviations. For example, construct 95–260 showed a significantly reduced transition rate to the closed conformation compared with the other constructs. Based on the MD simulations, we could show that this deviation is likely caused by the close proximity of residue T260 to residues involved in the formation of intermodular contacts. Thus, our study also highlights the importance of testing different labeling position in smFRET experiments to ensure that the fluorescent labeling does not drastically alter the properties of the biomolecule or interfere with its function.

To understand the origin of synergistic effects in cellulosomes, it is essential to obtain a detailed global picture of the structural organization and interactions of the individual functional modules. Our study suggests that cohesin–cohesin interactions might play an essential role for the precise spatial arrangement of the various enzymes. The structure of the cellulosome is inherently dynamic and needs to adapt to changing environments to ensure efficient access of the catalytic units to the crystalline cellulose within the complex mesh of hemicellulose, lignin, and pectin. As such, the flexibility of the scaffoldin protein provided by the intercohesin linkers is essential for its structural variability. Once the structural rearrangement is completed, however, cohesin–cohesin interactions may be essential for bringing the catalytic subunits into close contact again to provide the high cellulolytic activity through proximity-induced synergistic effects.

Cohesin–cohesin interactions are also an important factor to be considered in the design of artificial minicellulosomes for industrial applications. These designer cellulosomes are often chimeras of CohI modules from different organisms to allow control of the enzyme composition through orthogonal cohesin–dockerin interactions. Our results indicate that, in addition to the choice of enzymes, the compatibility of the applied cohesin modules and the flexibility of the linker should be considered to maximize the synergistic effects.

## Materials and Methods

**Protein Expression, Purification, and Fluorescent Labeling.** Protein expression and purification were performed as described previously (50). Proteins contained a His$_6$ tag for purification that was not removed. For fluorescent labeling, protein solutions were adjusted to 50 μM and oxygen was removed from the buffer (PBS). Labeling was performed at 10-fold molar excess of the dyes Atto532 and Atto647N (ATTO-TEC) for 3 h at room temperature in the presence of 1 mM TCEP. Unreacted dye was removed by ultrafiltration.

**smFRET Measurements.** smFRET experiments were performed using a custom-built setup as described previously (34) that combines PIE (40) with MFD (51). With MFD-PIE, it is possible to determine the FRET efficiency, labeling stoichiometry, fluorescence lifetime, and anisotropy for both donor and acceptor fluorophores for every molecule. Labeled CohI$_8$–CohI$_9$ constructs were diluted to a concentration of ∼100 pM in buffer containing 25 mM Hepes, 150 mM NaCl, and 2 mM CaCl$_2$ at pH 7.25. Unlabeled Cel8A or Cel48S was added at concentrations of 50 nM. Excitation powers of 100 μW were used for both donor and acceptor lasers (as measured at the back aperture of the objective). Bursts were identified using a sliding time window burst search using a time window of 500 μs and a count rate threshold of 10 kHz (52). Filtering of photobleaching and blinking events was achieved through the ALEX-2CDE filter with an upper limit of 10 (38). Further selection of double-labeled molecules was performed using the stoichiometry parameter with a lower limit of 0.45 and an upper limit of 0.80. Accurate FRET efficiencies were calculated based on the intensities in the donor and FRET channels using correction factors for spectral cross talk ($\alpha$) of 0.02 and direct excitation of the acceptor fluorophore ($\delta$) of 0.06. Differences in the detection efficiencies and quantum yields of the donor and acceptor fluorophores were accounted for using a $\gamma$-factor of 0.66. The accurate FRET efficiency is then given by the following (34, 53):

$$E = \frac{F_{GR} - \alpha\, F_{GG} - \delta\, F_{RR}}{\gamma\, F_{GG} + F_{GR} - \alpha\, F_{GG} - \delta\, F_{RR}}, \qquad [1]$$

where $F_{GG}$, $F_{GR}$, and $F_{RR}$ are the background-corrected photon counts in the donor channel after donor excitation, the acceptor channel after donor excitation (FRET signal), and the acceptor channel after acceptor excitation, respectively. Burstwise fluorescence lifetimes of the donor and acceptor fluorophore were determined using a maximum-likelihood estimator approach (34, 54). For the static FRET lines, the donor lifetime in the absence of the acceptor was determined using donor-only molecules from the measurements selected by a stoichiometry threshold ($S > 0.98$). Contributions of fast linker fluctuations to the static FRET line were accounted for using a Förster radius, $R_0$, of 59 Å and an apparent linker flexibility of 5 Å (32). All data analysis was performed using the open-source software package *PAM* written in MATLAB (55).

**Dynamic PDA.** For the PDA (31, 56), photon counts from selected single-molecule events were rebinned to equal time bins of 0.25-, 0.5-, and 1-ms length, and histograms of the proximity ratio (PR)were computed. The PR is calculated from the raw photon counts in the donor and FRET channels ($S_D, S_F$) by the following:

$$\mathrm{PR} = \frac{S_F}{S_D + S_F}. \qquad [2]$$

In dynamic PDA, the mixing of states during the fixed observation time as a function of interconversion rates can be solved analytically to describe the dynamic contribution to the observed PR histogram (32). Due to the dynamic interconversion between different states, the shape of the PR histogram changes depending on the time bin size. The data were fit using a two-state dynamic model with the addition of one or two minor static low-FRET states. The width of the respective distance distributions, $\sigma_R$, was globally fixed at a fraction of the interdye distance, $\sigma_R = 0.064\,R$. The proportionality factor was determined from measurements of static double-labeled double-stranded DNA molecules, and thus only accounts for apparent broadening of the distance distribution due to acceptor photophysics (57). This assumption reduces the number of free fit parameters significantly and is justified because no static broadening of the FRET efficiency distribution due to conformational heterogeneity is expected for the studied system. For each dataset, all fit parameters were globally optimized using the PR histograms obtained for the three different time bin lengths (*SI Appendix*, Fig. S5).

**Species-Selective FCS.** Species-selective fluorescence correlation functions were determined as follows: For every burst, photons in a time window of 50 ms around the edges of the burst were added. If another single-molecule event was found in the time window, the respective burst was excluded. Correlation functions were calculated for every individual burst and averaged to obtain the species correlation function (58, 59).

For fFCS analysis (33), microtime patterns for the low- and high-FRET efficiency species were obtained from subpopulations of the experiments directly using FRET efficiency thresholds (*SI Appendix*, Fig. S7*A*). Donor and FRET-induced acceptor decays were stacked, and filters were generated separately for the parallel and perpendicular detection channels (*SI Appendix*, Fig. S7 *B*–*D*), which were cross-correlated to circumvent the dead time of the TCSPC hardware and detectors. In this way, the fFCS correlation functions can be calculated down to a limit of 40 ns given our hardware configuration.

FRET-FCS and fFCS curves were fit to a standard single-component diffusion model with up to two kinetic terms, given by the following:

$$G(\tau) = \left[1 + \sum_{i=1}^{2} f_i \exp\left(-\frac{\tau}{\tau_{R,i}}\right)\right] G_{\mathrm{diff}}(\tau) + \mathrm{offset}, \qquad [3]$$

$$G_{\mathrm{diff}}(\tau) = \frac{\gamma}{N}\,\frac{1}{1+\frac{\tau}{\tau_D}}\,\frac{1}{\sqrt{1+\frac{\tau}{p^2\tau_D}}}. \qquad [4]$$

$G_{\mathrm{diff}}(\tau)$ is the diffusion part of the correlation function, where $N$ is the average particle number in the confocal volume, $\gamma = 1/\sqrt{8}$ is a geometric factor that accounts for the Gaussian shape of the observation volume, $\tau_D$ is the diffusion time, and $p$ is the ratio of the axial and lateral size of the confocal volume. The amplitudes of the kinetic terms are given by $f_i$ and the relaxation times by $\tau_{R,i}$. For FRET-FCS, the three correlation functions (donor × donor, FRET × FRET, and donor × FRET) were fit using a single kinetic term by globally linking the parameters of the diffusion term and the relaxation time of the kinetic term $\tau_R$, and letting the amplitude of the kinetic term assume negative values for the cross-correlation function. For fFCS, the four correlation functions between the two species A and B (A × A, A × B, B × A, B × B) were fit using two kinetic terms by globally linking the parameters of the diffusion term (with exception of the particle number $N$) and the relaxation times of the kinetic terms $\tau_{R,i}$, and letting the amplitudes of the kinetic terms $f_i$ for the cross-correlation functions assume negative values.

**MD Simulations.** A homology model for the two CohI modules was built using SWISS-MODEL (60–63) based on the crystal structures of $\mathrm{CohI}_9$ [Protein Data Bank (PDB) ID code 3KCP] (42) for the $\mathrm{CohI}_9$ module, and the crystal structure of $\mathrm{CohI}_7$ (PDB ID code 1AOH) (64) for the $\mathrm{CohI}_8$ module, with sequence similarities of 98.68% and 95.83%, respectively. Torsion-angle rigid-body MD simulations were performed using the crystallography and NMR system (CNS) (65–68). After addition of the linker peptide and relaxation of the structure, an 80-ns trajectory of the dimer was simulated at 300 K with a time step of 5 fs, treating the cohesin modules as rigid bodies while leaving the covalent bonds in the linker free to rotate. Since the aim of the simulation was to determine equilibrium distances of the extended state, no explicit solvent is included. Every 10 ps, possible positions of the fluorophores were determined using accessible volume (AV) calculations with standard parameters for Atto647N using the FPS software package (36). From the accessible volumes, expected average FRET efficiencies, $E(t)$, are calculated at every time step, $t$, by averaging over all possible combinations of donor and acceptor positions using a Förster $R_0$ radius of 59 Å. The FRET efficiencies, $E(t)$, are averaged over all time steps and converted back to distances, yielding the FRET-averaged expected distances of the simulation. Error bars are determined by bootstrapping.

All-atom MD simulations were performed with the AMBER16 MD package using the ff14SB force field (69). The molecule was solvated in a preequilibrated box of TIP3P water using a truncated octahedron geometry with a minimum distance between solute and the periodic boundaries of 2 nm. The charge of the system was neutralized by addition of 23 sodium ions. Two additional sodium and chloride ions were added, resulting in an excess salt concentration of 2 mM. Initial energy minimization of the extended starting structure was performed using the steepest descent method for 10 steps followed by 190 steps using the conjugate gradient method. For equilibration, the system was heated to 298 K over 50,000 steps with a step size of 2 fs at constant volume, and subsequently run for 50,000 additional steps at 298 K with pressure scaling enabled. Individual MD runs were performed for at least 100 ns at 2-fs step size using the NPT ensemble with the Monte Carlo barostat. Trajectories were written at a resolution of 10 ps. The individual trajectories were obtained using the same equilibrated starting structure with random assignment of the initial velocities. On a single Nvidia GTX 1080 Ti GPU, the simulation typically ran at 50 ns a day. Analysis of the MD trajectories was performed using the *cpptraj* utility of the AMBER16 software package (70). Clustering was performed using the hierarchical agglomerative algorithm using the average-linkage criterion and a cluster number of 12. Structural figures were generated using University of California, San Francisco, Chimera (71).

**ACKNOWLEDGMENTS.** We thank Alvaro H. Crevenna for help with obtaining homology models for the simulations and Sigurd Vogler for performing initial experiments. A.B. and D.C.L. gratefully acknowledge the financial support of the Deutsche Forschungsgemeinschaft through Grants SFB1035 (Projects A11), and support from the Ludwig-Maximilians-Universität through the Center for NanoScience and the BioImaging Network. Y.B. is the incumbent of Beatrice Barton Research Fellowship.

1. Brett CT, Waldron KW (1996) *Physiology and Biochemistry of Plant Cell Walls* (Chapman & Hall, London), 2nd Ed.
2. Warren RA (1996) Microbial hydrolysis of polysaccharides. *Annu Rev Microbiol* 50: 183–212.
3. Himmel ME, Bayer EA (2009) Lignocellulose conversion to biofuels: Current challenges, global perspectives. *Curr Opin Biotechnol* 20:316–317.
4. Jordan DB, et al. (2012) Plant cell walls to ethanol. *Biochem J* 442:241–252.
5. Doi RH, Kosugi A (2004) Cellulosomes: Plant-cell-wall-degrading enzyme complexes. *Nat Rev Microbiol* 2:541–551.
6. Fontes CMGA, Gilbert HJ (2010) Cellulosomes: Highly efficient nanomachines designed to deconstruct plant cell wall complex carbohydrates. *Annu Rev Biochem* 79: 655–681.
7. Gilbert HJ (2007) Cellulosomes: Microbial nanomachines that display plasticity in quaternary structure. *Mol Microbiol* 63:1568–1576.
8. Fierobe H-P, et al. (2002) Degradation of cellulose substrates by cellulosome chimeras. Substrate targeting versus proximity of enzyme components. *J Biol Chem* 277: 49621–49630.
9. Béguin P, Alzari PM (1998) The cellulosome of *Clostridium thermocellum*. *Biochem Soc Trans* 26:178–185.
10. Bayer EA, Morag E, Lamed R (1994) The cellulosome—a treasure-trove for biotechnology. *Trends Biotechnol* 12:379–386.
11. Lamed R, Setter E, Kenig R, Bayer EA (1983) The cellulosome—a discrete cell surface organelle of *Clostridium thermocellum* which exhibits separate antigenic, cellulose-binding and various cellulolytic. *Biotechnol Bioeng Symp* 13:163–181.

12. Tormo J, et al. (1996) Crystal structure of a bacterial family-III cellulose-binding domain: A general mechanism for attachment to cellulose. *EMBO J* 15:5739–5751.
13. Schoeler C, et al. (2015) Mapping mechanical force propagation through biomolecular complexes. *Nano Lett* 15:7370–7376.
14. Carvalho AL, et al. (2007) Evidence for a dual binding mode of dockerin modules to cohesins. *Proc Natl Acad Sci USA* 104:3089–3094.
15. Salamitou S, et al. (1994) Recognition specificity of the duplicated segments present in *Clostridium thermocellum* endoglucanase CelD and in the cellulosome-integrating protein CipA. *J Bacteriol* 176:2822–2827.
16. Stahl SW, et al. (2012) Single-molecule dissection of the high-affinity cohesin–dockerin complex. *Proc Natl Acad Sci USA* 109:20431–20436.
17. Lytle B, Myers C, Kruus K, Wu JH (1996) Interactions of the CelS binding ligand with various receptor domains of the *Clostridium thermocellum* cellulosomal scaffolding protein, CipA. *J Bacteriol* 178:1200–1203.
18. Yaron S, Morag E, Bayer EA, Lamed R, Shoham Y (1995) Expression, purification and subunit-binding properties of cohesins 2 and 3 of the *Clostridium thermocellum* cellulosome. *FEBS Lett* 360:121–124.
19. Smith SP, Bayer EA (2013) Insights into cellulosome assembly and dynamics: From dissection to reconstruction of the supramolecular enzyme complex. *Curr Opin Struct Biol* 23:686–694.
20. Smith SP, Bayer EA, Czjzek M (2017) Continually emerging mechanistic complexity of the multi-enzyme cellulosome complex. *Curr Opin Struct Biol* 44:151–160.
21. Bayer EA, Lamed R (1986) Ultrastructure of the cell surface cellulosome of *Clostridium thermocellum* and its interaction with cellulose. *J Bacteriol* 167:828–836.
22. Mayer F, Coughlan MP, Mori Y, Ljungdahl LG (1987) Macromolecular organization of the cellulolytic enzyme complex of *Clostridium thermocellum* as revealed by electron microscopy. *Appl Environ Microbiol* 53:2785–2792.
23. Molinier A-L, et al. (2011) Synergy, structure and conformational flexibility of hybrid cellulosomes displaying various inter-cohesins linkers. *J Mol Biol* 405:143–157.
24. Hammel M, Fierobe H-P, Czjzek M, Finet S, Receveur-Bréchot V (2004) Structural insights into the mechanism of formation of cellulosomes probed by small angle X-ray scattering. *J Biol Chem* 279:55985–55994.
25. Currie MA, et al. (2012) Scaffoldin conformation and dynamics revealed by a ternary complex from the *Clostridium thermocellum* cellulosome. *J Biol Chem* 287: 26953–26961.
26. Currie MA, et al. (2013) Small angle X-ray scattering analysis of *Clostridium thermocellum* cellulosome N-terminal complexes reveals a highly dynamic structure. *J Biol Chem* 288:7978–7985.
27. García-Alvarez B, et al. (2011) Molecular architecture and structural transitions of a *Clostridium thermocellum* mini-cellulosome. *J Mol Biol* 407:571–580.
28. Różycki B, Cazade P-A, O'Mahony S, Thompson D, Cieplak M (2017) The length but not the sequence of peptide linker modules exerts the primary influence on the conformations of protein domains in cellulosome multi-enzyme complexes. *Phys Chem Chem Phys* 19:21414–21425.
29. Galera-Prat A, Pantoja-Uceda D, Laurents DV, Carrión-Vázquez M (2018) Solution conformation of a cohesin module and its scaffoldin linker from a prototypical cellulosome. *Arch Biochem Biophys* 644:1–7.
30. Vazana Y, et al. (2013) A synthetic biology approach for evaluating the functional contribution of designer cellulosome components to deconstruction of cellulosic substrates. *Biotechnol Biofuels* 6:182.
31. Antonik M, Felekyan S, Gaiduk A, Seidel CAM (2006) Separating structural heterogeneities from stochastic variations in fluorescence resonance energy transfer distributions via photon distribution analysis. *J Phys Chem B* 110:6970–6978.
32. Kalinin S, Valeri A, Antonik M, Felekyan S, Seidel CAM (2010) Detection of structural dynamics by FRET: A photon distribution and fluorescence lifetime analysis of systems with multiple states. *J Phys Chem B* 114:7983–7995.
33. Felekyan S, Kalinin S, Sanabria H, Valeri A, Seidel CAM (2012) Filtered FCS: Species auto- and cross-correlation functions highlight binding and dynamics in biomolecules. *ChemPhysChem* 13:1036–1053.
34. Kudryavtsev V, et al. (2012) Combining MFD and PIE for accurate single-pair Förster resonance energy transfer measurements. *ChemPhysChem* 13:1060–1078.
35. Carvalho AL, et al. (2003) Cellulosome assembly revealed by the crystal structure of the cohesin-dockerin complex. *Proc Natl Acad Sci USA* 100:13809–13814.
36. Kalinin S, et al. (2012) A toolkit and benchmark study for FRET-restrained high-precision structural modeling. *Nat Methods* 9:1218–1225.
37. Hellenkamp B, et al. (2017) Precision and accuracy of single-molecule FRET measurements–A worldwide benchmark study. arXiv:1710.03807v2.
38. Tomov TE, et al. (2012) Disentangling subpopulations in single-molecule FRET and ALEX experiments with photon distribution analysis. *Biophys J* 102:1163–1173.
39. Felekyan S, Sanabria H, Kalinin S, Khnemuth R, Seidel CAM (2013) Analyzing Förster resonance energy transfer with fluctuation algorithms. *Methods Enzymol* 519:39–85.
40. Müller BK, Zaychikov E, Bräuchle C, Lamb DC (2005) Pulsed interleaved excitation. *Biophys J* 89:3508–3522.
41. Kapusta P, Wahl M, Benda A, Hof M, Enderlein J (2007) Fluorescence lifetime correlation spectroscopy. *J Fluoresc* 17:43–48.
42. Adams JJ, et al. (2010) Insights into higher-order organization of the cellulosome revealed by a dissect-and-build approach: Crystal structure of interacting *Clostridium thermocellum* multimodular components. *J Mol Biol* 396:833–839.
43. Noach I, et al. (2010) Modular arrangement of a cellulosomal scaffoldin subunit revealed from the crystal structure of a cohesin dyad. *J Mol Biol* 399:294–305.
44. Di Fiori N, Meller A (2010) The effect of dye-dye interactions on the spatial resolution of single-molecule FRET measurements in nucleic acids. *Biophys J* 98:2265–2272.
45. Lamed R, Setter E, Bayer EA (1983) Characterization of a cellulose-binding, cellulase-containing complex in *Clostridium thermocellum*. *J Bacteriol* 156:828–836.
46. Morag E, Bayer EA, Lamed R (1992) Unorthodox intrasubunit interactions in the cellulosome of *Clostridium thermocellum*. *Appl Biochem Biotechnol* 33:205–217.
47. Karpol A, et al. (2013) Structural and functional characterization of a novel type-III dockerin from *Ruminococcus flavefaciens*. *FEBS Lett* 587:30–36.
48. Slutzki M, et al. (2013) Intramolecular clasp of the cellulosomal *Ruminococcus flavefaciens* ScaA dockerin module confers structural stability. *FEBS Open Bio* 3:398–405.
49. Galera-Prat A, Moraïs S, Vazana Y, Bayer EA, Carrión-Vázquez M (2018) The cohesin module is a major determinant of cellulosome mechanical stability. *J Biol Chem* 293: 7139–7147.
50. Vazana Y, Moraïs S, Barak Y, Lamed R, Bayer EA (2010) Interplay between *Clostridium thermocellum* family 48 and family 9 cellulases in cellulosomal versus noncellulosomal states. *Appl Environ Microbiol* 76:3236–3243.
51. Eggeling C, et al. (2001) Data registration and selective single-molecule analysis using multi-parameter fluorescence detection. *J Biotechnol* 86:163–180.
52. Nir E, et al. (2006) Shot-noise limited single-molecule FRET histograms: Comparison between theory and experiments. *J Phys Chem B* 110:22103–22124.
53. Lee NK, et al. (2005) Accurate FRET measurements within single diffusing biomolecules using alternating-laser excitation. *Biophys J* 88:2939–2953.
54. Maus M, et al. (2001) An experimental comparison of the maximum likelihood estimation and nonlinear least-squares fluorescence lifetime analysis of single molecules. *Anal Chem* 73:2078–2086.
55. Schrimpf W, Barth A, Hendrix J, Lamb DC (2018) PAM: A framework for integrated analysis of imaging, single-molecule, and ensemble fluorescence data. *Biophys J* 114: 1518–1528.
56. Kalinin S, Felekyan S, Antonik M, Seidel CAM (2007) Probability distribution analysis of single-molecule fluorescence anisotropy and resonance energy transfer. *J Phys Chem B* 111:10253–10262.
57. Kalinin S, Sisamakis E, Magennis SW, Felekyan S, Seidel CAM (2010) On the origin of broadening of single-molecule FRET efficiency distributions beyond shot noise limits. *J Phys Chem B* 114:6197–6206.
58. Eggeling C, Fries JR, Brand L, Günther R, Seidel CA (1998) Monitoring conformational dynamics of a single molecule by selective fluorescence spectroscopy. *Proc Natl Acad Sci USA* 95:1556–1561.
59. Laurence TA, et al. (2007) Correlation spectroscopy of minor fluorescent species: Signal purification and distribution analysis. *Biophys J* 92:2184–2198.
60. Biasini M, et al. (2014) SWISS-MODEL: Modelling protein tertiary and quaternary structure using evolutionary information. *Nucleic Acids Res* 42:W252–W258.
61. Guex N, Peitsch MC, Schwede T (2009) Automated comparative protein structure modeling with SWISS-MODEL and Swiss-PdbViewer: A historical perspective. *Electrophoresis* 30(Suppl 1):S162–S173.
62. Kiefer F, Arnold K, Künzli M, Bordoli L, Schwede T (2009) The SWISS-MODEL Repository and associated resources. *Nucleic Acids Res* 37:D387–D392.
63. Arnold K, Bordoli L, Kopp J, Schwede T (2006) The SWISS-MODEL workspace: A web-based environment for protein structure homology modelling. *Bioinformatics* 22: 195–201.
64. Tavares GA, Béguin P, Alzari PM (1997) The crystal structure of a type I cohesin domain at 1.7 Å resolution. *J Mol Biol* 273:701–713.
65. Brünger AT, et al. (1998) Crystallography & NMR system: A new software suite for macromolecular structure determination. *Acta Crystallogr D Biol Crystallogr* 54: 905–921.
66. Brunger AT (2007) Version 1.2 of the crystallography and NMR system. *Nat Protoc* 2: 2728–2733.
67. Brunger AT, Strop P, Vrljic M, Chu S, Weninger KR (2011) Three-dimensional molecular modeling with single molecule FRET. *J Struct Biol* 173:497–505.
68. Choi UB, et al. (2010) Single-molecule FRET-derived model of the synaptotagmin 1-SNARE fusion complex. *Nat Struct Mol Biol* 17:318–324.
69. Case DA, et al. (2017) *AMBER 2017* (University of California, San Francisco).
70. Roe DR, Cheatham TE, 3rd (2013) PTRAJ and CPPTRAJ: Software for processing and analysis of molecular dynamics trajectory data. *J Chem Theory Comput* 9:3084–3095.
71. Pettersen EF, et al. (2004) UCSF Chimera—a visualization system for exploratory research and analysis. *J Comput Chem* 25:1605–1612.

## B.4 Paper 4: Covalent Dye Attachment Influences the Dynamics and Conformational Properties of Flexible Peptides

PLOS | ONE

RESEARCH ARTICLE

# Covalent dye attachment influences the dynamics and conformational properties of flexible peptides

**Manuel P. Luitz**[1☯], **Anders Barth**[2☯], **Alvaro H. Crevenna**[3], **Rainer Bomblies**[1], **Don C. Lamb**[2], **Martin Zacharias**[1]*

**1** Department Physik, T38, Technische Universität München, 85748 Garching, Germany, **2** Department Chemie, Physikalische Chemie, Ludwig-Maximilians-Universität München, 81377 München, Germany, **3** Instituto de Tecnologia Química e Biológica António Xavier, Universidade Nova de Lisboa, 2780-157 Oeiras, Portugal

☯ These authors contributed equally to this work.
* mzacharias@mytum.de

**Citation:** Luitz MP, Barth A, Crevenna AH, Bomblies R, Lamb DC, Zacharias M (2017) Covalent dye attachment influences the dynamics and conformational properties of flexible peptides. PLoS ONE 12(5): e0177139. https://doi.org/10.1371/journal.pone.0177139

**Editor:** Heinrich Sticht, Friedrich-Alexander-Universitat Erlangen-Nurnberg, GERMANY

**Received:** February 27, 2017

**Accepted:** April 21, 2017

**Published:** May 23, 2017

**Data Availability Statement:** All relevant data are within the paper and its Supporting Information file.

**Funding:** The authors thank the Deutsche Forschungsgemeinschaft (DFG/SFB1035 project A11 and B02) for financial support. This work was also supported by the LRZ supercomputer center (Leibniz Rechenzentrum) through grant pr48po. The funders had no role in study design, data collection and analysis, decision to publish, or preparation of the manuscript.

## Abstract

Fluorescence spectroscopy techniques like Förster resonance energy transfer (FRET) and fluorescence correlation spectroscopy (FCS) have become important tools for the *in vitro* and *in vivo* investigation of conformational dynamics in biomolecules. These methods rely on the distance-dependent quenching of the fluorescence signal of a donor fluorophore either by a fluorescent acceptor fluorophore (FRET) or a non-fluorescent quencher, as used in FCS with photoinduced electron transfer (PET). The attachment of fluorophores to the molecule of interest can potentially alter the molecular properties and may affect the relevant conformational states and dynamics especially of flexible biomolecules like intrinsically disordered proteins (IDP). Using the intrinsically disordered S-peptide as a model system, we investigate the impact of terminal fluorescence labeling on the molecular properties. We perform extensive molecular dynamics simulations on the labeled and unlabeled peptide and compare the results with *in vitro* PET-FCS measurements. Experimental and simulated timescales of end-to-end fluctuations were found in excellent agreement. Comparison between simulations with and without labels reveal that the $\pi$-stacking interaction between the fluorophore labels traps the conformation of S-peptide in a single dominant state, while the unlabeled peptide undergoes continuous conformational rearrangements. Furthermore, we find that the open to closed transition rate of S-peptide is decreased by at least one order of magnitude by the fluorophore attachment. Our approach combining experimental and *in silico* methods provides a benchmark for the simulations and reveals the significant effect that fluorescence labeling can have on the conformational dynamics of small biomolecules, at least for inherently flexible short peptides. The presented protocol is not only useful for comparing PET-FCS experiments with simulation results but provides a strategy to minimize the influence on molecular properties when chosing labeling positions for fluorescence experiments.

**Competing interests:** The authors have declared that no competing interests exist.

## Introduction

Structural changes of biomolecules are often closely related to their function. For proteins, usually large rearrangements of domains occur during the functional cycle. In the family of intrinsically disorderd proteins (IDP) certain regions undergo continuous structural changes. The transition from disorder to order is often part of the biological function mechanism of these proteins but may otherwise be an artifact of the genetic evolution [1]. Due to the lack of stable structure, they elude conventional structural biology approaches. Fluorescence spectroscopy techniques provide a useful toolbox to investigate the dynamics and extent of structural rearrangements of biomolecules *in vitro* and *in vivo* [2–6]. One of the most common approaches is the use of Förster resonance energy transfer (FRET) between two fluorophores attached to the molecule of interest [7]. The radiationless transfer of energy from the excited donor dye to the red-shifted acceptor dye depends on the relative orientation and distance between the fluorophores. Its high sensitivity in the range of 20–100 Å renders the effect interesting for experimental determination of distances on the molecular scale. Another example of radiation-less energy transfer is photoinduced electron transfer (PET) [2, 3, 8–11]. The excited-state energy may dissipate via electron transfer from the fluorophore to the quencher or vice versa, depending on the redox potentials of the excited state fluorophore and quencher. Relaxation to the ground state then occurs non-radiatively by charge recombination of the radical donor/acceptor ion pair. The timescale of the PET reaction resides in the range of femtoseconds to picoseconds [12, 13] which is significantly faster than the fluorescence lifetime of the fluorophores of typically a few nanoseconds [14, 15]. The efficiency of PET decays exponentially with distance on the length scale of a few Å, showing effectively an all-or-nothing quenching behaviour.

PET enables the *in vitro* time resolved detection of closed and open contacts between fluorophore and quencher in proteins and other biomolecules. Due to the on-off characteristics of PET, it is commonly combined with fluorescence correlation spectroscopy (FCS) [16] to study the timescale of the dynamic changes of the fluorescence signal. FCS is based on the analysis of the time correlation of the detected signal and is thus sensitive to all processes that effect the fluorescence signal. Most commonly, FCS is being used to study the diffusion properties of molecules [17], but it is also a powerful tool to study conformational dynamics when combined with FRET or PET [18, 19].

In biomolecules, the strongest fluorescence quenching of commonly used fluorophores for PET (e.g. Atto655, MR121 and Atto Oxa11) is observed for tryptophan in proteins and guanine in nucleic acids due to their oxidation potentials that allow them to act as electron donors [20, 21]. If tryptophan is not part of the protein sequence, PET experiments can be performed by engineering a Trp residue in the region of interest by either mutation or the adherence of an additional residue. On the other hand, Trp residues which might interfere in an undesirable way with the fluorophore need to be deleted from the protein. The labeling of proteins with fluorophores usually requires modification of the protein sequence. Typically, labeling is performed by reacting a maleimide derivative of the fluorescent dye with cysteine residues in the protein. To achieve specificity, this approach requires the removal of natural cysteine residues or the introduction of additional cysteine residues by mutation. Other labeling approaches target amino groups or rely on bioorthogonal labeling strategies based on the addition of unnatural amino acids [22]. After attaching the fluorophore to the molecule of interest, careful control measurements have to be performed to ensure that the photophysical properties are not altered by the local environment, and that no sticking interactions occur which would impair the rotational freedom of the fluorophore.

Although fluorescence techniques have been applied successfully on a variety of systems [5, 23, 24], usually little information is available to what extent the structural or dynamical properties of the studied system are modified by the attachment of the fluorescence labels. Molecular dynamics studies can help in the interpretation of experimental results and detection of potential artifacts introduced by the dye label [25–27]. As the fluorophores typically exceed the size of naturally occurring amino acids, it is expected that at least the local diffusivity is modified. Furthermore, many readily available fluorophores contain rigid ring systems which function as light absorbing centers (e.g. oxazine derivatives MR121, Atto655 and Atto Oxa11) and potentially facilitate hydrophobic or $\pi$-stacking interactions with other aromatic ring structures especially of the quencher. A significant influence of the fluorescent label on the local structure, the conformational dynamics and the overall functionality of the protein can thus usually not be excluded, and careful controls have to be performed to ensure the validity of the experimental results.

In the present study we conducted a comparative *in vitro* and *in silico* study on the 14 amino acid long truncated S-peptide, which historically served as a model system for intrinsically disordered peptides [28–32]. S-peptide is a fragment of RNAse-S formed after proteolytic cleavage of bovine Ribonuclease A by the subtilisin protease [33, 34]. While S-peptide is intrinsically disordered in solution, it adopts a stable helical fold upon association to S-protein forming the complex RNAse-S [32]. We N-terminally attached fluorophore Atto655 and added a tryptophan residue to the C-terminus serving as a fluorescence quencher [2]. For the labeled peptide, the fluorescence quenching autocorrelation was measured and analyzed with respect to the dynamic contribution, which is a measure for the end-to-end dynamics of the peptide chain. Additionally, we performed extensive, continuous molecular dynamics (MD) simulations on S-peptide with and without the fluorescence labels, to provide atomistic insight into the dynamics and sampled conformational regimes of the peptides.

Quantitative agreement of the experimental quenching autocorrelation of labeled S-peptide and *in silico* results was obtained. Comparison of the simulations reveals, that the dynamical and conformational regime of the flexible S-peptide was significantly altered by the attachment of Atto655 and Trp15. This study sheds light on systematic modifications of macromolecular properties introduced by fluorescence labeling and provides valuable insight for the design of future fluorescence spectroscopy experiments.

# Results

## MD simulations

Extensive molecular dynamics simulations were performed for the labeled and unlabeled versions of the S-peptide over 30 μs for each trajectory. Both trajectories were started from extended peptide configurations. To give qualitative insight in the folding dynamics of intrinsically disordered S-peptide, the evolution of the RMSD with respect to the starting structure was calculated (Fig 1) and trajectories were visually inspected. To allow direct comparison between RMSD regimes of both systems, the RMSD was only calculated for residues 1 to 14 (without Atto655 and Trp15).

Unlabeled S-peptide rapidly fluctuated between conformational modes on the timescale of several nanoseconds as expected for a intrinsically disordered peptide. Fluctuation of the RMSD indicated no stable conformation surviving in the microseconds time regime throughout the whole simulation. Labeled S-peptide, however, showed a significantly reduced bandwidth of RMSD fluctuations with several plateaus in the RMSD evolution. Visual inspection confirmed metastable states surviving for several microseconds during the trajectory. Many configurations revealed close contacts between the two ring systems of terminal Atto655 and

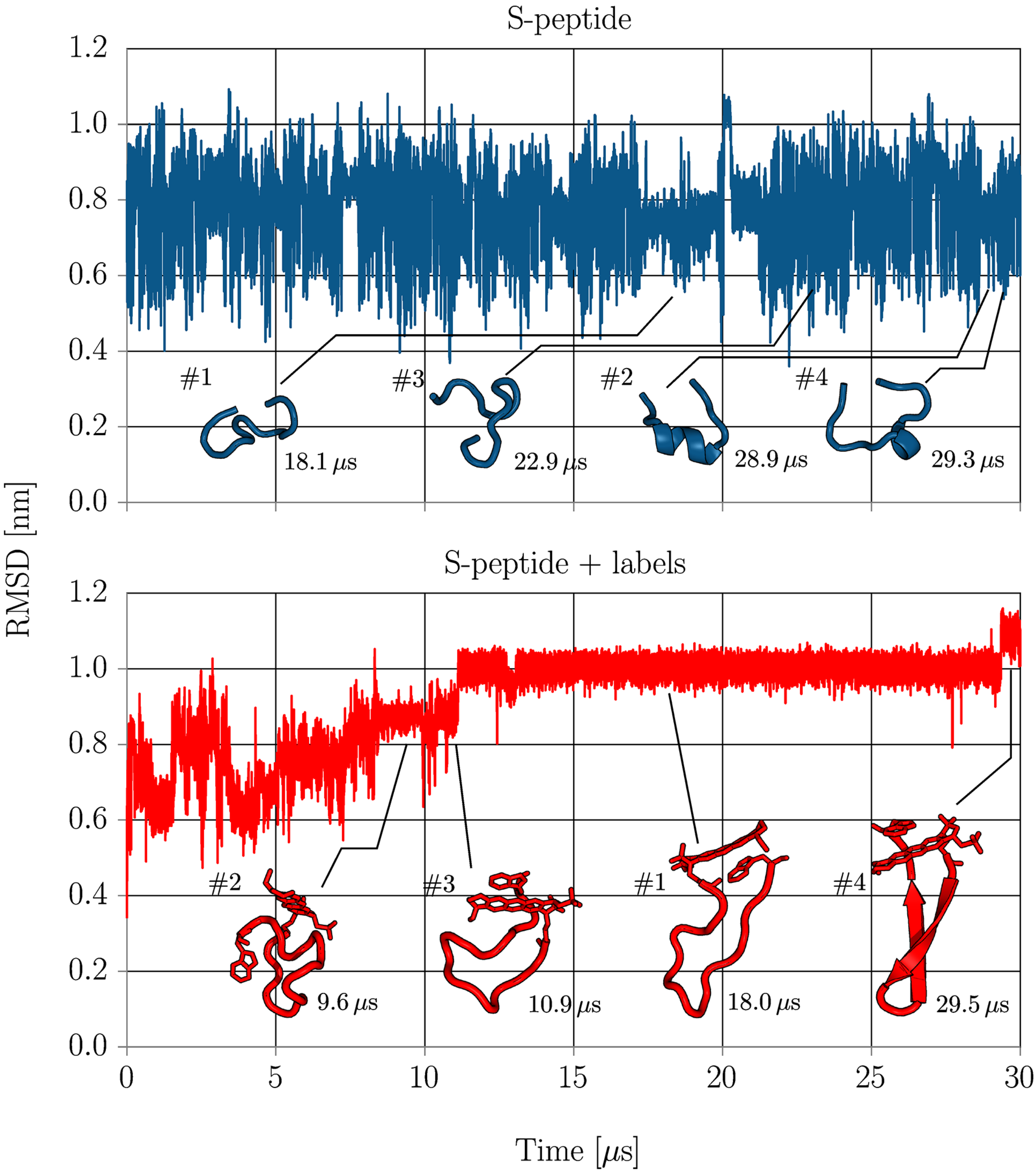

**Fig 1. The RMSD of non-hydrogen (heavy) atoms of residues 1-14 with respect to the unfolded starting structure for simulations with (lower panel) and without (upper panel) labels.** The mean structures of the respectively four largest clusters are shown and their cluster index is indicated (#). Additionally, the simulation time when the clusters mean structures were observed during the simulation is indicated at the bottom right of each cluster structure.

https://doi.org/10.1371/journal.pone.0177139.g001

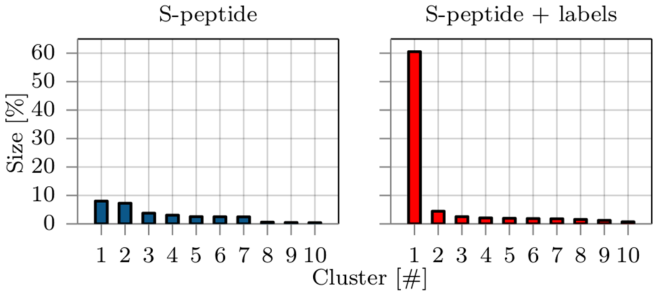

**Fig 2. The population size of the ten largest clusters in percentage of lifetime compared to the whole trajectory from simulations without (left panel) and with (right panel) fluorescence labels.** Clustering was based on the RMSD and the single linkage algorithm [35] with a 0.25 nm cutoff was used.

https://doi.org/10.1371/journal.pone.0177139.g002

Trp15 indicating a strong stacking interaction that traps the system in a quenched state. After about 12 µs, the backbone locked into a stable $\beta$-sheet like configuration and remained in this state until finally folding to a $\beta$-sheet structure after 29 µs (see Figs 1 and 2 and conformational regime clusters #1 and #4).

## Sampled conformational regimes

Conformations from MD trajectories were clustered for both systems separately to quantify the impact of labeling on the relevant conformational regimes. Clustering along the RMSD was performed with the single-linkage algorithm using a RMSD cutoff of 0.25 nm and $10^5$ frames from each trajectory [35]. Clusters were sorted and numbered by their frequency of occurrence and the distribution of the ten biggest clusters is shown in Fig 2.

As expected from visual inspection of the trajectories, cluster sizes of unmodified S-peptide reflect the typical conformational behavior of an intrinsically disordered peptide. The decrease in probability with increasing cluster index is relatively moderate suggesting low free energy differences between neighboring clusters. A total of about 4700 clusters was found and the S-peptide adopted conformations belonging to the largest cluster only during 6% of the total simulation time. The mean structures of the first four clusters are depicted in Fig 1 and give insight into the variability of conformations.

With the attachment of Atto655 and Trp15 to the termini of S-peptide, the conformational behavior however changed significantly. The variability of clusters narrowed down to about 1000 different clusters, with many showing stacked Atto655/Trp15 configurations. The largest cluster, found between 12–29 µs, dominates the accessible conformational regimes with a probability of over 60% and indicates a shift from intrinsic disorder to a metastable folded peptide, reducing the conformational variability significantly. Three out of four mean structures of the largest clusters show strong stacking interaction between terminal labels (Fig 1). Interestingly, the conformation of the largest cluster #1 was never adopted by the trajectory of S-peptide without labels (according to the 0.25 nm threshold used for clustering). The closest structure had a distance of RMSD = 0.30 nm. As it is unlikely that this finding is attributed to insufficient sampling (see section conformational dynamics), it is a strong indicator that the attachment of the labels creates a deep minimum in the conformational landscape that is not present for the unlabeled peptide. Note, even within the first 12 µs, the sampled states of the S-peptide with terminal labels showed only little overlap with the most populated clusters of the S-peptide simulation without dyes. None of the sampled conformations approached the mean structure of the 10 most populated clusters of the S-peptide simulation without terminal dyes to less than the cluster RMSD cutoff of 0.25 nm (smallest deviation 0.28 nm).

## Conformational dynamics

To characterize the effect of the fluorescent labels on the conformational dynamics of the S-peptide, we compare the simulations with and without fluorescence labels by defining a two-state model (open/close) based on the end-to-end distance $d$ of the peptide. The distance $d$ was calculated between C-$\beta$ atoms of residues Lys1 and Asp14 again for both systems with and without labels. We split the distance ensemble in two regimes, to characterize the switching dynamics between a structured and disordered regime of S-peptide. Distances $d < 1.3$ nm were assigned to a "close" regime while distances $d > 2.5$ nm were assigned to an "open" regime. By counting the number of transition ($N_T$) from one regime to the other and dividing it by the total simulation time, a mean rate of opening and closing events of the peptide was calculated. For the S-peptide without labels, a open to closed transition rate of 50.1 $\mu s^{-1}$ was found ($N_T = 1503$ in 30 μs), while refolding dynamics for labeled S-peptide were slowed by more then one order of magnitude to 6.6 $\mu s^{-1}$ during the initial 12 μs ($N_T = 80$). Not a single open to close transition event was observed in the simulation interval 12–30 μs ($N_T = 0$) confirming the strong trapping of labeled S-peptide in this conformational regime.

## Circular dichroism spectra

The MD simulations suggest that the labeled S-peptide adopts a metastable $\beta$-sheet conformation induced by $\pi$-stacking interaction between the termini. To investigate to what extent the $\beta$-sheet conformation is part of the equilibrium regime and to quantify the modification in the accessible conformational regimes by dye/quencher interactions, we measured circular dichroism (CD) spectra of labeled S-peptide and compared it with the spectrum of S-peptide labeled with Atto655 but without Trp15 (Fig 3). Comparison with a previously published CD spectrum of native 20 residue S-peptide reveals qualitative similarity with the spectrum of labeled S-peptide without Trp15 where both spectra exhibit a local peak at 220 nm [36, 37]. When Trp15 is added to the peptide, however, the peak at 220 nm vanishes, consistent with the increase in $\beta$-sheet structure in our simulations, possibly induced by the $\pi$-stacking interaction between the terminal labels. The CD spectrum reveals that the relevant conformational regime is not dominated by only $\beta$-sheet structures but includes contributions of helical and random coil conformations. This supports the results from the 30 μs simulation where the labeled S-peptide adopted $\beta$-sheet conformation only during a fraction of the simulation time and exposed random coil backbone configurations otherwise (Fig 1, cluster #1).

## PET-FCS measurements

The dye/quencher dynamics of the labeled S-peptide can be adressed experimentally by PET-FCS. The full PET-FCS correlation function is shown in Fig 4. Fluorescence correlation spectroscopy (FCS) analyzes the fluctuations of the recorded fluorescence signal and is thus sensitive to all processes affecting the fluorescence signal. Multiple phenomena spanning the timescale from picoseconds to seconds can be observed in the autocorrelation curve (regimes I-IV). Photon antibunching (I), a typical property of quantum emitters, occurs on the timescale of the fluorescence lifetime of $\sim 2$ ns for Atto655 [38]. Diffusion through the confocal volume (IV) is observed on timescales between several tenths of μs to ms, depending on the size of the observation volume and the diffusion coefficient of the molecule. The measured diffusion time of the labeled S-peptide is 51 μs, translating to a diffusion coefficient of about 185 $\mu m^2 s^{-1}$ (based on the lateral size of the focal volume of 195 nm), as is expected for a small

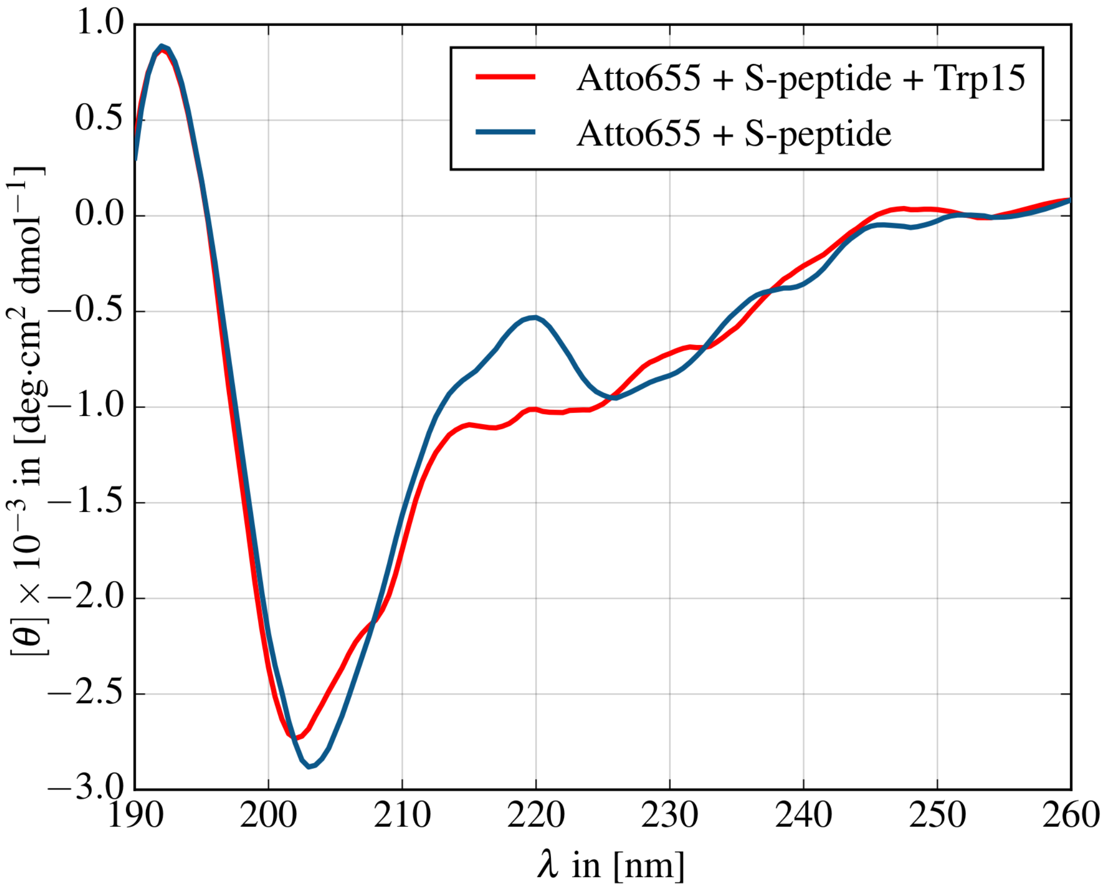

**Fig 3. CD spectra of labeled S-peptide with and without Atto655 stacking partner Trp15.** The peak at 220 nm indicates residual $\alpha$-helix formation and less $\beta$-sheet contribution in the labeled S-peptide without Trp15.

https://doi.org/10.1371/journal.pone.0177139.g003

peptide. Most fluorescent dyes can undergo intersystem crossing from the excited singlet state into a dark triplet state with lifetimes in the range of several μs (III). Here, we find a triplet relaxation time of 2.4 μs for Atto655. The amplitude of this triplet contribution is dependent on the incident laser power (Fig A in S1 File). Any conformational dynamics are superimposed onto these processes. The fast chain dynamics of intrinsically disordered peptides or unfolded proteins usually occur on the submicrosecond timescale [39], while slower conformational dynamics involving large conformational rearrangements usually take place in the range of ms to s [40].

The quenching contribution to the correlation function is indicated in regime II (Fig 4). To determine the timescales of the quenching dynamics, we fit the correlation function with a model accounting for the listed contributions (Eq (3)). By careful inspection of the weighted residuals between model and data, we find that the addition of a second dynamic contribution to the model function improves the quality of the fit significantly (Fig B in S1 File and Table A in S1 File). Because the length of the MD simulation is not sufficient to address the existence of two dynamic contributions, however, we can not determine whether the second component arises from an alternative conformational regime of S-peptide. Therefore, we limit our discussion to the average timescale and overall amplitude of the two components. This result,

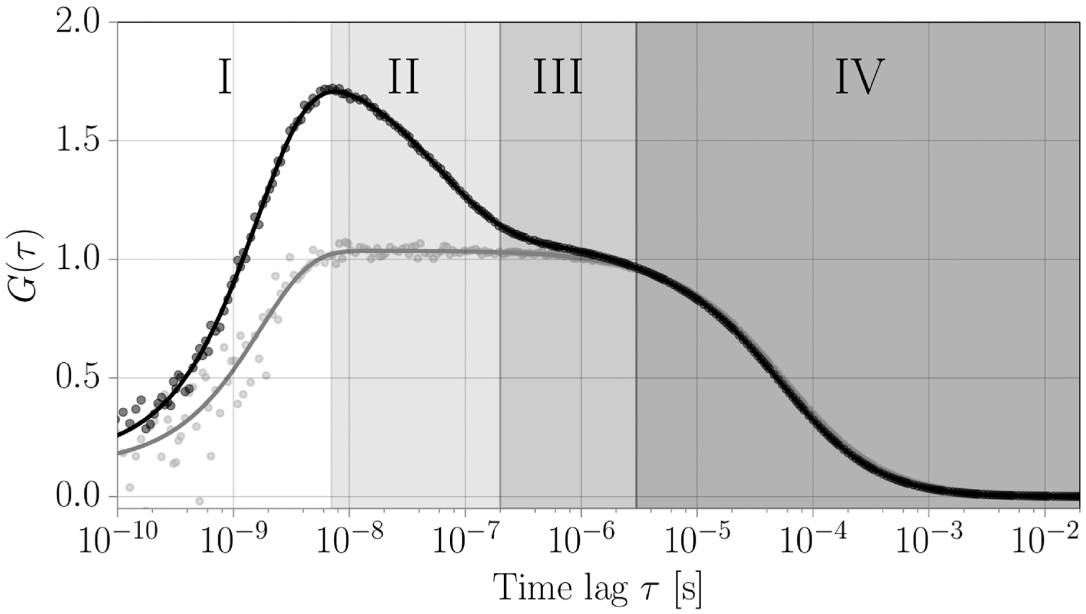

**Fig 4. Experimentally obtained FCS curve and model fit function for labeled S-peptide in the presence (black) and absence (gray) of the quenching tryptophan.** Indicated are the four main time regimes of the relevant processes. (I) Photon antibunching: The lifetime of the excited state of the fluorophore determines the shortest temporal separation between two photon emission events. This leads to a decrease in the correlation function for correlation times faster than the lifetime of the excited state. (II) Timescale of the internal conformational dynamics that lead to quenching/unquenching of the fluorophore and dominate the autocorrelation function. These timescales are to be compared with the MD simulations. (III) Photophysical artifacts: Intersystem crossing from the excited singlet state into a dark triplet state with lifetimes in the range of several μs (IV) This correlation regime is dominated by the diffusion of labeled peptides through the confined detection volume of the FCS setup.

https://doi.org/10.1371/journal.pone.0177139.g004

however, indicates that the conformational dynamics may be more complex than discussed in this work. To directly compare the measured dynamics to the correlation functions obtained from MD, we isolate the dynamic contribution by dividing the correlation function by the contributions of diffusion, photophysics and antibunching (Fig 5B). We converted the observed amplitude of 0.67 and relaxation time of 80 ns to off- and on-rates by Eqs (4) and (5) yielding an off-rate $k_{\text{off}} = 5.0\ \mu\text{s}^{-1}$ and an on-rate $k_{\text{on}} = 7.4\ \mu\text{s}^{-1}$.

## Quenching dynamics from MD

The result obtained for the conformational dynamics of the S-peptide with labels based on the classification into "unfolded" and "folded" states by means of the end-to-end distance ($2.7\ \mu\text{s}^{-1}$) only roughly correlates with the rates of quenching contact formation as measured in the PET-FCS experiment (average rate of $6.2\ \mu\text{s}^{-1}$). The quenching on- and off-rates describe the kinetics of quenching contact formation between the fluorophore Atto655 and the quencher Trp15, which are different from the conformational dynamics. To compare the experimental result with the simulations, a simple distance criterion between dye and quencher is applied.

Configurations of Atto655/Trp15 from simulation were classified as "dark" state when the distance between the geometric centers of their ring compounds was below a quenching distance of $r^* < 0.55$ nm or as fluorescent otherwise [41–43]. The quenching autocorrelation

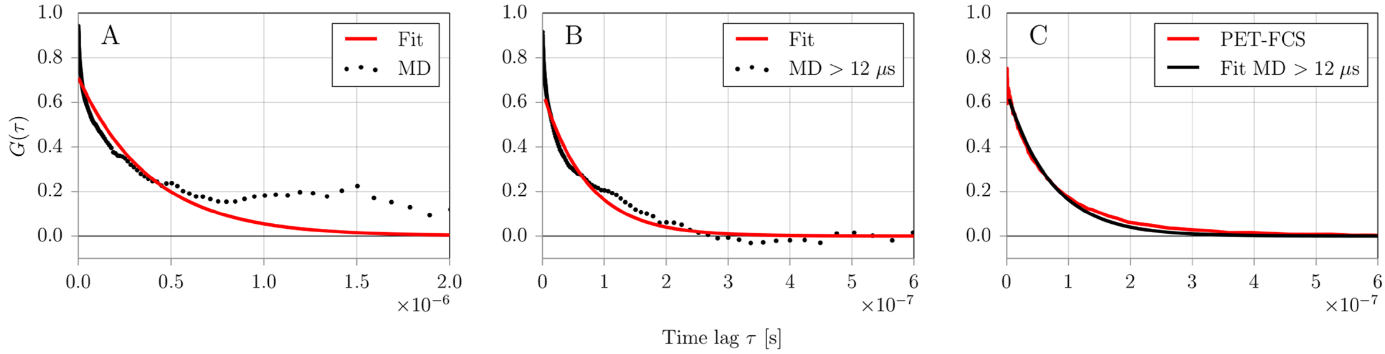

**Fig 5. Atto655/Trp15 fluorescence quenching autocorrelation data fitted with a two-state exponential model function.** Data and fits are shown for MD simulations (A, B) and experimental PET-FCS measurement (C). (A) Data from MD calculated over the whole simulation time (30 μs). (B) Data from MD where the initial 12 μs of the simulation was omitted. (C) Dynamic part of the correlation curve from experimental PET-FCS measurement (red) overlayed with the fitted MD data collected after 12 μs (black).

https://doi.org/10.1371/journal.pone.0177139.g005

function was fit to a two-state kinetic model with single exponential kinetics (Eq (1)). Due to the global conformational rearrangements of S-peptide during the initial 12 μs and the associated metastable states with lifetimes in the microsecond regime, the convergence of quenching autocorrelation data was insufficient. This is especially visible at large correlation times $\tau >$ 500 ns (Fig 5A). The long-lived metastable states however dominated the quenching dynamics resulting in relaxation timescales of $\tau_r = 391$ ns (Table 1).

Because the S-peptide locked in a quasi-stable folded $\beta$–sheet like configuration after 12 μs simulation time, we decided to treat the initial 12 μs as equilibration time and recalculate the quenching autocorrelation for only the second part of the simulation (Fig 5B). The resulting quenching relaxation timescale of $\tau_r = 72$ ns was about 4–5 times faster as dye and quencher could not diffuse far away from each other by the confined $\beta$-sheet like backbone structure. In the investigated simulation time window (12–30 μs), no global backbone rearrangements of S-peptide were observed and lifetimes of quenching states of the fluorescence labels were found in the range of hundreds of nanoseconds (see Fig 6). Omitting the initial 12 μs as equilibration also led to a significantly better agreement between the single exponential fit model and the simulation data especially for long relaxation times $\tau_r$. Similar to PET-FCS data treatment, we also calculated the on- and off-rates by Eqs (4) and (5) from the correlation amplitude and

**Table 1. Relaxation time scales ($\tau_r$) and amplitudes ($a_r$) of the fluorescence autocorrelation fitted with a single exponential two-state model for the experimental PET-FCS measurement and MD simulations over the total simulation (MD all) and discounting the initital 12 μs.** For the PET-FCS result, the sum of kinetic amplitudes and the average relaxation time of the two dynamic components are shown. Additionally, relaxation times and amplitudes have been converted to microscopic on- and off-rates of the related quenching process using the Formulas (4) and (5). The rates correspond well with the average opening and closing frequency of quenching contact formation between dye and quencher in labeled S-peptide observed in the MD simulation.

| | $a_r$ | $\tau_r$ [ns] | $k_{on}$ [$\mu s^{-1}$] | $k_{off}$ [$\mu s^{-1}$] |
|---|---|---|---|---|
| PET-FCS | 0.67 | 80.4 | 7.4 | 5.0 |
| MD >12 $\mu s$ | 0.65 | 72.1 | 8.4 | 5.5 |
| MD all | 0.71 | 391.3 | 1.5 | 1.1 |

https://doi.org/10.1371/journal.pone.0177139.t001

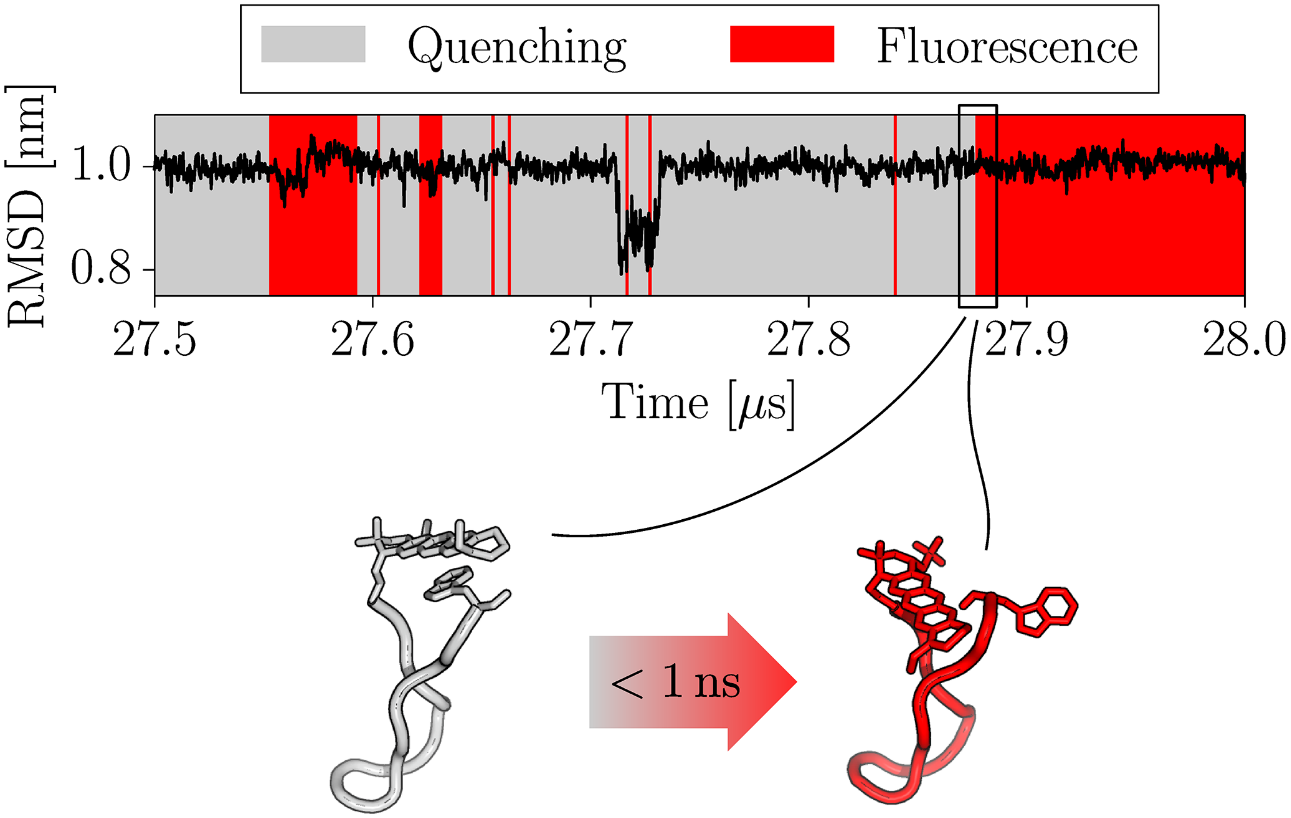

**Fig 6. Time evolution of non-hydrogen atoms RMSD of residues 1-14 with respect to the unfolded starting structure and classification into quenched and fluorescent states in the time frame between 27.5–28.0 μs.** Although the backbone was mostly locked in cluster #1 conformation during this time span, spontaneous unstacking of Atto655/Trp15 was observed. Two exemplary structures shortly before and after an unstacking event are shown below. The stacked (grey) configuration quenches the Atto655 fluorescence, while the unstacked (red) configuration allows fluorescence. Unstacking was observed to occur on the subnanosecond timescale and is not coupled to a noticable change of the overall RMSD in this cluster.

https://doi.org/10.1371/journal.pone.0177139.g006

relaxation time. Comparative data between experiment and simulation for fitted relaxation parameters and rates are shown in Table 1. We find that the quenching dynamics for simulation data after 12 μs are in good agreement with the experimental results of 80 ns.

## Discussion

The interpretation of fluorescence spectroscopy measurements depends on the assumption that the artificial attachment of fluorophores does not alter the conformations and dynamics of the target molecule itself. To address this problem, one should whenever possible ensure the functionality of the labeled molecule e.g. by biochemical assays probing specific interactions or ATP turnover rates whenever possible. If such a test is not available, MD can provide important insight with respect to the influence of the fluorescence labels. We performed comparative MD simulations and PET-FCS measurements on fluorescently labeled 14 residue S-peptide, serving as a model system of an intrinsically disordered peptide. Our results reveal that the labeling strongly affects both the conformational and dynamical properties of the S-peptide, shifting it from the disordered conformational regime to a semi-stable fold with $\beta$-sheet content. This drastic change is caused mainly by the strong $\pi$-stacking interaction between the rigid ring systems of Atto655 and Trp15, which traps the termini of the peptide to remain in close vicinity. This effect may occur with many widely used fluorophores containing rigid ring systems as their light absorbing centers that facilitate stacking interactions with other aromatic ring structures.

The agreement between quenching correlation functions from MD simulations and PET-FCS measurement is surprisingly good, although only when skipping the initial 12 μs of the MD trajectory as equilibration time (Table 1). As the labeled S-peptide was started from an arbitrary extended starting structure, we assumed that the system requires some time to reach equilibrium and treated the initial 12 μs as equilibration time, thereby dividing the dynamic S-peptide regime in two characteristic regimes. The first part of the simulation was dominated by global backbone rearrangements and slow quenching dynamics as the peptide backbone continuously stretched and refolded. During the second part of the simulation, the S-peptide backbone locked into a meta-stable fold with only the label side chains stacking and unstacking from time to time. Simulation time, however, is finite, therefore it remains unclear to what degrees these two regimes contribute to the equilibrium regime. As we reproduce good agreement between simulation and experiment for the second regime with faster quenching dynamics, we assume that S-peptide preferably resides in this regime. However, the fit quality of experimental PET-FCS data can be improved by adding an additional dynamic term with a slower relaxation coefficient (Fig B in S1 File). We speculate, that this second dynamic term might correspond to the regime of global rearrangements seen in the initial part of MD simulations. It is interesting to note, that the PET-FCS method does not necessarily detect global structural dynamics. As long as the global dynamics are not strongly coupled to the local dynamics of dye and quencher, they might remain undetected in the experiment. Surprisingly, such a scenario is possible even for short sequences as of the S-peptide. Our simulations reveal, that stacking/unstacking dynamics occuring simultaneously with a stable backbone configuration in one regime are difficult to distinguish with solely experimental data from another regime with large conformational backbone rearrangements (Fig 6).

The good agreement between experiment and simulation is even more surprising as the quenching state is judged only by a simple distance criterion, which was proposed earlier by Vaiana et. al [41] and was based on a fit of fluorophore MD trajectories to correlation spectroscopy data. Previous studies successfully demonstrated that the connection between atomistic MD simulations and experimental PET-FCS measurements can be drawn with such a simple criterion [42]. It should be noted that effects evolving from the photoinduced charge separation among Atto655 and Trp15 are not included in the approach as the MD parameters represent only the neutral state. We speculate that the opposite charges could increase the interaction between the dyes due to the coulomb attraction, a question that could in principle be targeted by measurements at different salt concentrations. Gaining a more detailed understanding of the relation between dye/quencher orientation and fluorescence quenching would require to derive redox potentials for single MD frames via quantum chemical calculations. Here, we use the experimental PET-FCS measurements for the validation of our labeled S-peptide simulations, whereas only the comparison between simulations with and without labels reveal the stark influence of fluorescence labeling on the dynamics and sampled conformational regimes of the peptide. The circular dichroism measurements of labeled and unlabeled S-peptide strongly support these findings.

When using fluorescence to study biomolecules, two major types of artifacts need to be considered. On the one hand, the properties of the fluorophore may be altered by the local environment of the biomolecule, changing the quantum yield, leading to spectral shifts of emission or absorption spectra or hindering the rotational motion through sterical hindrance or specific interactions. Our study, on the other hand, sheds light on the effect of the chemical modification on the target biomolecule and shows that the fluorescence label can significantly affect the conformational and dynamical properties. In particular, PET-FCS experiments, which intrinsically require that the fluorophore and quencher can come into close contact, suffer from possible interactions between them. The influence of specific dye-quencher or dye-dye interactions on the conformational dynamics is especially pronounced when investigating intrinsically disordered systems as presented here, for which PET and FRET are often the method of choice. Although the effect of fluorescence labeling on the dynamics and conformations of the peptide in this study was found to be significant, other systems might be affected to different degrees. Combined MD and FRET studies of labeled polyproline for example, found only little impact of the fluorophores on the sampled conformational regimes. However, polyproline is characteristic for its rigid structure with deep energy minima and slow trans/cis isomerisation dynamics on timescales beyond minutes, which were not covered directly by that study [27]. Nevertheless, it is very likely that especially small peptides with a large degree of intrinsic disorder and a relatively flat energy landscape suffer most from fluorescence labeling artifacts. For larger and more stable proteins with clear conformational preferences, on the other hand, we expect the artifacts induced by the fluorophores to be of reduced importance.

In summary, great care needs to be taken when designing and interpreting fluorescence experiments. Especially when fluorescence labeling is used to study systems for which the size of the dye is comparable to the target molecule, a single dye interaction can dominate the conformational properties and severely effect the results. The position for the fluorescent label should be chosen in a well-structured and solvent-exposed part of the protein sequence to minimize the influence of the fluorophore on the local structure and dynamics, especially when partly disordered proteins are studied. We demonstrate that MD is a valuable tool that complements PET-FCS experiments by offering an atomistic interpretation of the experimental result. Furthermore, simulations provide a useful strategy to predict the influence of labeling configurations on systematic properties when designing fluorescence experiments. On the other hand, fluorescence experiments prove useful to validate *in silico* results by providing a reference for dynamic parameters of the system.

## Methods

### Molecular dynamics

Two simulations of the S-peptide, one with and the other without labels, were started from extended peptide conformations. The periodic box boundaries were set at a minimal distance of 1 nm to the peptide. The peptide was parametrized with the Amber99sb-ILDN forcefield [44]. Parameters for the Atto655 fluorophore were generated as follows. First two conformations of the fluorophore were geometry optimized at *ab initio* B3LYP/6-31G$^*$ level using the Gaussian09 software [45–48]. Second the partial charges were generated by fitting the electrostatic potential derived from HF/6-31G$^*$ quantum mechanical calculations with the restraint electrostatic potential protocol (RESP) [49]. Finally, atom types and bonded/nonbonded parameters were assigned from the general amber forcefield (GAFF) [50]. The parametrization protocol followed the guidelines of GAFF which was designed to be compatible with the Amber forcefields. Both systems were energy minimized and equilibrated in NPT ensemble (298 K, 1.01 bar) after the addition of explicit solvent Tip3P water molecules [51]. Respectively four positive and negative counter ions were added to the solution keeping the box charge neutral. The production run was performed at a time step of 3 fs with the GROMACS 5.0 MD software suite [52, 53] using the velocity rescaling thermostat in the NVT ensemble (298 K) [54]. Bonds involving hydrogens were constrained with the LINCS algorithm [55].

## Peptide synthesis

The 14 amino acid truncated S-peptide (KETAA AKFER QHMD) was used as a model system for an intrinsically disordered peptide [28–31]. To fluorescently label the S-peptide for PET-FCS measurements, the fluorophore Atto655 was attached to the N terminus and an additional tryptophan was added to the C terminus serving as a fluorescence quencher [3]. The resulting sequence of the labeled S-peptide was Atto655 KETAA AKFER QHMDW. Peptide synthesis, labeling and purification was performed as described previously [56].

## PET-FCS measurements

PET-FCS measurements were performed on a custom-built confocal single-molecule fluorescence microscope. The sample was excited with a diode laser (LDH-D-C-640, PicoQuant) operated in continuous wave mode at an average laser power of 280 μW as measured before the aperture of the objective. The fluorescence signal was passed through a pinhole and split on two avalanche photodiodes (SPCM-AQR-14, Perkin Elmer Optoelectronics) by a 50:50 beam splitter to avoid detector dead time, connected to two independent channels of the time-correlated single photon counting (TCSPC) hardware (HydraHarp400, PicoQuant). Fluorescence signal was passed through an emission filter (ET670/30, AHF Analysentechnik). The range of the emission filter was chosen as to avoid detector crosstalk due to the breakdown flash of the APDs [57]. Individual photon arrival times were recorded with 16 ps resolution. S-peptide was dissolved in standard PBS buffer with 0.005% Tween-20 to prevent sticking to the cover slide surface, and diluted to a final concentration of $\sim 1$ nM. FCS data was collected over a time of 16 h at room temperature.

## Quenching autocorrelation

Configurations of Atto655/Trp15 from simulation were classified as "dark" state when the distance between the geometric centers of their ring compounds was below the quenching distance of $r^* < 0.55$ nm, or as fully fluorescent otherwise [41–43]. To calculate the quenching autocorrelation function, $10^6$ frames from the 30 μs MD trajectory were analyzed. The quenching signal autocorrelation data was fitted with a two-state model with a single exponential signal decay

$$G_{\mathrm{dyn}}(\tau) = a_r e^{-\tau/\tau_r} \tag{1}$$

where $a_r$ is the amplitude and $\tau_r$ the relaxation time constant of the quenching relaxation autocorrelation.

## FCS data analysis

The second order intensity cross-correlation function $G_{ij}(\tau)$ between two channels $i$ and $j$ is defined by:

$$G_{ij}(\tau) = \frac{\langle I_i(t) I_j(t+\tau)\rangle}{\langle I_i(t)\rangle\langle I_j(t)\rangle} \tag{2}$$

where $I_i(t)$ is the intensity in channel $i$ at time $t$, $\tau$ is the time lag and $\langle\rangle$ denotes time averaging. Cross-correlation functions between the two detectors were computed using custom-written software based on a multiple-tau correlation algorithm [58]. Error bars are determined by splitting the measurement into ten segments of equal length and computing the standard error of mean of the correlation functions. Fitting of the correlation function was performed in MATLAB (The Mathworks, Inc.) using the non-linear least squares fit routine by minimizing the weighted residuals. Confidence intervals (95%) of determined parameters are computed from the covariance matrix obtained from the fit procedure. FCS curves are fit using a model accounting for photon antibunching, triplet kinetics and diffusion, as well as one or two additional bunching terms for the observed kinetics:

$$\begin{aligned} G(\tau) \;=\; & \frac{\gamma}{N}\left(1+\frac{\tau}{\tau_D}\right)^{-1}\left(1+\frac{\tau}{p^2\tau_D}\right)^{-1/2}\times \\ & \left(1-A_{ab}e^{-\tau/\tau_{ab}}\right)\left(1+\frac{T}{1-T}e^{\frac{\tau}{\tau_T}}\right)\times \\ & \left(1+a_{r,1}e^{-\tau/\tau_{r,1}}+a_{r,2}e^{-\tau/\tau_{r,2}}\right) \end{aligned} \tag{3}$$

where $a_{r,1/2}$ are the amplitudes and $\tau_{r,1/2}$ the relaxation time constants of the quenching relaxation autocorrelation [20], $\tau_D$ is the diffusion time constant, $N$ is the average number of particles in the focus, $\gamma = 2^{-3/2}$ is a correction factor accounting for the shape of the confocal volume, $p$ is the ratio of axial to lateral size of the confocal volume, $\tau_T$ is the triplet time constant, $T$ is the triplet fraction, and $\tau_{ab}$ and $A_{ab}$ are the photon antibunching amplitude and relaxation time. The parameters of the dynamic quenching term are related to the off- and on-rates of the quenching process by [59]:

$$\tau_r = \frac{1}{k_{\text{on}}+k_{\text{off}}} \tag{4}$$

$$a_r = \frac{k_{\text{off}}}{k_{\text{on}}} \tag{5}$$

In terms of the system at hand, $k_{\text{on}}$ and $k_{\text{off}}$ can be interpreted as the microscopic rate constants of end-to-end contact formation and dissociation.

## Circular dichroism

CD measurements were performed on a Jasco J-715 spectrophotometer at 25°C. Labeled S-peptide with and without Trp15 was solvated at 1 mg ml$^{-1}$ concentration in DPBS buffer (Sigma-Aldrich). The samples were measured in a quartz cell with 0.2 mm path length. Data is expressed in terms of mean residue molecular elliptisity $[\theta]_\lambda$. CD data was smoothed using a Savitzky-Golay-Filter with order 3 and a window of 10 nm [60].

## Supporting information

**S1 File. The supporting information gives details on the PET-FVS dynamics, control experiments and results on the PET-FCS measurements. Fig A, PET-FCS dynamics.** Fit of the experimental correlation function using a model accounting for one kinetic component and two kinetic components. **Fig B, Control experiments. Table A, Fit results for PET-FCS measurement.**
(PDF)

## Acknowledgments

We gratefully thank Christina Stutzer for her kind introduction into circular dichroism spectrometry and the Micro-Chemistry Core Facility of the Max Planck Institute of Biochemistry (Martinsried, Germany) for peptide synthesis. We gratefully acknowledge the support from the Ludwig-Maximilians-Universität through the Center for NanoScience and the BioImaging Network.

## Author Contributions

**Conceptualization:** MPL AB DCL MZ.

**Data curation:** MPL AB AHC RB.

**Formal analysis:** MPL AB AHC.

**Funding acquisition:** DCL MZ.

**Investigation:** MPL AB AHC RB.

**Methodology:** MPL AB DCL MZ.

**Project administration:** DCL MZ.

**Resources:** DCL MZ.

**Software:** MPL MZ.

**Supervision:** DCL MZ.

**Validation:** MPL AB RB DCL MZ.

**Visualization:** MPL AB.

**Writing – original draft:** MPL AB DCL MZ.

**Writing – review & editing:** DCL MZ.

## References

1. Kiefhaber T, Bachmann A, Jensen KS. Dynamics and mechanisms of coupled protein folding and binding reactions. Current Opinion in Structural Biology. 2012; 22(1):21–29. https://doi.org/10.1016/j.sbi.2011.09.010 PMID: 22129832
2. Neuweiler H, Sauer M. Using photoinduced charge transfer reactions to study conformational dynamics of biopolymers at the single-molecule level. Current pharmaceutical biotechnology. 2004; 5(3):285–298. https://doi.org/10.2174/1389201043376896 PMID: 15180550
3. Doose S, Neuweiler H, Sauer M. Fluorescence Quenching by Photoinduced Electron Transfer: A Reporter for Conformational Dynamics of Macromolecules. ChemPhysChem. 2009; 10(9-10):1389–1398. https://doi.org/10.1002/cphc.200900238 PMID: 19475638
4. Jares-Erijman EA, Jovin TM. FRET imaging. Nature biotechnology. 2003; 21(11):1387–1395. https://doi.org/10.1038/nbt896 PMID: 14595367
5. Weiss S. Fluorescence spectroscopy of single biomolecules. Science. 1999; 283(5408):1676–1683. https://doi.org/10.1126/science.283.5408.1676 PMID: 10073925
6. Ha T. Single-Molecule Fluorescence Resonance Energy Transfer. Methods. 2001; 25(1):78–86. https://doi.org/10.1006/meth.2001.1217 PMID: 11558999
7. Förster T. Zwischenmolekulare Energiewanderung und Fluoreszenz. Annalen der physik. 1948; 437(1-2):55–75. https://doi.org/10.1002/andp.19484370105
8. Kavarnos GJ. Fundamentals of photoinduced electron transfer. vol. 98. Wiley-VCH; 1994.
9. Kavarnos GJ, Turro NJ. Photosensitization by reversible electron transfer: theories, experimental evidence, and examples. Chemical Reviews. 1986; 86(2):401–449. https://doi.org/10.1021/cr00072a005
10. Weller A. Photoinduced electron transfer in solution: exciplex and radical ion pair formation free enthalpies and their solvent dependence. Zeitschrift für Physikalische Chemie. 1982;.
11. de Silva AP, Gunaratne HQN, Gunnlaugsson T, Huxley AJM, McCoy CP, Rademacher JT, et al. Signaling Recognition Events with Fluorescent Sensors and Switches. Chemical Reviews. 1997; 97(5):1515–1566. https://doi.org/10.1021/cr960386p PMID: 11851458

**12.** Zhong D, Pal SK, Wan C, Zewail AH. Femtosecond dynamics of a drug–protein complex: daunomycin with Apo riboflavin-binding protein. Proceedings of the National Academy of Sciences. 2001; 98 (21):11873–11878. https://doi.org/10.1073/pnas.211440298

**13.** Li X, Zhu R, Yu A, Zhao XS. Ultrafast photoinduced electron transfer between tetramethylrhodamine and guanosine in aqueous solution. The Journal of Physical Chemistry B. 2011; 115(19):6265–6271. https://doi.org/10.1021/jp200455b PMID: 21491918

**14.** Michalet X, Kapanidis AN, Laurence T, Pinaud F, Doose S, Pflughoefft M, et al. The power and prospects of fluorescence microscopies and spectroscopies. Annual review of biophysics and biomolecular structure. 2003; 32(1):161–182. https://doi.org/10.1146/annurev.biophys.32.110601.142525 PMID: 12598370

**15.** Tinnefeld P, Sauer M. Branching out of single-molecule fluorescence spectroscopy: Challenges for chemistry and influence on biology. Angewandte Chemie International Edition. 2005; 44(18):2642–2671. https://doi.org/10.1002/anie.200590060 PMID: 15849689

**16.** Elson EL, Magde D. Fluorescence correlation spectroscopy. I. Conceptual basis and theory. Biopolymers. 1974; 13(1):1–27. https://doi.org/10.1002/bip.1974.360130102

**17.** Elson EL. Fluorescence Correlation Spectroscopy: Past, Present, Future. Biophysical Journal. 2011; 101(12):2855–2870. https://doi.org/10.1016/j.bpj.2011.11.012 PMID: 22208184

**18.** Sahoo H, Schwille P. FRET and FCS—Friends or Foes? ChemPhysChem. 2011; 12(3):532–541. https://doi.org/10.1002/cphc.201000776 PMID: 21308943

**19.** Felekyan S, Kalinin S, Sanabria H, Valeri A, Seidel CAM. Filtered FCS: Species Auto- and Cross-Correlation Functions Highlight Binding and Dynamics in Biomolecules. ChemPhysChem. 2012; 13(4):1036–1053. https://doi.org/10.1002/cphc.201100897 PMID: 22407544

**20.** Sauer M, Neuweiler H. PET-FCS: probing rapid structural fluctuations of proteins and nucleic acids by single-molecule fluorescence quenching. Fluorescence Spectroscopy and Microscopy: Methods and Protocols. 2014; p. 597–615.

**21.** Zhang Y, Yuan S, Lu R, Yu A. Ultrafast fluorescence quenching dynamics of Atto655 in the presence of N-acetyltyrosine and N-acetyltryptophan in aqueous solution: proton-coupled electron . . .. The Journal of Physical Chemistry. 2013; 117(24):7308–7316. https://doi.org/10.1021/jp404466f PMID: 23721323

**22.** Milles S, Tyagi S, Banterle N, Koehler C, VanDelinder V, Plass T, et al. Click Strategies for Single-Molecule Protein Fluorescence. Journal of the American Chemical Society. 2012; 134(11):5187–5195. https://doi.org/10.1021/ja210587q PMID: 22356317

**23.** Haustein E, Schwille P. Fluorescence correlation spectroscopy: novel variations of an established technique. Annu Rev Biophys Biomol Struct. 2007; 36:151–169. https://doi.org/10.1146/annurev.biophys.36.040306.132612 PMID: 17477838

**24.** Moerner W, Fromm DP. Methods of single-molecule fluorescence spectroscopy and microscopy. Review of Scientific Instruments. 2003; 74(8):3597–3619. https://doi.org/10.1063/1.1589587

**25.** Daidone I, Neuweiler H, Doose S, Sauer M, Smith JC. Hydrogen-bond driven loop-closure kinetics in unfolded polypeptide chains. PLoS Computational Biology. 2010; 6(1):e1000645. https://doi.org/10.1371/journal.pcbi.1000645 PMID: 20098498

**26.** Schröder GF, Alexiev U, Grubmüller H. Simulation of fluorescence anisotropy experiments: probing protein dynamics. Biophysical Journal. 2005; 89(6):3757–3770. https://doi.org/10.1529/biophysj.105.069500 PMID: 16169987

**27.** Hoefling M, Lima N, Haenni D, Seidel CAM, Schuler B, Grubmüller H. Structural Heterogeneity and Quantitative FRET Efficiency Distributions of Polyprolines through a Hybrid Atomistic Simulation and Monte Carlo Approach. PLoS ONE. 2011; 6(5):e19791. https://doi.org/10.1371/journal.pone.0019791 PMID: 21629703

**28.** Finn F, Dadok J, Bothner-By A. Proton nuclear magnetic resonance studies of the association of ribonuclease S-peptide and analogs with ribonuclease S-protein. Biochemistry. 1972; 11(3):455–461. https://doi.org/10.1021/bi00753a025 PMID: 5062062

**29.** Bastos M, Pease JH, Wemmer DE, Murphy KP, Connelly PR. Thermodynamics of the helix-coil transition: Binding of S15 and a hybrid sequence, disulfide stabilized peptide to the S-protein. Proteins: Structure, Function, and Bioinformatics. 2001; 42(4):523–530. https://doi.org/10.1002/1097-0134(20010301)42:4%3C523::AID-PROT100%3E3.0.CO;2-B

**30.** Cole R, Loria JP. Evidence for flexibility in the function of ribonuclease A. Biochemistry. 2002; 41 (19):6072–6081. https://doi.org/10.1021/bi025655m PMID: 11994002

**31.** Marshall GR, Feng JA, Kuster DJ. Back to the future: ribonuclease A. Peptide Science. 2008; 90 (3):259–277. https://doi.org/10.1002/bip.20845 PMID: 17868092

32. Bachmann A, Wildemann D, Praetorius F, Fischer G, Kiefhaber T. Mapping backbone and side-chain interactions in the transition state of a coupled protein folding and binding reaction. Proceedings of the National Academy of Sciences. 2011; 108(10):3952–3957. https://doi.org/10.1073/pnas.1012668108
33. Richards FM. ON THE ENZYMIC ACTIVITY OF SUBTILISIN-MODIFIED RIBONUCLEASE. Proceedings of the National Academy of Sciences of the United States of America. 1958; 44:162–166. https://doi.org/10.1073/pnas.44.2.162 PMID: 16590160
34. Richards FM, Vithayathil PJ. The Preparation of Subtilisin-modified Ribonuclease and the Separation of the Peptide and Protein Components. Journal of Biological Chemistry. 1959; 234:1459–1465. PMID: 13654398
35. Murtagh F, Contreras P. Algorithms for hierarchical clustering: an overview. Wiley Interdisciplinary Reviews: Data Mining and Knowledge Discovery. 2012; 2(1):86–97.
36. Simons ER, Blout ER. Circular Dichroism of Ribonuclease A, Ribonuclease S, and Some Fragments. The Journal of biological chemistry. 1968; 243(1):218–221. PMID: 5635944
37. Tamburro A, Scatturin A, Rocchi R, Marchiori F, Borin G, Scoffone E. Conformational-transitions of bovine pancreatic ribonuclease S-peptide. FEBS letters. 1968; 1(5):298–300. https://doi.org/10.1016/0014-5793(68)80137-1 PMID: 11945325
38. Mets Ü, Widengren J, Rigler R. Application of the antibunching in dye fluorescence: measuringthe excitation rates in solution. Chemical Physics. 1997;.
39. Nettels D, Gopich IV, Hoffmann A, Schuler B. Ultrafast dynamics of protein collapse from single-molecule photon statistics. Proceedings of the National Academy of Sciences of the United States of America. 2007; 104(8):2655–2660. https://doi.org/10.1073/pnas.0611093104 PMID: 17301233
40. Weiss S. Measuring conformational dynamics of biomolecules by single molecule fluorescence spectroscopy. Nature Structural Biology. 2000;.
41. Vaiana AC, Neuweiler H, Schulz A, Wolfrum J, Sauer M, Smith JC. Fluorescence quenching of dyes by tryptophan: interactions at atomic detail from combination of experiment and computer simulation. Journal of the American Chemical Society. 2003; 125(47):14564–14572. https://doi.org/10.1021/ja036082j PMID: 14624606
42. Noé F, Doose S, Daidone I, Löllmann M, Sauer M, Chodera JD, et al. Dynamical fingerprints for probing individual relaxation processes in biomolecular dynamics with simulations and kinetic experiments. Proceedings of the National Academy of Sciences. 2011; 108(12):4822–4827. https://doi.org/10.1073/pnas.1004646108
43. Kalinin S, Peulen T, Sindbert S, Rothwell PJ, Berger S, Restle T, et al. A toolkit and benchmark study for FRET-restrained high-precision structural modeling. Nature Methods. 2012; 9(12):1218–1225. https://doi.org/10.1038/nmeth.2222 PMID: 23142871
44. Lindorff-Larsen K, Piana S, Palmo K, Maragakis P, Klepeis JL, Dror RO, et al. Improved side-chain torsion potentials for the Amber ff99SB protein force field. Proteins. 2010; 78(8):1950–1958. https://doi.org/10.1002/prot.22711 PMID: 20408171
45. Frisch MJ, Trucks GW, Schlegel HB, Scuseria GE, Robb MA, Cheeseman JR, et al.. Gaussian 09 Revision D.01;.
46. Becke AD. Density-functional exchange-energy approximation with correct asymptotic behavior. Phys Rev A. 1988; 38:3098–3100. https://doi.org/10.1103/PhysRevA.38.3098
47. Lee C, Yang W, Parr RG. Development of the Colle-Salvetti correlation-energy formula into a functional of the electron density. Phys Rev B. 1988; 37:785–789. https://doi.org/10.1103/PhysRevB.37.785
48. Hariharan PC, Pople JA. The influence of polarization functions on molecular orbital hydrogenation energies. Theor Chim Acta. 1973; 28(3):213–222. https://doi.org/10.1007/BF00533485
49. Bayly CI, Cieplak P, Cornell WD, Kollman PA. A Well-Behaved Electrostatic Potential Based Method Using Charge Restraints for Deriving Atomic Charges: The RESP Model. J Phys Chem. 1993; 97(40):10269–10280. https://doi.org/10.1021/j100142a004
50. Wang J, Wolf RM, Caldwell JW, Kollman PA, Case DA. Development and testing of a general amber force field. J Comput Chem. 2004; 25(9):1157–1174. https://doi.org/10.1002/jcc.20035 PMID: 15116359
51. Jorgensen WL, Chandrasekhar J, Madura JD, Impey RW, Klein ML. Comparison of simple potential functions for simulating liquid water. J Chem Phys. 1983; 79(2):926–935. https://doi.org/10.1063/1.445869
52. Hess B, Kutzner C, Spoel DVD, Lindahl E. GROMACS 4: Algorithms for highly efficient, load-balanced, and scalable molecular simulation. J Chem Theory Comput. 2008; 4:435–447. https://doi.org/10.1021/ct700301q PMID: 26620784

**53.** Van Der Spoel D, Lindahl E, Hess B, Groenhof G, Mark AE, Berendsen HJC. GROMACS: Fast, flexible, and free. J Comput Chem. 2005; 26(16):1701–1718. https://doi.org/10.1002/jcc.20291 PMID: 16211538

**54.** Bussi G, Donadio D, Parrinello M. Canonical sampling through velocity rescaling. The Journal of chemical physics. 2007; 126(1):014101. https://doi.org/10.1063/1.2408420 PMID: 17212484

**55.** Hess B, Bekker H, Berendsen HJC, Fraaije JGEM. LINCS: A linear constraint solver for molecular simulations. Journal of Computational Chemistry. 1997; 18(12):1463–1472. https://doi.org/10.1002/(SICI)1096-987X(199709)18:12%3C1463::AID-JCC4%3E3.0.CO;2-H

**56.** Crevenna AH, Naredi-Rainer N, Lamb DC, Wedlich-Söldner R, Dzubiella J. Effects of Hofmeister Ions on the a-Helical Structure of Proteins. Biophysical Journal. 2012; 102(4):907–915. https://doi.org/10.1016/j.bpj.2012.01.035 PMID: 22385862

**57.** Kurtsiefer C, Zarda P, Mayer S, Weinfurter H. The breakdown flash of Silicon Avalance Photodiodes—backdoor for eavesdropper attacks? arXivorg. 2001;(13):2039–2047.

**58.** Felekyan S, Kühnemuth R, Kudryavtsev V, Sandhagen C, Becker W, Seidel CAM. Full correlation from picoseconds to seconds by time-resolved and time-correlated single photon detection. Review of Scientific Instruments. 2005; 76(8):083104. https://doi.org/10.1063/1.1946088

**59.** Neuweiler H, Johnson CM, Fersht AR. Direct observation of ultrafast folding and denatured state dynamics in single protein molecules. Proceedings of the National Academy of Sciences. 2009; 106 (44):18569–18574. https://doi.org/10.1073/pnas.0910860106

**60.** Greenfield NJ. Using circular dichroism spectra to estimate protein secondary structure. Nature Protocols. 2006; 1(6):2876–2890. https://doi.org/10.1038/nprot.2006.202 PMID: 17406547

## B.5 Paper 5: PAM: A Framework for Integrated Analysis of Imaging, Single-Molecule, and Ensemble Fluorescence Data

Biophysical *Journal*
Computational Tool

# PAM: A Framework for Integrated Analysis of Imaging, Single-Molecule, and Ensemble Fluorescence Data

Waldemar Schrimpf,[1] Anders Barth,[1] Jelle Hendrix,[2,3] and Don C. Lamb[1,*]
[1]Department of Physical Chemistry, Center for Integrated Protein Science Munich (CIPSM), Nanosystems Initiative Munich (NIM) and Center for Nanoscience (CeNS), Ludwig-Maximilians-Universität, Munich, Germany; [2]Dynamic Bioimaging Lab, Biomedical Research Institute (BIOMED), Advanced Optical Microscopy Centre, Faculty of Medicine and Life Sciences, Hasselt University, Diepenbeek, Belgium; and [3]Laboratory for Photochemistry and Spectroscopy, Molecular Imaging and Photonics Division, KU Leuven, Heverlee, Belgium

ABSTRACT Fluorescence microscopy and spectroscopy data hold a wealth of information on the investigated molecules, structures, or organisms. Nowadays, the same fluorescence data set can be analyzed in many ways to extract different properties of the measured sample. Yet, doing so remains slow and cumbersome, often requiring incompatible software packages. Here, we present PAM (pulsed interleaved excitation analysis with MATLAB), an open-source software package written in MATLAB that offers a simple and efficient workflow through its graphical user interface. PAM is a framework for integrated and robust analysis of fluorescence ensemble, single-molecule, and imaging data. Although it was originally developed for the analysis of pulsed interleaved excitation experiments, PAM has since been extended to support most types of data collection modalities. It combines a multitude of powerful analysis algorithms, ranging from time- and space-correlation analysis, over single-molecule burst analysis, to lifetime imaging microscopy, while offering intrinsic support for multicolor experiments. We illustrate the key concepts and workflow of the software by discussing data handling and sorting and provide step-by-step descriptions for the individual usage cases.

## INTRODUCTION

Fluorescence microscopy and spectroscopy have become important tools in the life and material sciences over the past decades. Research institutes nowadays often house high-end fluorescence microscopes for recording fluorescence time traces and multicolor images or time-lapse videos. The recorded data convey a wealth of information that is encoded in the multidimensional parameter space of the fluorescence signal (1), and many advanced analysis methods have been developed over the past decades. Among the properties of the fluorescence signal are fundamental parameters, such as time, space, fluorescence lifetime, polarization, and spectrum, as well as derived parameters, including molecular brightness, labeling stoichiometry, and distances between fluorescent labels (2). Further information on diffusion, flow, and molecular interactions is encoded in the seemingly random fluctuations of the fluorescence signal, which can be extracted using the many variants of fluorescence fluctuation spectroscopy (3,4). Because each individual method only analyzes a fraction of the information contained in the data, a global understanding of the system is only possible by performing a combined analysis.

An illustration of how a combined analysis can lead to synergetic insights is single-molecule Förster resonance energy transfer (FRET) by burst extraction (2,5,6). With this method, intra- and intermolecular distances can be accurately measured on the nanometer scale based on the signal intensities in the FRET donor and acceptor detection channels. Additional parameters such as the fluorescence lifetime, anisotropy, or labeling stoichiometry are typically used to gain valuable information about properties and dynamics of the studied sample. Photon distribution analysis (PDA) enables a quantitative analysis of conformational heterogeneity and conformer interconversion kinetics (7,8). This information can be supplemented by subensemble fluorescence correlation spectroscopy (FCS), which provides additional information on biomolecular

---

*Submitted November 6, 2017, and accepted for publication February 12, 2018.*

*Correspondence: d.lamb@lmu.de

Waldemar Schrimpf and Anders Barth contributed equally to this work.

Editor: Jochen Mueller.

https://doi.org/10.1016/j.bpj.2018.02.035

hydrodynamic properties (9). Conformational changes can also be evaluated using filtered-FCS (10), making it possible to investigate dynamics between the different species on the nanosecond to the millisecond timescale.

Another good illustration of an integrated quantitative sample analysis comes from confocal imaging. Instead of only addressing the average signal, fluorescence fluctuations in the recorded images can be analyzed to investigate protein mobility and interactions (11–18). Correlating the signal through space and time (or both) can extract valuable information about the spatial distribution or the diffusion of the fluorescent molecules. By analyzing the image cross correlation function, one can study molecular interactions more accurately than with intensity-based colocalization analysis. Finally, fluorescence lifetime imaging allows one to study both the local environment and the molecular interactions in cells, and, by combining this information with fluctuation analysis, even the dynamics of subspecies in complex mixtures can be investigated (16).

As it has become customary to openly provide the respective software with publications, a multitude of software for analyzing advanced fluorescence data are available. However, these programs are often too specific, complex, or inflexible to provide the user with a clear approach to a global data analysis. Software attached to the publication of new methods is generally designed specifically for that single application and often also requires a particular file format to work. This makes it highly impractical and cumbersome to employ multiple methods, as they necessitate the use of different software and reformatting of the data. Although script-based implementation of such applications allows for easier adjustment to new projects or hardware, it also makes them difficult to apply for the novice user without programming experience. Conversely, implementations of advanced analysis methods by microscope manufacturers are expensive, usually only offer a basic framework excluding customization options, and are incompatible with data generated by other microscopy hardware. Lastly, commercial software is hardly ever designed by the end users, who logically have a better understanding of what is needed for a proper analysis of the data. Open-source development, on the other hand, offers the possibility for both experts and end users to improve and extend existing software packages by implementing their newest methods. As such, it provides a platform for the continuous development and extension of the software, enabling researchers to join efforts on new developments. In recent years, a number of software packages in the field of single-molecule fluorescence have been made openly available (19–22). For an optimal workflow incorporating multiple analysis techniques, one requires a fast and easy-to-use software framework that implements the various methods but is also designed to provide an efficient communication between the different modules.

Here, we present PAM (pulsed interleaved excitation (PIE) analysis with MATLAB (The MathWorks, Natwick, MA)), an open-source software package that combines leading quantitative fluorescence microscopy and spectroscopy analysis methods and offers an integrated and extendible support for multiparameter and multicolor experiments. The three main applications of PAM are 1) ensemble spectroscopy, including correlation spectroscopy, and fluorescence lifetime and anisotropy analysis; 2) single-molecule analysis; and 3) image analysis (Fig. 1). To the best of our knowledge, PAM is the only program that implements all three of these fields in a single software package. PAM implements state-of-the-art signal processing algorithms commonly used for quantitative analysis of fluorescence experiments, i.e., fluctuation spectroscopy (FCS, fluorescence cross correlation spectroscopy, fluorescence lifetime correlation spectroscopy, nanosecond FCS, filtered-FCS, and pair-correlation) (23–25), burst-wise single-molecule analysis (including Förster resonance energy transfer and PDA) (5,7,26), fluorescence lifetime imaging microscopy (FLIM) via the phasor approach (27), and fluctuation imaging (image correlation spectroscopy (ICS), raster ICS (RICS), cross correlation RICS, number and brightness analysis, temporal ICS (TICS), arbitrary region RICS, image mean-square displacement (iMSD), and spatiotemporal ICS (STICS)) (15,16,28).

## RESULTS AND DISCUSSION

### Motivation and key concepts

The motivation for designing and publishing PAM is to provide 1) an easy-to-use software package with 2) a high degree of automation that is 3) compatible with a variety of measurement schemes and setups. This program allows the user to perform 4) a variety of different quantitative fluorescence analysis techniques on the same data set, including 5) several unique and cutting-edge methods and variants. At the same time, the program should be 6) versatile and adaptable by the expert user. A brief description of implementation of these points is given in the following paragraphs.

#### *Ease-of-use*

To be adopted by a broad variety of users, an analysis software needs to be fast and easy to learn and have a clear workflow with feedback about the current state of the progress and the data. To achieve this simplicity and to streamline the workflow, PAM has a modular structure (Fig. 2). It is divided into the core PAM program used for data sorting and (pre)processing and several modules for the individual method groups. All these subprograms are based on graphical user interfaces (GUIs) that clearly show the possible actions that can be taken and display all relevant information about the data. PAM is highly configurable both for

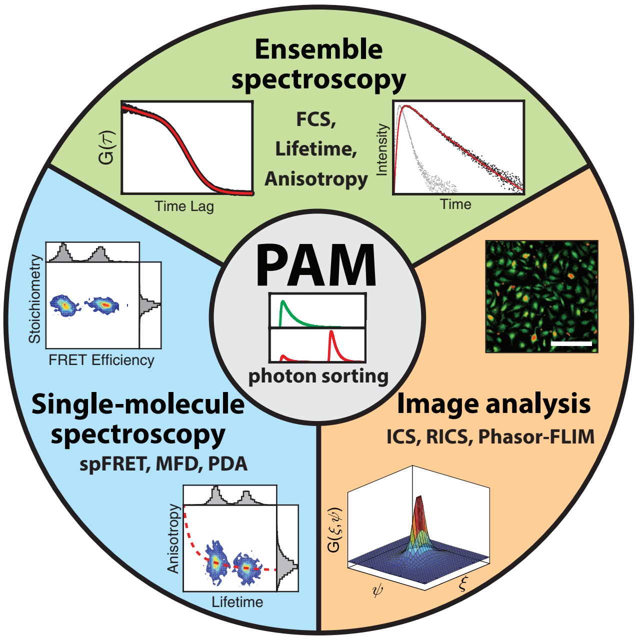

FIGURE 1 Overview of the functionalities of the PAM software package. Photon sorting is performed in the main module PAM. The main applications are divided into three areas: ensemble spectroscopy (*top*), single-molecule spectroscopy (*left*), and image-based analysis methods (*right*). Each area incorporates a number of analysis methods. FCS, fluorescence correlation spectroscopy; spFRET, single-pair Förster resonance energy transfer; MFD, multiparameter fluorescence detection; PDA, photon distribution analysis; ICS, image correlation spectroscopy; RICS, raster image correlation spectroscopy; FLIM, fluorescence lifetime imaging microscopy. To see this figure in color, go online.

defining specific workflows as well as for displaying data. All these settings are stored in custom profiles, allowing the user to quickly switch between settings for different microscopes or techniques. After each step in the analysis, the data can be saved in an intermediate file format, giving the user the possibility to reanalyze the data at a later time point without the need of reprocessing. Additionally, all important parameters and plots can be exported to external programs (e.g., Excel, Origin, ImageJ, etc.) or as ready-for-publication figures.

### Automation

Advanced fluorescence techniques often require the analysis of many large data sets. Analyzing each measurement individually results in the user spending a significant time just waiting for the computer to load or process the data. To mitigate this problem, PAM contains a batch analysis option for most computationally intensive steps that require no or low direct user interaction. Hereby, the user sets up the parameters for the analysis and PAM automatically performs the calculations (e.g., burst-extraction or correlation) sequentially for all selected datasets with the same settings. Additionally, all computationally demanding algorithms are written in C++ and can run on multiple cores to decrease calculation times and optimize performance.

### Compatibility

The methods in PAM are meant to be applicable to all fluorescence data and independent of the microscope or the file format used. For this, PAM includes read-in methods for all common time-correlated single-photon-counting (TCSPC) formats (e.g., Becker&Hickl .spc, Picoquant .ptu, etc.), which are the main data type used for many methods. However, PAM does not necessarily require TCSPC data and is compatible with simple photon counting and, to some extent, prebinned data. A detailed list is given in the Supporting Material. All imaging methods additionally support direct loading of tagged image file format (TIFF)-based data, extending the capabilities to camera-based microscopes. Although these options already cover a large fraction of file formats, they cannot possibly include all commercial and, especially, home-built microscopes and setups. For this, PAM has a dedicated option for custom read-in functions, which allows the user to dynamically add their own read-in functions without having to modify the central code.

### Integrated methods

One of the key concepts of PAM is the combination of the various methods in a single platform. This encourages the user to explore multiple aspects of the data simultaneously, which, in our experience, is an important step to fully

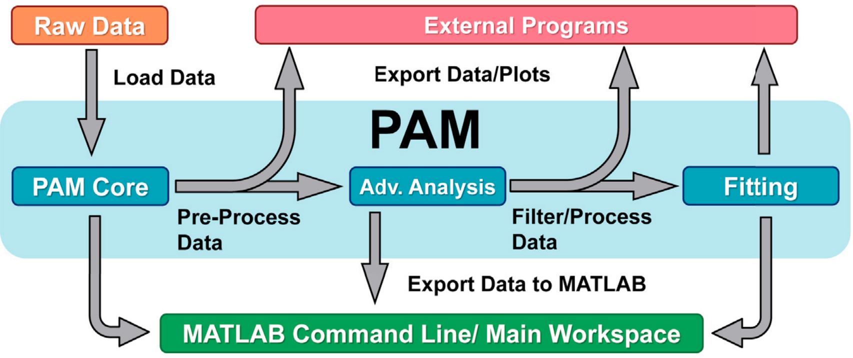

FIGURE 2 Schematic representation of the data- and workflow of PAM, showing the connection between the modules of PAM (*blue*), general file formats for use with spreadsheet programs, text editors or image processing tools (*red*), and the MATLAB command line functionalities (*green*). To see this figure in color, go online.

understanding complex biological systems. A good example for the benefits of combining different techniques is our recent study on the early steps of human immunodeficiency virus assembly (29).

### *Unique methods*

PAM is not only a collection of established techniques; it is constantly updated and expanded and contains many cutting-edge methods and variations not available in any other software. One key feature of PAM is that all its methods are fully compatible with PIE (23), the historic origin of the name PAM. Even though it has been introduced more than 10 years ago, the widespread application of PIE is still limited despite its benefits for quantitative multicolor fluorescence (cross)correlation spectroscopy. Although many researchers are in possession of PIE-capable microscopes, few are actively taking advantage of them because of the lack of readily available software implementations. As PAM has a strong focus on TCSPC data, it also includes the option to correct for count-rate-dependent shifts of the instrument response function (30). For multicolor FRET, PIE or alternating laser excitation (ALEX) (31) is essential for determining all interdye distances (32,33). The burst analysis framework in PAM offers full support for three-color FRET experiments, including specific three-color burst search methods and calculation of advanced parameters. Another unique method of PAM is the recently developed arbitrary region RICS (15). This extension to the standard image correlation techniques decreases the requirements for the image quality in terms of spatial shape and heterogeneity. By filtering the data to remove unwanted contributions, it increases the amount of usable data and allows the accurate measurement of (co)diffusion even in highly dynamic and heterogeneous systems.

### *Adaptability*

The field of fluorescence spectroscopy and microscopy is highly specialized and dynamic, and almost every new project requires a modification of the approaches and methods employed. PAM uses several different concepts to achieve a flexible workflow. One approach is that, in most cases, the fit models are based on simple text files instead of being hard-coded. This allows the user to create their own models or modify existing functions even without programming experience. The expert users, on the other hand, can make use of the open-source nature of PAM and adjust the code to their own needs. The modular structure of PAM and its use of MATLAB-based file formats help to simplify this process. The user can simply use the (intermediary) data in their own scripts or insert new functions into the dataflow between existing modules. For small modifications or experimental prototyping, they can exploit the advantages of MATLAB as an interpreted language and its powerful command-line capabilities to tweak the code on the fly. For this, PAM allows quick access to the data in the form of global variables. For larger and permanent modifications, PAM uses the Git version control system for distributed development. Active involvement and improvements by the users, e.g., by pointing out bugs, suggesting improvements, or even adding functionalities, is not only accepted but also encouraged.

Because of the large number of different methods included in PAM, we cannot describe all techniques and processes in detail. Instead, we provide a basic description of the workflow for the main functionalities in the PAM software package: data inspection, sorting and preprocessing, FCS, image fluctuation analysis, burst-wise single-molecule analysis, and fluorescence lifetime imaging using the phasor approach. A more detailed description of the individual functionalities, the algorithms involved, and the particular GUIs and controls is presented in the manual (see Availability and Supporting Material). Additionally, we provide verification of all presented functionalities using simulated data (Table S1).

## PAM core functionalities

In most cases, the analysis starts with the core module PAM. The main function of this core module is to load raw data and to sort the photon records based on the detection and the excitation channel (Fig. 3). This main program is meant to work with confocal single photon counting data, with a focus on TCSPC data. However, by using the custom read-in option, it is also possible to work with non-TCSPC or even binned data. Processed imaging data from scanning or widefield microscopes, on the other hand, do not have to go through the core module at all and can be loaded directly into the image processing subprograms.

Once the data is loaded, each photon record is first assigned to a detection module and, if applicable, a routing channel. These correspond to the physical detectors used for e.g., the different spectral ranges or polarizations. Additionally, photon records are defined by two parameters. The first is the macro-time or the arrival time of the photon relative to the start of the experiment, in multiples of the synchronization clock. The second value can be used to encode a variety of parameters, e.g., the spectral information or the ALEX channel, but is most commonly used to store the micro-time data (Fig. 3 *A*). The micro-time is the photon arrival time relative to the synchronization source, encoding, for example, the fluorescence lifetime. PAM uses this secondary parameter to sort the photons into different photon gates (Fig. 3 *B*). When PIE is used, this micro-time information allows the user to further separate the signal by the excitation source.

Based on these detector and photon gates, the program displays intensity traces, photon arrival time, histograms, histograms, photon counting histograms, and images that can be used for a first data evaluation (Fig. 3, *C* and *D*). The photon sorting is followed by one or more primary data-processing steps specific to the particular method used. At the moment

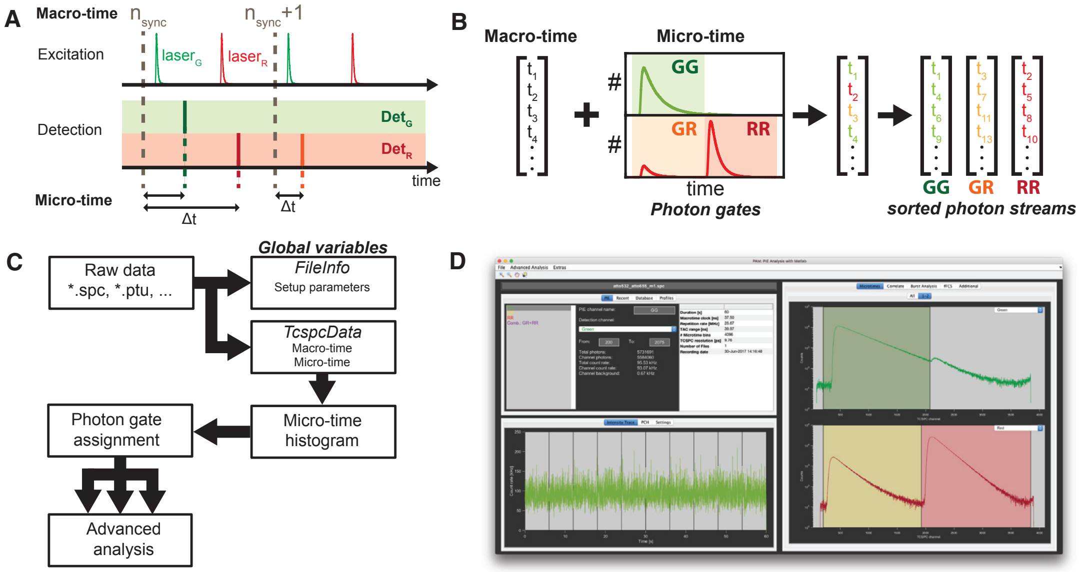

FIGURE 3 Photon-sorting in the PAM main module. (*A*) In two-color pulsed interleaved excitation (PIE), two lasers are alternated on the nanosecond timescale such that every synchronization period contains both laser pulses. The TCSPC data format records the macro-time (time passed since the start of the measurement in units of the synchronization clock), the micro-time (time between photon detection and the last synchronization signal), and the color channel in which the photon was detected in (*B*). In PIE, the micro-time information is used to sort the macro-time stamps using photon gates defined by the excitation source and the detected color channel. GG, green excitation, green detection; GR, green excitation, red detection (FRET, cross talk, cross-excitation); RR, red excitation, red detection. (*C*) The workflow in PAM for photon sorting is shown. The raw data (e.g., *.spc or *.ptu file formats) are loaded into PAM. Extracted setup parameters (e.g., synchronization clock frequency) are stored in the global variable FileInfo, and photon records (i.e., the macro-time, micro-time, and channel) are stored in TcspcData. The micro-time histograms are used to define the time ranges for the different photon gates, and photons are assigned accordingly before being processed further. (*D*) The main graphical user interface of PAM used to sort photons by photon gates is shown. Top left: a list of photon channels and controls for photon gate definition is shown. Bottom left: the count rate as a function of time for the selected channel is shown. Right: a micro-time histogram of the detectors with the defined photon gates GG (*green*), GR (*orange*), and RR (*red*, *shaded areas*) is shown. To see this figure in color, go online.

of this writing, the different processing methods are auto- and cross correlation of single-point data, pair-correlation for line or circle scans, burst identification for single-molecule analysis, fluorescence lifetime and anisotropy analysis, phasor FLIM analysis, and generation of image stacks for fluctuation imaging. These calculations are usually the most computationally intensive steps. We have estimated the computation times of the core algorithms for typical data set sizes and found that they perform on timescales faster than 30 s (Fig. S1). For a more efficient workflow, these calculations can additionally be done in a batch analysis, automatically performing the computations with the same settings on multiple similar datasets without the need for direct user interaction. The workflow for some of the most important methods will be discussed in more detail in the following sections.

## FCS

FCS is one of the most widely applied quantitative fluorescence analysis methods (34). It can be used to extract information about concentration, diffusion, interactions (23,35,36), and conformational dynamics encoded in the fluctuations of the signal (10,37). The workflow for FCS analysis in PAM is shown in Fig. 4. All calculations of correlation functions are based on the defined photon gates. This photon sorting allows e.g., the removal of spectral cross talk and cross-excitation in multicolor cross correlation spectroscopy (23) or the analysis of two-focus FCS data (38). Furthermore, photons from multiple photon gates or detector channels (e.g., from different polarizations) can be pooled to take advantage of all available photons for maximizing the signal-to-noise ratio. The correlation algorithm is based on a multiple-$\tau$ correlation scheme (25). Calculations are performed for all single channels (autocorrelation) or pairs of channels (cross correlation) that were selected by the user. For goodness-of-fit estimation, the data set is automatically divided into time segments that are correlated independently and used to determine the statistical uncertainty.

The standard algorithm only uses the macro-time information to calculate the correlation functions. However, the user can also select to include the micro-time to extend the resolution to the nano- and picosecond regime (25). For data with rapid scanning, the signal can alternatively be divided into different focus positions to perform pairwise correlations between these spatial bins (39). PAM also includes methods to perform statistical filtering during correlation analysis. Usually, the algorithm treats all selected

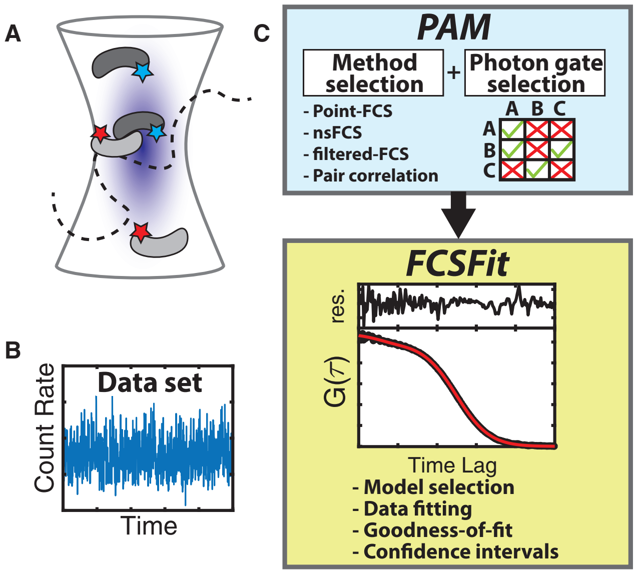

FIGURE 4 Fluorescence correlation spectroscopy (FCS) in PAM. (*A*) In FCS, the signal fluctuations arising from the diffusion of molecules in and out of the observation volume are analyzed to extract information about diffusion and interactions. (*B*) A typical signal trace of an FCS experiment is shown. (*C*) The workflow for FCS in PAM is shown. The calculation of the correlation function is performed in the FCS submodule of the PAM GUI. The user selects the correlation method and uses the correlation matrix to select which photon gates should be cross-correlated. Quantitative evaluation of the correlation functions is performed in the FCSFit module. Standard fit models are available, and user-defined model functions are easily implemented. The fit result is evaluated by means of goodness-of-fit indicators and confidence intervals for the determined parameters. To see this figure in color, go online.

photons equally, giving them a weight of one, but it is also possible to calculate filter functions based on the lifetime (fluorescence lifetime correlation spectroscopy), spectrum (fluorescence spectral correlation spectroscopy), polarization, or a combination of these parameters (10,40,41). Additional functions in PAM include an automatic removal of bright aggregates or dust, correction for detector after-pulsing, and batch analysis of multiple data sets.

Once the correlation function is calculated, the data is saved and can be analyzed with the FCSFit module, which is used to fit temporal correlation data. All fitting functions are based on text files, making it easy to modify existing model functions or to create new model functions when needed. The parameters used for fitting can be individually fixed or globally linked between all files currently loaded, and confidence intervals for the fit result can be calculated. The module includes several normalization methods to better compare different measurements and allows direct export of the plots and the fitted parameters.

## Burst-wise single-molecule analysis

Single-molecule spectroscopy in solution using burst analysis is a powerful method to obtain single-molecule information about biomolecules with high throughput and no need for surface immobilization. It relies on the free diffusion of molecules through the observation volume of a confocal microscope (Fig. 5 *A*), which, at low concentration, results in isolated bursts of fluorescence from single molecules (Fig. 5 *B*) (5,42). Depending on the excitation and detection scheme used, a number of different parameters can be calculated from the fluorescence signal (1,2).

The general outline for burst analysis in PAM is given in Fig. 5. Once the experimental setup and the different detection channels have been defined (see Fig. 3 *B*), an appropriate burst search algorithm has to be selected. PAM offers two different burst search methods using a threshold either on the count rate determined using a sliding time window (26) or on the interphoton time (43). Additionally, the burst search can be performed on all photons together (all-photon burst search) or independently on the photons after donor or acceptor excitation (dual-channel burst search) (26). The latter option allows one to exclude donor- or acceptor-only molecules directly because only events with high signal in both channels will be detected. These events may also be cleaned up after the burst search using the stoichiometry parameter. Most burst-wise parameters are automatically determined after the burst identification step, whereas additional, more computationally expensive parameters are calculated on demand. The burst-wise fluorescence lifetime is determined for both the donor and acceptor fluorophore by a maximum likelihood estimation using a single exponential model function (2,44). Additionally, the ALEX-2CDE and FRET-2CDE filters can be calculated, which rely on kernel density estimation to detect fluctuations between two channels, allowing the detection of dye blinking and bleaching events (ALEX-2CDE) or FRET fluctuations originating from conformational dynamics (FRET-2CDE) (45).

The simplest scheme for single-molecule FRET by burst analysis is obtained by using a single excitation laser for the FRET donor dye and two spectral detection channels for donor and acceptor fluorescence. The most important parameter available from the experiment is the FRET efficiency, together with general parameters such as the laboratory time of the single-molecule event, the burst duration, or the number of photons. The use of alternating acceptor excitation by means of PIE or ALEX adds the labeling stoichiometry to the parameter space (2,6). The stoichiometry allows the exclusion of molecules with only a single donor or acceptor dye as well as the investigation of the composition of higher-order complexes. Isolating single-labeled molecules also allows one to obtain the required correction factors directly from the experiment to determine quantitative FRET efficiencies and thus perform accurate distance measurements (2). By the use of pulsed lasers and TCSPC electronics, it is additionally possible to determine the burst-averaged fluorescence lifetime. This introduces an independent alternative to determining the FRET efficiency

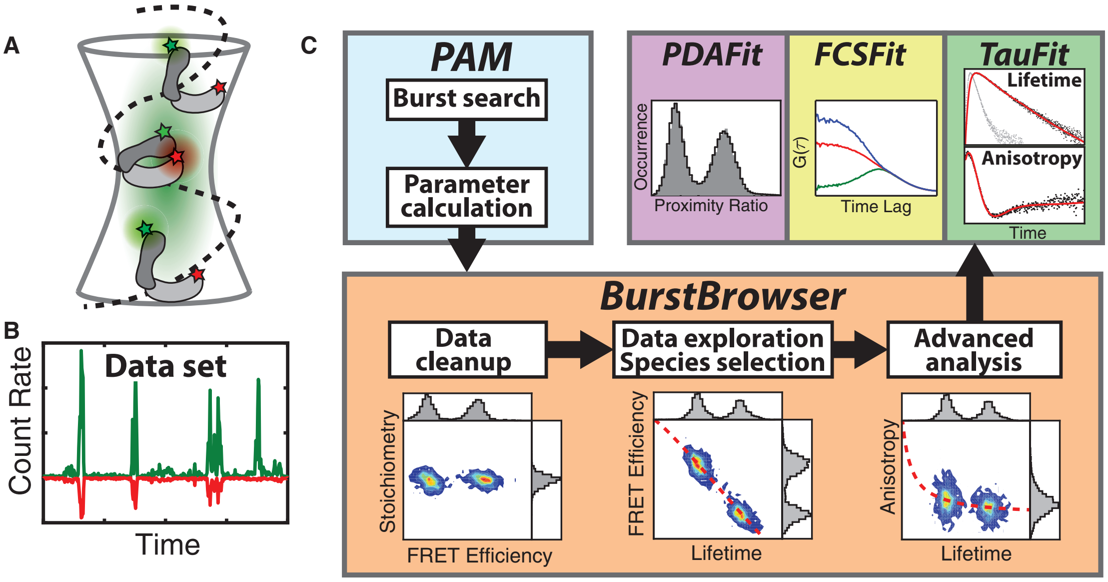

FIGURE 5 Single-molecule spectroscopy using burst analysis in PAM. (*A*) In burst analysis, molecules are labeled with a donor- and acceptor-fluorophore (*green* and *red*, respectively). Förster resonance energy transfer (FRET) reports on the distance between them to detect conformational dynamics. (*B*) At low concentrations, the data consist of bursts of fluorescence when a molecule traverses the focus. The fluorescence of the donor dye is shown in green, and the inverted acceptor signal is shown in red. (*C*) The workflow for burst analysis in PAM is shown. Burst identification and calculation of burst-wise parameters are performed using the Burst Analysis submodule in the PAM GUI. The processed data set is then explored, filtered, and analyzed in the BurstBrowser module. Finally, selected populations can be subjected to more detailed analysis in the TauFit, FCSFit, and PDAFit modules. To see this figure in color, go online.

from the quenching of the donor fluorophore and makes it possible to identify conformational dynamics on the sub-millisecond timescale (8). When polarization-sensitive detection is employed, the fluorescence anisotropy reports on the rotational properties of the fluorophore and the biomolecule, offering a readout for detecting complex formation and the possibility to detect unwanted interactions of the fluorophore with the surface of the biomolecule. Lastly, three-color FRET studies can be performed by implementation of an additional color channel and fluorescent label, which allows more complex questions to be addressed by monitoring three distances simultaneously (32,46).

The analyzed data are stored in an intermediate file format that can be loaded into the BurstBrowser module for interactive exploration of the data set. Parameter distributions can be examined using 1D or 2D histograms. For comparison between different species of a single measurement or between different datasets, multiple data selections can be defined simultaneously. Quantitative analysis of parameter distributions can be performed by fitting with bivariate normal distributions to obtain distribution means and widths. Important plots related to the fluorescence lifetime information are predefined and can be inspected at a glance, and associated theoretical curves are easily added to these plots for a more quantitative analysis. Molecule selections can further be analyzed by performing subensemble TCSPC analysis of the fluorescence and anisotropy decays, correlation analysis of diffusion and conformational dynamics (purified-FCS and filtered-FCS) (10,47), and PDA (7,8) in the modules TauFit, FCSFit, and PDAFit. PDA can be used to analyze static distance heterogeneity using Gaussian distance distributions or to infer interconversion rates in dynamic systems. Additionally, three-color FRET experiments are supported by all described methods. The display of the data can be customized to a high degree, and publication-ready plots are available at all points. Additionally, an integrated database functionality enables the convenient management and cataloging of large measurement series.

## Fluctuation imaging

Fluctuation imaging describes a group of methods that apply the concepts of fluorescence fluctuation spectroscopy to image data. These methods can be divided into different categories based on the dimensions used for the analysis. The first group uses only the temporal dimension to extract information and includes TICS (48), also called imaging FCS (49) and number and brightness analysis (17). The second category is based on correlations of the two spatial dimensions and includes ICS (50) and RICS (18,51). The last group correlates the data through both time and space. STICS (12) and iMSD (52) are examples of these 3D correlation methods. Depending on the particular method used, one can gain information about the size, oligomerization state, and (co)mobility of molecules or even whole cellular structures.

Image fluctuation analysis in PAM is performed with the Microtime Image Analysis (MIA) submodule, and the workflow is illustrated in Fig. 6. It starts with loading the data, either directly from image files, e.g., TIFFs, or from the sorted photon data of the core PAM module. MIA works with up to two channels that can be used for auto- and cross correlation. The user then selects a rectangular region of interest (ROI) that is the basis for all further calculations. Next, individual pixels, regions, and/or frames can be selectively discarded. This arbitrary region selection can be done automatically, e.g., by intensity thresholds, or manually by freehand drawing on either the full image stack or on a frame-by-frame basis. The voids created by the excluded data are accounted for in the correlation algorithms (15). Once the relevant pixels are selected, an image-correction step is performed to remove unwanted contributions from the data. As an example, in a RICS analysis, one is usually only interested in correlations caused by fast-diffusing particles, whereas spatial correlations from the cell shape and the slow movement of large cellular structures interfere with the useful signal. To remove the latter, it is useful to subtract the mean of the pixel intensity over several frames, removing static spatial heterogeneity while retaining fast fluctuations occurring within a few frames. To restore the original average intensity of the image, the mean pixel intensity of each frame or the complete image series is added back to the data. A variety of additional correction methods are available to remove particular contributions for the individual analysis methods (16).

The final step in MIA is the actual image-correlation calculation (11), either in 1D through time, 2D through space, or in 3D through both time and space, depending on the particular technique used. All correlation functions are displayed directly in MIA for a preliminary analysis, but the main interpretation is done in dedicated fitting modules: either FCSFit for 1D data (TICS and iMSD) or MIAFit for 2D (ICS, RICS) and 3D (STICS) correlation functions. MIAFit works similarly to FCSFit, as described in the previous section, but it is designed to analyze and display 2D data.

## Fluorescence lifetime image analysis using the phasor approach

FLIM uses the lifetime of dye molecules to obtain a spatial map of the FRET efficiency, quenching, or the presence of certain analytes in the sample. The phasor approach exploits concepts and rules of the fluorescence decay in the Fourier space to interpret FLIM data in a semiquantitative way without the need to fit the fluorescence decays to single- or multiexponential model functions (27).

The main workflow of phasor analysis in PAM is shown in Fig. 7. The first step involves the calculation of the phasor data for each individual pixel in the phasor panel of the main PAM GUI. This requires reference data with a known monoexponential lifetime that is used to remove the influence of the instrument response function. For TIFF-based time- or frequency-domain FLIM data, an additional module is provided to reference and calculate the phasor data. Once the phasor data are calculated, they are stored in an intermediate file for analysis with the Phasor module. Here, the intensity image is displayed together with a pixel-wise phasor histogram. The user has different options to establish a relationship between the two. The first is to select different ROIs in

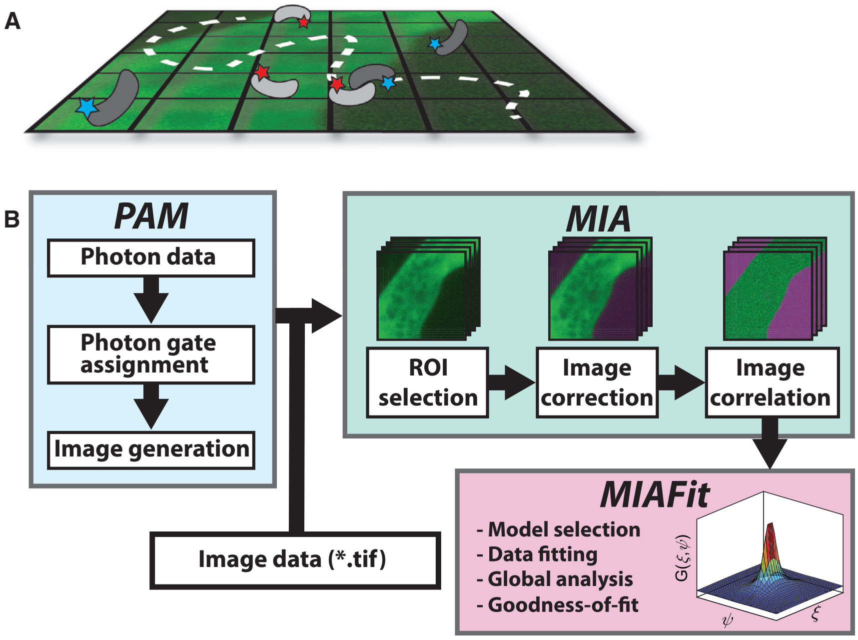

FIGURE 6 Fluctuation imaging in PAM. (*A*) In fluctuation imaging, the spatial heterogeneity or the temporal dynamics are recorded to analyze the diffusion and interactions of the studied molecules. (*B*) The workflow for image correlation spectroscopy in PAM is shown. The photon data is sorted into photon gates, and an image series is generated using the pixel, line, or image start-stop times. Alternatively, image data can be directly used for analysis in MIA. A region of interest is selected, and the appropriate corrections are applied to the image series in MIA, e.g., to remove static heterogeneities and slow cell movement. The image correlation function can be loaded in MIAFit for quantitative analysis by fitting to model functions. To see this figure in color, go online.

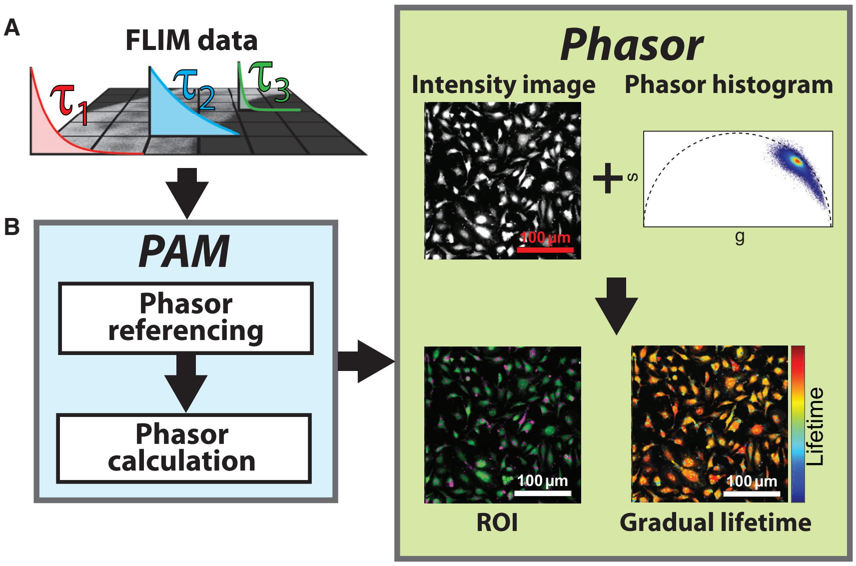

FIGURE 7 Phasor FLIM analysis in PAM. (*A*) In lifetime imaging, both the signal intensity as well as the information about the lifetime are recorded for every pixel and can be used to investigate molecular interactions or dynamics via FRET or to analyze the local environment of the fluorophores. (*B*) The workflow for Phasor-FLIM analysis in PAM is shown. A sample with known lifetime is used as reference for the pixel-wise phasor calculation. In the Phasor module, the data set can be explored using the phasor histogram to color-code the intensity image by the fluorescence lifetime, either by using regions of interest (ROIs) defined in the phasor space or by using a gradual lifetime scaling. To see this figure in color, go online.

the phasor plot. The selected pixels are then indicated with the corresponding color in the intensity images. This makes it easy to highlight different, clearly separated lifetime populations in the images. For the second method, the user defines a line or curve in the phasor histogram. The program then projects the pixel phasors on this line and encodes their relative position with a color-map. This is useful to indicate gradual changes of the lifetime. Lastly, it is also possible to plot a quenching trajectory, as is needed, for example, in systems undergoing FRET (53). By accounting for background-signal and unquenched-donor molecules, the FRET efficiency for the population can be estimated. The particular FRET value for the whole trajectory can be indicated in the intensity image via color-coding. As for all modules, all images, histograms, and selected trajectories can be exported to publication-ready plots.

## CONCLUSIONS

Here, we presented an overview of our in-house software package PAM, which has been developed and used for many publications from our laboratory and several other groups over the past years. It encompasses a multitude of different quantitative analysis methods within a well-structured and efficient workflow. With the design of PAM, we attempt to encourage novice users to experiment with new methods by providing a user-friendly interface, while simultaneously inviting expert users to contribute and extend the software and the underlying methods through open-source availability. The software is under continuous development with respect to improvements of the user experience and extension of implemented or addition of new methods. Current development projects include the implementation of spectrally resolved data, structure detection for particle- or cell-averaged analysis, and quantitative three-color FRET analysis.

### Availability

The software is available as source code, requiring MATLAB or a precompiled, standalone distribution for Windows or MacOS at http://www.cup.uni-muenchen.de/pc/lamb/software/pam.html or hosted in Git repositories under http://www.gitlab.com/PAM-PIE/PAM and http://www.gitlab.com/PAM-PIE/PAMcompiled. Sample data are provided under http://www.gitlab.com/PAM-PIE/PAM-sampledata. A detailed manual is found at http://pam.readthedocs.io.

## SUPPORTING MATERIAL

One figure, one table, and four data files are available at http://www.biophysj.org/biophysj/supplemental/S0006-3495(18)30295-9.

## AUTHOR CONTRIBUTIONS

A.B. and W.S. designed the core program and the correlation features. A.B. developed the FRET and lifetime sections. W.S. developed the image fluctuation and phasor sections. J.H. contributed to several modules and improved the overall usability of the program. D.C.L. supervised the project and offered advice on the feature development. All authors wrote the manuscript.

## ACKNOWLEDGMENTS

We gratefully acknowledge code contributions to an earlier version of the software from Volodymyr Kudryavtsev, Matthias Höller, Wolfgang Kügel, Martin Sikor, and Nikolaus Naredi-Rainer as well as contributions to ongoing development by Chen Qian, Nader Al Danaf, Philipp Messer (LMU Munich), Niels Vandenberk, and Guillermo Solís-Fernández (KU Leuven).

D.C.L. gratefully acknowledges the financial support of the Deutsche Forschungsgemeinschaft (SFB1032, B3 and SFB1035, A11) and of Ludwig-Maximilians-Universität through the Center for NanoScience and the

BioImaging Network. This work was supported by a grant from the Research Foundation Flanders (FWO Vlaanderen), grant number G0B4915N.

## REFERENCES

1. Widengren, J., V. Kudryavtsev, …, C. A. Seidel. 2006. Single-molecule detection and identification of multiple species by multiparameter fluorescence detection. *Anal. Chem.* 78:2039–2050.
2. Kudryavtsev, V., M. Sikor, …, D. C. Lamb. 2012. Combining MFD and PIE for accurate single-pair Förster resonance energy transfer measurements. *ChemPhysChem.* 13:1060–1078.
3. S. Y. Tetin, ed 2013. Methods in Enzymology, Fluorescence Fluctuation Spectroscopy (FFS), Part A. Elsevier, Amsterdam, the Netherlands.
4. S. Y. Tetin, ed 2013. Methods in Enzymology, Fluorescence Fluctuation Spectroscopy (FFS), Part B. Elsevier, Amsterdam, the Netherlands.
5. Zander, C., M. Sauer, …, C. A. Seidel. 1996. Detection and characterization of single molecules in aqueous solution. *Appl. Phys. B.* 63:517–523.
6. Lee, N. K., A. N. Kapanidis, …, S. Weiss. 2005. Accurate FRET measurements within single diffusing biomolecules using alternating-laser excitation. *Biophys. J.* 88:2939–2953.
7. Antonik, M., S. Felekyan, …, C. A. Seidel. 2006. Separating structural heterogeneities from stochastic variations in fluorescence resonance energy transfer distributions via photon distribution analysis. *J. Phys. Chem. B.* 110:6970–6978.
8. Kalinin, S., A. Valeri, …, C. A. Seidel. 2010. Detection of structural dynamics by FRET: a photon distribution and fluorescence lifetime analysis of systems with multiple states. *J. Phys. Chem. B.* 114:7983–7995.
9. Eggeling, C., J. R. Fries, …, C. A. Seidel. 1998. Monitoring conformational dynamics of a single molecule by selective fluorescence spectroscopy. *Proc. Natl. Acad. Sci. USA.* 95:1556–1561.
10. Felekyan, S., S. Kalinin, …, C. A. Seidel. 2012. Filtered FCS: species auto- and cross-correlation functions highlight binding and dynamics in biomolecules. *ChemPhysChem.* 13:1036–1053.
11. Petersen, N. O., P. L. Höddelius, …, K. E. Magnusson. 1993. Quantitation of membrane receptor distributions by image correlation spectroscopy: concept and application. *Biophys. J.* 65:1135–1146.
12. Hebert, B., S. Costantino, and P. W. Wiseman. 2005. Spatiotemporal image correlation spectroscopy (STICS) theory, verification, and application to protein velocity mapping in living CHO cells. *Biophys. J.* 88:3601–3614.
13. Kolin, D. L., D. Ronis, and P. W. Wiseman. 2006. k-Space image correlation spectroscopy: a method for accurate transport measurements independent of fluorophore photophysics. *Biophys. J.* 91:3061–3075.
14. Toplak, T., E. Pandzic, …, P. W. Wiseman. 2012. STICCS reveals matrix-dependent adhesion slipping and gripping in migrating cells. *Biophys. J.* 103:1672–1682.
15. Hendrix, J., T. Dekens, …, D. C. Lamb. 2016. Arbitrary-region raster image correlation spectroscopy. *Biophys. J.* 111:1785–1796.
16. Hendrix, J., W. Schrimpf, …, D. C. Lamb. 2013. Pulsed interleaved excitation fluctuation imaging. *Biophys. J.* 105:848–861.
17. Digman, M. A., R. Dalal, …, E. Gratton. 2008. Mapping the number of molecules and brightness in the laser scanning microscope. *Biophys. J.* 94:2320–2332.
18. Digman, M. A., C. M. Brown, …, E. Gratton. 2005. Measuring fast dynamics in solutions and cells with a laser scanning microscope. *Biophys. J.* 89:1317–1327.
19. Murphy, R. R., S. E. Jackson, and D. Klenerman. 2014. pyFRET: a python library for single molecule fluorescence data analysis. *arXiv.*
20. Ingargiola, A., E. Lerner, …, X. Michalet. 2016. FRETBursts: an open source toolkit for analysis of freely-diffusing single-molecule FRET. *PLoS One.* 11:e0160716.
21. Preus, S., S. L. Noer, …, V. Birkedal. 2015. iSMS: single-molecule FRET microscopy software. *Nat. Methods.* 12:593–594.
22. Müller, P., P. Schwille, and T. Weidemann. 2014. PyCorrFit-generic data evaluation for fluorescence correlation spectroscopy. *Bioinformatics.* 30:2532–2533.
23. Müller, B. K., E. Zaychikov, …, D. C. Lamb. 2005. Pulsed interleaved excitation. *Biophys. J.* 89:3508–3522.
24. Elson, E. L. 2013. 40 years of FCS: how it all began. *Methods Enzymol.* 518:1–10.
25. Felekyan, S., R. Kühnemuth, …, C. A. Seidel. 2005. Full correlation from picoseconds to seconds by time-resolved and time-correlated single photon detection. *Rev. Sci. Instrum.* 76:083104.
26. Nir, E., X. Michalet, …, S. Weiss. 2006. Shot-noise limited single-molecule FRET histograms: comparison between theory and experiments. *J. Phys. Chem. B.* 110:22103–22124.
27. Digman, M. A., V. R. Caiolfa, …, E. Gratton. 2008. The phasor approach to fluorescence lifetime imaging analysis. *Biophys. J.* 94:L14–L16.
28. Wiseman, P. W. 2013. Image Correlation Spectroscopy: Mapping Correlations in Space, Time, and Reciprocal Space, First Edition. Elsevier Inc, Amsterdam, the Netherlands.
29. Hendrix, J., V. Baumgärtel, …, D. C. Lamb. 2015. Live-cell observation of cytosolic HIV-1 assembly onset reveals RNA-interacting Gag oligomers. *J. Cell Biol.* 210:629–646.
30. Otosu, T., K. Ishii, and T. Tahara. 2013. Note: simple calibration of the counting-rate dependence of the timing shift of single photon avalanche diodes by photon interval analysis. *Rev. Sci. Instrum.* 84:036105.
31. Kapanidis, A. N., N. K. Lee, …, S. Weiss. 2004. Fluorescence-aided molecule sorting: analysis of structure and interactions by alternating-laser excitation of single molecules. *Proc. Natl. Acad. Sci. USA.* 101:8936–8941.
32. Lee, N. K., A. N. Kapanidis, …, S. Weiss. 2007. Three-color alternating-laser excitation of single molecules: monitoring multiple interactions and distances. *Biophys. J.* 92:303–312.
33. Lee, J., S. Lee, …, S. Hohng. 2010. Single-molecule four-color FRET. *Angew. Chem. Int. Ed. Engl.* 49:9922–9925.
34. Magde, D., E. Elson, and W. W. Webb. 1972. Fluorescence correlation spectroscopy. *Phys. Rev. Lett.* 29:705.
35. Schwille, P., F. J. Meyer-Almes, and R. Rigler. 1997. Dual-color fluorescence cross-correlation spectroscopy for multicomponent diffusional analysis in solution. *Biophys. J.* 72:1878–1886.
36. Weidemann, T., and P. Schwille. 2013. Dual-Color Fluorescence Cross-Correlation Spectroscopy with Continuous Laser Excitation in a Confocal Setup, First Edition. Elsevier Inc, Amsterdam, the Netherlands.
37. Felekyan, S., H. Sanabria, …, C. A. Seidel. 2013. Analyzing Förster Resonance Energy Transfer with Fluctuation Algorithms, First Edition. Elsevier Inc, Amsterdam, the Netherlands.
38. Dertinger, T., V. Pacheco, …, J. Enderlein. 2007. Two-focus fluorescence correlation spectroscopy: a new tool for accurate and absolute diffusion measurements. *ChemPhysChem.* 8:433–443.
39. Digman, M. A., and E. Gratton. 2009. Imaging barriers to diffusion by pair correlation functions. *Biophys. J.* 97:665–673.
40. Kapusta, P., M. Wahl, …, J. Enderlein. 2007. Fluorescence lifetime correlation spectroscopy. *J. Fluoresc.* 17:43–48.
41. Benda, A., P. Kapusta, …, K. Gaus. 2014. Fluorescence spectral correlation spectroscopy (FSCS) for probes with highly overlapping emission spectra. *Opt. Express.* 22:2973–2988.
42. Brooks Shera, E., N. K. Seitzinger, …, S. A. Soper. 1990. Detection of single fluorescent molecules. *Chem. Phys. Lett.* 174:553–557.
43. Schaffer, J., A. Volkmer, …, C. A. Seidel. 1999. Identification of single molecules in aqueous solution by time-resolved fluorescence anisotropy. *J. Phys. Chem. A.* 103:331–336.
44. Maus, M., M. Cotlet, …, C. A. Seidel. 2001. An experimental comparison of the maximum likelihood estimation and nonlinear least-squares

fluorescence lifetime analysis of single molecules. *Anal. Chem.* 73:2078–2086.

45. Tomov, T. E., R. Tsukanov, …, E. Nir. 2012. Disentangling subpopulations in single-molecule FRET and ALEX experiments with photon distribution analysis. *Biophys. J.* 102:1163–1173.
46. Clamme, J. P., and A. A. Deniz. 2005. Three-color single-molecule fluorescence resonance energy transfer. *ChemPhysChem.* 6:74–77.
47. Laurence, T. A., Y. Kwon, …, D. Barsky. 2007. Correlation spectroscopy of minor fluorescent species: signal purification and distribution analysis. *Biophys. J.* 92:2184–2198.
48. Srivastava, M., and N. O. Petersen. 1998. Diffusion of transferrin receptor clusters. *Biophys. Chem.* 75:201–211.
49. Krieger, J. W., A. P. Singh, …, T. Wohland. 2015. Imaging fluorescence (cross-) correlation spectroscopy in live cells and organisms. *Nat. Protoc.* 10:1948–1974.
50. Kolin, D. L., and P. W. Wiseman. 2007. Advances in image correlation spectroscopy: measuring number densities, aggregation states, and dynamics of fluorescently labeled macromolecules in cells. *Cell Biochem. Biophys.* 49:141–164.
51. Digman, M. A., P. W. Wiseman, …, E. Gratton. 2009. Detecting protein complexes in living cells from laser scanning confocal image sequences by the cross correlation raster image spectroscopy method. *Biophys. J.* 96:707–716.
52. Di Rienzo, C., E. Gratton, …, F. Cardarelli. 2013. Fast spatiotemporal correlation spectroscopy to determine protein lateral diffusion laws in live cell membranes. *Proc. Natl. Acad. Sci. USA.* 110: 12307–12312.
53. Hinde, E., M. A. Digman, …, E. Gratton. 2012. Biosensor Förster resonance energy transfer detection by the phasor approach to fluorescence lifetime imaging microscopy. *Microsc. Res. Tech.* 75:271–281.